UNIVERSITY OF SOUTHAMPTON

FACULTY OF NATURAL & ENVIRONMENTAL SCIENCES

School of Ocean and Earth Sciences

Trace Metal Chemistry of Hydrothermal Plumes

by

Alastair Jason Mackenzie Lough

Thesis for the degree of Doctor of Philosophy

August 2016

UNIVERSITY OF SOUTHAMPTON

ABSTRACT

FACULTY OF NATURAL & ENVIRONMENTAL SCIENCES

Ocean and Earth Sciences

Doctor of Philosophy

TRACE METAL CHEMISTRY OF HYDROTHERMAL PLUMES

by Alastair Jason Mackenzie Lough

This thesis examines the nature of trace metal cycling in hydrothermal plumes, which have only recently been recognized as a significant source of Fe to the oceans. To study the influence of hydrothermal vents and their plumes on global trace metal cycles, two “black smoker” type vents and a previously unrecognized type of off-axis venting are examined. The trace metal chemistry of previously uncharacterized vents from the Von Damm vent field (VDVF) and the Beebe vent field (BVF) on the Mid-Cayman Rise (MCR) are described along with the processes of colloid formation in plumes over the Mid-Cayman Rise. Also Fe isotope analyses of a hydrothermal plume in the Southern Ocean reveals distinct isotope signatures to deep-waters dependent on plume chemistry.

The role of soluble, colloidal and particulate partitioning of trace metals is understood to mediate the entire inventory of hydrothermal trace metals entering the ocean. In plumes over the MCR colloids are found to dominate dissolved iron (dFe) (48 to 87 % at Beebe and 14 to 81 % at Von Damm) in hydrothermal plumes. At Beebe soluble Fe (sFe) remains stable throughout plume dispersion, while particulate Fe is enriched (~25 %) by aggregating colloids. In the Von Damm plume colloidal Fe (cFe) and sFe maxima appear in the most dispersed regions of the plume where particulate Fe (pFe) is low. Plume processing of cFe and pFe will control the flux of dFe to the deep ocean from hydrothermal systems. This study shows that in order to accurately model the flux of dFe from vents, the behaviour of cFe needs to be incorporated into models of hydrothermal vent dFe fluxes, which at present do not consider these processes.

Iron isotopes provide a means to measure the impact of hydrothermal venting on the oceanic Fe inventory, but no studies have examined the mechanism producing hydrothermal dFe isotope compositions. This study demonstrates that δ^{56}Fe values of dFe (δ^{56}dFe) within the hydrothermal plume change dramatically during plume dispersal, ranging from -2.39 ± 0.05 ‰ to -0.13 ± 0.06 ‰ (2 SD). The isotopic composition of total dissolvable Fe (δ^{56}TDFe) was consistently heavier than dFe consistent with Fe oxyhydroxide precipitation as the plume ages. It is estimated that stable dFe exported from the plume will have a δ^{56}dFe of -0.28 ‰, and this provides the first highly resolved constraint on hydrothermal plumes as a source of dFe isotopes to the ocean interior. This suggests that this distinctive isotope signature can be used to trace plume dFe inputs to the deep ocean. This will help constrain the impact of hydrothermal Fe on ocean biogeochemistry.

Table of Contents

List of tables

List of figures

DECLARATION OF AUTHORSHIP

I, Alastair Jason Mackenzie Lough declare that this thesis and the work presented in it are my own and has been generated by me as the result of my own original research.

Trace Metal Chemistry of Hydrothermal Plumes ....

....

I confirm that:

1. This work was done wholly or mainly while in candidature for a research degree at this University;
2. Where any part of this thesis has previously been submitted for a degree or any other qualification at this University or any other institution, this has been clearly stated;
3. Where I have consulted the published work of others, this is always clearly attributed;
4. Where I have quoted from the work of others, the source is always given. With the exception of such quotations, this thesis is entirely my own work;
5. I have acknowledged all main sources of help;
6. Where the thesis is based on work done by myself jointly with others, I have made clear exactly what was done by others and what I have contributed myself;

7. Chapter 4 of this work has been submitted for publication and at the time of submission was under review in *Geochimica et cosmochimica acta*:

   Lough, A. J. M.a,b*, Klar, J. K., Homoky, W. B., Comer-Warner, S.A., Milton, J.A., Connelly, D. P., James, R. H., Mills, R. A.

   “Opposing controls on the isotopic signature of dissolved iron in hydrothermal plumes”

   Geochimica et cosmochimica acta, in review.

In which my contribution was the development and handling of the reported analytical work, sample analysis, writing the paper with advice from the co-authors, producing the figures and leading the responses to the peer reviews.

Signed: ....

Date:14/11/16 ....

Acknowledgements

I wouldn't have been able to complete this thesis without the support of my friends, family and work colleagues. Particularly my fiancé Emma, who has always encouraged me to look on the bright side when things were not going to plan and reminded me that a PhD is supposed to be difficult. Despite frequently asking me "when are you going to get a real job?" my family have always been interested in my research and I would of struggled over the last 6 months without the help of my parents, who probably thought they were done providing financial support for my studies.

I would also like to thank my supervisors, Rachel, Doug and Will, for their support and guidance over the last 4 years in helping me to complete this work. They have always encouraged me to develop my own ideas and been enthusiastic about my research throughout my PhD project. My panel chair Rachel James has also played a key role in keeping things on track and discussing my research and I am grateful to her for her help throughout.

With regards to the research presented in this thesis I am grateful to Matt Cooper for analysing the concentrations of elements in hydrothermal vent fluids and Sophie Comer-Warner for microscopy analysis of particles from Beebe and E2. Matt has always been available to answer any questions about lab stuff or vents and it was a great experience supervising Sophie through her MSc project. I am particularly grateful to Jessy Klar for taking the time to pass on her methods and good practices in analysing iron. It's been great fun working closely with her on iron isotopes making the long hours in the clean lab a lot easier. I would also like to thank Andy Milton, Jeff Hawkes, Christian Schlosser, Joaquin Pampin-Baro and Peter Statham who have all at one point or another passed on their wisdom of analytical methods helping me to develop my own lab work. Especially Andy who is never in too much of a hurry to go into the details of how a mass spectrometer works and Jeff who I learned a lot from during research voyages. I'd also like to thank Cathy Cole, Torben Stichel and Dakota Gibbs who I've enjoyed working alongside in the clean labs at different stages over the last 4 years.

I've been lucky enough to go through the PhD experience with some great friends from my office and the NOC PhD group who have kept me sane allowing me to de-stress over tea, coffee or beer. Especially the lunch club team of Gywn, Leigh and occasionally Laura who have been supportive throughout. Tim has always made excellent tea when he's not multi-tasking between watching question time and work. Everyone involved in the various re-incarnations of the NOC 5 a side football team, despite the vast number of players that rotate through the squad we still lose or draw more games than we win but it's always fun. Both research voyages I was involved in were amazing experiences and I'd like to thank everyone involved in JC80 and JC82 with special mention to the "A team" of Alfred and Anni who were an endless source of laughs during JC80. Massive thanks to Sam and Despo for making an awesome cake and sorting the post viva celebrations.

Definitions and Abbreviations

MOR	Mid-ocean ridge
ESR	East Scotia Ridge
SWIR	Southwest Indian Ridge
MAR	Mid-Atlantic Ridge
EPR	East Pacific Rise
E2	Hydrothermal vent field of the ESR
MORB	Mid-ocean ridge basalt
MCSC	Mid-Cayman spreading centre
VDVF	Von Damm Vent Field
BVF	Beebe Vent Field
BP	Buoyant Plume
NBP	Neutrally Buoyant Plume
LMSW	Low metal sea water
NOCS	National Oceanography Centre
ROV	Remotely operated vehicle
CTD	Conductivity, temperature and depth
OTE	Ocean Test Equipment
SAPS	Stand Alone Pump System
LSS	Light scattering sensor
Eh	Reductive potential
M	Moles per kilogram
nM	nano moles per litre
μM	micro moles per litre

mM	milli moles per litre
Fe	Iron
TDFe	Total dissolvable Fe
DFe	Dissolved Fe
PFe	Particulate Fe
CFe	Colloidal Fe
SFe	Soluble Fe
H_2S	Hydrogen sulphide
Cl^-	Chloride
Mg	Magnesium
SO_4^{2-}	Sulphate
Mn	Manganese
V	Vanadium
Pb	Lead
Ni	Nickel
Zn	Zinc
Cu	Copper
Cd	Cadmium
Co	Cobalt
REE	Rare earth element
ICP-MS	Inductively coupled plasma - mass spectrometry
MC-ICP-MS	Multi-collector inductively coupled plasma - mass spectrometry
LDPE	Low density polyethylene
PTFE	Polytetrafluoroethylene

UV	Ultra violet radiation
SB	Sub boiled
HNO_3	Nitric acid
HCl	Hydrochloric acid
S.D.	Standard deviation
Lod	Limit of detection

Chapter 1: Introduction

1.1 The behaviour and importance of trace metals in seawater

Phytoplankton in the oceans are responsible for half of the photosynthetic fixation of carbon (primary productivity) on Earth (Field et al., 1998). Iron is a key limiting nutrient for primary productivity in high nutrient low chlorophyll (HNLC) zones (Boyd et al., 2000) and Fe Limitation of primary productivity in the Southern Ocean has been hypothesised to be a key component in shifting the Earth's climate between glacial and interglacial cycles (Martin, 1990). Other trace metals (Ni, Cu, Zn, Co and Cd) display similar water column profiles to macronutrients (nitrate, phosphate, silicate) indicative of their role in biochemical processes (Moore et al., 2013). These elements are important for production of proteins and enzyme activity (Morel and Price, 2003) but can be toxic at elevated concentrations (Mann et al., 2002) or co-limiting at low concentrations (Morel et al., 1994) (Figure 1.1). Manganese has been shown to be co-limiting (Browning et al., 2014) in surface waters and is a useful tracer of hydrothermal input at depth (James and Elderfield, 1996).

Until recently there was limited data on the distribution of these elements globally. To improve data coverage the GEOTRACES programme began a large scale sampling effort to map the distribution of these elements in each of the ocean basins (Henderson et al., 2007). An inter-comparison of 13 global biogeochemical models showed that all struggle to fully re-produce the distribution of dissolved Fe (dFe) in the ocean (Tagliabue et al., 2016). With different models able to define dFe distribution features from specific sources but not all the features observed in the data (Figure 1.2).

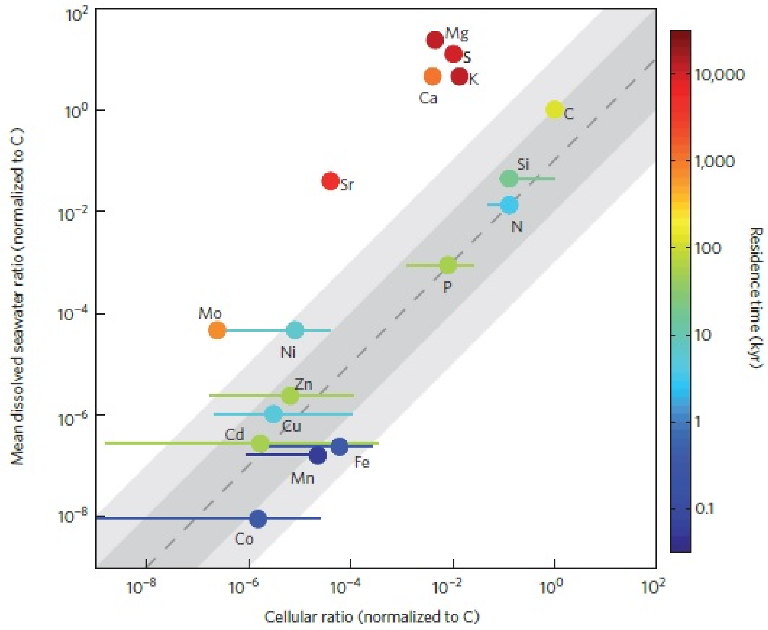

Figure 1.1 Representative (circles) and observed ranges (bars) of element ratios in phytoplankton (normalized to carbon) plotted against element ratios dissolved in seawater. Colours indicate ocean residence times with dark and light grey areas indicating <10 and <100 fold excesses and deficiencies relative to nitrogen. Hence elements in the grey areas have potential to limit or co-limit productivity. Taken from Moore et al. (2013).

This is shown in Figure 1.2 where the profiles simulated by the BEC model largely reflect mineral dust input to the eastern Atlantic surface ocean (<1000 m) with subsequent remineralization at depth. The distribution of dFe in the BLING model shows on average lower Fe concentrations with a more distinctive subsurface sedimentary plume coming in from the East and dFe depleted open ocean surface waters. The PISCES 2 model is the closest to re-producing the observed distribution of dFe (in this particular area of the ocean). Areas of dFe depletion in the open surface ocean and dFe enrichments in the eastern surface margin from PISCES 2 are similar to observations. PISCES 2 is the only model to show significant dFe enrichment over the Mid-Atlantic Ridge (MAR) similar to that observed in the N. Atlantic (Figure 1.2). The extent of the plume in the model appears to be greater than the observed plume. The three models shown in Figure 1.2 all include rivers, sediments and dust as Fe sources. Only BEC and PISCES 2 consider a hydrothermal dFe source. The differences in the average dFe concentrations of the models is a result of the differences in input and output fluxes which results in different residence times for dFe. For example; BEC has the highest dFe fluxes at a total of 124.5 Gmol yr^{-1} with a residence time of 8.1 yr, the total Fe flux into PISCES is 71.0 Gmol yr^{-1} with a lower residence time of 15.7 yr and the total Fe input to BLING is 12.4 with a residence time of 42.4 yr. Lower input fluxes into BLING result in lower average concentration for the N.Atlantic of 0.37 nM compared to BEC (0.74 nM) and PISCES (0.81 nM). The longer residence time of BLING promotes internal recycling of Fe compared to BEC and PISCES otherwise the average concentration would be even lower. Furthermore sediments represent the greatest flux of dFe in this model which partly explains why the sedimentary inputs from the Eastern margin are the most striking feature of the BLING cross-section (Figure 1.2). Of 13 models tested the ocean residence time of Fe ranged from 3.7 to 626.3 (Tagliabue et al., 2016). This reflects the variability in Fe sources used in the different models and also the variability in biological uptake, particle scavenging and re-mineralization rates that recycle Fe in the open ocean. For example PISCES 2 accounts for ligand production during re-mineralization which ensures that the deep ocean has on average higher Fe concentrations than the surface ocean. Overall all models performed poorly in attempts to re-produce observed ocean dFe however, the models that considered hydrothermal inputs largely performed better than models that did not consider a hydrothermal source (Tagliabue et al., 2016). Particularly when it came to simulating the distribution of dFe in the open ocean away from coastal regions. This underlines the importance of hydrothermal vents as a source of dFe to the open oceans in-comparison to other sources where there impact on carbon cycling is restricted to the ocean margins.

These results highlight the limited understanding of trace metal global biogeochemical cycles and the need to improve model simulations of trace metals, better quantifying the drivers and variability of the carbon cycle (Tagliabue et al., 2016). In order to fully understand the processes that control the distribution of trace metals in the modern ocean, studies that focus on the biogeochemical processes occurring at the boundary between the oceans and Fe sources such as sediments, hydrothermal systems, aerosols and ice are needed.

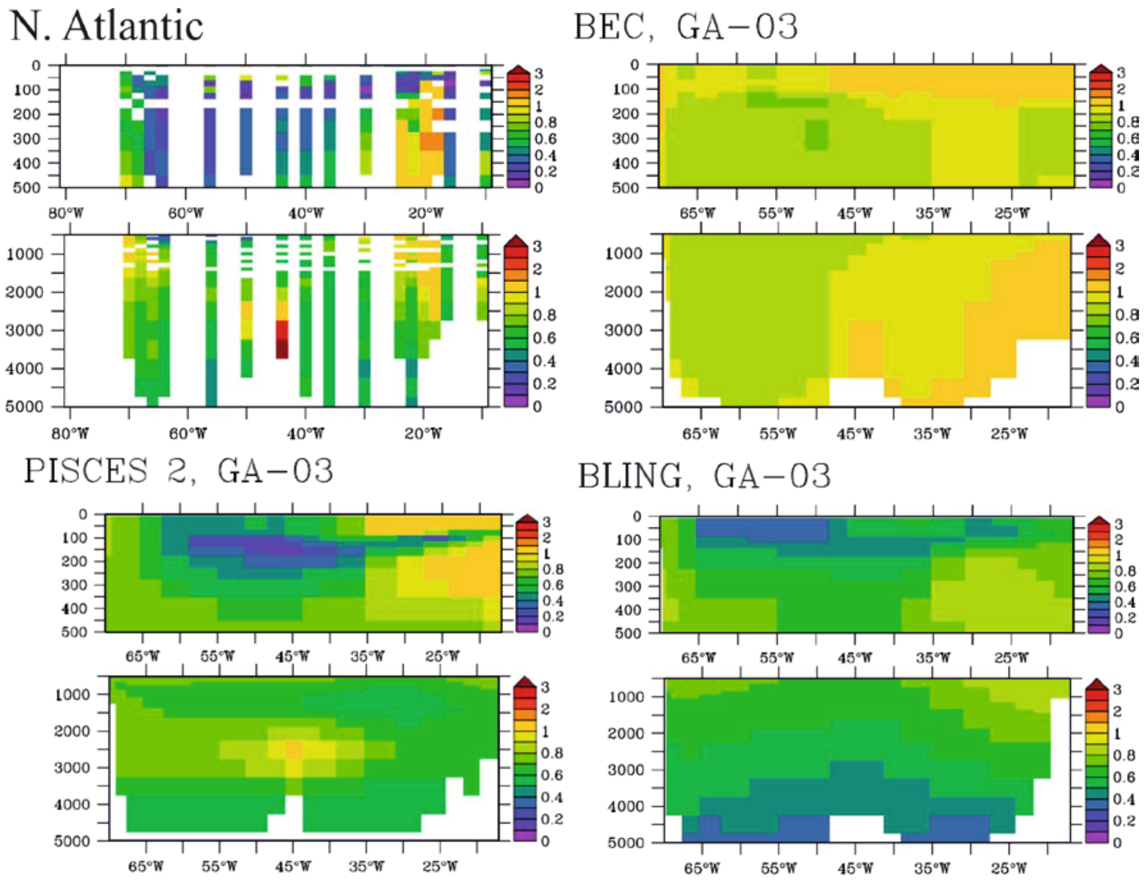

Figure 1.2 GA-03 is the measured ocean dFe concentrations through a section of the N. Atlantic (Hatta et al., 2015). Other panels show the predicted dissolved Fe distribution over the same section from 3 different biogeochemical models (Taken from (Tagliabue et al., 2016).

In the open ocean trace metals are present at nanomolar (nM) and picomolar (pM) concentrations. The concentration of trace metals in aqueous media is determined by the strength of metal complexation with ligands, the solubility of hydroxide and carbonate species and adsorption onto organic and inorganic solids. Metal complexation by dissolved organic matter (usually bi or polydentate ligands) allows metals to be present in the ocean at higher concentrations than would be predicted from equilibrium with inorganic hydroxide and carbonate species (monodentate ligands) alone. Typically organic ligands have more than one donar atom able to associate with the central metal atom and therefore may form stable metal complexes. Organic polydentate ligands are referred to as chelates as the ligands surround the central metal atom. In the surface ocean phytoplankton are known to release organic ligands as a method of obtaining metals (Morel and Price, 2003).

Polynuclear clusters are an intermediary between individual metal complexes and larger nanoparticles or colloids where there is more than one metal atom present with bonding between these metal atoms. All of these species can be separated from a bulk sample by ultrafiltration.

The separation of trace metals between dissolved (usually operationally defined as anything passing through 0.2 µm pore size of filters) and solid particulates (usually operationally defined as anything >0.2 µm) is complicated by colloids, which are typically characterised as being 0.001 to 0.4 µm. Colloidal particles are smaller than the filters typically used in environmental science, which have pore sizes of 0.2 or 0.45 µm (Figure 1.3). Generally colloids behave more like particles than aqueous species i.e. the surface charge of the colloid will dictate chemical behaviour rather than the charge of individual atoms dictating chemical reactions. The behaviour of colloids is highly dependent on their size and is increasingly dictated by surface charge with larger sized colloids. The large surface area and charged surface of particles such as Fe oxyhydroxides means they are highly efficient at adsorbing other elements (This is discussed further in section 1.3). In solutions with high ionic strength such as seawater colloidal aggregation is promoted by the solvation effect (dipole related interactions between water molecules and ions in solution) (Mylon et al., 2004). This means that smaller colloids which are less stable due to a larger surface area will tend to aggregate to form a larger more stable particle with less exposed surface area relative to its volume (Baumgartner and Faivre, 2015). The rate at which this process proceeds can also be dictated by the adsorption of organic matter onto inorganic colloidal particles (Mylon et al., 2004). The term colloid can refer to either organic or inorganic species produced biotically or abiotically. There is evidence to suggest that colloids can also be used as nutrients by phytoplankton in the surface ocean (Fitzsimmons et al., 2015, Birchill, 2016). Small bacteria and viruses are also included in this size fraction that will contain metals present in enzymes and other cell structures that will add to the concentration of metals in the colloidal size fraction.

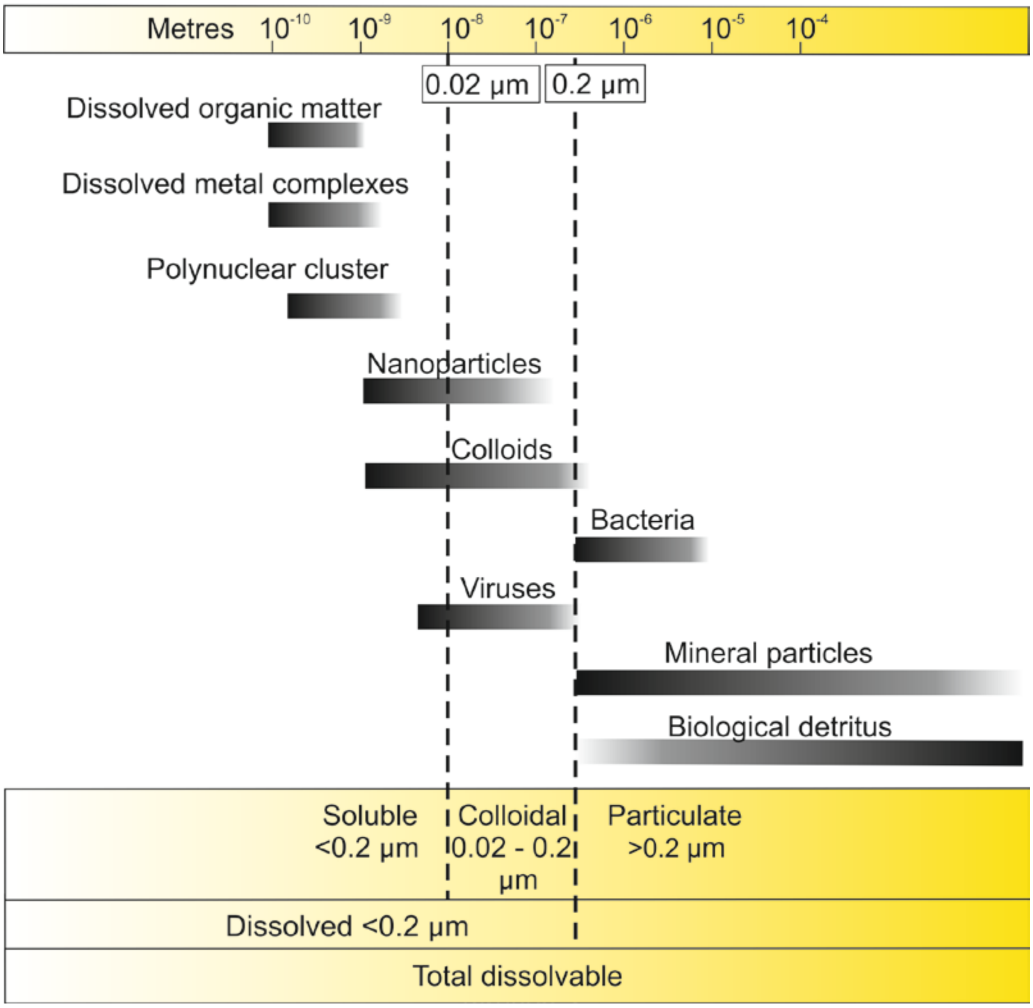

Figure 1.3 Different chemical species that add to the concentration of trace metals in different size fractions. The pore sizes of filters typically used are shown by dashed lines. Soluble, dissolved and total dissolvable are the operational definitions used in this study. Total dissolvable is defined as anything that dissolves in an unfiltered sample after being acidified with 1 µl HNO_3 per ml of sample for >1 year. The colloidal fraction is derived as the difference between soluble and dissolved. In some instances, the particulate fraction is derived from the difference between dissolved and total dissolvable.

It is important to stress at this point that there is no clear chemical differences between colloids and nanoparticles and these two terms have often been used interchangeably in chemical oceanography research. Recent research in chemical oceanography uses the term nanoparticles when referring to species of inorganic mineralogical composition such as FeS_2 nanoparticles. The term colloids is more often used when discussing species in the 0.2 to 0.02 μm size range that may be an inorganic colloid associated organic matter or composed entirely of dissolved organic matter. The terms nanoparticles and colloids are used throughout this thesis consistent with these definitions.

Larger mineral particles will precipitate from solution due to the insolubility of metal oxide and carbonate phases in oxygenated waters or precipitate as sulphides under reducing conditions. Metals will also accumulate in living organisms and larger phyto and zoo plankton will be part of the particulate fraction. When organisms die and decay the biological detritus of large particulate organic matter (POM) can adsorb metals by forming inner sphere complexes with carboxyl and hydroxyl functional groups on the surface of the particle (Balistrieri et al., 1981, Guo et al., 2006). This process is often referred to as scavenging and is an important mechanism for exporting metals from the deep ocean to sediments. Metals on the surface and within POM will be released during remineralization and therefore the balance between scavenging and remineralization is important in controlling the concentration of metals in the deep ocean (Johnson et al., 1997).

Concentrations and the speciation of trace metals in the ocean are affected by the supply of these elements from different sources and sinks and the equilibrium conditions with other chemical species that form complexes with metals. Of the trace metals with the potential to limit primary productivity Co, Mn and Fe are deficient relative to N (Figure 1.1). Fe has a higher biological demand as whilst some elements can substitute for Mn and Co in metal containing enzymes Fe often cannot be substituted and is a requirement for chlorophyll production (Morel and Price, 2003, Saito et al., 2008, Dupont et al., 2010) therefore Fe supply is more prone to limiting primary productivity and for this reason is considered to be the most important trace metal in the ocean. This is why research in this area largely focuses on Fe and why this study will focus on Fe.

Until recently the main sources of dissolved Fe to the ocean were considered to be aeolian dust particles dissolving in the surface ocean and transfer of dissolved iron from sediment pore waters to the overlying water column (referred to as the benthic Fe shuttle). Hydrothermal vents represent a potentially important and previously overlooked source of iron to the ocean.

1.1.1 Sources of dissolved Fe to the ocean

The global ranges of fluxes from multiple sources that deliver Fe to the ocean are shown in Figure 1.4. The contribution from each of these sources to the dissolved Fe (dFe) ocean reservoir varies geographically and temporally over annual and geological time scales. This is reflected in the range of values for each Fe source in Figure 1.4 and hence global fluxes are difficult to constrain. From the range of fluxes presented in Figure 1.4 it is apparent that dust provides the largest amount of Fe followed by, freshwaters, sediments and then finally hydrothermal vents.

The extent of atmospheric dust deposition into the oceanic dFe inventory depends on the mineralogy of dust particles and their resultant dissolution rate in rain or seawater (Mahowald et al., 2006). Estimates of fractional solubility for dust particles range from 2-17 % (Moore et al., 2004, Fan et al., 2006) with a further 3 % dissolving as dust particles sink through the water column (Moore et al., 2004). In the Equatorial Atlantic dust fluxes are a more significant source of Fe to the surface ocean due to large inputs of dust blown from the Saharan desert. In the Southern Ocean upwelling and freshwater fluxes are more important as the land masses are ice covered.

River waters have higher dFe concentrations than seawater, however uptake by phytoplankton and flocculation in estuaries causes aggregation of Fe colloids that removes up to 90% of dFe (Mylon et al., 2004). As a result the vast majority of Fe from this source does not reach the open ocean as it is used up by primary production in coastal waters.

Other freshwater fluxes to the ocean include sub glacial and iceberg melt-waters. Concentrations of dFe in oxic sub glacial melt waters range between 2-200 nM (Statham et al., 2008, Wadham et al., 2013). Higher concentrations of 3-3000 µM have been measured in anoxic sub glacial melt waters, however much of this dFe may precipitate as Fe oxyhydroxides beneath the glacier or on the continental shelf (Wadham et al., 2013). Few studies have assessed the flux of dFe from ice berg melt. Concentrations of 0.69 nM in ice melt from Antarctic icebergs that contain potentially bioavailable nanoparticulate goethite indicate ice melt is a significant source of dFe for ice-marginal seas, but globally it is a small flux compared to other sources (Raiswell et al., 2008). Similarly to other freshwater Fe sources any Fe fertilization from glaciers or icebergs will be restricted to waters adjacent to the ice.

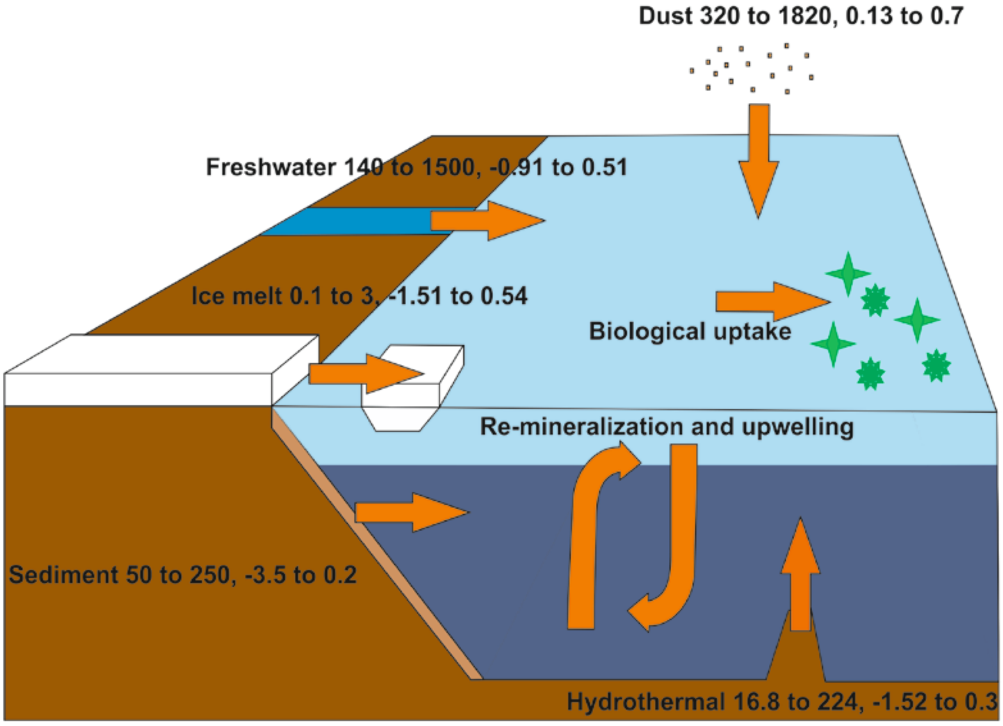

Figure 1.4 Schematic diagram of the Fe biogeochemical cycle. All flux estimates are in units of Gg dFe y^{-1} followed by measured δ^{56}Fe relative to IRMM014 per mil (‰). Flux estimates from Jickells et al. (2005), Tagliabue (2010), Raiswell (2012), Bennett et al. (2008), Carazzo et al. (2013), Fitzsimmons et al. (2014) and Resing et al. (2015). δ^{56}Fe values from Sharma et al. (2001), Beard et al. (2003), Escoube et al. (2009), Homoky et al. (2013) and Conway and John (2014f) .

Diagenetic recycling of sediment on the continental shelf is another source of dFe to the ocean and the extent of this flux depends on supply of organic carbon to the seafloor (Elrod, 2004). Organic carbon produces pore waters rich in Fe(II) as a result of microbial reduction and dissolution of iron minerals during anoxic diagenesis. The Fe supply from sediments further depends on the mineralogy of Fe-bearing lithogenic phases (Homoky et al., 2011), the penetration depth of oxygen from the overlying water column into sediments (Homoky, 2012, Homoky et al., 2013) and the amount of bio-irrigation (Elrod, 2004, Severmann et al., 2006). The presence of Fe rich mineral phases is required as a source of Fe for pore waters. The diffusion of Fe rich pore waters to the overlying water column can be restricted by the depth of oxygen penetration from the overlying water column into sediments. Highly porous sediments will create a larger oxic surface layer of sediment causing Fe (II) to precipitate as Fe oxyhydroxides and not be transferred to the overlying water column. Bio-irrigation by benthic organisms can aid Fe (II) diffusion from the anoxic layer by providing an advection pathway through the oxic layer of sediments (Aquilina et al., 2014). Unlike freshwater sources the input of Fe from sediments at depth allows for some Fe export from ocean margins to the open ocean. This processes has been termed the benthic Fe shuttle and is considered a particularly important processes during the Phanerozoic when oxygen was restricted to the surface ocean and anoxia at depths allowed transport of Fe(II) diffusing from sediments with minimal oxidation to Fe (III) and subsequent Fe oxyhydroxide formation (Severmann et al., 2008). In the modern ocean the oxic benthic shuttle of Fe is facilitated by the formation of colloids and ligand complexation in porewaters as well as the presence of oxygen minimum zones overlying sediments (Fitzsimmons et al., 2015, Homoky et al., 2011). The flux of dFe from these sediments is likely to have the largest impact on surface waters in upwelling regions adjacent to oxygen minimum zones as well as supplying an amount of Fe to the open ocean (Bruland et al., 2005, Elrod, 2004, Siedlecki et al., 2012). The impact of Fe fluxes from the oxic benthic shuttle is expected to increase as oxygen minimum zones expand due to warming and stratification of the worlds surface ocean lowering oxygen concentration of the ocean interior (Keeling et al., 2010).

Aeolian dust may represent one of the largest fluxes of dFe to the surface ocean (Figure 1.4) but this source is highly variable over decadal to millennial time scales (Mahowald et al., 2006) due to natural changes in land vegetation and desertification. This variation could be enhanced by anthropogenic land use removing or increasing vegetation. Terrestrial and continental shelf sources of Fe are also likely to be sensitive to the predicted changes in sea level, sediment distribution, organic matter inputs, and coastal anoxia resulting from anthropogenic climate change (Homoky et al., 2013, Lohan and Bruland, 2008, Pakhomova et al., 2007). Fe fluxes from sediments depend on high organic carbon input from coastal regions and freshwater inputs are restricted to coastal regions. In all the above cases the majority of Fe supplied from these sources is restricted to the ocean margins. Although dust is transported offshore and is a source to surface waters this is restricted to certain regions i.e. N. Atlantic whereas hydrothermal vents are present throughout all ocean basins. Whilst hydrothermal vents provide a potentially smaller flux of Fe to the oceans compared to these other sources they are the only Fe source that supplies Fe directly to the open ocean across all ocean basins. This makes them a particularly important source of Fe to the Southern Ocean where dust, sedimentary and freshwater inputs are limited. It has recently estimated that Fe supply from hydrothermal vents may support between 15 to 30 % of carbon export in the modern Southern Ocean (Resing et al., 2015). It is therefore important to investigate the hydrothermal Fe flux as it causes a significant amount of Fe fertilization in the Southern Ocean which results in carbon export from the atmosphere to the deep ocean influencing the Earth's climate.

1.2 Hydrothermal Circulation

Active hydrothermal vent fields are located near spreading centres of the Earth's crust (Figure 1.5) where magma in the ocean crust acts as a heat source driving hydrothermal circulation through rocks with sufficient permeability.

Hydrothermal circulation occurs as ocean water percolates down through cracks in the ocean crust. As this water comes into close proximity with shallow magma bodies the water is conductively heated to temperatures of up to 450°C reacting with the surrounding rock of the ocean crust. This process is referred to as the reaction zone (Figure 1.6). In this zone, anhydrite and smectite minerals form removing magnesium and sulphate from the fluid, decreasing the pH of the fluid to between 5 or 6 (German and Von Damm, 2004). The increased acidity and temperature results in leaching of metals from host rocks. The resulting fluid is enriched in transition metals and rare earth elements (Michard et al., 1983, Campbell et al., 1988, Trefry et al., 1994, Von Damm, 1995). Volatile gases such as H_2, CH_4, H_2S, CO_2 and ^3He are also incorporated by magmatic degassing and inorganic synthesis (Butterfield and Massoth, 1994, Welhan, 1988) as well as being produced from water-rock reactions.

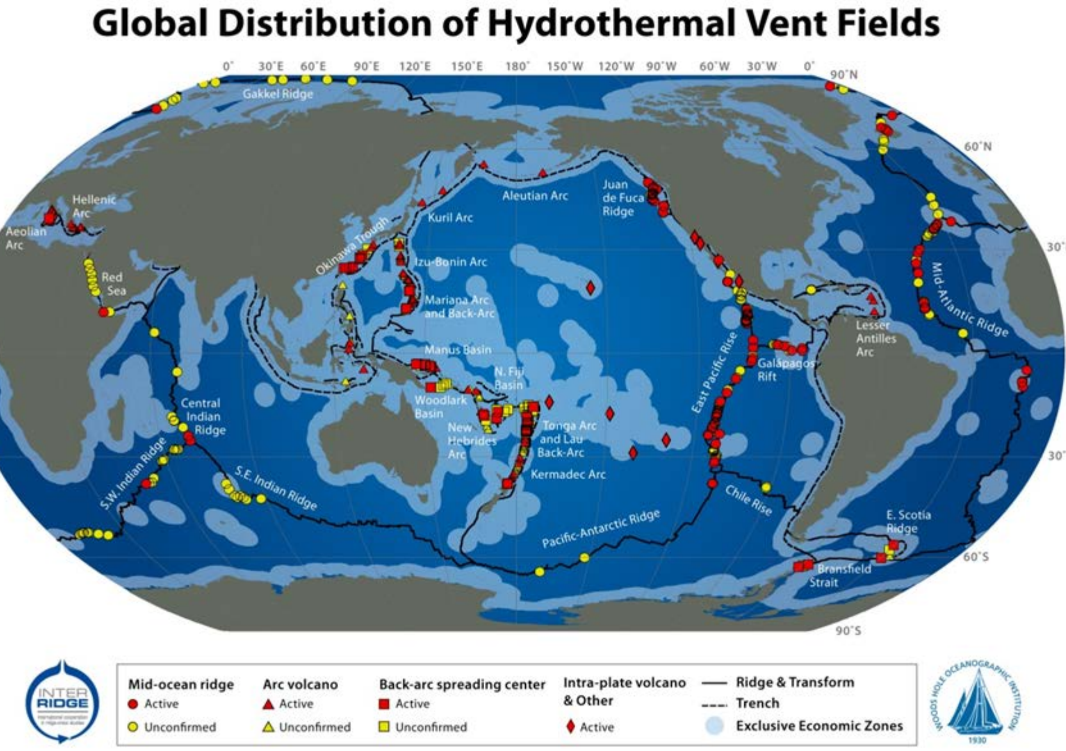

Figure 1.5 The global distribution of hydrothermal vents discovered so far. Red symbols show vents that have been visually confirmed and yellow symbols are vent sites inferred from water column anomalies. Taken from the inter ridge society (http://www.interridge.org).

Phase separation of the hydrothermal fluid occurs in the reaction zone if the critical temperature or pressure of water is reached. At depths of 2000 m - 3000 m where many hydrothermal vent fields are located, phase separation occurs in the reaction zone when temperatures reach >400 °C (Bischoff and Pitzer, 1985). Phase separation partitions the circulating waters into a brine phase and a vapour phase. Concentrations of Cl^- are higher in the brine phase and thus cations remain in this phase complexed by Cl^- with the vapour phase enriched in the volatile gases (German and Von Damm, 2004). Subsequently vent fluids exiting hydrothermal vents always have Cl^- concentrations different to the concentration of Cl^- in seawater. This difference is used as an indicator of the degree of phase separation in the subsurface (Bischoff and Pitzer, 1985).

As a result of the conductive heating in the reaction zone the hydrothermal fluid rises back up through the crust under its own buoyancy and is expelled into the overlying seawater. Some of the hydrothermal fluid is focused through hydrothermal vent chimneys or diffuses from cracks (Figure 1.6). Vent chimneys form as anhydrite precipitates from Ca^{2+} and SO_4^{2-} in seawater that is heated to temperatures >150 ˚C and mixes with the fluid being expelled from the crust (Von Damm, 1990). The precipitation of anhydrite forms the framework of the chimney that confines the vent fluid. This slows the process of mixing between seawater and vent fluid. The fluid within the chimney structure cools at a slower rate as a result. This allows metal sulphide minerals to precipitate within the anhydrite structure as the fluid cools and becomes super-saturated with respect to these solid phases (Haymon, 1983).

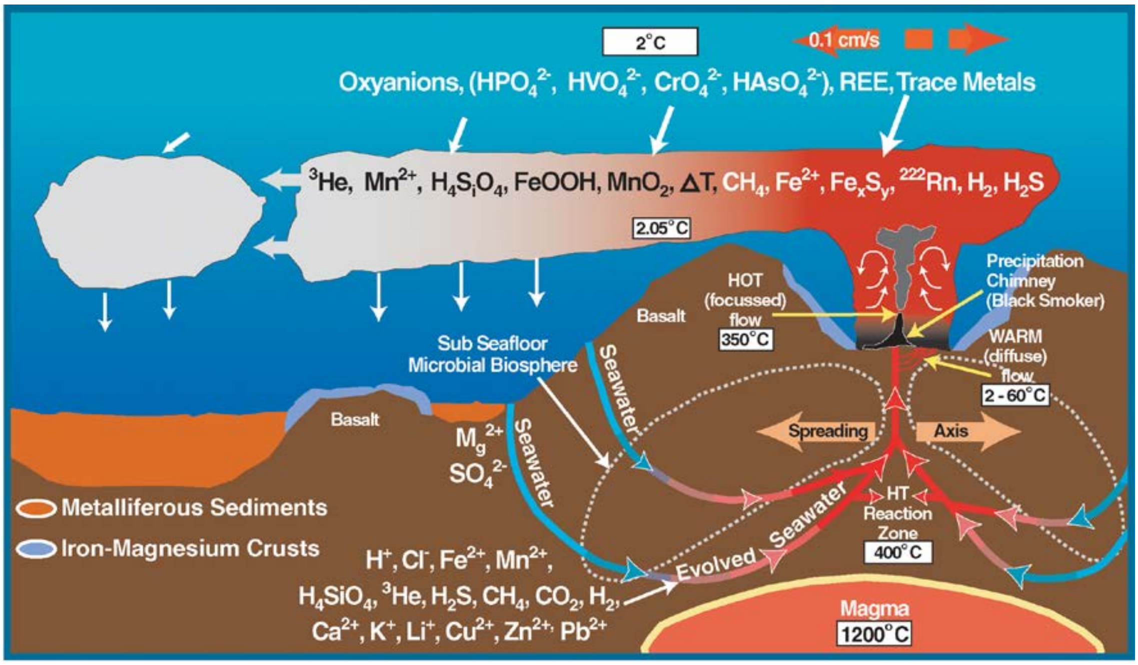

Figure 1.6 Conceptual diagram of hydrothermal circulation through the crust and the resulting hydrothermal plume (Rawls, 1998). Chemical species leeched from the crust by the fluid are labelled at the bottom on the crustal part of the diagram. Species enriched in the hydrothermal plume relative to seawater are labelled on the plume. Species scavenged from seawater are labelled at the top.

Hydrothermal vents have been discovered near spreading centres of mid-ocean ridges and back arc basins at a range of depths from 5000 m (Connelly et al., 2012) to 750 m (Kelley et al., 2001) in crustal rocks of basalt to peridotite composition. Vents in different geological settings at different depths display a wide range of differing chemical compositions. For example, concentrations of Fe and H_2S range from 24,000 – 2 µM and 141,500 – 46.5 µM respectively.

1.3 Hydrothermal Plumes

Hydrothermal plumes occur in the water column over sites of active venting where buoyant hydrothermal fluids are expelled from hydrothermal vents. Chemical processes active during the dispersion of the hydrothermal plumes modify the chemical composition of the plume compared to that of the hydrothermal vent source. In order to calculate chemical fluxes from hydrothermal vents to the ocean an understanding of the processes that occur as the vent fluid mixes with seawater in the plume is essential.

The distinct chemistry of hydrothermal plumes in comparison to seawater is used to locate new hydrothermal vent fields. Typically plumes are detected by anomalies in temperature, salinity, reduction potential (Eh) and particulate material present in the water column.

At the boundary between the crust and the overlying ocean the hot (>300 ˚C), acidic, metal rich vent fluid mixes with cold (<2 ˚C) oxic seawater. Mixing with seawater immediately cools the vent fluid and Fe, Zn and Cu form sulphide mineral particles with dissolved H_2S (pyrite, chalcopyrite, sphalerite). The formation of these particles creates the optical illusion of black smoke coming from the vent, which is why hydrothermal vents where this occurs are named black smokers.

The temperature difference between the hot venting fluid and the cold stratified ocean causes the plume to rise up through the water column under its own buoyancy progressively entraining seawater and cooling. The rising stage of the plume is referred to as the buoyant plume. When the density of the rising plume matches that of the surrounding seawater the plume rises no further. This happens when the vent fluid is diluted by a factor of 8000-10,000 by mixing with the surrounding seawater (McDuff, 1995). This stage of the plume is referred to as the neutrally buoyant or non-buoyant plume (NBP).

Once the plume attains neutral buoyancy with the surrounding water it disperses laterally depending on the movement of surrounding water masses.

Hydrothermally altered seawater is also discharged from areas of diffuse venting adjacent to hydrothermal vents and on the ridge flanks. These areas of venting are more widespread than the focussed flow from hydrothermal vents. The water flowing from areas of diffuse venting is lower in temperature and not as acidic in comparison to focussed flow from vents. Due to the lower acidity and temperature of these fluids, less metal is leached from the host rocks so concentrations of trace metals in these diffuse fluids is lower than that of high temperature vents. The metal concentration is also lower as a result of seawater mixing in the subsurface and precipitation of metal sulphides. Fluids from diffuse venting are less buoyant than higher temperature venting and therefore cannot rise to the same vertical extent. Therefore diffuse fluids are not dispersed to the same extent as high temperature vent fluids. The lack of dispersion and the lower enrichment of trace metals means the impact of diffuse areas of venting on global biogeochemical cycles of trace metals is likely to be much less in comparison to focussed flow from hydrothermal vents.

The amount of Fe that immediately precipitates as metal sulphides as vent fluids mix with seawater depends on the ratio of Fe to H_2S and other chalcophile elements such as Cu and Zn. Where a significant amount of sulphide is present in vent fluids relative to Fe, Fe sulphides (FeS and FeS_2) precipitate (Klevenz et al., 2011). During buoyant plume rise dFe remaining in the plume undergoes further mixing with entrained oxic seawater, oxidising Fe (II) to Fe (III), which precipitates as Fe oxhydroxides (Mottl and McConachy, 1990). At vent sites where fluids circulate through ultramafic lithologies, Fe precipitates in the buoyant plume mainly as Fe oxyhydroxides. There is little Fe sulphide formation in these plumes as the vent fluids have low sulphide concentrations (Douville et al., 2002).

The formation of Fe oxyhydroxide particles in hydrothermal plumes causes the co-precipitation and scavenging of oxyanions of uranium, vanadium, phosphorus, chromium, arsenic (Feely et al., 1996, Edmonds and German, 2004, Hawkes et al., 2014) and rare earth elements (Klinkhammer et al., 1983). The term scavenging is used to describe the transfer of elements from the dissolved to the particle phase. Scavenging encompasses several processes which include adsorption of solutes at the mineral surface as hydrated species, absorption of the solute into the surface mineral structure or ion exchange. During ion exchange an ion becomes sorbed to the mineral surface by changing places with a similarly charged ion previously sorbed to the surface. These processes are the result of exposed ions of mineral surfaces which have an unsatisfied bond resulting in charged mineral surfaces. The mineral surface acts as an amphoteric substance and therefore the surface charge changes with pH. Fe oxyhydroxides are particularly efficient at scavenging due to their amorphous structure which provides a large surface area relative to volume. At seawater pH (<7.6) the surface of Fe oxyhydroxides has an overall positive charge and therefore adsorbs negatively charged ions such as VO_4^{3-}, PO_3^{4-}, CrO_4^{2-}, AsO_4^{3-} with positively charged REEs adsorbing to specific OH^- sites. If the mineral continues to grow sorbed elements will be either incorporated into or trapped within the mineral structure depending on the size to charge ratio of the element. This results in a non-homogenous mineral structure and the substitution of elements within the mineral structure is referred to as solid solution. Through the processes of Fe oxyhydroxide particle scavenging hydrothermal activity has a direct influence on the biogeochemical cycles of U, V, P, As, Cr, REEs and other scavenged elements.

The rate at which Fe (II) is oxidised to Fe (III) is an important control on particulate Fe oxyhydroxide formation and hence the concentration of dFe in the hydrothermal plume (Field and Sherrell, 2000). If Fe (II) is added to well oxygenated seawater the Fe(II) will precipitate entirely as Fe oxyhydroxides within 10 mins. The pseudo-first order rate constant (k_1) for Fe (II) oxidation is shown below in equation 1.1.

1.1

$$-d\frac{[Fe(II)]}{dt} = k_1\,Fe[(II)]$$

Which is a second degree function of pH as follows in equation 1.2 (Millero et al., 1987):

1.2

$$k_{1=}k\,[O_2][OH^-]^2$$

Giving the overall rate constant as:

1.3

$$-d\frac{[Fe(II)]}{dt} = k\,Fe[(II)][O_2][OH^-]^2$$

Where oxidation rate is faster at increased concentrations of Fe (II), oxygen and higher pH. The effect of ionic strength (*I*) and temperature (*T*) (in Kelvin) on the reaction rate are:

$$\log k = \log k_0 - 3.29\, I^{\frac{1}{2}} + 1.52\, I \qquad 1.4$$

1.5

$$\log k_0 = 121.56 - \frac{1545}{T}$$

Equation 1.4 shows that increased ionic strength will result in slower oxidation rates and equation 1.5 shows a decrease in temperature will also result in slower oxidation rates. In the deep ocean there is negligible change in ionic strength and temperature and changes in Fe(II) oxidation rates are largely determined by changes in oxygen concentration and pH. The pseudo first order oxidation half-life of Fe (II) varies with changes in oxygen and pH between deep ocean basins from 2.1 minutes in the relatively oxygenated, high pH Atlantic, to 6 hours in the less oxygenated, and more acidic Pacific (Millero et al., 1987, Field and Sherrell, 2000, Statham et al., 2005). For example, the slower oxidation rate of Fe in the Pacific results in more plume dilution before Fe (II) is oxidised to Fe (III). This decreases the chances of Fe oxyhydroxide nanoparticles coagulating to form larger Fe oxyhydroxide particles (Field and Sherrell, 2000) which will settle out of the water column to sediments faster.

1.3.1 Hydrothermal vents as an Fe source “The leaky vent hypothesis”

Initial studies of mid-ocean ridge axial high temperature and diffuse low temperature hydrothermal sites estimated gross fluxes of Fe to the ocean of 2.3-19 x10^{10} mol y^{-1}, this is approximately equal in size to the estimated flux from rivers of 2.3 x10^{10} mol y^{-1} (Elderfield, 1996). The net input of dFe to deep waters from this flux however was considered to be negligible due to Fe mineral precipitation and settling of these particles close to the vents, creating metal rich sediments proximal to vents (Elderfield, 1996, Mottl and McConachy, 1990) (Figure 1.6).

Concentrations of Fe in vent fluids can be as much as seven orders of magnitude greater than that in seawater. Therefore, even if a small amount of this Fe remains in the dissolved fraction it can have a significant impact on the ocean dFe reservoir. In recent years with the advent of high resolution sampling programmes and new techniques for analysing trace elements, hot spots of Fe (concentrations ~80 nM) have been observed in the Atlantic (Conway and John, 2014f), Indian (Nishioka et al., 2013) Pacific (Wu et al., 2011a, Fitzsimmons et al., 2014) Arctic (Klunder et al., 2012) and Southern Oceans (Klunder et al., 2014, Klunder et al., 2011). Hot spots of high Mn have been observed in the Atlantic (Noble et al., 2012), Arctic (Middag et al., 2011), Pacific (Fitzsimmons et al., 2014) as well as higher concentrations of Zn in the North Atlantic (Conway and John, 2014a).

Several mechanisms have been proposed to explain the transport of dFe from hydrothermal vents. The complexation of Fe (III) by organic ligands prevents the formation of Fe (oxyhyr)oxides particles stabilising 4-7.5 % of the total hydrothermal Fe emitted from a vent in the dissolved fraction (Bennett et al., 2008, Hawkes et al., 2013a). The formation of inorganic and organic Fe colloids in the hydrothermal plume will also facilitate the transport of hydrothermal dFe off-axis away from vent sites (Sands et al., 2012, Yucel et al., 2011, Fitzsimmons et al., 2014).

In comparison to other fluxes the hydrothermal flux of dFe may be relatively constant over millennial time scales (Tagliabue, 2010). Therefore, the addition of hydrothermal dFe to the deep ocean and the resulting supply of dFe from upwelling deep waters to the surface ocean is a potentially continuous source of dFe in paleoenviroments when other inputs of dFe were minimised or sporadic. The relatively constant supply of dFe from hydrothermal vents may provide a baseline amount of dFe to the ocean over geological time scales buffering the Fe cycle against any changes in the more variable dFe sources. Moreover hydrothermal vents have been identified as particularly important dFe source to the Southern Ocean where there is negligible input of Fe from dust and sediments (Tagliabue, 2010, Resing et al., 2015). Hydrothermal Fe inputs maybe responsible for between 15 to 30 % of carbon export to the deep ocean from the modern Southern Ocean (Resing et al., 2015). Changes in carbon export from the Southern Ocean are considered to be the most important factor in drawing down atmospheric CO_2 and shifting the Earth's climate from interglacial to glacial periods.

In order to better predict how the Fe cycle influences the drawdown of carbon via the biological pump it is important to understand how hydrothermal vents supply dFe to the ocean. To do this the chemical processes in hydrothermal plumes that control the flux of dFe from hydrothermal vents to the ocean needs to be examined in detail.

1.4 Fe Isotopes in Hydrothermal Systems

In recent years the analysis of Fe isotopes has emerged as a useful tool for tracing the input of Fe from different sources to the ocean, particularly where Fe inputs may not be immediately apparent from changes in Fe concentrations. Fe isotope analysis of Atlantic seawater samples verified the long range transport of hydrothermal dFe and also reveal input of hydrothermal dFe into the surface ocean from depth (Conway and John, 2014f).

Fe has four stable isotopes ^{54}Fe, ^{56}Fe, ^{57}Fe, ^{58}Fe with the natural abundances 5.82 %, 91.66 %, 2.19 % and 0.33 %, respectively. Fe isotope values are reported in delta (δ) notation relative to a reference material. Fe isotope values in this thesis are reported as the ratio of $^{56}Fe/^{54}Fe$ normalised to the $^{56}Fe/^{54}Fe$ ratio of the IRMM-14 reference material. These values are expressed in δ notation according to:

$$\delta^{56}Fe = 1000 \left[\frac{(^{56}Fe/^{54}Fe)_{sample}}{(^{56}Fe/^{54}Fe)_{IRMM-14}} - 1 \right] \tag{1.6}$$

Natural variations in stable Fe isotopes compositions are caused by biological and abiotic redox processes with either kinetic or equilibrium fractionation effects (Anbar, 2004, Johnson et al., 2004, Welch et al., 2003).

High temperature hydrothermal vent fluids have an Fe isotope composition ranging from -0.69 to -0.10 ‰ (Figure 1.7) (Beard et al., 2003, Bennett et al., 2009, Rouxel et al., 2008, Severmann et al., 2004). The Fe isotope composition of the vent source is altered upon mixing with seawater by Fe isotope fractionation as Fe sulphides and Fe oxyhydroxide mineral particles precipitate in the plume. Thus the Fe isotope signature of dFe exported from hydrothermal plumes will differ from the isotope composition of the vent source.

In basalt hosted hydrothermal systems 25 to 50 % of the Fe dissolved in the vent fluid precipitates as Fe sulphides in the buoyant plume (Rudnicki and Elderfield, 1993). This process causes a kinetic isotope fractionation resulting in the lighter Fe isotopes being preferentially precipitated as Fe sulphide mineral particles. This results in isotopically light Fe sulphide particles leaving the remaining dissolved Fe isotopically heavier in comparison to the δ^{56}Fe of the vent fluid source (Rouxel et al., 2008).

Hydrothermal vents hosted in ultramafic rock have a low Fe/H_2S ratio and as a result <4 % of the vent fluid Fe precipitates as sulphides. In these settings the precipitation of Fe oxyhydroxides will dominate Fe isotope fractionation in the plume (Severmann et al., 2004). In the hydrothermal plumes sourced from basalt hosted vents with higher Fe/H_2S ratios, dFe remaining in the plume after Fe sulphide precipitation will be fractionated by Fe oxyhydroxide precipitation.

The overall Fe isotope fractionation during the precipitation of ferrihydrite, an Fe oxyhydroxide mineral, is the result of two processes. Firstly, the oxidation of $Fe(II)_{aq}$ to $Fe(III)_{aq}$ enriches the $Fe(III)_{aq}$ in the heavy Fe isotope (Welch et al., 2003, Anbar, 2004). The $Fe(III)_{aq}$ then precipitates as ferrihydrite, which can potentially kinetically fractionate the light isotope depending on the rate of precipitation (Skulan et al., 2002). Overall, the ferrihydrite precipitated from solution is enriched in the heavier isotope due to the instability of $Fe(III)_{aq}$ in solution (Bullen et al., 2001).

Fe isotopes measured in hydrothermal vent fluids (-0.69 to 0.28 ‰), plume particles (-0.70 to 1.28 ‰) and sediments (-1.89 to 0.03 ‰) show a wide range of isotope values (Figure 1.7), however there has not yet been a focussed study on the Fe isotope composition of dFe in a hydrothermal plume. This is important as it is the dFe that adds to the dFe ocean reservoir and its Fe isotope composition.

John and Adkins (2012) reported $\delta^{56}Fe_{IRMM\text{-}014}$ of +0.30 to +0.45 ‰ near Bermuda in the upper ocean (<1500 m) and +0.45 to +0.71 ‰ in the deep ocean (1500-2500 m) over a concentration range of 0.12 to 0.89 nM. The heaviest Fe concentrations and δ^{56}Fe values in their study occurred at similar depths as the highest δ^{3}He values (John and Adkins, 2012). Despite a limited depth resolution it was suggested that the heavier δ^{56}Fe values observed maybe the result of hydrothermal input to the deep ocean. This is consistent with the estimates from Bennett et al. (2009), which predict that stabilised dFe from a basalt hosted hydrothermal source will have a positive Fe isotope composition in the range of -0.8 to +0.8 ‰.

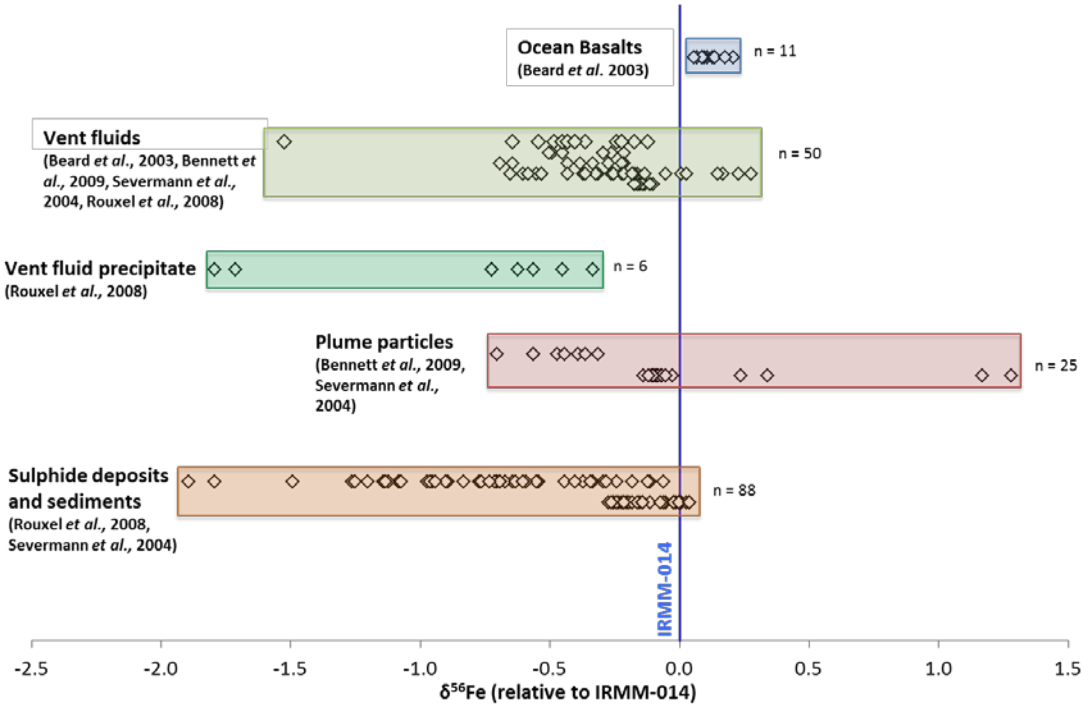

Figure 1.7 The range of Fe isotope values measured in a hydrothermal environment relative to IRMM-014 isotope standard. All values calculated using equation 1.6.

More recently Conway and John (2014f) measured isotopically light δ^{56}Fe values of -0.92 to -1.35 ± 0.03 ‰ (n = 5) in the North Atlantic over the Mid-Atlantic ridge. These were measured at the depths of 3252 to 3420 m with Fe concentrations that were 29 to 57 nM, an order of magnitude greater than concentrations measured at shallower depths. Isotopically lighter values at 0.5 km depth were also interpreted as hydrothermal dFe input directly to the mixed layer of the ocean. The source of this isotopically light hydrothermal dFe was assumed to be from the Trans-Atlantic Geotraverse (TAG), the nearest hydrothermal vent on the Mid-Atlantic Ridge to the sampling station. The Fe isotope composition of TAG end member vent fluids has been measured previously as -0.4 ‰ (Severmann, Johnson et al. 2004).

The work of Conway and John (2014) is contradictory to the earlier work of Bennett, Rouxel et al. (2009) and John and Adkins (2012) as it suggests the flux of dFe from hydrothermal inputs has a significantly lighter Fe isotope composition than was previously thought.

The measured plume Fe isotope value of -1.35 ‰ (Conway and John 2014) is also significantly lighter than the hydrothermal end member value of -0.4 ‰ at TAG (Severmann, Johnson et al. 2004). This suggests that hydrothermal plume processes significantly alter the δ^{56}Fe of the dissolved fraction from the vent fluid end member.

The possibility of isotopically lighter values at 0.5 km depth in the North Atlantic (Conway and John 2014) being the result of direct hydrothermal dFe input to the sub-surface ocean raises the question of hydrothermal vents as a source of dFe not only to the deep ocean but also to depths <1000 m.

The chemistry of hydrothermal plumes differs between ocean basins and therefore the balance between kinetic and equilibrium fractionations in hydrothermal plumes may differ between vent sites. This could explain the differences in Fe isotope values measured at the same depth as tracers of hydrothermal input in different ocean basins (John and Adkins 2012, Conway and John 2014). These differences are important to consider as they will affect the δ^{56}Fe of any stabilised hydrothermal dFe exported to the ocean.

To quantify the impact of hydrothermal venting on the oceanic Fe cycle and to be able to use Fe isotopes as a tracer of hydrothermal input, the chemistry and Fe isotope systematics of hydrothermal plumes must be examined.

This thesis examines the separation of Fe and other trace metals between different size fractions and their Fe isotope composition in hydrothermal plumes from three recently discovered vent sites. Two of these sites are black smokers and the third vents clear high temperature fluids from a conical sulphide mound. Several different methods have been used to examine speciation, concentration and Fe isotope composition in these hydrothermal plumes. Variations in Fe concentration and isotope composition are compared to variations in concentrations of other trace metals, some of which are derived from hydrothermal venting and others which are derived from background seawater. This data is compared to previously published data for trace metals in order to assess the chemical processes occurring at each of these sites and what this means for the role hydrothermal vents play in the global biogeochemical cycles of trace metals.

1.5 Aims and objectives

Hydrothermal vents represent the only environments capable of injecting Fe directly into the open ocean compared to other sources that are located around the ocean margins. This thesis aims to test the hypothesis that hydrothermal vents are an important supply of Fe (and potentially other trace metals) for sustaining primary productivity in the surface ocean. This hypothesis is tested by examining the mechanisms which separate Fe between dissolved and particulate fractions. The processes controlling the separation of Fe between the dissolved and particulate fractions will ultimately control how much Fe is added to the ocean from hydrothermal vents. This is because larger particles that form as the vent fluid mixes with seawater will eventually settle out of the water column to sediments, whilst dissolved species will remain in the water column and eventually be transported from the deep ocean to the surface ocean in regions of upwelling and possibly in regions of turbulent mixing over Mid Ocean Ridges (MOR).

In order to evaluate how regional differences in ocean chemistry may alter the hydrothermal Fe flux three vent sites are studied with different geological settings in different ocean basins. It is important to investigate these differences to determine how important hydrothermal vent sources are in dictating the Fe budget of different ocean basins. Assessing these different hydrothermal settings will enable the key chemical processes that dictate the hydrothermal Fe flux to be constrained. Elucidating these chemical controls on the hydrothermal Fe flux will help predictions of how these environments may influence the ocean climate system in the modern ocean and throughout the history of the Earth.

1.6 Introduction to the Thesis

The chemistry of vent fluids and particles sampled from the immediate stages of plume mixing is discussed in chapter 2. These results cover the dramatic chemical changes that occur in the first few metres of the plume and describe the chemistry of newly discovered vents on the Mid-Cayman Rise. The separation of Fe between different size fractions in rising hydrothermal plumes from vent sites on the Mid-Cayman Rise is investigated in chapter 3 to test the hypothesis that Fe colloids formed in hydrothermal plumes are an important source of dFe to the deep ocean. This is followed by work on how other trace metals such as Cd, Cu, Pb, Co, Zn are partitioned between the same size fractions in plume samples to examine the importance of hydrothermal plumes in the biogeochemical cycle of these elements. Fe isotope analysis of total (particulate + dissolved) and dissolved samples in the buoyant plume (BP) at E2 on the East Scotia Ridge (ESR) is discussed in chapter 4. This work shows how Fe isotopes are fractionated in the BP and how these processes control the Fe isotope signature of hydrothermal dFe. Together these chapters will demonstrate how trace metals and Fe isotopes are separated between different size fractions in three distinct hydrothermal plumes originating from vent fields with differing geology and geochemistry. The results presented in each chapter will be considered in a global context, thus improving our understanding of the influence hydrothermal plumes may have on global ocean budgets of trace metals and how hydrothermal Fe impacts the Fe isotope composition of the ocean.

Chapter 2: Trace metal incorporation into particles above hydrothermal vents.

ABSTRACT

Until recently hydrothermal plumes were considered to be a sink for many trace metals in global biogeochemical cycles; sequestering the vent derived metals into hydrothermal particles and removing them to metalliferous sediments. More recent studies have identified leakage of dissolved trace metals from plumes into the ocean interior. In order to assess the significance of trace metal fluxes from hydrothermal plumes an understanding of the speciation and incorporation of metals into particles is required.

In this study, the first 1m of the hydrothermal plume above the Beebe (BVF) and Von Damm vent fields (VDVF) were sampled for fluids and plume particles. Much of what we know about hydrothermal impacts on trace metals in the ocean is based on 'black smoker' type vents and the VDVF represent a new type of venting that may be present throughout the oceans located away from ridge axis.

Metal concentrations in both fluid and particles were analysed by inductively coupled plasma mass spectrometry (ICP-MS) and the composition of particles was examined using scanning electron microscope energy dispersive x-ray (SEM-EDX). At both sites metal (Fe, Zn, Cu) sulphides were the dominant particle phase. At BVF Cu and Co were associated with chalcopyrite precipitation and Zn, Cd and Pb linked to sphalerite precipitation. The BVF differs from other typical 'black smokers' as FeS plume particles were dominated by pyrrhotite rather than pyrite. The presence of large amounts of pyrrhotite in the BVF plume may facilitate the addition of Fe back to the dissolved fraction during plume dispersal as pyrrhotite, is less stable than pyrite in oxic seawater. VDVF particles were predominantly chalcopyrite and pyrtie with sulphur rich particles identified which contained trace amounts of Fe, Cu and U. Scavenging of trace metals by oxidised sulphur particles in the VDVF plume represents a process by which trace metals could be transferred to non-buoyant plume height and ultimately the deep ocean.

This study describes the processes occurring during the immediate stages of plume mixing at two closely related hydrothermal vent sites with contrasting chemistry and geological setting. Differences in particle formation between vents with low metal/H_2S like VDVF compared to sites with high metal/H_2S will be important for constraining regional differences in removal and addition of trace metals from the deep ocean.

2.1 Introduction

Hydrothermal circulation of seawater through ocean crust at plate boundaries results in large fluxes of metals from hydrothermal vents into the surrounding seawater. These fluxes impact the local environment around vents as well as playing an important role in global trace element budgets (Elderfield and Schultz, 1996, Tagliabue, 2010). Concentrations of metals in hydrothermal fluids are dependent on the rock and sediment composition that hydrothermal fluids circulate through, as well as the pH, temperature, redox conditions and concentrations of sulphide (H_2S) and chloride ligands, which complex metals in solution (Von Damm, 1990, Von Damm, 1995).

Metal rich particles form almost immediately due to the dramatic change in temperature, pH and redox conditions at the point of venting as vent fluids mix rapidly with cold oxygenated seawater (Campbell et al., 1988, German et al., 1991, Rudnicki and Elderfield, 1993). The mixing process results in hydrothermal plumes with high concentrations of metal rich particles. Typically hydrothermal plumes develop chemically in two stages; firstly the early, reduced plume (several meters above the vent) has high H_2S concentrations (up to 12 μM H_2S) (Findlay et al., 2014). Mixing between seawater and vent fluid lowers the temperature and pH of the fluid and the solubility of metals decreases, which leads to precipitation as metal sulphides (Seyfried and Ding, 1993, Rickard, 1995, Rickard and Luther, 1997). The second stage of plume development is the more gradual formation of Fe and Mn oxyhydroxides, which precipitate and scavenge oxyanions (Feely et al., 1996, Feely et al., 1998).

Initial studies of hydrothermal vents concluded that the impact of vents on global seawater budgets of trace metals was negligible (Mottl and McConachy, 1990). This was due to the quantitative precipitation of metals as particles, which were thought to ultimately settle out of the water column to form hydrothermal sediments (Rudnicki and Elderfield, 1993, Bostrom and Peterson, 1966, Mills et al., 1993). Recent studies however have shown that hydrothermal vents can be an important flux of stabilised Fe due to the formation of pyrite nano-particles (Yucel et al., 2011, Gartman et al., 2014) and/or complexation of Fe by organic ligands (Bennett et al., 2008, Hawkes et al., 2013a). Pyrite nano-particles formed in the early stages of venting settle out of the water column at rates of 1 to 2 m per year (Yucel et al., 2011) and oxidise four times slower than ground pyrite (Gartman and Luther, 2014).

In this study "trace" elements are defined as those that are typically at nM to pM concentrations in seawater. Recent research has focussed on Fe due to its key role as a micronutrient in the ocean however organic ligands and sulphide nanoparticles could also play an important role in the cycles of other trace metals. This is because nano-particulate pyrite may also incorporate other metals and organic ligands could also complex other metals in the plume (Sander and Koschinsky, 2011, Gartman et al., 2014).

In order to fully understand the oceanic impact of hydrothermal vents on trace element cycling, the chemical changes that occur as the vent fluid mixes with seawater throughout the entirety of the plume need to be characterised. Previous studies have focussed on the composition of hydrothermal vent fluid and sub-seafloor processes (Edmond et al., 1979, Campbell et al., 1988, Butterfield and Massoth, 1994, Trefry et al., 1994, Von Damm, 1995, Douville et al., 2002, Schmidt et al., 2007, James et al., 2014, Hodgkinson et al., 2015, Ishibashi et al., 2015), the hydrothermal plume rise over the first 10's to 100's of m's (James and Elderfield, 1996, Hawkes et al., 2013a, Estapa et al., 2015, Rudnicki and Elderfield, 1993) and the lateral dispersion of the non-buoyant plume (NBP) (Saito et al., 2013, Resing et al., 2015). These studies all improved understanding of chemical fluxes from hydrothermal vents however, in comparison, there is a considerable lack of information on processes occurring in the immediate stages of vent fluid seawater mixing in the first few meters of plume rise (Klevenz et al., 2011, Findlay et al., 2015).

Processes occurring at the interface between the vent chimney and seawater are important to examine as most of mineral particles form in the region of, 50-60 % seawater mixing (Klevenz et al., 2011). Particle formation in the early plume will influence the rest of the plumes chemistry as particles that form in the immediate stages of mixing may re-dissolve, oxidise, scavenge or settle out at a later stage of plume dispersion.

Gartman et al. (2014) and Findlay et al. (2015) examined the geochemistry of the <0.2 μm filtered fraction of hydrothermal fluids and (>0.2 μm) associated particles. They found nano-particulate pyrite (<0.2 µm) at Rainbow, TAG and Snake-Pit and that Cu, Co, Zn Pb and Cd were predominantly associated with >0.2 µm particles. However similar associations were not observed in Rainbow vents where Fe/H_2S ratios were 24 which is much higher than that of TAG and Snake-pit which were 1.7 and 0.5 (Douville et al., 2002), which facilitated the formation of Fe oxide and Fe bearing silicate particles. Vent systems with ultramafic lithologies are under sampled amongst these studies with the Rainbow vent site being the most frequently studied. The significance of metal/H_2S ratios in controlling the amount of metal that forms particles was also shown for MAR vents by Klevenz et al. (2011) where vent fluids with a higher metal/H_2S ratio result in a higher percentage of dissolved metals in the vent fluid being converted to metal particles. Metal sulphide particle formation is therefore controlled by vent fluid chemistry and temperature with pressure unlikely to have a significant effect on the precipitation of metal sulphides (Reed and Palandri, 2006) despite the wide range of pressures at different vent sites at depths of 1000 to 5000 m.

In order to build upon previous work this study examines the chemistry of venting from two vent fields located on the ultra-slow Mid-Cayman Spreading centre (MCSC). The two vent fields from the MCSC studied were, the Beebe vent field (BVF) and the Von Damm vent field (VDVF). The VDVF represents a type of off-axis hydrothermal venting previously undiscovered at other ridge crests which emits clear fluids. The BVF is a more typical black smoker type system. Investigating vents on ultra-slow spreading centres is of critical importance as current models of hydrothermal element fluxes based on ridge spreading rate do not consider vents along these ridges to be a significant source of elements such as Fe (Tagliabue, 2010, Saito et al., 2013).

Surveys searching for hydrothermal vents focus over ridge axes and off axis features remain largely unexplored for hydrothermal activity. Undiscovered off axis features similar to the VDVF could be wide spread, previously unrecognised environments for exchanging heat and chemicals between seawater and oceanic crust (Hodgkinson et al., 2015). If other off-axis vent sites emit similar clear, intermediate temperature fluids like the VDVF these sites could easily be overlooked during exploration using a traditional CTD package. Using a redox potential sensor Baker et al. (2016) discovered that the number of vent sites on the EPR is likely to be up to 6 fold higher than previous estimates based on traditional CTD profiles with a quarter of these undiscovered sites being from particle poor plumes. It is therefore likely that the number of hydrothermal vent sites has been underestimated globally and lower temperature particle poor sites are likely to have been overlooked. This highlights the importance of investigating sites like the VDVF to constrain the importance of these previously overlooked sites to global hydrothermal element fluxes.

Considering the segregation of metals between the fluid and particles present in the samples allows the differences in metal precipitation between the two different sites to be assessed. Samples examined in this study cover a range of 3 to 89 % seawater mixed with vent fluids, as estimated for Mg content, which is roughly equivalent to the first meter of plume rise directly over vents (based on video footage of sample collection). Results are compared with equivalent data from other ocean ridge settings in order to assess the importance of vent fluid chemistry on metal fluxes to the deep ocean from hydrothermal vents.

2.2 Geological Setting

The Cayman Trough is located in the Caribbean Sea south of the Cayman Islands (Figure 2.1). The Mid Cayman Spreading Centre is a 110 km long ultraslow spreading ridge (<20 mm yr^{-1}) bisecting the Cayman Trough. Spreading was initiated here at 49 Ma and is continuing at a full spreading rate of 15 mm yr^{-1} (Leroy et al., 2000).

The VDVF and BVF were sampled in 2012 (Connelly et al., 2012). The Beebe Vent Field (BVF) is located close to the axis of the Mid-Cayman spreading Centre (MCSC) and consists of six discrete metal sulphide mounds with active and inactive black smoker chimneys and areas of diffuse flow (Figure 2.1 & Figure 2.2). Areas of active venting are associated with the three southernmost largest mounds ~60 m wide.

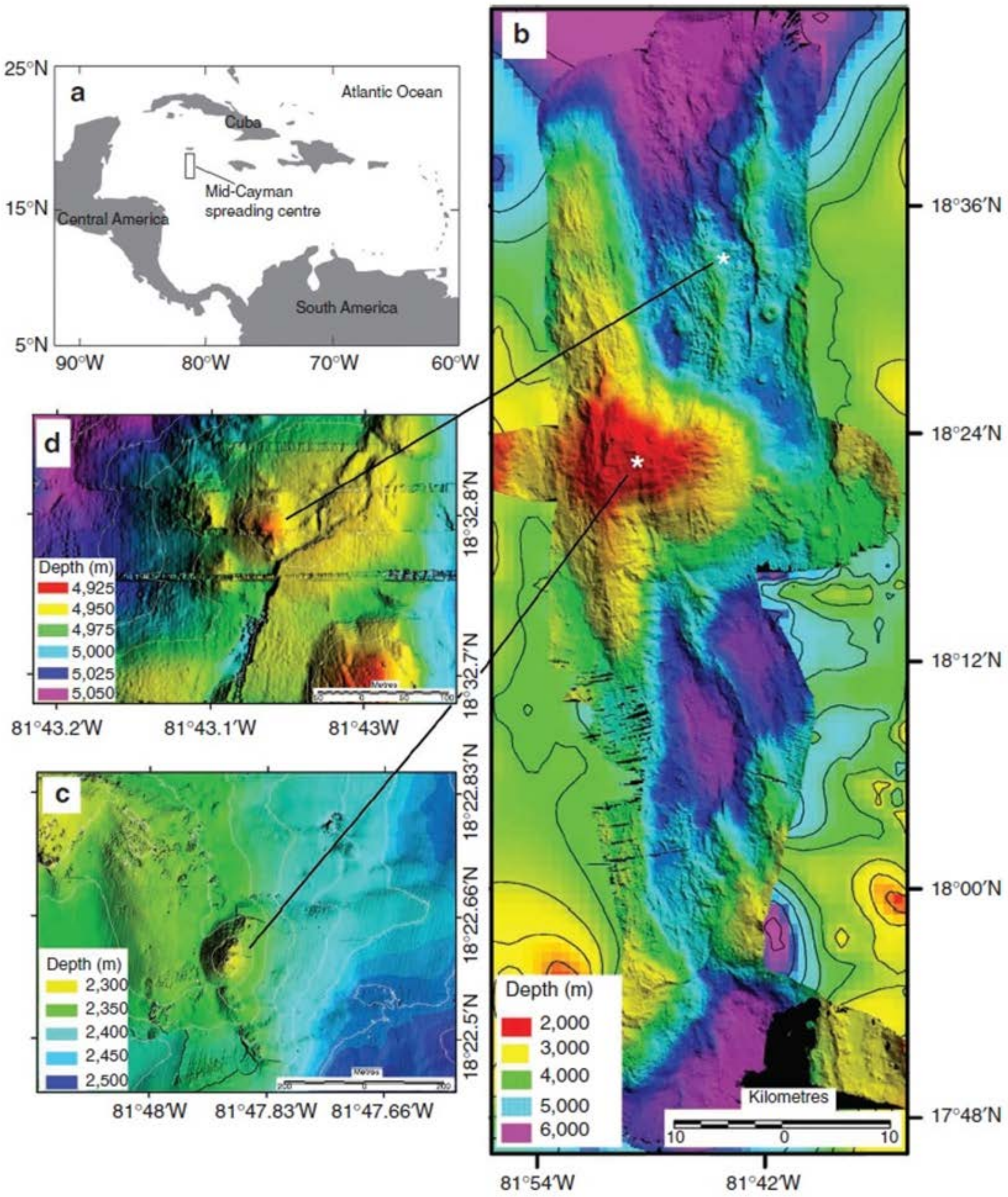

Figure 2.1 A. Location of Mid-Cayman spreading centre (MCSC) in the Carribbean Sea. B. Bathymetry map of the Mid Cayman Rise. C. Map of the VonDamm Vent Field (VDVF). D. Map of the Beebe Vent Field (BVF) (Taken from (Connelly et al., 2012)).

The BVF is located at 18˚22.605 N 18˚47.875 W at a depth of 4960 m making it the deepest hydrothermal vent field discovered to date (Connelly et al., 2012). There are three sites of active black smoker type venting. Beebe Woods is located to the south of the site at a depth of 4956 m (Figure 2.2). Beebe 125 and Deepest Vents are located on a separate mound 50 m to the north of Beebe Woods at depths of 4657 and 4964 m, respectively (Figure 2.2). The temperature and pH of fluids emanating from vents at Deepest Vents and Beebe 125 ars similar in the ranges of 393 to 401 ˚C and 3.9 to 2.9 respectively. Temperature of fluids from Beebe Woods is lower at 350 ˚C with a slightly higher pH range of 3.5 to 4.8. It has been proposed that hydrothermal fluids circulate through mafic and ultramafic lithologies beneath the BVF (Webber *et al.* 2015).

The VDVF is located at 18˚22.605'N 18˚47.875'W, 13 km west of the MCSC spreading axis and sits atop the Mount Dent, Oceanic Core Complex (OCC) at a depth of 2300 m. An OCC is a common feature of slow and ultra-slow spreading ridges formed by detachment faulting associated with slow spreading. During the faulting and spreading process crustal (gabbroic) rocks from depth are uplifted exposing mantle rocks (peridotite) (Smith et al., 2006). Due to this uplift the VDVF lies 2700 m above the MCSC axis (Figure 2.1).

At present there are several known types of hydrothermal system. The most widely discovered type being black smokers that emit low pH (2-5), high temperature (up to 400 ˚C) metal rich fluids. The extent of metal enrichment in these vents varies depending on host rock through which hydrothermal fluids circulate. Ultramafic hosted vent sites such as Rainbow on the MAR have higher Fe concentrations relative to sulphide whilst basalt hosted systems tend to have lower Fe concentrations in comparison. Other less frequently observed vent sites include white smokers that emit lower temperature (up to 300 ˚C), high pH (9-11), fluids rich in Ca, Ba and silica (McCarthy et al., 2005) and other low temperature (<40 to 90 ˚C) high pH alkaline vents that emit hydrogen and methane rich fluids from calcium carbonate chimneys (Kelley et al., 2005). The VDVF is a third type of hydrothermal system emitting clear, moderately low pH (6-7) fluids with temperatures up to 215 ˚C.

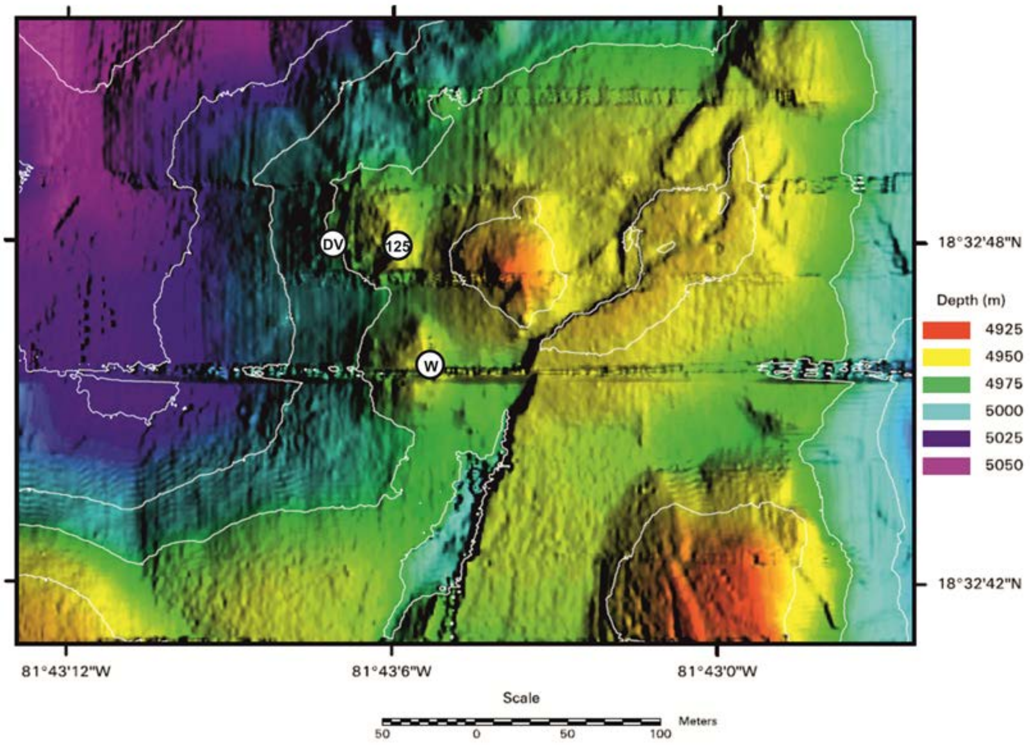

Figure 2.2 Bathymetry map of the BVF showing sites of active venting. DV is Deepest Vents, 125 is Beebe 125, W is Beebe Woods.

It has been suggested that the heat required for hydrothermal venting at the VDVF is provided by cooling of the exhumed lower crust at the foot wall of the OCC (Hodgkinson et al., 2015). This makes it different in comparison to more typical hydrothermal systems where the heat source driving circulation is magmatic (German et al., 2016).

The VDVF consists of four overlapping cones of talc ($Mg_3Si_4O_{10}(OH)_2$) breccia 20 to 75 m high and 75 to 150 m wide (Figure 2.3). Hydrothermal fluids vent from a series of talc chimneys. The largest of these is the 3 m tall 1 m diameter “Spire”, which vents clear fluids with a temperature of 215 ˚C and pH of 6.1. At the base of the spire to the west a 1 m diameter hole (“hotter than hole”) vents 133 ˚C clear fluids with a pH of 6.3 (Figure 2.4). On the southern margin of the largest cone a smaller site of venting named “chimlets” has vent fluids with a temperature of 107 ˚C and a pH of 6.6. On the smallest and southern most cone a site named X15 has vent fluids with a temperature of 110 ˚C and a pH of 6.67.

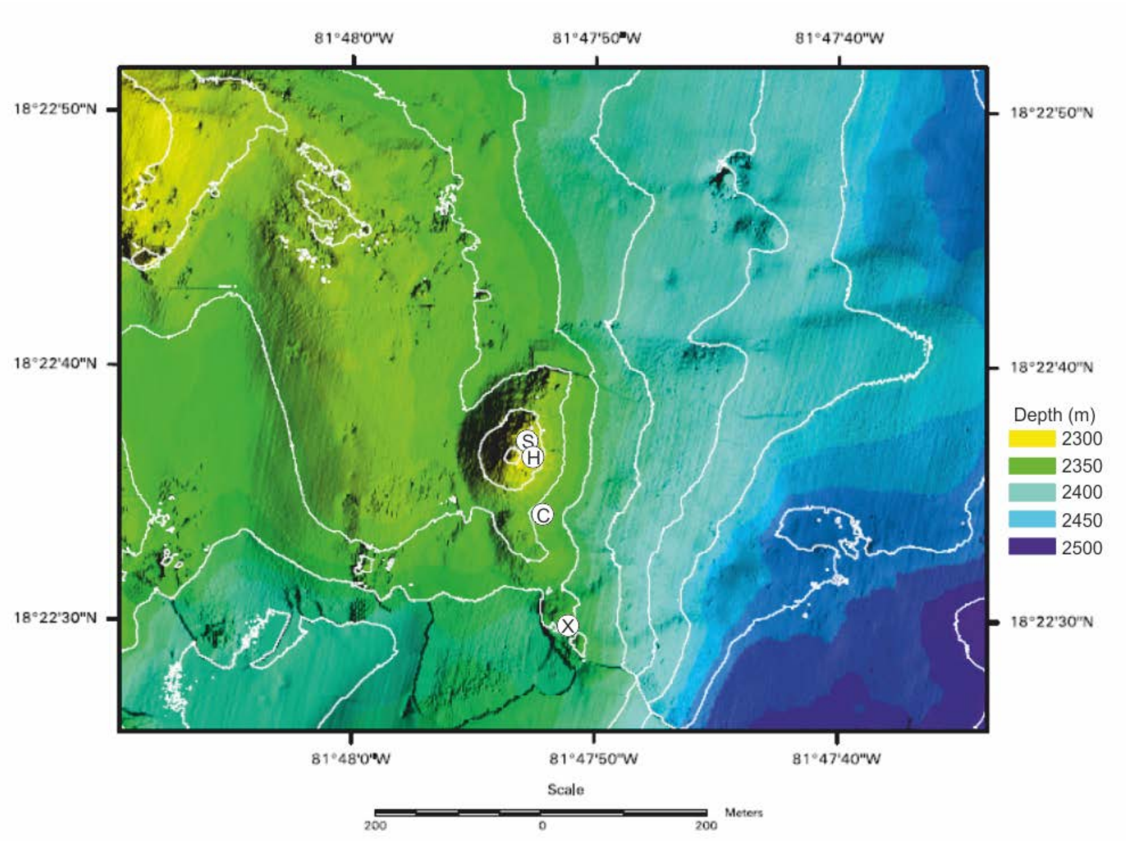

Figure 2.3 Bathymetry map of VDVF with sites of active venting labelled. Site S is the Spire, H is hotter than hole, X is X15 (marker left by American research group) and C is chimlets.

Both vent fields on the MCSC provide habitats for several species some of which are endemic. The most abundant at both sites is *Rimicaris hybisae* shrimp with differences in population structure and carapace size between the two vent fields, which could be influenced by the chemical differences between the two sites (Connelly et al., 2012, Nye et al., 2013).

Previously other works have referred to the VDVF as “Europa” and the BVF as “Piccard” after the discovery of hydrothermal plume signals in the water column (German et al., 2010). In this study the names Beebe and Von Damm are used after the discovery paper, which visually confirmed vents on the seafloor in these areas (Connelly et al., 2012). These are also the names used to list these sites in the InterRidge database.

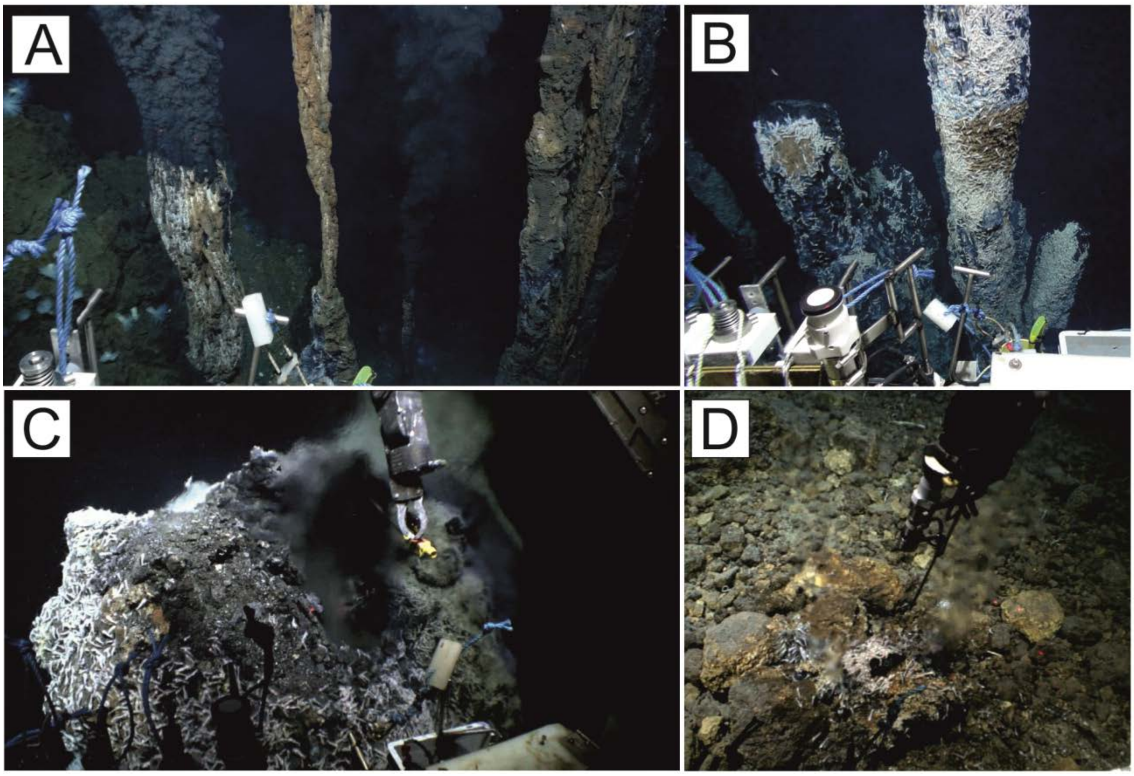

Figure 2.4 Images of different venting styles on the MCSC. (A) Beebe 125 on the BVF showing chimney structure typical of Beebe 125 and Deepest Vents sites. Chimney on the right hand side of the image is 30 cm in diameter. (B) Beehive chimneys of Beebe Woods, which are 50 to 100 cm in diameter. White patches on the chimneys are areas covered by shrimp. (C) Main spire on the VDVF showing clear fluids venting from the chimney typical of the main spire and hotter than hole. The chimney orifice is 20 cm wide. (D) Chimlets 2 on the VDVF showing venting style typical at Chimlet and the X15 site. The two venting holes either side of the aggregation of shrimp are 5 cm wide.

Hydrographically the deep water in the Cayman Trench has temperature, salinity and O_2 concentration consistent with altered North Atlantic Deepwater (NADW) (Connelly et al., 2012). It is likely that this water enters the Cayman basin via the Oriente Fracture Zone from the Windward Passage (Johns et al., 2002). Due to a lack of oceanographic research in the Caribbean Sea there is little data on the chemistry and movement of deep water masses in the Cayman Trough. Where data is unavailable for the Cayman Trough, values for

NADW are shown in Table 2.1 from the stations closest to the Windward Passage.

The samples in this study were collected aboard the RSS James Cook on voyage JC82 during February 2013. This cruise sampled both vent fields in the Cayman Trough, the Von Damm Vent Field (VDVF) and the Beebe Vent Field (BVF) (Figure 2.2).

Table 2.1 Chemistry of Cayman Trench deep water

	Cayman Trough Deep Seawater
pH *in-situ*	7.9[c]
dFe (nmol kg^{-1})	0.7[b]
dMn (nmol kg^{-1})	0.1[b]
Dissolved O_2 (µmol kg^{-1})	220[a]
Dissolved Inorganic Carbon (DIC ; µmol kg^{-1})	2170[b]
Total alkalinity (TA ; µmol kg^{-1})	2325[b]
Dissolved P (µmol kg^{-1})	1.25[b]
Dissolved Si (µmol kg^{-1})	25[b]

a; data from Cayman Trough (Connelly et al. 2012)

b; data from nearest station to Windward Passage http://www.egeotraces.org/ section GA03.

c; Calculated with CO_2 SYS (http://cdiac.ornl.gov/oceans/co2rprt.html) using data from a and pCO_2 from nearest station on the A05 section in the eWOCE (http://cdiac.ornl.gov/oceans/woce_a05.html).

2.3 Methods

2.3.1 Sampling of hydrothermal vents and elemental analysis

Gas tight samplers (IFREMER, Brest, FR) were used during JC82 in February 2013 to sample high temperature vent fluids and particles from Beebe and Von Damm vents with temperatures measured separately within the chimney orifice using a probe deployed by the remote operated vehicle (ROV) *Isis*.

The combined sample of vent fluid and suspended particles were removed from gas tight samplers into acid clean polyethylene vials for trace metal analysis (see Appendix A for lab ware acid cleaning procedure). After emptying the sampler it was rinsed with de-ionised water (18MΩ Milli-Q) to recover any remaining particles that had settled to the base of the sampler over the 2 to 3 hour period of sample recovery. These larger settled particles were stored separately suspended in de-ionised water in crimp sealed auto sampler vials for microscopy analysis on-shore at NOCS. These vials were filled with de-ionised water and crimped without leaving an air bubble. The vials were then sealed again with plastic paraffin film (parafilm). This process was important to prevent any gas exchange between atmosphere and de-ionised which could alter particle composition during storage. The sampling process is outlined in Figure 2.5.

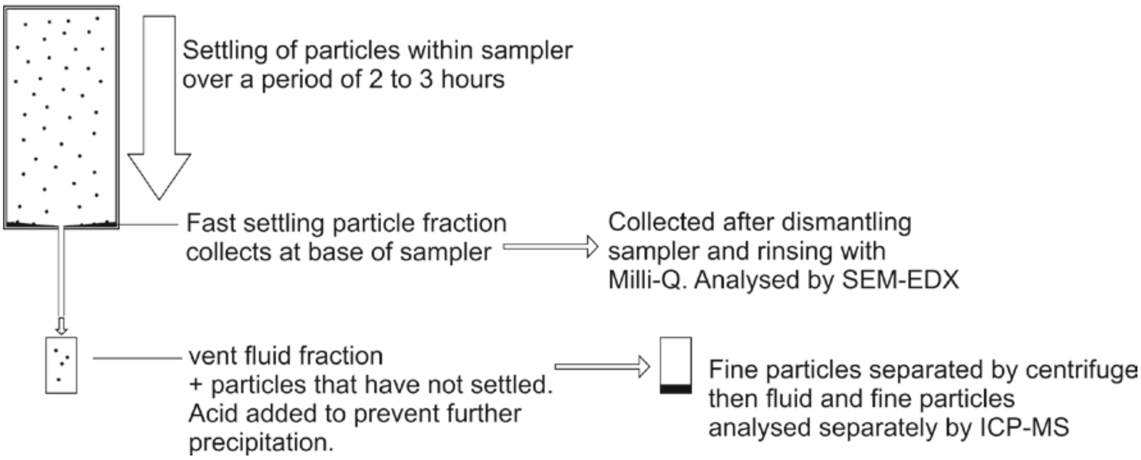

Figure 2.5 Separation of vent fluid from particles for analysis

At the end of the cruise combined vent fluid and suspended particle samples were preserved by adding 1 µl of ~15 M ultra-pure HNO_3 (ROMIL UpA) per 1 ml of sample. Resulting in a final sample HNO_3 concentration of 0.015 M with a pH of ~2. This was in order to prevent any particle precipitation during storage. This may have dissolved some particles and this is discussed further in section 2.4.2. These samples were analysed by ICP-MS ~1 year after initial sampling on-shore at NOCS.

Fine suspended vent particles were separated from vent fluids on shore by centrifuge. The usual procedure for investigating hydrothermal end member concentrations is to combine these two aliquots but here they are separated to understand trace metal partitioning during early plume mixing. Particles recovered from the samples were weighed in order to reconstruct original concentrations of metals in particulates. The mass of suspended particles was 1 to 10 % of the total vent fluid plus fine particle mass. Fine suspended particles were dissolved for element analysis in Teflon vials (Savillex) with *aqua* *regia* (concentrated HNO_3 and HCl mixed in a 1:3 ratio) and on a hot plate at 60 °C for 72 hours. The concentrated *aqua regia* in each vial was evaporated on the hot plate until each vial was dry. Samples were then re-constituted in 3 ml of 0.3 M S.B. HNO_3.

The vent fluid and particle digest solutions were diluted 100 to 2500 fold in 0.3 M S.B HNO_3 depending on the elements to be measured and the instrument used. The 0.3 M S.B HNO_3 acid was spiked with 20 ppb Be, 5 ppb In, and 5 ppb Re as internal standards. The vent fluid solutions were analysed for all elements (see results for list) by ICP-AES (iCAP 6000, *Thermo Scientific*) and ICP-MS (X-series, *Thermo Scientific*). Instrument performance determined the method blank and error. All concentrations measured were sufficiently higher than the instrument l.o.d and blank to avoid baseline interferences. The error was quantified by the relative standard deviation (RSD %) of instrument analysis on all elements measured by ICP-AES and ICP-MS. This ranged from 0.5 to 3 % across all elements analysed. Chloride and sulphate in vent fluid was analysed by Ion Chromatography (Dionex). Sulphide was measured immediately after recovery of the gas tight sampler on the ship by iodometric titration (Pawlak and Pawlak, 1999).

Scanning electron microscopes (SEMs) are useful tools for imaging and determining the morphology of a sample. The sample is analysed under vacuum and coated in a conductive element (in this case C) due to the reliance of this technique on electron transport. A tungsten filament is used to emit and direct electrons onto the sample surface and produces both secondary and backscattered electrons. The secondary electrons are reflected off the surface and detected by the secondary electron detector (SED). Signal strengths are proportional to the tilt direction of the surface they were created on. This allows determination of the sample topography to a resolution of nanometres and the production of an image. The backscattered electrons collide with atoms in the sample, and because elastic collision probability increases as atomic number increases, backscattered electrons arriving at the backscatter detector (BSD) are a function of atomic number. In practise this leads to heavier elements producing a brighter image, and allows the qualitative identification of sample elements (Goldstein et al., 2003). An electron dispersive x-ray (EDX) may be coupled to the SEM to quantitatively determine a sample's elemental composition. An electron beam is emitted which hits the sample and excites a core electron, ejecting it from the sample. The resultant electron hole is filled by a higher energy electron which emits an X-ray photon with a wavelength characteristic of that element. The detection of these wavelengths and their associated intensities allows the quantitative composition of the particle to be determined (Goldstein *et al.,* 2003).

Particle analysis was performed using a Carlseiz LEO 1450VP SEM located at The National Oceanography Centre, Southampton, with operating conditions of 19 mm working distance, 20 kV Beam Energy and a nominal probe current of 700 pA. The samples were analysed for metal bearing mineral particles identified using the SEM's Backscatter Detector. Using this technique it was possible to distinguish the metal bearing particles (brighter particles) from the biological debris, to identify particles of interest for elemental analysis. The filters were studied systematically (Appendix E, Figure E1) to try and get the most representative results of the whole sample, with the brighter particles were chosen for spot elemental analysis.

Elemental analysis was performed on the selected particles using a Princeton Gamma Technology Light Element Detector EDX analyser built-in to the SEM. This produced qualitative spectra allowing spectra peaks and subsequently the composition of the particle to be identified (Figure 2.14), and quantitative analysis identifying the relative percent's of each element present within certain minerals.

Large settled particles stored in de-ionised water were transferred onto polycarbonate filters (0.2 µm pore size, 47 mm diameter) to increase number of particles per area for examination. Filters were cut using ceramic scissors, which were rinsed with de-ionised water before use. Filter segments were mounted onto metal stubs or particles were mounted onto glass lenses and made into resin blocks.

Areas of the filter segment or resin block were selected for examining particles using a systematic grid pattern focussing on particles that appeared brighter in the back scatter image and were therefore more likely to consist of heavier elements such as transition metals. The mineralogy of particles was determined using the relative atomic percent of elements calculated from the weight % of elements determined by EDX and the atomic weights of elements.

This is similar to the method used by Klevenz et al. (2011) for determining the composition of hydrothermal particles.

The results achieved may not be truly representative of the filter for two reasons; the preparation method for SAPS resins may have resulted in residual particles on the filter, the analysis of a grid of particles to represent the whole sample may not be fully representative due to the number of particles present making it difficult to analyse enough points. The quantitative analysis used is normalised which may alter the absolute percentage of each element in the sample and the accuracy of lighter elements is limited with the weight percent detection limit of sodium 0.195% compared to that of calcium which is only 0.085% (Goldstein et al., 2003). The determined sizes of particles and aggregates may be less than the actual values due to the angle of the particle under the SEM. The true quantity of aggregates may be lower than observed in this study, due to clustering on filters and the non-turbulent precipitation environment of the within titanium samplers compared to the plume.

2.3.2 Thermodynamic modelling of vent fluid seawater mixing

Equilibrium reaction path models were used in order to (1) consider the role of kinetic effects on mineral formation in the plume, (2) to compare mineral phases predicted by models to those observed using SEM-EDX. The hydrothermal end member in plume mixing models is the end member vent fluid concentrations reconstructed from extrapolation to zero Mg content. In the sub-surface at temperatures >200 ˚C, Mg precipitates from solution and the concentration of Mg in the circulating hydrothermal fluid decreases to <1 mmol kg^{-1} from seawater values of 53 mmol kg^{-1} (Bischoff and Dickson, 1975). Ideally metal concentrations should correlate linearly with Mg in order to extrapolate the hydrothermal end member concentrations at zero Mg. This was only possible for BVF where metal concentrations are observed to decrease linearly with increasing Mg. For modelling the VDVF plume the average fluid concentration is used as the hydrothermal end member because the metal-Mg correlations are highly scattered. The mixing model reacts vent fluid with seawater across the range of vent fluid-seawater mixtures observed in samples (up to 90 % seawater) and runs the system through to thermodynamic equilibrium.

Temperature was defined by a polythermal path dependent on the extent of vent fluid-seawater mixing and assumes each fluid has a constant heat capacity. The formation of silicate minerals (Quartz, Tridymite, Chalcedony, Cristobalite), which are likely to be kinetically inhibited in hydrothermal plumes, was suppressed in the model for simplicity and in order to be more representative of plume processes (Klevenz et al., 2011, Breier et al., 2012). Hematite and magnetite formation was also suppressed as the formation of stable Fe oxide minerals is very unlikely in a hydrothermal plume setting during the earliest stages of mixing (Rudnicki and Elderfield, 1993, Klevenz et al., 2011). As a result there is no possibility of Fe oxides precipitating in the model as there was no thermo data for other Fe minerals such as Ferrihydrite in the model.

Models were conducted using the React module of the Geochemist's Workbench (GWB) (Bethke, 1996). Thermodynamic databases were created using DBCreate (Xiang-Zhao et al., 2013) to calculate Log K values through the temperature and pressure ranges of both vent sites (250 and 500 bar and 4 to 405 °C). DBCreate generates thermodynamic data using SUPCRT 92 and thermodynamic properties were taken from the 2006 revised version of the SUPCRT database. The modelling approach assumes ideal compositions for minerals and therefore no substitutions and solid solutions taken into account.

2.4 Results

2.4.1 Sample quality and composition of vent fluids

Due to the fragile friable nature of vent chimneys fluid samples may have become contaminated with small particles of chimney material that broke off during sampling. Calcium, like Mg, behaves conservatively during mixing, but vent chimneys are partly composed of anhydrite ($CaSO_4$) and if any chimney material contaminates the fluid sample then Mg/Ca will not plot on a linear vent-seawater mixing line.

This was the case for several of the VDVF and BVF samples (Figure 2.6). These fluid samples were therefore excluded from further interpretation as they are not representative of the vent fluid composition (Figure 2.6). Association of elements in the remaining samples was defined by examining linear and curvilinear trends with significant trends identified by r^2 values >0.6 and p-values <0.005 i.e 60 % of the trend can be explained by association between the two elements with a 0.5 % chance of obtaining a result different to that observed.

For the BVF vents an end member can only be reliably quantified by linear regression through all samples for Mn of 620 µmol kg^{-1} (Figure 2.7). Linear trends with Mg for Zn, Cd and Pb have lower r^2 values of 0.73, 0.64 and 0.74 (Figure 2.7) (Appenix B). Therefore there was more uncertainty associated with the extrapolated end member concentration. For Fe, Cu and Co negative linear correlation with Mg is only evident in samples from Beebe 125 and thus only these samples are included in the linear regression analysis in order to estimate the hydrothermal end member (Figure 2.7). Using this criteria a trace metal hydrothermal end member for the BVF is approximated of 6794 (Fe), 1.3 (Co), 73 (Zn), 0.3 (Pb), 0.1 (Cd), 144 (Cu) µmol kg^{-1}.

H_2S in BVF samples ranged from 0.3 to 6.9 mM (Table 2.4) and end member H_2S concentrations cannot be calculated in the same way as metal concentrations however, the average H_2S across all vents was 3.4 mmol kg^{-1} (Table 2.4). The combined concentrations of major transition metals (Fe + Zn + Cu = MeS) was on average greater than the sulphide concentrations with an average MeS/H_2S of 5 (Table 2.4), which shows that across the site metal fluid concentrations were often in excess of sulphide.

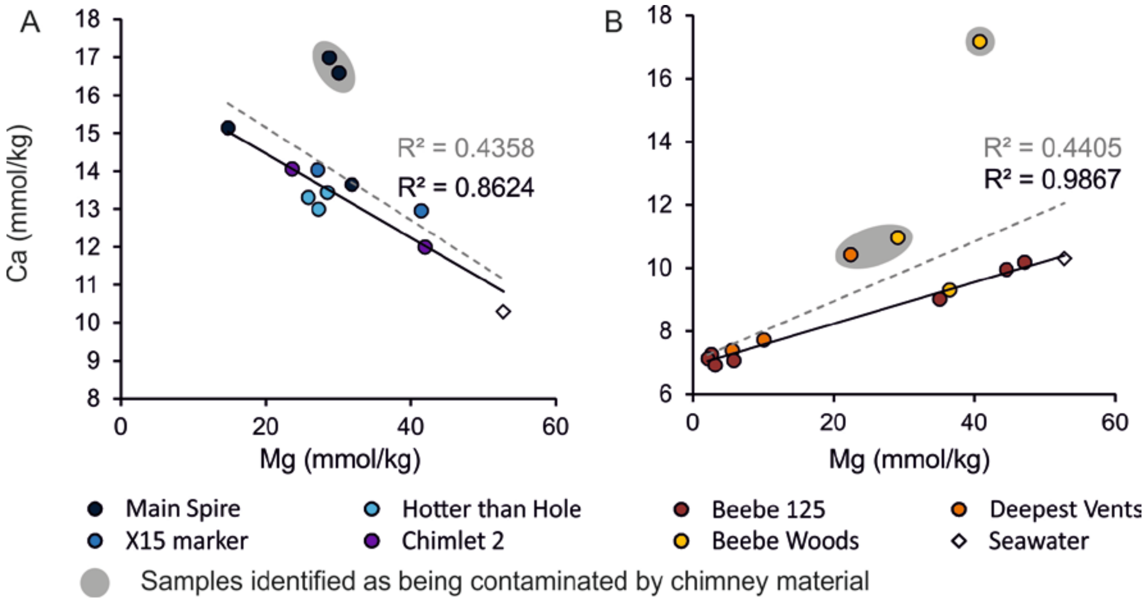

Figure 2.6 Concentrations of Mg and Ca in VDVF fluid samples (A) and BVF fluid samples (B). Different colours represent different chimneys sampled on each vent field. Outlier samples suspected of chimney material contamination highlighted by grey circles due to excess Ca. Grey dashed lines and text is linear regression through all points. Black lines are regression through samples deemed to be free of contamination from chimney material.

End member hydrothermal vent fluid compositions could not be calculated for VDVF where p values of 0.3 to 0.009 indicate no significant linear trends between Mg and trace metals (see Appendix B for statistics). Metal concentrations were lower than BVF for Fe, Co, Mn and Cu. All other metals (Ni, Cd, Pb, U, Mo, Zn) had several fluid samples with concentrations higher than BVF however it is important to note that these covered a wider range with more samples at the lower end of the range (Figure 2.18, Table 2.4).

H_2S concentrations of VDVF vent fluids ranged from 0.3 to 1.7 mM with the lowest concentrations from hotter than hole and the highest from X15. The average H_2S concentration across all vents was 0.9 mmol kg^{-1} with an average MeS/H_2S of 1 indicating that despite lower H_2S concentrations metals were still in excess relative to H_2S on average across all vents on the site.

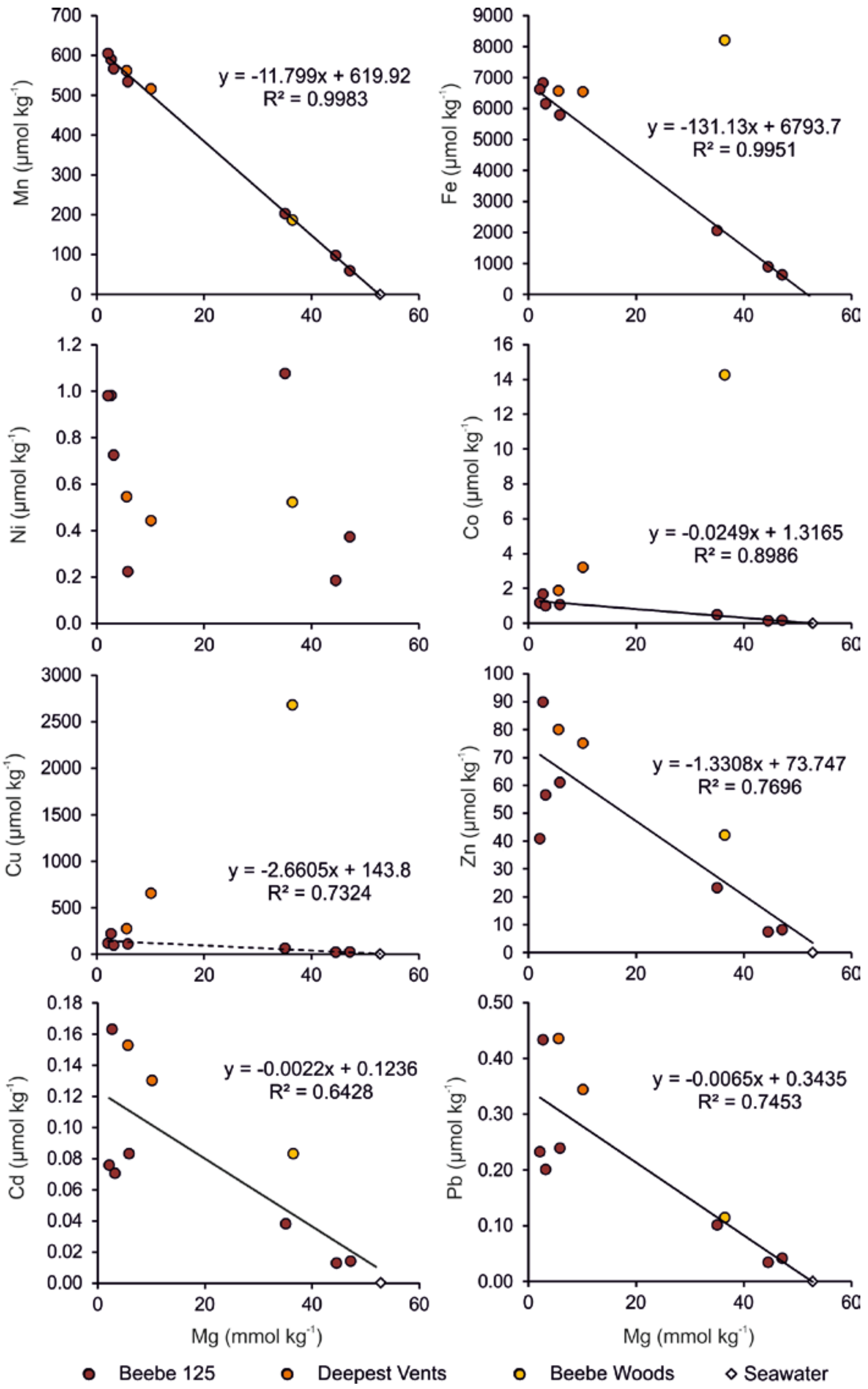

Figure 2.7 BVF vent fluid trace metal concentrations of different vents (different colours) plotted against Mg, which is a conservative tracer of vent seawater mixing. Linear regression for Mn, Cd, Pb and Zn is through all samples. For Co, Cu and Fe linear regression is through Beebe 125 samples only. Black lines are significant trends determined by r^2 >0.6 and p values <0.005. Dashed lines are non-significant (p >0.005).

2.4.2 Potential artefacts due to sample collection

Recovery of samples from depth took 2-5 hours and during this time the metals could have precipitated as a result of changes in pressure and temperature during sampling. Samples will have initially been at temperatures >200 °C and cooled to seawater temperatures of 4 °C during transport of the sample from depth to the surface. Cooling is most likely to affect the solubility of chalcopyrite and sphalerite as these minerals show sharp decreases in solubility between temperatures of 200 to 400 °C (Seyfried and Ding, 2013). In contrast to this previous studies have demonstrated that Fe precipitation during sample collection of vent fluids is negligible (<2 % Fe precipitation as pyrite) (Trefry et al., 1994, Yucel et al., 2011). This is because cooling of the samples decreases the rate of precipitation dramatically (36 fold decrease) thus preserving particle and fluid chemistry (Gartman and Luther, 2014, Yucel et al., 2011). Whilst cooling dramatically slows metal sulphide precipitation this does not prevent the growth of particles entrained in the sampler at the time of sampling (Gartman and Luther, 2013) therefore larger particle aggregates observed by SEM may have formed within the samplers. It is not anticipated that a significant fraction of dissolved metals precipitated in the sampler as a result of cooling.

Metal sulphide solubility is only weakly dependent on pressure (Reed and Palandri, 2006) and pressure changes are unlikely to cause a significant quantity of metal sulphides to precipitate from solution during sample recovery (Hsu-Kim et al., 2008, Findlay et al., 2015). It can be concluded that pressure changes during sample recovery has had a negligible effect on the sample.

Solubility of metal sulphides is also pH dependent and the change in pH due to vent fluid – seawater mixing is thought to be the main controlling factor on metal sulphide precipitation in hydrothermal plumes (Klevenz et al., 2011). Temperature and pressure change during sample recovery is likely to decrease the pH (by 0.5 to 2) as aqueous H^+ complexes that are strongly associated at high temperature and pressure become unstable (Ding and Seyfried, 2007).

The resulting decrease of pH during sample recovery will keep metals in solution.

If particles had formed predominantly in samplers due to temperature, pressure and pH change (rather than in the plume) the percentage of metals in the particulate fraction should increase depending on vent fluid - seawater mixing. This is not the case as can be seen in Figure 2.8 & Figure 2.16 where samples that have a higher percentage of seawater mixed in do not have higher concentrations of metals in the particle fraction. Furthermore no trend was observed between these Mg which is a tracer of seawater mixing and particulate metal concentrations (Appendix B). This supports the hypothesis that the majority of particles were entrained during sampling rather than formed in the sampler.

Based on previous work on hydrothermal vent fluids which show negligible particle formation in samplers (Trefry et al., 1994, Yucel et al., 2011), the cooling of the sampler which is expected to decrease precipitation rate and the decrease in sample pH which will increase metal solubility, it is unlikely that a significant fraction of the particles measured are a result of sample recovery. The majority of particles are likely to have formed in the plume *in-situ* and been entrained during the sampling procedure (Klevenz et al., 2011, Findlay et al., 2015) along with any broken chimney fragments disturbed by the sampling snorkel.

The time between addition of HNO_3 and separation of fine suspended particles from vent fluids may have re-dissolved some of the fine metal sulphide particles captured during sampling. Therefore particle concentrations represent particles small enough to remain suspended in the sampler, formed *in-situ* and are not dissolved in 0.015 M HNO_3. The fluid represents dissolved concentrations plus any metals added from the dissolution of fine particles by adding HNO_3.

2.4.3 Segregation of metal between the fluid and particle fractions at BVF

The majority of trace metals in BVF samples are in the fluid fraction, particularly for samples from Beebe 125 (Figure 2.8 & Figure 2.9). Fe and Cu represent the largest concentrations in both fluid and particles across all chimneys (Figure 2.8). Ratios of elements in the fluid and particulate fractions from Deepest vents and Beebe woods differ significantly from Beebe 125 with larger concentrations of Fe, Co, Cu, Cd, Mo and Zn in particulates. This may explain why end member concentrations for Co and Fe could only be calculated from regression through Beebe 125 samples as these samples contained a larger portion of metals in the fluid fraction (Figure 2.9). This difference in fluid composition is attributed to the morphology of chimneys (Figure 2.4) as the Deepest vents and Beebe Woods chimneys are more breakable beehive structures making it harder to sample these vents without metal sulphides breaking off from the fragile outer structure of the chimneys and being entrained into the fluid sample.

2.4.4 Association of trace metals with Fe in vent fluids and plume particles at BVF

Cu concentration in fluids were correlated ($r^2 = 0.996$) with Co and both Cd and Pb are correlated with Zn ($r^2 > 0.94$) (Figure 2.10). Correlations between these metals suggest that they are associated with precipitation of and/or adsorption onto the same mineral phase, removing metals from the fluid fraction. Linear correlation of Cu and Co in the fluid fraction indicates these elements are removed from the fluid at constant molar ratios. Alternatively there could be nanoparticles present in the fluid fraction and the correlation between these metals may reflect the presence of nanoparticles or metals leached from particles during storage. Similarly correlations were apparent between particulate Cu and Co and between particulate Zn with Cd and Pb (Figure 2.11). This is further indicating that these metals were associated with the same mineral phase within the particulate fraction.

Fe shows strong linear correlation with Mn (Figure 2.12) in BVF samples ($r^2 = 0.999$, $p = 9 \times 10^{-8}$) when Beebe Woods is excluded as an outlier (r^2 decreases to 0.53 with an insignificant p value of 0.01 if included). Mn does not rapidly oxidise to form particles and behaves near-conservatively in the early stages of plume mixing, correlation between Fe and Mn indicates that seawater dilution must be the primary reason for decreasing Fe fluid concentrations with Fe mineral precipitation exerting less of a control on Fe concentrations in BVF samples during vent-seawater mixing.

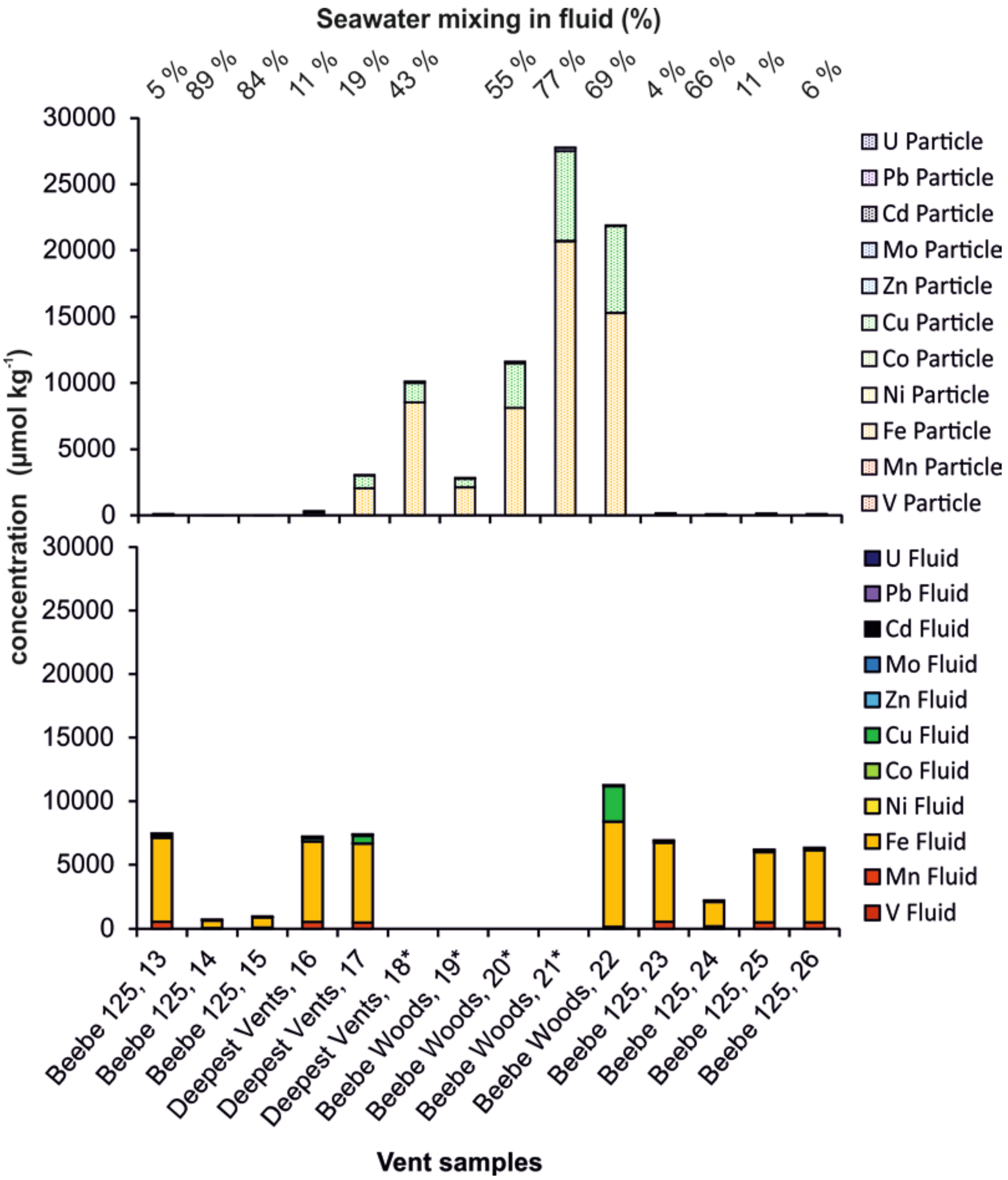

Figure 2.8 Concentrations of metals in fluid and particle fractions in BVF samples. Sample names with a * are samples where only the particle fraction is examined as the fluid fraction was either not analysed or considered to be contaminated by chimney material based on Ca/Mg shown in (Figure 2.6). Higher particle concentrations are observed in samples from beehive chimneys of Beebe Woods and Deepest Vents.

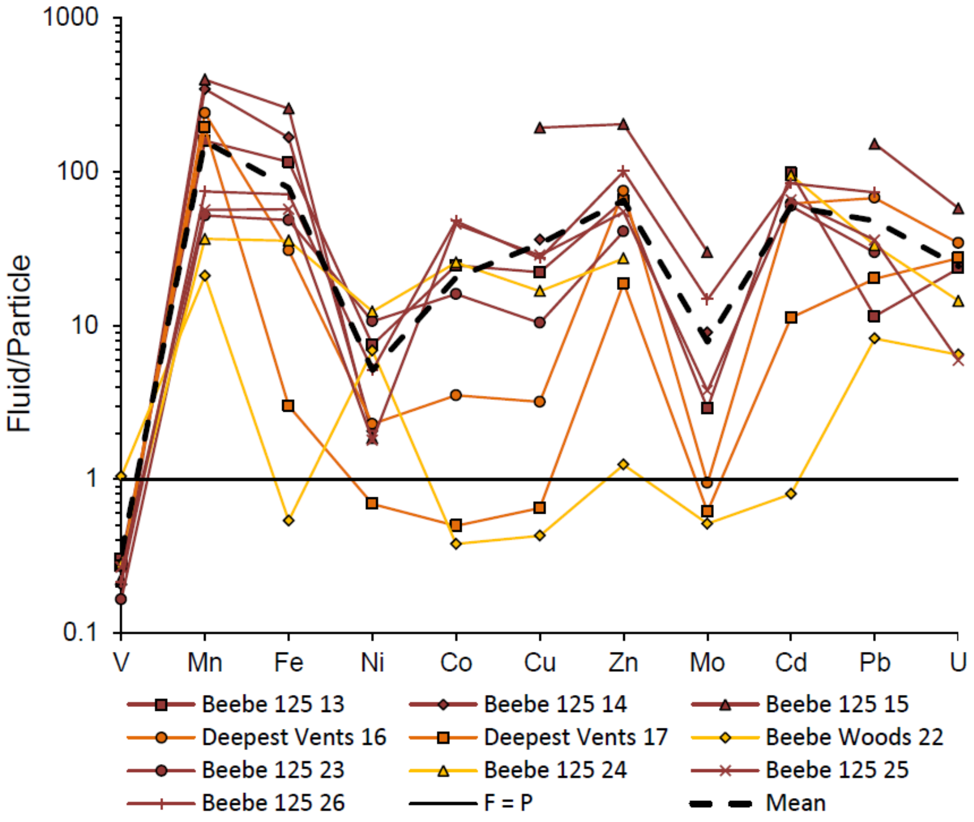

Figure 2.9 Segregation of metals between the vent fluid and particle sample fractions at BVF. Different shapes and colours represent samples collected from different sampler deployments.

In BVF vent fluids Zn, Cd and Pb show the same curvilinear trends relative to Fe whilst Cu and Co show a different trend (Figure 2.12). This indicates removal of Cu and Co from the fluid via a different precipitation pathway to that of Zn, Pb and Cd. Association of these elements by in mineral particles is further evidenced by the highest correlation in particle concentrations between Fe with Cu and Co (r^2 = 0.961 and 0.959, p = 7.2 x 10^{-10} and 2 x 10^{-8}) indicating that particulate Fe is associated with Cu and Co (Figure 2.13). Zn, Cd, and Pb also all show similar trends relative to Fe in particles but with lower r^2 values and p values.

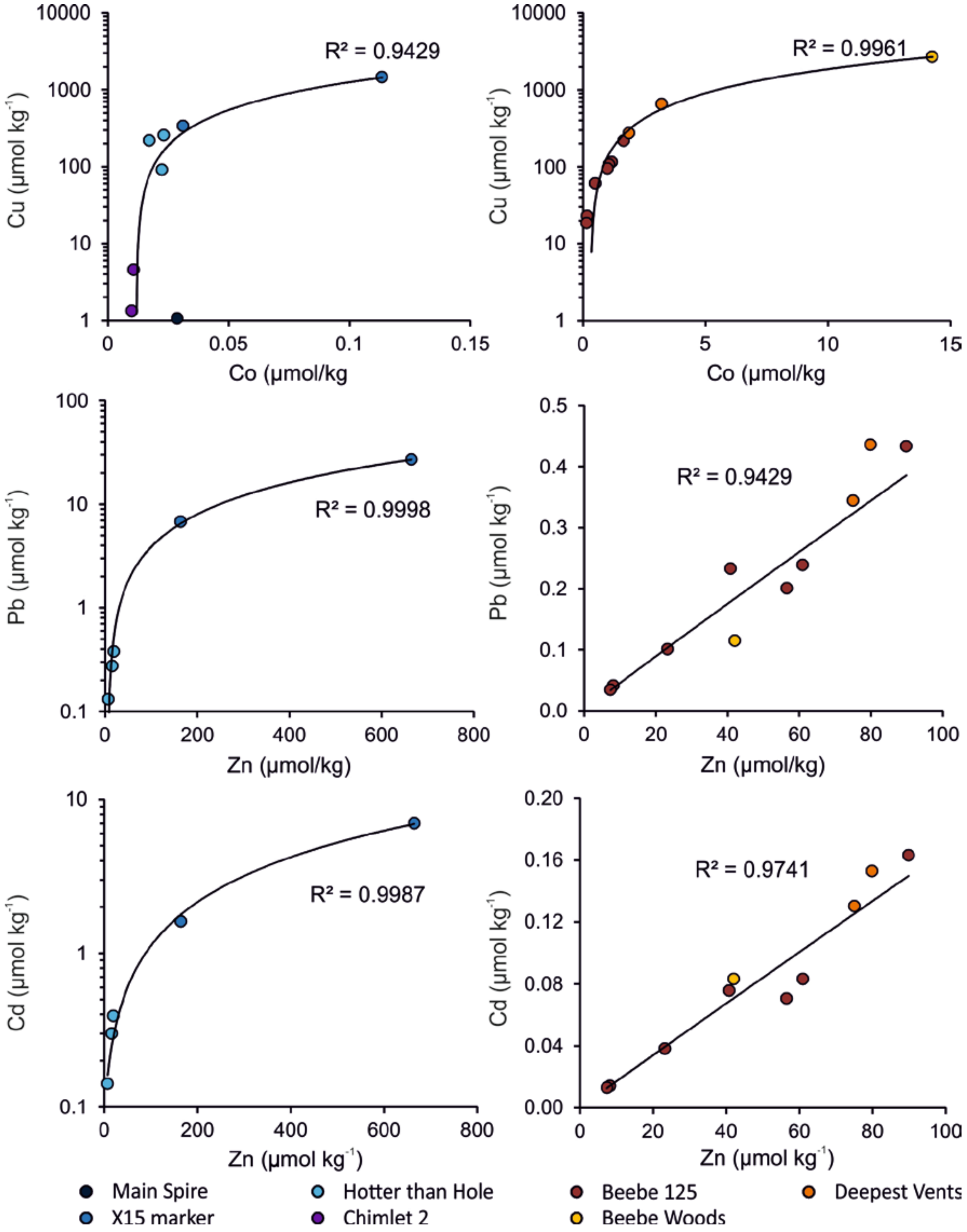

Figure 2.10 Association of Cu with Co and Zn with Pb and Cd in vent fluids. Note that all y-axis have log scales therefore linear trend appears as a curved line. The exception being BVF Cd and Pb, which do not have log scales.

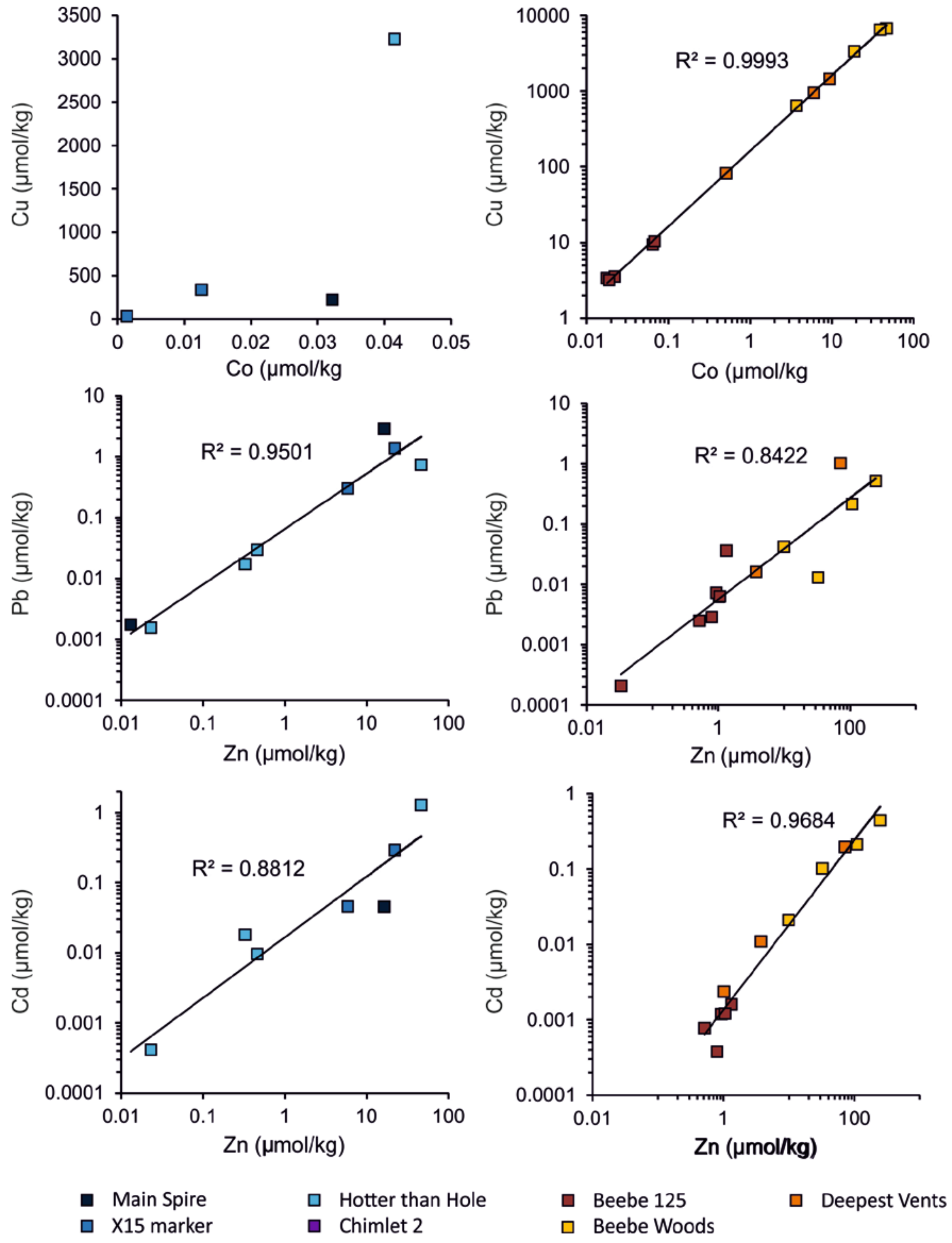

Figure 2.11 Association of Cu with Co and Zn with Pb and Cd in particles. Note log scales for all graphs except VDVF Co/Cu. All lines represent power law regression. Lower no. of sample points for VDVF Co/Cu as several samples had Co concentrations <l.o.d. Colour scheme is the same as previous figures.

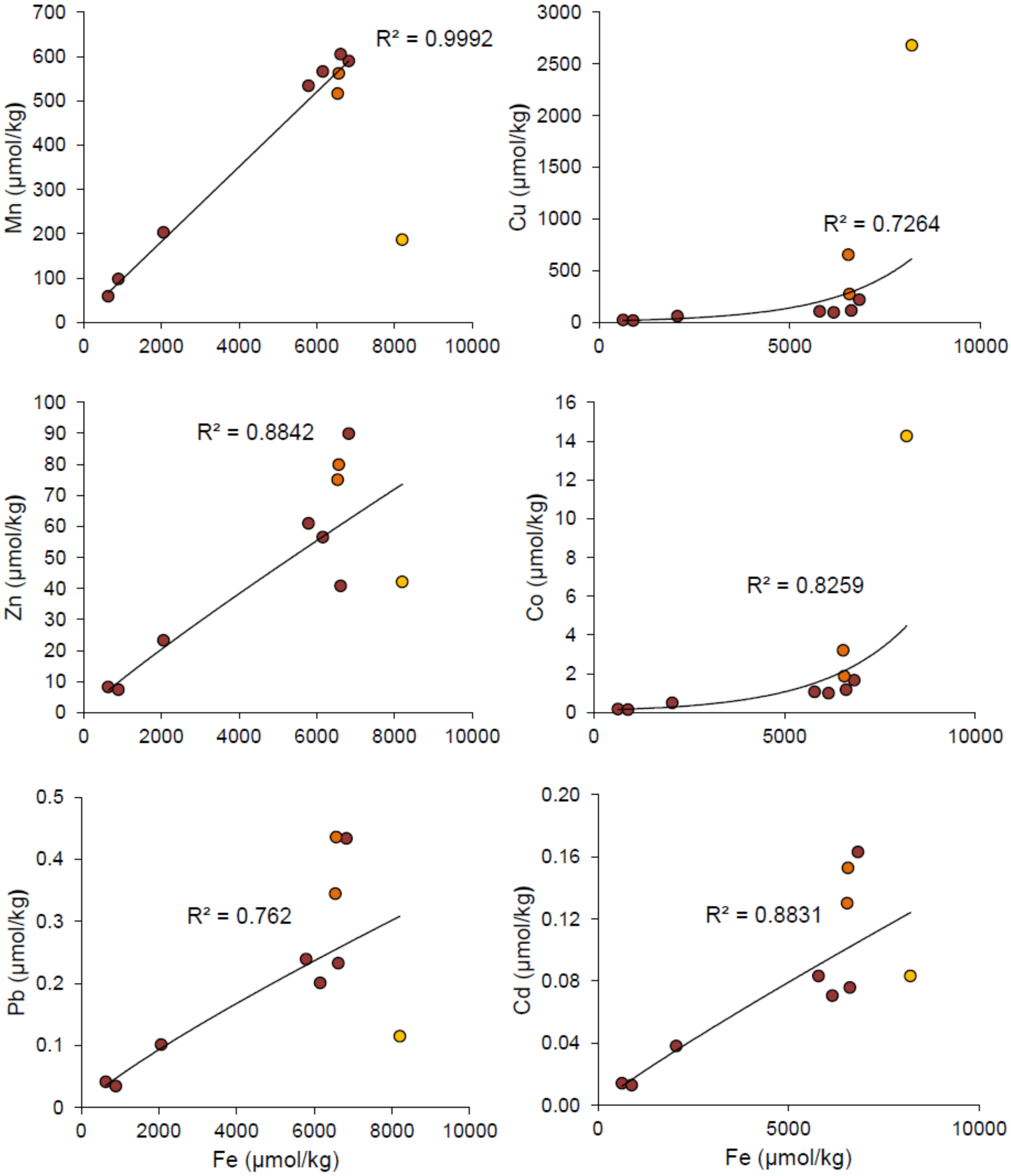

Figure 2.12 Vent fluid metal concentrations relative to Fe concentration in BVF samples. Colour scheme is the same as previous figures for data points.

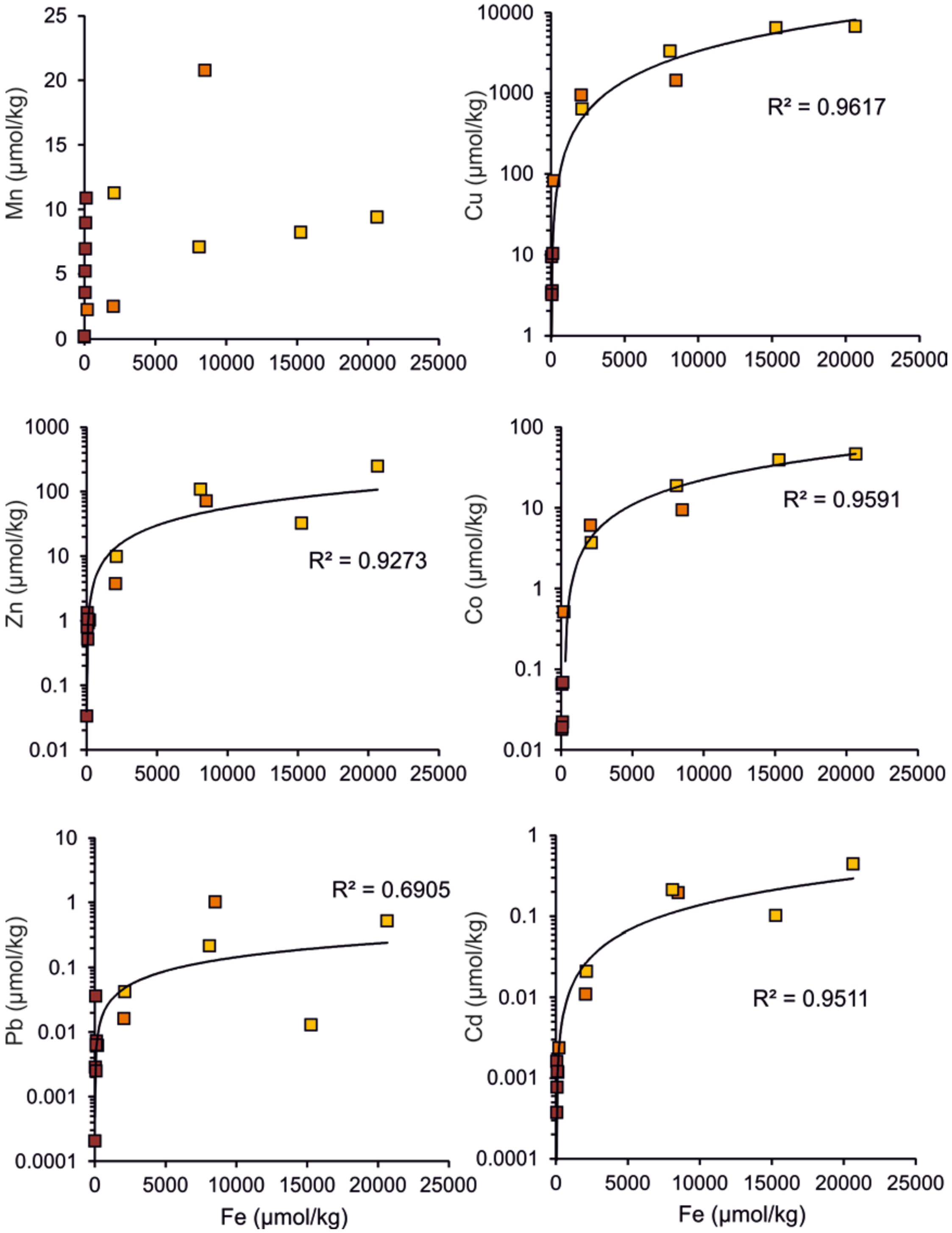

Figure 2.13 The concentration of Fe in plume particles relative to other metals in particles from BVF samples. Fe/Co trend is linear whereas Fe/Pb, Fe/Zn, Fe/Cd, Fe/Cu are best described by power law curves.

2.4.5 BVF vent particle composition from SEM-EDX

A total of 40 metal bearing particles from settled particles collected from the Beebe Woods plume (BVF FLU 19) were examined using SEM-EDX. These samples were chosen as they had some of the highest metal concentrations in the particle fraction. FeS (pyrrhotite) was the dominant particle type except for 3 particles, which were $CuFeS_2$ (chalcopyrite) and FeS_2 (pyrite) (Table 2.3). All particles were 10 µm in size or greater and aggregates composed of smaller ~1 µm sized particles. Chalcopyrite, pyrite and pyrrhotite minerals exhibited a typical cubic to hexagonal euhedral morphology.

Table 2.2 SEM-EDX analysis of particles from BVF and VDVF

	BVF	
Mineralogy	Number of particles	Percent of total (%)
$CuFeS_2$	1	2
FeS	40	89
FeS_2	1	2
FeOOH	0	0
ZnS	0	0
S rich	0	0
Other*	2	4
Total	45	100

*Particles with no peaks for transition metals (e.g $CaSO_4$)

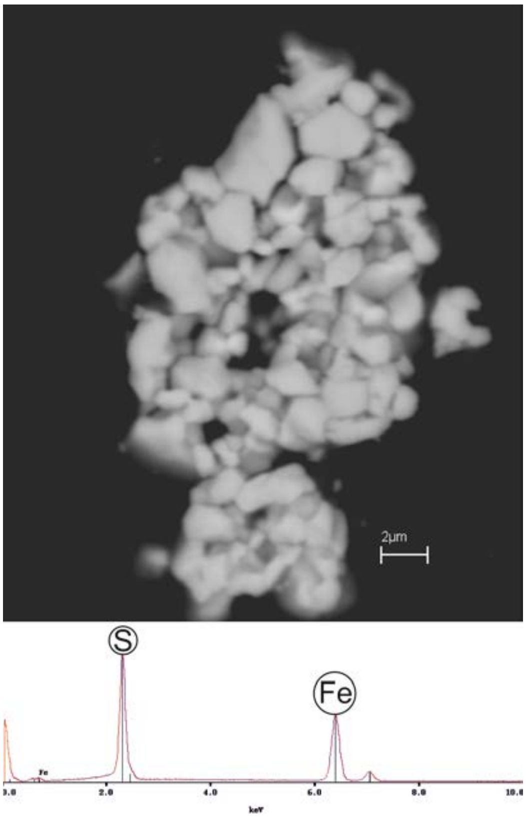

Figure 2.14 SEM image and EDX spectra of a pyrrhotite aggregate particle. The ratio of Fe/S is 1.1 after normalising weight % from spectra to atomic masses of Fe and S.

2.4.6 Modelling of BVF metal precipitation

Thermodynamic modelling of initial plume mixing using GWB predicts the formation of coesite, barite plus metal sulphides in the BVF model. The model did not predict the formation of pyrrhotite or chalcopyrite, which SEM-EDX analysis suggested was the predominant particle mineralogy (Figure 2.15). The model likely overestimated the amount of covellite forming, which was predicted to be the only Cu sulphide mineral in the plume model however this is unlikely to be the case due to the slower kinetic rates controlling the formation of covellite, which is a secondary replacement mineral for chalcopyrite in hydrothermal chimneys, sediments and subsurface (Mottl and McConachy, 1990, Webber et al., 2015, Janecky and Seyfried, 1984). Chalcopyrite was only predicted to form when bornite and covellite were supressed.

Both the prediction of covellite and pyrite at high temperatures are followed by re-dissolution at lower temperatures. This is due to the lack of any Fe oxide minerals in the model with hematite and magnetite supressed and no thermodynamic data for ferrihydrite rather than being a realistic prediction of metal sulphide dissolution in the plume.

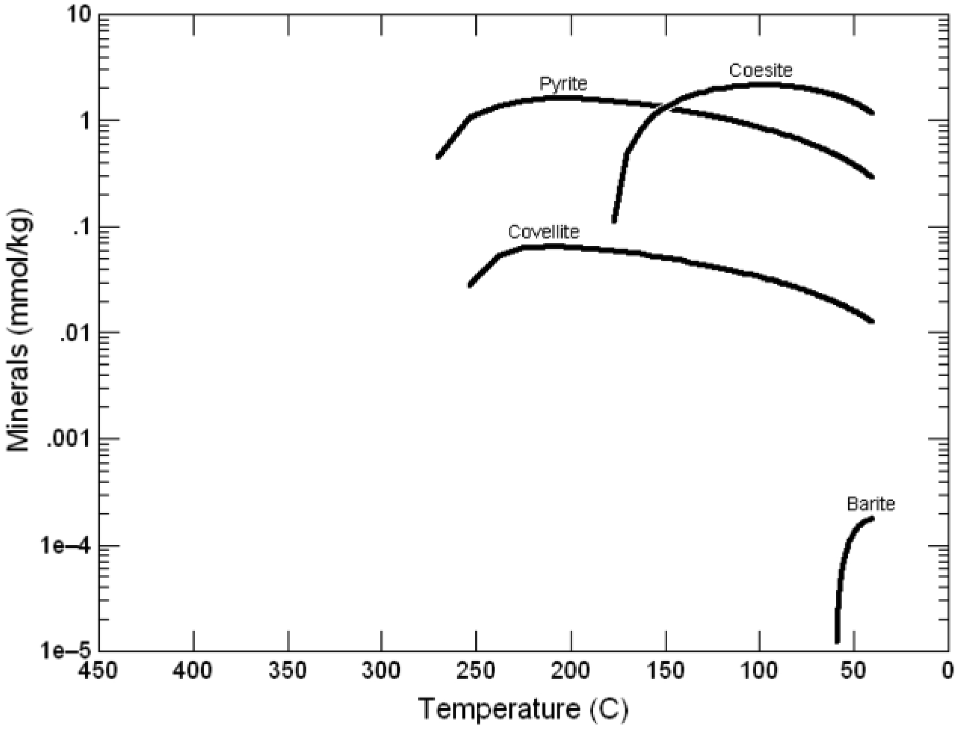

Figure 2.15 Results of the plume mixing model, which used the end member vent fluid composition of the BVF calculated by extrapolating elements concentrations to 0 Mg.

2.4.7 Segregation of metal concentrations between vent fluids and particles at VDVF

Similar to BVF the vast majority of metal concentrations were in the fluid fraction in VDVF samples. Fe, Cu, Zn and Mo represent the largest concentrations of transition metals in the fluids (Figure 2.16). The highest concentrations of elements in the particulate fraction were Fe, Cu and Mo. The highest metal concentrations were observed in samples from hotter than hole and X15 (Figure 2.16). The presence of Mo as a major component of the fluid and particle fraction is a surprising result as this element is typically depleted in hydrothermal fluids and particles relative to other transition metals such as Zn and Mn (German and Von Damm, 2004).

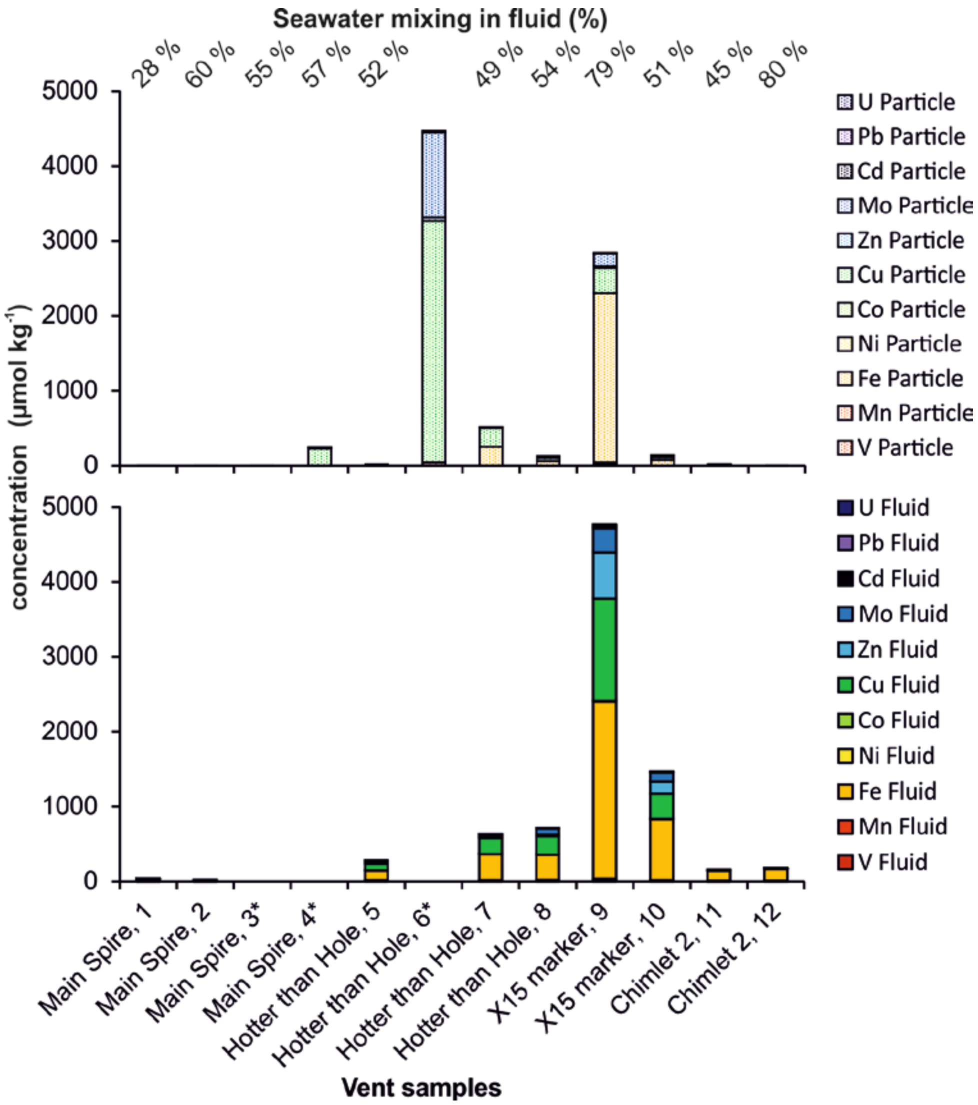

Figure 2.16 Concentrations of metals in fluid and particle fractions in VDVF samples. Sample names with a * are samples where only the particle fraction is examined as the fluid fraction was either not analysed or considered to be contaminated by chimney material based on Ca/Mg shown in (Figure 2.6).

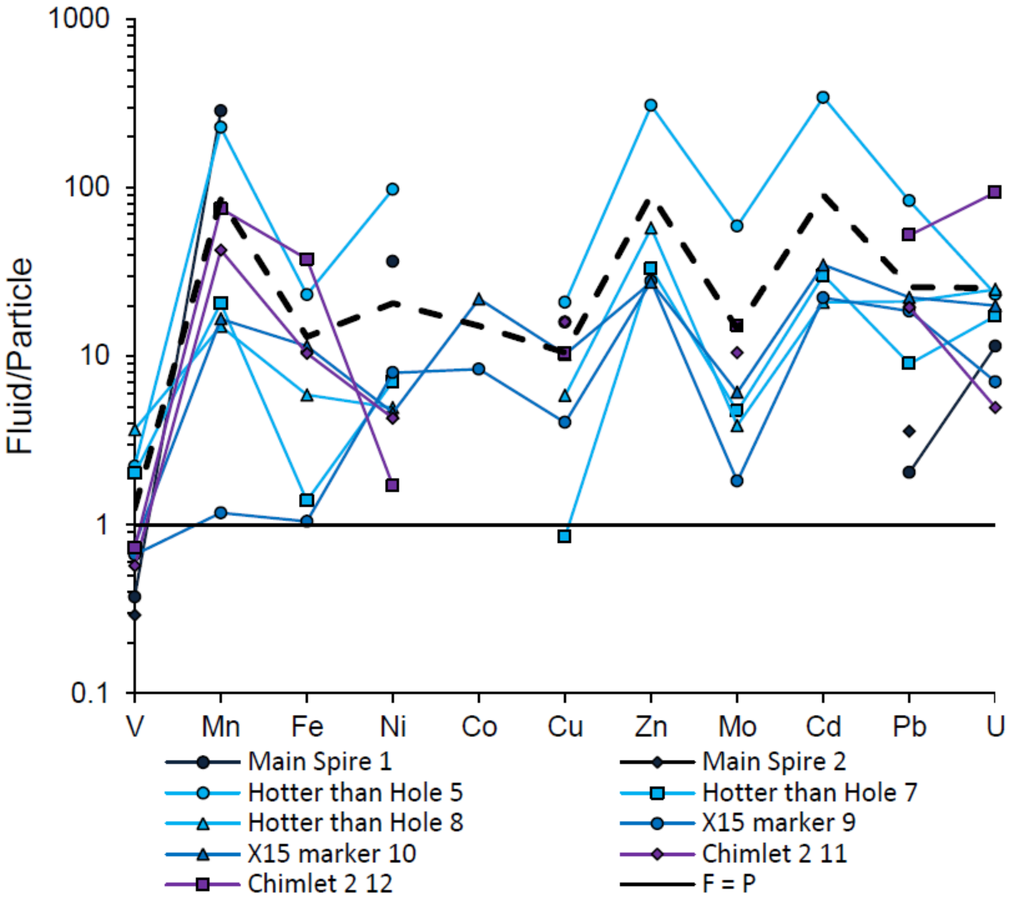

Figure 2.17 Segregation of metals between the vent fluid and particle sample fractions at VDVF. Different shapes and colours represent samples collected from different vents.

In comparison to BVF the average fluid particle ratios of Mn, Fe, Cu and Pb are lower as a higher portion of the total element concentrations are present in the particle fraction. Whereas ratios of Zn and Cd were higher on average in VDVF samples (Zn f/p = 65, Cd f/p = 59) showing that more Zn and Cd was present in the fluid fraction in VDVF samples compared to Beebe (Zn f/p = 60, Cd f/p = 36). The segregation of Fe and Cu predominantly into the particle fraction is an unexpected result given that the venting at this site appears clear and particle free (Figure 2.4) and the formation of Fe and Cu sulphides is what creates the characteristic “black smoke” of black smoker type vents.

2.4.8 Association of trace metals with Fe in VDVF fluids and particles

All major transition metals show linear profiles with Fe except Mn (Figure 2.18). It can therefore be concluded that plume dilution is the predominant control lowering the concentrations of these elements as seawater is mixed into the plume. The contrasting curvilinear profile of Mn with Fe indicates non-conservative behaviour for Mn in the immediate stages of the plume and this behaviour is in contrast to most plumes where Mn behaves near conservatively. For Mn, Co, Zn and Cu the defined trends with Fe in vent fluids rely heavily on one or two samples with higher concentrations (Figure 2.18).

Concentrations of chalcophile metals in VDVF fluids were an order of magnitude lower than those in BVF fluids (Figure 2.18 & Figure 2.18) with the exception of Cd and Pb, which is an order of magnitude higher in fluids from X15. The same linear trends between Fe/Cd and Fe/Zn observed in the VDVF fluid fraction were re-produced in the particle fraction. Particulate Fe/Mn shows a linear trend and it is possible that particulate Mn in the VDVF particles is associated with particulate Fe (Figure 2.19) by either adsorption or incorporation into the same particle species. Similar to the vent fluids the caveat to these trends in particles is that two or three samples had much higher concentrations than the other six or seven samples.

For all VDVF samples, particulate metal concentrations were similar to BVF with the exception of Co (Figure 2.13 & Figure 2.19), which was higher in BVF samples by up to 10^3. Particles in VDVF samples contained 1×10^{-4} to 0.04 µmol kg^{-1} Co in comparison to BVF samples in the range of 0.01 to 46 µmol kg^{-1}.

VDVF fluids and particles show some notable similarities with BVF despite the different geological setting. Cu concentration in fluids were linearly correlated with Co and both Cd and Pb were correlated with Zn (Figure 2.10), this relationship is clearer in BVF fluids where there is a greater range of concentrations sampled. Curvilinear regression shows significant correlation for Zn/Pb and Zn/Cd in both BVF and VDVF particles (Figure 2.11). These similarities are likely due to most of the metals being associated with metal sulphide particles at both sites, despite the VDVF venting fluids appearing clear and particle free. Notably the correlation between Cu and Co observed in BVF particles was not observed in VDVF particles.

All fluids and particles in VDVF samples were significantly enriched in U and Mo (fluid 0.08 – 340 µmol kg^{-1} Mo and 0.002 to 22 µmol kg^{-1} U) at concentrations several orders of magnitude higher than BVF samples (fluid 0.07 – 1.7 µmol kg^{-1} Mo and 0.005 to 1.2 µmol kg^{-1} U) (Table 2.4).

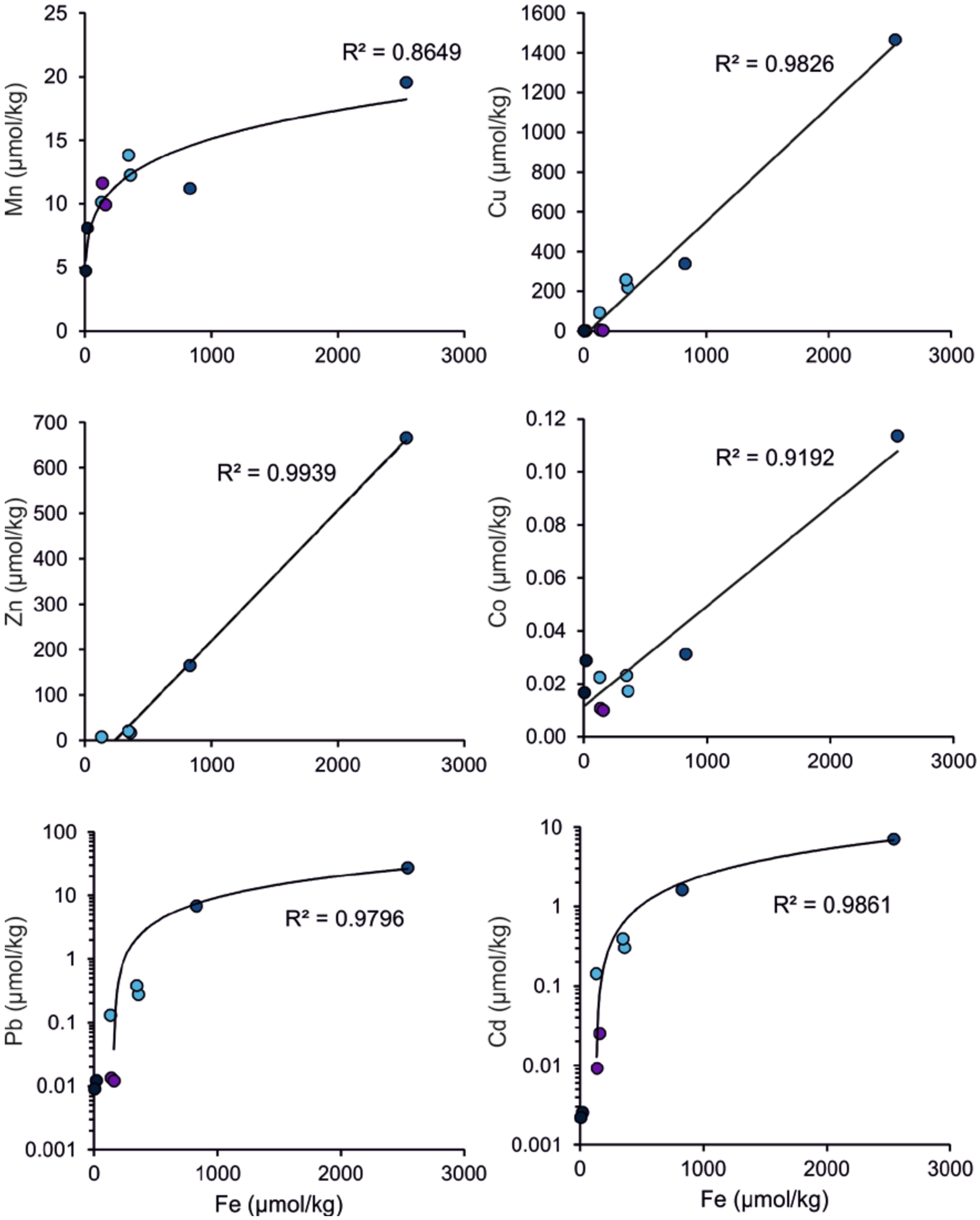

Figure 2.18 VDVF vent fluid metal concentrations relative to Fe concentration. Note log scale for Pb and Cd. All trends are linear except Fe/Mn, which is exponential.

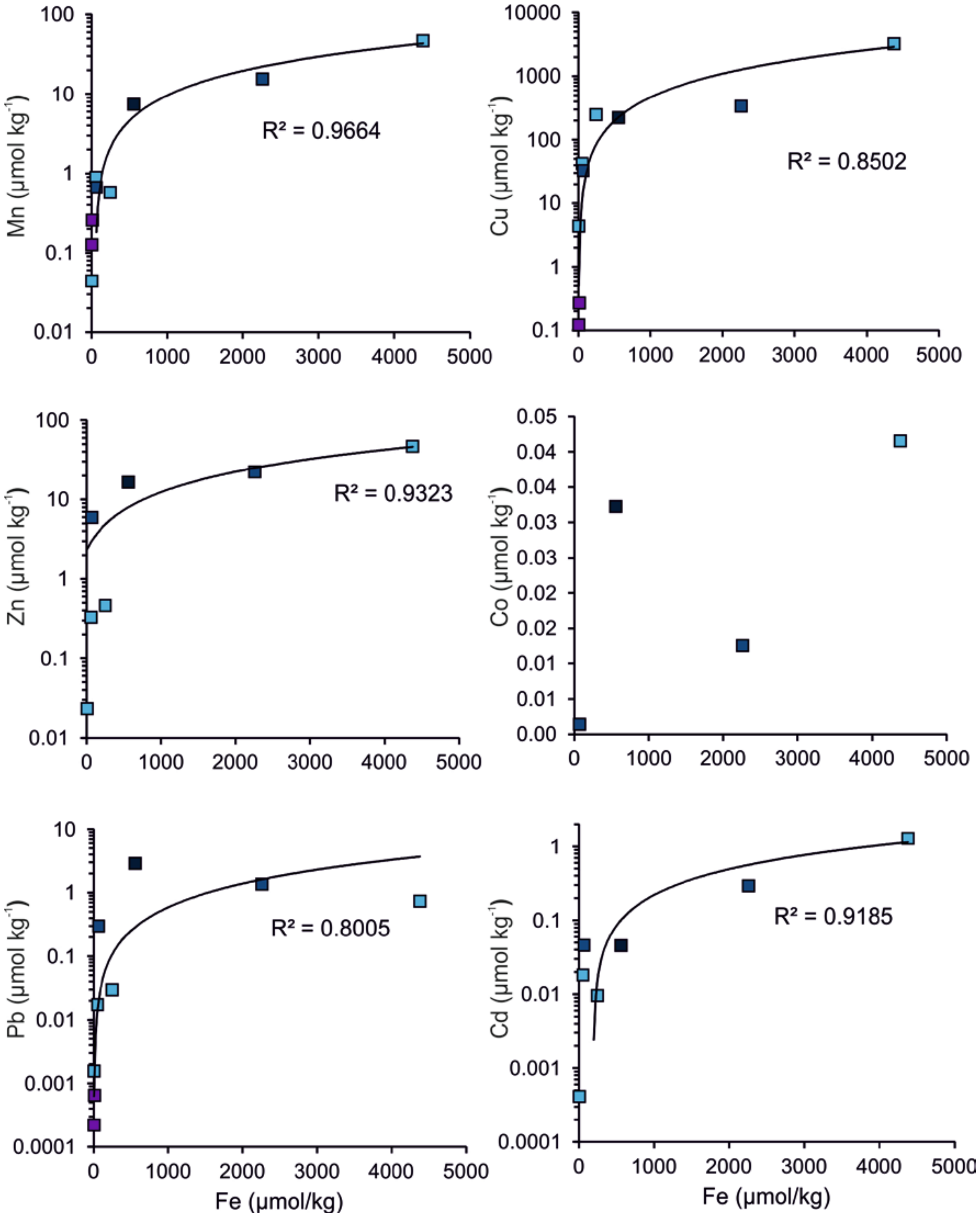

Figure 2.19 The concentration of Fe in plume particles relative to other metals in VDVF samples. Note log scales for Cu and Cd. All trends are linear except Fe/Pb and Fe/Cu, which are best described by a power law trend. Colour scheme is the same as previous figures for data points.

2.4.9 VDVF vent particle composition from SEM-EDX

8 particles from one sample collected at VDVF hotter than hole were examined using SEM-EDX. This sample was chosen as it had some of the highest metal concentrations in the particle fraction. It is also the largest venting orifice on the VDVF so is likely to provide the largest flux of particles to the overlying plume. Areas of the filter segment were selected for examining particles using a systematic grid pattern.

VDVF particle composition showed more variability than BVF. $CuFeS_2$ (chalcopyrite) was the most dominant mineral in VDVF particles (Table 2.3). Pyrite was also identified along with another particle predominantly composed of sulphur with elevated levels of U and trace levels of Fe and Cu (Figure 2.20).

Table 2.3 SEM-EDX analysis of particles from BVF and VDVF

	VDVF	
Mineralogy	Number of particles	Percent of total (%)
$CuFeS_2$	5	71
FeS	0	0
FeS_2	1	14
FeOOH	0	0
ZnS	0	0
S rich	1	14
Other*	0	0
Total	7	100

*Particles with no peaks for transition metals (e.g $CaSO_4$)

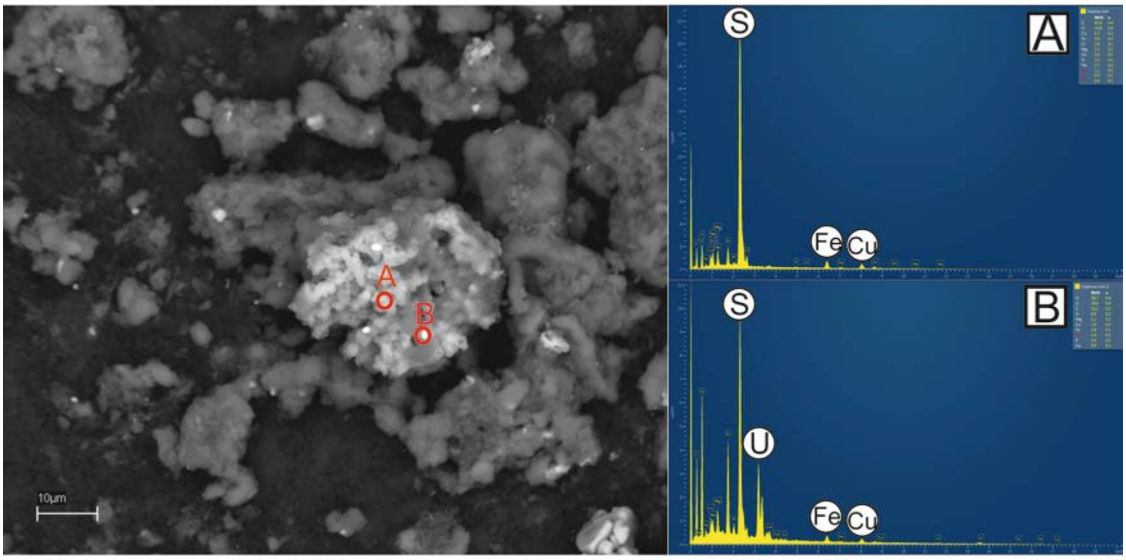

Figure 2.20 Image and EDX spectra of S rich aggregate particles from Hotter than Hole. Particles that appear brighter in the image (B) were enriched in U compared to others (A). Trace amounts of Fe and Cu were detected. Detectable elements in both (A) and (B) at keV <2 include Si, P, As, V and Zn, elements of limited detection include C, O and Mg.

Table 2.4 Additional vent fluid and particle data for constraining the chemistry of VDVF and BVF vents

				Fluid Fraction				Particle Fraction		Total[a]	
Chimney		Temp.	pH	Cl	H_2S	Mo	U	Mo	U	MeS[b]	MeS/H_2S
VDVF											
Main Spire	1	215	6.0	643	1.0	0.08	0.002	$<7 \times 10^{-4}$	0.0002	20	0.02
	2		6.2	592	0.9	0.07	0.006	$<7 \times 10^{-4}$	$<4 \times 10^{-5}$	7	0.01
	3		6.3	610	0.9	E	E	$<7 \times 10^{-4}$	$<4 \times 10^{-5}$		
	4		NA		1.0	E	E	2	0.08		
Hotter than Hole	5	133	6.2	599	0.3	33	1	1	0.06	240	0.7
	6		NA	603	1.0	NA	NA	1135	21		
	7		6.1		0.5	33	2	7	0.09	1079	2.4
	8		6.2		1.0	87	3	21.65	0.1	701	0.7
X15 marker	9	111	NA		1.7	340	22	174.66	2.9	6968	4.0
	10		NA		0.8	120	6	19.35	0.3	1425	1.8
Chimlet 2	11	107	6.2		0.7	4	0.1	0.39	0.02	148	0.2
	12		7.0		NA	4	0.2	0.26	0.002	161	
Average		141	6	609	0.9	69	3.9	151	2.42	1194	1.2
BVF											
Beebe 125	13	401	3.1		0.3	0.2	0.005	0.07	0.0002	6910	26
	14		6.1	541	4.7	0.2	0.02	0.02	$<4 \times 10^{-5}$	636	0.1
	15		6.0	541	1.8	0.07	0.01	0.002	0.0002	848	0.5
Deepest Vents	16	393	2.9		5.1	0.2	0.03	0.2	0.001	6906	1.3
	17		3.0		6.9	0.2	0.03	0.3	0.001	9854	1.4
	18		3.4		3.7	E	E	3	0.02		
Beebe Woods	19	350	3.7		4.4	E	E	2	0.002		
	20		3.5		2.6	E	E	0.3	0.001		
	21		4.8		4.4	E	E	0.3	0.003		
	22		4.3		1.9	0.07	0.009	0.1	0.001	32816	17.3
Beebe 125	23	401	3.1	372	4.2	0.06	0.001	$<7 \times 10^{-4}$	$<4 \times 10^{-5}$	6449	1.5
	24		3.9	499	1.3	0.1	0.01	$<7 \times 10^{-4}$	0.001	2067	1.6
	25		3.1	389	3.2	0.05	0.001	0.01	0.0002	5745	1.8
	26		3.0	378	3.2	0.06	0.001	0.004	$<4 \times 10^{-5}$	5843	1.8
Average		386	3.8	453	3.4	0.13	0.011	0.539	0.00293	7807	5.3

NA = not analysed, E = transition metal fluid data excluded based on Ca/Mg correlation following the InterRidge vent fluid protocols 39 (Beaulieu et al., 2013), < = below stated l.o.d. Cl, H_2S concentrations are mM, U and Mo are μmol kg^{-1}. [a] Total concentrations are fluid + particle concentration normalized to the weight of particles recovered from the sample [b] MeS is the combined concentration of Fe, Cu, and Zn.

2.4.10 Modelling of VDVF metal precipitation

Thermodynamic modelling of the VDVF site predicted the formation of talc along with metal sulphides. All metal sulphides predicted have been observed in particles examined in this study or in chimney material examined in other studies (Hodgkinson et al., 2015). Key exceptions are the absence of any elemental sulfur and chalcopyrite in the VDVF model. Chalcopyrite was observed to be the predominant sulphide mineral in VDVF chimneys (Hodgkinson et al., 2015) as well as being present in plume samples examined in this study by SEM-EDX (2.4.9).

No manganese minerals are predicted from modelling approaches, despite high concentrations of pMn relative to the vent fluid, however this maybe a result of the limited thermodynamic data included in the database for Mn minerals. The precipitation of barite and uraninite are predicted at low temperatures in the late stages of mixing. The presence of uraninite could explain high concentrations of U in particles (Table 2.4) and observed peaks of U in EDX spectra (Figure 2.20) but the amount of uraninite formation in the model (1x10^{8} μmol kg^{-1}) could only account for a maximum of 0.005 % of the U measured in the particle sample with the lowest U concentration.

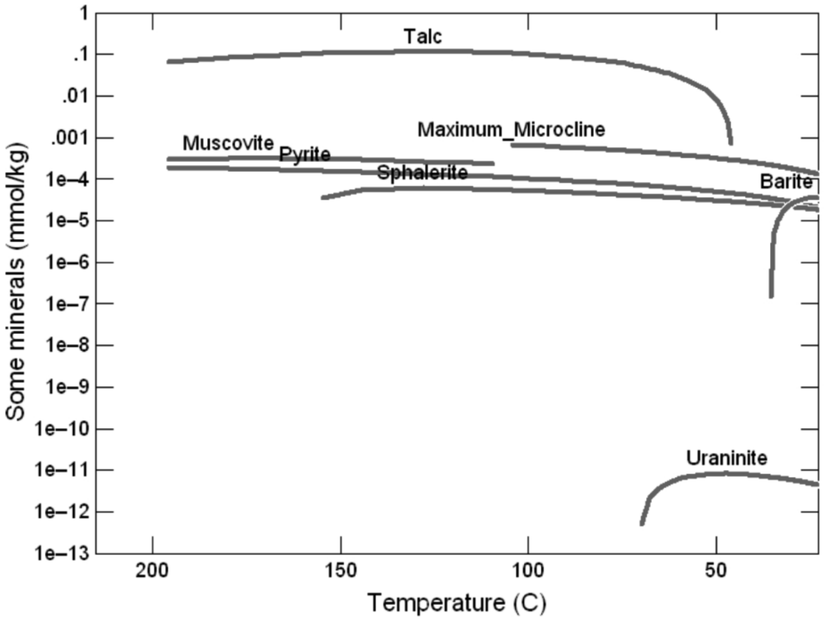

Figure 2.21 Results of the plume mixing model, which used the average element composition of VDVF samples as the hydrothermal end member.

The model indicates that talc will re-dissolve at lower temperatures (Figure 2.21). This process could explain why Mg did not show trends with metals in the VDVF plume. If talc is re-dissolving at lower temperatures then Mg may not behave conservatively in the VDVF plume. This would explain why it was not possible to use Mg as a mixing proxy in the VDVF plume in order to extrapolate back to 0 Mg and predict the concentration of the hydrothermal end member.

2.5 Discussion

2.5.1 Metal sulphide precipitation and metal enrichment in fluid and particles between vent sites

Associations of trace metals in vent fluids and particles indicates similarities between the two sites but also notable differences. Both sites show a correlation between Fe and Cu in both the particle and fluid fractions suggesting that at both sites chalcopyrite formation is an important control on the concentrations of Fe and Cu in the plume (Figure 2.12, Figure 2.13, Figure 2.18, Figure 2.19). Correlation of Zn with Cd and Pb in fluids and between Zn, Cd, Pb in particles is also evidence of Cd and Pb incorporation into sphalerite, which is the major Zn mineral particle in hydrothermal plumes and has been shown to incorporate Cd and Pb (Hsu-Kim et al., 2008, Klevenz et al., 2011, Findlay et al., 2015). These mineral forming processes are typical of early hydrothermal plume mixing (German et al., 1991, Klevenz et al., 2011, Findlay et al., 2015).

Chalcopyrite precipitates more readily than pyrite or pyrrhotite during plume mixing due to its lower solubility at temperatures <300 ˚C (Klevenz et al., 2011). As a result dissolved concentrations of Cu and Fe decrease by chalcopyrite particle formation before Fe precipitates as pyrite or pyrrhotite. The differences in solubility between chalcopyrite and sphalerite dictates that chalcophile metals precipitate in the order of Cu, Co, Zn, Cd and Fe (Douville et al., 2002, Klevenz et al., 2011). The concentrations of metals in BVF fluids relative to Fe indicates that this is the case, Cu and Co show a similar exponential decrease with decreasing Fe concentration (Figure 2.12). This indicates that Cu and Co precipitate as chalcopyrite from solution preferentially followed by sphalerite, which in turn incorporates both Pb and Cd and these elements showed the same trends for Zn, Cd and Pb (Figure 2.12). These elements were also correlated in VDVF fluids but did not display the same trends as BVF fluids where Cd, Co, Zn, Pb and Cu were best described by a linear trend with Fe (Figure 2.18), which indicates conservative behaviour relative to Fe for these metals. The presence of chalcopyrite particles in VDVF samples examined by SEM-EDX would suggest that this mineral may have precipitated first out of solution consuming the available H_2S (up to 1.7 μmol kg^{-1}). Based on the linear conservative trends for Cu and Co with Fe in the VDVF fluids, observations of chaplcopyrite in particles but absence of chalcopyrite in the plume mixing model it is probable that chalcopyrite precipitated in the subsurface at VDVF as the hydrothermal fluid rises and cools to venting temperatures <350 °C. The particles that form in the subsurface are then carried by venting fluids into the overlying plume.

Intuitively the difference between the concentration of metals in the fluids and the particles between sites should be the result of the concentration of metals in the fluid. For example, if the vent fluid has a higher metal concentration at one site then the concentration of metals in the particle fraction is expected to be higher. When comparing the concentrations of metals in fluids and particles from both sites this is only the case for Fe and Co where VDVF vent fluids are depleted in these metals in comparison to BVF fluids (Figure 2.12 & Figure 2.18) and therefore the particles at VDVF are also depleted in Fe and Co relative to BVF (Figure 2.13 & Figure 2.19). Similarly Mo and U have higher concentrations in VDVF particles in comparison to BVF particles as the fluid they are derived from has higher concentrations of these metals (Table 2.4). Despite lower vent fluids concentrations Mn and Cu concentrations of VDVF particles were within a similar range to that of BVF particles (Figure 2.13 & Figure 2.19). For Cu this gives further evidence to the theory that chalcopyrite particles form at the subsurface at this site rather than in the plume. Mn oxidation rates and reactions with sulphide in plumes are much slower than that of other metals and thus it does not typically precipitate in hydrothermal plumes to the same extent as other metals (Field and Sherrell, 2000, Klevenz et al., 2011, Sands et al., 2012). One possible explanation for the high VDVF particulate Mn concentrations is the presence of Mn sulphides, which have been observed only once previously in samples from the EPR (Breier et al., 2012). Thermodynamic modelling did not predict the formation of any Mn minerals however the thermodynamic database is limited to data for manganosite (MnO) and rhodocrosite ($MnCO_3$). The other explanations for particulate Mn is adsorption of Mn^{2+} onto other particles (Feely et al., 1994a) or incorporation into amorphous silicate minerals (Findlay et al., 2015). Increased DOC concentration in Von Damm vents has been attributed to greater subsurface mixing at this site compared to other vents (Hawkes et al., 2015) and this is likely to increase the probability that Mn oxyhydroxides or Fe oxyhydroxides that scavenge Mn will form. Similar association between Mn and Fe has been attributed to Fe oxyhydroxide formation in a hydrothermal caldera (Hawkes et al., 2014) where there is also likely to be increased subsurface mixing. Given the association of Fe with other metals reflects co-precipitation with sulphides it is unlikely that Fe oxyhydroxides are present in significant amounts. As the oxidation rate of Fe (II) is faster than that of Mn (II) this makes the presence of Mn oxyhydroxides unlikely unless facilitated by biological processes as has been observed in distal hydrothermal plumes (Cowen et al., 1990). It cannot be said definitively without further SEM-EDX analysis of VDVF particles which mineralogy these high Mn particle concentrations are associated with.

Me/H_2S ratios are an important controlling factor in the amount of metals precipitating as sulphides. VDVF samples have lower total metal (Table 2.4) to sulphide ratios (Me/H_2S) of 0.01 to 4 in comparison to BVF where Me/H_2S range from 0.1 to 26. The lower Me/H_2S ratios in VDVF samples are therefore the main reason why Cu, Fe and Co are separated predominantly into the particulate fraction at this site, in comparison to BVF (Figure 2.9 & Figure 2.17) where metal concentrations are in excess relative to sulphide. Globally in black smoker type vents, H_2S concentrations are on average higher than metal concentrations in vent fluids with mean Me/H_2S ratios of ~0.3 (Von Damm, 1995, German and Von Damm, 2004). At both sites vent fluids have a Me/H_2S is >1 (Table 2.4) more dissolved metals are added to the plume as metal concentrations are in excess of sulphide. Using the end member metal concentrations calculated from Beebe 125 samples (see section 2.4.1) the Me/H_2S of the BVF end member is 3. This is lower than the Rainbow vent site, which has the highest measured Me/H_2S of 24 (Douville et al., 2002) but higher than most typical basalt hosted vent systems, which have Me/H_2S of <1(Bennett et al., 2009, Douville et al., 2002, James et al., 1995). Rainbow has a high

Me/H_2S ratio as a result of the ultramafic rocks through which hydrothermal circulation takes place in the sub-surface and this is also the case for the BVF (Webber et al., 2015). The Me/H_2S of the hydrothermal end member at VDVF cannot be calculated due to the non-linear profiles of metals with Mg (Appendix D) however the mean Me/H_2S from VDVF vents is 1.2 with metals in excess of sulphide on average. Vent fluids with Me/H_2S ratio's >1 at both sites indicate that even if H_2S precipitated quantitatively with trace metals there would still be metals remaining in the fluid fraction in the rising plume.

Metal sulphides will undergo oxidative dissolution in the buoyant plume transferring metals back to the dissolved fraction (Metz, 1993), which would then remain in the dissolved fraction or form Fe oxyhydroxides. This is an important consideration for dissolved metal fluxes as the mineral composition of plume particles can determine the rate of mineral dissolution. At BVF the majority of Fe particles examined were discovered to be FeS (Table 2.3), which is less stable in oxygenated seawater than FeS_2 (Feely et al., 1987) and therefore more likely to undergo oxidative dissolution in a later stage of plume dispersion (Seyfried and Ding, 2013).

The rate of pyrrhotite dissolution in the plume ($1x10^{10}$ cm s^{-1}) is an order of magnitude faster than that of pyrite ($1.1 \text{ x } 10^{11}$ cm s^{-1}) (Feely et al., 1987). Comparison of settling rates for the early stages of the plume (5 m) to mineral dissolution rates (Table 2.5) reveals that any pyrrhotite in the early stages of the BVF plume is likely to re-dissolve before settling to the seafloor. This is a conservative estimate given that it is likely the buoyancy of the plume will carry particles to heights greater than 5 m above the vent, and the particles will also settle to the seafloor, which is deeper than the height of the vent. It is also worth noting that 2 µm sized particles represent the smallest particles we observed and dissolution rates will be higher with larger particles however *in-situ* particle size studies of the BVF plume reveal most of the particles were 3 µm (Estapa et al., 2015). Based on this information if it is assumed that all of the Cu in the BVF end member (114 µmol kg^{-1}) is converted to chalcopyrite then 1.7 % of end member hydrothermal Fe (6794 µmol kg^{-1}) is converted to chalcopyrite. If all pyrrhotite formed is re-oxidised then this means that up to 98.3 % of the Fe in the BVF hydrothermal end member will remain dissolved or form Fe oxyhydroxides.

Despite the high Fe/H_2S ratio at BVF of 3, no Fe oxides or silicates were observed as has been the case at other ultramafic hosted vents such as Rainbow, which has a high Fe/H_2S of 24. Fe sulphides in Rainbow samples are predominantly pyrite (FeS_2) rather than pyrrhotite (FeS) so it is unlikely that the formation of pyrrhotite particles in BVF samples are the result of an excess of Fe relative to sulphide (high Fe/H_2S ratio) as the Fe/H_2S ratio of Rainbow is higher and there has been no pyrrhotite observed at this site (Findlay et al., 2015). This means that having an excess of Fe in vent fluids relative to H_2S does not make it more likely that the ratio of Fe/S in particles will be equal. Instead the formation of pyrrhotite in BVF particles is more likely to be the result of reaction kinetics or a result of the supercritical venting temperature and pressures of BVF as the formation of pyrrhotite was not predicted by vent fluid-seawater mixing modelling (Figure 2.15).

Table 2.5 Settling rates of different plume particles

Plume mineral particles	Settling rate[a] ($m\ s^{-1}$)	Settling time for 5 m (days)	Days to totally dissolve 2 µm mineral[b]
pyrrhotite	4.1×10^{-6}	14	11
chalcopyrite	3.6×10^{-6}	16	964
sphalerite	3.5×10^{-6}	17	48
pyrite	4.6×10^{-6}	13	106
sulphur (elemental)	1.1×10^{-6}	48	

a. Settling rates calculated using stokes law (Schwarzenbach et al., 1993)
b. Mineral dissolution data for plume particles from *in-situ* study of JdFR plume (Feely et al., 1987).

2.5.2 Consequences for metal fluxes of sulphide oxidation in the VDVF plume

Up to 87 % of H_2S from vents is oxidised by a combination of abiotic and biotic pathways (Luther et al., 2011), which lowers the concentration of H_2S available to form metal sulphide particles. Therefore even vents with lower Me/H_2S ratios may still add dissolved metals to the rising plume if a significant amount of H_2S is oxidised before it can react with available metals. This means that not only does the Me/H_2S ratio determine the flux of dissolved metals to the buoyant plume but also the amount biological activity using up H_2S in the near vent environment.

Based on incubation experiments of sulphide oxidation by free floating and symbiotic chemoautotrophs from vent environments it is likely that anywhere between 1 to 21 % of vent fluid sulphide will be converted to elemental sulphur by biological processes (Luther et al., 2011). These incubation experiments were conducted at a similar pH range (6 to 6.6) and sulphide concentration (0.65 µM) as VDVF fluids and are therefore likely to be representative of this site (Luther et al., 2011). Compared to BVF, plume cell counts (18×10^3 cells/ml) are similar in the VDVF plume (24×10^3 cells/ml) with 7 % abundance of sulphur oxidising bacteria (*Sulfurimonas)* at both sites (German et al., 2010). This indicates similar biological demands for sulphide with less sulphide available at VDVF initially. This will result in less sulphide available to react with metal after biological oxidation. If 21 % of sulphide is oxidised by biological processes at VDVF this would raise the average Me/H_2S to 1.7 transferring more dissolved metals to the rising plume. Given the lesser number of macrofauna around black smoker BVF chimneys (Figure 2.4 A) and lower plume cell counts it is expected that biological sulphide oxidation is less important at BVF compared to abiotic processes. Possibly with the exception of the beehive chimneys of Beebe Woods (Figure 2.4 B) which had a higher number of macrofauna.

Low Fe concentrations and the formation of more stable Fe mineral particles such as chalcopyrite ($CuFeS_2$) and pyrite (FeS_2) will decrease the transfer of dissolved Fe and Cu to the buoyant plume over the VDVF. The presence of trace metals either incorporated into or adsorbed onto sulphur rich particles represent a different mechanism by which Fe and other metals could be transferred to the overlying plume (Figure 2.20). The presence of a similar type of sulphur rich particle has been noted previously (Klevenz et al., 2011, Findlay et al., 2014, Feely et al., 1994a) in vent fluid samples from the MAR where elemental sulphur on the surface of talc was observed as well as on its own. The particles observed are similar in size and Mg and Si were observed but peaks for Mg and Si are relatively small compared to sulphur with atomic weight % ratios of 1.3 to 3.5 for Mg/Si higher than what would be expected from the stoichiometry of talc ($Mg_3Si_4O_{10}(OH)_2$, Mg/Si = 0.75) (Figure 2.20). This shows that particles are mostly made up of sulphur (along with any other low mass elements poorly detected by EDX such as C) and unlikely to be composed of or adsorbed onto the surface of talc despite talc being a major component of chimney material (Hodgkinson et al., 2015). Other studies have observed similar sulphur rich particles in the buoyant and non-buoyant plumes over the EPR and speculate that these sulphur rich particles are the result of sulphur oxidising microbes (Feely et al., 1994a, Breier et al., 2012). It has been proposed (Breier et al., 2012) that these particles form as a result of sulphur oxidising microbes in the non-buoyant plume (NBP) plume. Alternatively other researchers (Feely et al., 1994a) have proposed that sulphur rich particles are the result of sulphur oxidising microbes associated with bacterial mats being entrained into the plume in the near vent environment after explosive eruption events. Given the non-eruptive nature of venting at VDVF it is hard to reconcile our observation of sulphur rich particles in the immediate stages of plume mixing with (Feely et al., 1994a) the hypothesis of sulphur rich particles being entrained as a result of flocculation of bacterial mats. Our observation of sulphur rich particles in the immediate mixing stage of the plume is also not consistent with the theory of these sulphur rich particles being formed in the NBP either (Breier et al., 2012). Elemental sulphur was not predicted to form in thermodynamic models (Figure 2.21), which suggests its formation could be a result of biological processes or catalysed by dissolved metals (Vazquez et al., 1989). Sulphur oxidising microbes have been observed in plumes from both vents on the MCSC with higher abundances in the VDVF plume (German et al., 2010). Furthermore the framboid structure of these particles indicates they have developed on time scales of hours to days (Wilkin and Barnes, 1997), which would require maturation in the subsurface or in the chimney pore space. It is therefore proposed that these particles are likely to be the result of sulphur oxidising bacteria in the near vent environment and these sulphur rich particles could easily be transported to shallower depths in the rising plume due to slow settling rates (Table 2.5). This is consistent with models of primary production in plumes where formation of elemental sulphur in the early plume provides an important source of energy (McCollom, 2000). Importantly the settling rates of these particles are much slower than that of metal sulphide mineral particles found in the plume, which may settle out in the immediate stages of venting. The extended residence time of these sulphur rich particles in the plume means there is more time for re-dissolution to take place or remineralisation if they are of a biological composition and this may increase trace metal fluxes from the plume to the deep ocean.

Recent studies in different environments have demonstrated the role of particles influencing dissolved metal concentrations (Labatut et al., 2014, Revels et al., 2015). From the observations presented here the impact of sulphur rich particles on VDVF plume metal fluxes cannot be reliably quantified. Assuming that all the Cu in the particle fraction is present as chalcopyrite with a 1:1 empirical ratio with Fe, chalcopyrite can account for anywhere between 2 to 97 % of Fe particle concentrations in VDVF particles. Samples from hotter than hole have the lowest percentage of Fe associated with chalcopyrite of 2 to 26 % and this is the same chimney from which the particles were examined by SEM-EDX. This means that 98 to 74 % of Fe concentrations must be accounted for by sulphur rich and pyrite particles in VDVF samples from hotter than hole. This is consistent with the thermodynamic model that shows pyrite as the most abundant metal sulphide particle in the VDVF plume (Figure 2.21). This is of particular importance as hotter than hole vents a larger volume of water than the other chimneys at this site due to the size of the orifice (Figure 2.4) and therefore will be the main source of venting waters to the overlying plume.

The presence of sulphur rich particles, which showed peaks of U in EDX spectra may be important for controlling the flux of U from VDVF vents as U is highly enriched in both VDVF fluids and particles (Table 2.4). The sulphur rich particles were the only particles that showed significant peaks for U using EDX. This could be from the presence of uraninite, which the mixing model shows may precipitate at low temperatures (Figure 2.21). The enrichment of both U and Mo in fluids and particles in VDVF samples is a surprising feature as U is not known to be enriched in vent fluids (German and Von Damm, 2004). Vent fluids are typically depleted in U due to the low amounts present in ultramafic (0.7 μmol kg^{-1}) and basaltic (7 μmol kg^{-1}) rocks, it is also immobile under reducing conditions such as those typical of hydrothermal fluids circulating through the crust. The solubility of Mo is similar to that of Cu and Co and decreases rapidly from temperatures of 300 to 400 ˚C. Mo is usually incorporated into chalcopyrite in the plume and depleted relative to seawater in vent fluid end members with temperatures <350 ˚C (~0.1 μmol kg^{-1} Mo) (Metz and Trefry, 2000). VDVF vent fluids have temperatures <350 ˚C and therefore concentrations of Mo higher than vents with temperatures >350 ˚C would not be anticipated. The enrichment of U and Mo in fluids could be the result of these metals becoming concentrated in a brine phase in the subsurface consistent with an increased chloride content of 22 % in VDVF fluids relative to seawater (Figure 2.6) with additional U and Mo supplied by increased subsurface mixing in comparison to other vent sites (Hawkes et al., 2015). Alternatively U, Fe and Cu have all been shown to adsorb onto the surface of talc (Sprynskyy et al., 2011) and the unique mineralogy of the vent chimneys at this site may play a role in controlling the unique chemistry of the vent fluids. Finally enrichments in U in hydrothermal sediments have been attributed to microbial activity previously (Mills et al., 1994) and this is consistent with our idea of the U enriched sulphur particles being formed by microbial processes in the near vent environment.

2.5.3 Presence of metal sulphide nanoparticles in the fluid fraction

As hydrothermal plumes are progressively diluted by seawater, the chemistry transfers from a sulphidic to an oxygenated system (Trocine and Trefry, 1988). There were no metal oxide mineral particles observed from either site in this study indicating that all samples were taken in the H_2S dominated part of the plume. It is in this early stage of venting where high sulphide concentrations facilitate the formation of metal sulphide nanoparticles, which have been identified as a widespread feature of venting on the MAR, EPR and Lau Basin.

Metal associations of (Zn, Cd, and Pb) (Cu, Co, and Fe) in the fluid samples at both sites indicate (Figure 2.10) that they are likely to contain metal sulphide nanoparticles. This cannot be said definitively as particles were separated by settling rather than filtering which would give a specific particle size limit from filter pore sizes. SEM images of metal sulphides show that larger particles are often aggregates of smaller particles (Figure 2.14) (Gartman et al., 2014, Yucel et al., 2011) and the aggregation of smaller particles maybe facilitated by the sampling process, which traps the particles in the confined space of the sampling vessel. This is in contrast to the turbulent plume environment where particles will be subject to complex mixing regimes. Determining the rate of aggregation within samplers should be an important focus of future work to determine the true concentration of nanoparticles *in-situ*. So far pyrite nanoparticles have only been observed directly in the first 1 to 5 m of plume rise (Gartman et al., 2014, Yucel et al., 2011). Determining the extent to, which nanoparticles aggregate in a hydrothermal plume remains a problem for constraining fluxes of these nanoparticles from vents. If a large fraction of FeS_2 nanoparticles aggregate to form larger particles within the first few meters of plume rise then there input to rising plume and deep ocean will be limited due to rapid settling rates.

2.6 Conclusions

The separation of metals between the particulate and fluid fraction in the immediate stages of plume mixing show some similarities with some notable differences for specific elements between the two vent sites from the MCSC. A higher proportion of Fe was present as particulates in VDVF samples in comparison to BVF samples where Fe concentrations were generally higher in the fluid fraction. This was unexpected given that vent fluids emanating from VDVF chimneys appear clear in comparison to particle dense black smokers. The higher proportion of metals in particles at VDVF are likely to be a consequence of precipitation in the sub-surface due to increased mixing between hydrothermal and seawater end members prior to venting at the seafloor.

Relationships between metals that precipitate as metal sulphides observed in BVF samples where typical of other black smoker type vents studied on the MAR (Klevenz et al., 2011, Findlay et al., 2015). This is consistent with the current chemical model of particle formation in hydrothermal plumes (Klevenz et al., 2011, Rudnicki and Elderfield, 1993, Trocine and Trefry, 1988). The only exception being the predominance of pyrrhotite over pyrite and this may have implications for Fe plume fluxes from these vents due to the un-stable nature of pyrrhotite in oxygenated seawater in comparison to pyrite and chalcopyrite (Gartman and Luther, 2014). Excess Fe relative to Cu (Figure 2.13) in all the BVF particles is attributed to the major Fe forming mineral being pyrrhotite. Pyrrhotite is likely to re-dissolve in the rising plume increasing the concentration of dissolved Fe in the rising plume. However further particle composition analysis of other vents is needed to confirm the presence of pyrrhotite particles venting from other chimneys.

The style of venting at VDVF is unique in comparison to that observed on any other ridge axis globally. Results indicate that chalcopyrite and pyrite are the dominant mineral phases with high variability in Fe and Cu particle concentrations indicating different abundances between these two mineral phases at different VDVF vent sites. The association of metals in VDVF samples is complicated by the presence of sulphur rich particles, which may adsorb/incorporate trace metals. The presence of sulphur rich particles in the immediate stages of mixing suggests they are formed in the near vent environment or subsurface and not in the NBP (Klevenz et al., 2011, Breier et al., 2012, Rudnicki and Elderfield, 1993, Trocine and Trefry, 1988, Feely et al., 1994a).

Mn is predominantly in the particulate fraction in VDVF samples suggesting non-conservative behaviour of this element during vent fluid seawater mixing in the early plume. This will decrease the amount of dMn transferred to the rising plume. The presence of Mn oxyhydroxides is unlikely due to the lack of any Fe oxyhydroxides which should form first due to faster oxidation rates of Fe (II) compared to Mn (II). No Mn was observed in the particles examined by SEM-EDX so without further analysis it cannot be said definitively which mineralogy Mn is associated with.

VDVF fluids are highly enriched in U and Mo compared with all other vent sites globally. These metals are typically depleted in vent fluids relative to seawater due to a low enrichment in hydrothermal host rocks. This is the first time to my knowledge that a vent site has been found with elevated concentrations of these elements in fluids and particles. If other off-axis or diffuse venting sites behave in a similar manner the cycling of U and Mo through these environments could have important implications for constraining the cycling of these elements in the ocean.

This study is one of few to examine the initial stages of vent fluid-seawater mixing (Klevenz et al., 2011, Findlay et al., 2015, Cotte et al., 2015) and the first to examine this process on vents both on and off axis located on an ultra-slow spreading ridge. Our results show that particle forming processes during the initial stages of vent fluid-seawater mixing can be different depending on vent chemistry, which is a result of the host geology. In off axis vent sites with lower temperatures and higher H_2S concentrations relative to metals the extent of biological breakdown of H_2S may be important in facilitating fluxes of transition metals to the rising plume along with subsurface mixing. In higher temperature black smoker vents inorganic metal sulphide precipitation dominates metal chemistry. The stability of metal sulphide particles in oxygenated seawater will determine the extent to which particulate metal is added to hydrothermal sediments and how much adds to dissolved concentrations in the deep ocean. The differences in particle forming processes between vent sites will impact the fluxes of trace metals in the overlying plume and consequently fluxes to the deep ocean.

Chapter 3: Trace metal size fractionation in hydrothermal plumes

ABSRACT

Iron (Fe) limits or co-limits primary productivity and nitrogen fixation in large regions of the world's oceans. Hydrothermal vent supply of Fe to the deep ocean is now known to be extensive; however the mechanism of Fe plume stabilisation in the deep ocean is poorly understood. To examine this process, hydrothermal plumes above the Beebe and Von Damm vent fields were sampled for Total dissolvable Fe (unfiltered) dissolved Fe (<0.2 µm) and soluble (<0.02 µm). Plume particles sampled in situ were characterised using scanning electron microscopy.

We show that 49 to 87 % of dFe in the Beebe hydrothermal plume is present as colloidal Fe (defined as the difference between dissolved and soluble). In the first 100 m of plume rise 22 % of the particulate Fe fraction (defined as the difference between dissolved and total dissolvable) is added to the colloidal Fe fraction. Soluble Fe behaves conservatively during plume dispersion. Particulate Fe increases by 25 % in the neutrally buoyant plume along with a 22 % decrease in colloidal Fe, which is a result of colloid aggregation in the non-buoyant plume. Dissolved Fe in the Von Damm plume contained 14 to 81 % cFe. The highest colloidal Fe concentrations of 6 nmol kg-1 were measured in the most dispersed plume samples, which had the lowest particulate Fe concentrations of 1 nmol kg-1.

Beebe Fe plume profiles can be explained by plume dilution and exchange of Fe between different size fractions. In contrast Von Damm Fe plume profiles may reflect the variability between multiple vent sources adding Fe to the plume as well as exchange of Fe between size fractions.

This study highlights the differences and similarities in metal partitioning between soluble, colloidal and particulate fractions during plume dispersion above two hydrothermal sites that are 21 km apart on the Mid-Cayman Rise. Formation and removal of Fe-rich colloids and particles will control the amount and physio-chemical composition of dFe supplied to the deep ocean from hydrothermal systems.

3.1 Introduction

Understanding biogeochemical processes that control the exchange of trace metals between the soluble (<0.02 µm) colloidal (0.02 to 0.2 µm) and particulate (>0.2 µm) size fractions is key to predicting how hydrothermal plumes influence the chemistry of the deep ocean. There is limited data on the partitioning of trace metals between the soluble, colloidal and particulate fractions with most studies focussing on plume particles (German et al., 1991, Feely et al., 1994k, Feely et al., 1996, Feely et al., 1998, Edmonds and German, 2004, Toner et al., 2009a, Toner et al., 2009d, Klevenz et al., 2011, Breier et al., 2012).

Hydrothermal fluids are enriched in Fe, Zn, Pb and Co, and may be either enriched or depleted Cu and Cd relative to seawater (German and Von Damm, 2004). Fe, Zn, Co, Cu and Cd are known to play an important role in ocean biogeochemistry, however there have been few studies that have examined how dissolved (<0.2 µm) concentrations of these metals in hydrothermal plumes differ from deep ocean water (James and Elderfield, 1996, Bennett et al., 2008, Hawkes et al., 2013a). This is important for constraining the impact of hydrothermal fluxes on the biogeochemical cycling of these metals in the ocean.

Early studies examining hydrothermal particles established that where concentrations of elevated H_2S persist, elements such as Cu, Zn, Fe, Co, Pb and to a lesser extent Cd precipitate as metal sulphides such as pyrite, chalcopyrite and sphalerite (German et al., 1991, Feely et al., 1994a, Edmonds and German, 2004). Where H_2S is depleted in hydrothermal plumes, the mineralisation of trace metals is dominated by the oxidation of reduced metal ions and metal sulphide minerals. Oxidative dissolution of particulate metal sulphides may also transfer Cu, Cd and Pb back in to a dissolved size-fraction (German et al., 1991, Metz, 1993, Klevenz et al., 2011).

Rapid oxidation of Fe (II) to Fe (III) in hydrothermal plumes results in the formation of Fe oxyhydroxides, which scavenge dissolved and particle-reactive elements such as Cu and Pb (Trocine and Trefry, 1988). Fe, Mn and Cu can also be associated with organic particles in hydrothermal plumes (Feely et al., 1994k, Toner et al., 2009a, Breier et al., 2012). While there is evidence of dissolved Mn being scavenged by bacteria, and for Mn sulphide precipitation in hydrothermal plumes (Cowen et al., 1986, Breier et al., 2012), this represents only a minor fraction of vent derived Mn, and the great majority remains dissolved due to its slow oxidation rate (Cowen et al., 1990, James and Elderfield, 1996, Findlay et al., 2015).

Recent studies measuring different size fractions have established that between 5 to 96 % of dissolved Fe (dFe) is present as colloidal Fe (cFe) in hydrothermal plumes (Hawkes et al., 2013a, Fitzsimmons et al., 2014, Fitzsimmons et al., 2015). Measured concentrations of soluble (sFe) in hydrothermal plumes are also higher than seawater concentrations despite representing a small fraction of hydrothermal dFe (Hawkes et al., 2013a, Fitzsimmons et al., 2014, Fitzsimmons et al., 2015). These discoveries along with isotope (Conway and John, 2014f) and modelling studies (Tagliabue, 2010) have resurrected the idea of hydrothermal vents as an important source of dFe to the oceans.

The speciation of cFe, sFe and the processes by which Fe is exchanged between these fractions and the particulate fraction (pFe) is largely unknown, both in hydrothermal plumes, and more widely in the open ocean. At least three different species of dFe have been identified in different stages of hydrothermal plumes that could explain the occurrence of elevated levels of cFe and/or sFe. Colloidal sized pyrite (FeS_2) has been observed in vent fluids in the first 1.5 m of the buoyant plume (Yucel et al., 2011, Gartman et al., 2014, Findlay et al., 2015). Pyrite may account for up to 25 % of dFe (Gartman et al., 2014) in hydrothermal vent fluids and this kinetically stable mineral may account for the high concentrations of cFe observed in plumes. Pyrite particles <0.2 μm are yet to be observed in more dispersed areas of plumes so it is also possible that colloidal sized pyrite may just be an intermediate stage in the formation of larger pyrite aggregates that settle out of the water column to sediments (Gartman et al., 2014, Yucel et al., 2011).

Several studies have also shown that a fraction of dFe is stabilised by complexation with organic ligands in the plume, which slows the process of Fe (II) oxidation and the subsequent formation of Fe oxyhydroxide particles (Statham et al., 2005, Bennett et al., 2008, Sander and Koschinsky, 2011, Hawkes et al., 2013a). On average 30 ± 21 % of plume dFe may be complexed by organic ligands (Hawkes et al., 2013a) making up a significant fraction of the dFe exported from hydrothermal plumes. These ligands maybe sourced from hydrothermal plumes (Bennett et al., 2008, Hawkes et al., 2013a) or from the deep ocean (Buck et al., 2015). Several unanswered questions remain as to how much Fe (II) may be complexed in the plume, how inorganic sulphide complexes influence the method used to detect organic ligands in the plume

(Hawkes et al., 2013a) and how much cFe and sFe is complexed by organic ligands.

Many studies have confirmed the prevalence of Fe oxyhydroxide particles in plumes (Breier et al., 2012, Feely et al., 1996, Feely et al., 1994a, Feely et al., 1994k, Feely et al., 1998, German et al., 1991, Klevenz et al., 2011, Sands et al., 2012), which are presumed to form by the aggregation of smaller colloidal Fe oxyhydroxides (James and Elderfield, 1996, Field and Sherrell, 2000, Sands et al., 2012). Therefore it is likely that a fraction of hydrothermal cFe may be Fe oxyhydroxides, especially given their prevalence in many other aqueous environments (Hochella et al., 2008, Hawkings et al., 2014), but there have been no direct measurements of colloidal Fe oxyhydroxides in hydrothermal plumes thus far.

It is most likely that elevated concentrations of dFe are due to a combination of the different species discussed above and understanding their formation and stability with transport into the deep ocean is key to understanding the impact of hydrothermal venting on the Fe cycle and the cycling of other metals.

Plumes and vents over ultra-slow spreading ridges are under sampled globally compared to other ridge axes and in this study samples were taken from plumes over the Beebe Vent Field (BVF) and the Von Damm Vent Field (VDVF). The BVF vents are black smoker type vents whilst the vents at the VDVF represent a new type of off axis hydrothermal venting with distinct chemistry (Hodgkinson et al., 2015) (see chapter 2 for descriptions). Venting fluids from chimneys at both sites mix with deep waters of similar oxygen and pH therefore oxidation rates at both sites are similar and deep waters are likely to contain the same types of ligands. The similarity of seawater mixing with vent fluids at both sites presents a unique opportunity to learn how different vent fluids influence the fate of trace metals in hydrothermal plumes – details that are presently missing from models of hydrothermal dFe fluxes in ocean biogeochemical models (Tagliabue, 2010, German, 2016).

The proportion of trace metals that precipitate as mono sulphides (Fe, Cu, Zn, Pb, Cd), pyrite (Fe, Cu) or are scavenged by Fe oxyhydroxides (Mn, Cu, Pb) is used to infer the likely speciation of trace metals in separate size fractions. This will add to the limited number of hydrothermal plume studies that have measured soluble (<0.02 μm) and dissolved (0.2 μm) Fe (Hawkes et al., 2013a, Fitzsimmons et al., 2014) and other trace metals in these size fractions, data for, which is extremely scarce (Findlay et al., 2015).

Understanding the processes that control the partitioning of dissolved trace metals into soluble (<0.02 µm) and colloidal (0.02 – 0.2 µm) fractions is key to improving flux estimates of metals from plumes to the deep ocean. The aim of this study is to assess how the separation of metals between the soluble, colloidal and particulate fractions evolves as plumes are dispersed. To answer these questions the variation in metal concentrations between size fractions of two plumes sourced from two chemically distinct hydrothermal vent fields is examined. The location of two vent fields with very different physical and chemical properties in the same ocean basin allows us to assess how the chemistry of vents may influence the formation of soluble, colloidal and particulate metals relative to the chemistry of deep ocean waters.

3.2 Methods

3.2.1 Plume Sampling

Seawater samples from the buoyant plume (BP) and neutrally or non-buoyant plume (NBP) were collected, filtered and acidified on the RRS *James Cook* during cruise JC082 in the Caribbean Sea in February 2013. Samples were analysed back on-shore at the National Oceanography Centre Southampton.

Detection and sampling of the hydrothermal plumes was conducted using a Seabird 911 plus conductivity, temperature and depth (CTD) profiler system that was attached to a titanium frame that holds 24 externally sprung 10 litre OTE (Ocean Test Equipment) water sampling bottles and a Stand Alone Pumping System (SAPS) for the collection particles from large seawater volumes. OTE bottles were cleaned at the start of each cruise by filling each bottle with freshwater and an aliquot of HCl. The Niskin bottles are Teflon lined with Teflon taps and non-metallic parts to prevent any contamination during sampling of waters with low concentrations of trace metals. A light scattering sensor (LSS) and an Eh detector (Ko-ichi Nakamura) were also mounted on the base of the titanium rosette frame.

Particles from the BVF neutrally buoyant plume (NBP) were collected by *in situ* filtration of 1060 L of seawater at a depth of 4089 m. In the VDVF plume, 945 L of seawater was filtered from an Eh anomaly of the NBP depth of 2140 m. SAPS filters (1 μm pore size, Whatman, 293mm), were rinsed on deck by immediately after recovery. Filter surfaces were rinsed by adding enough de-ionised water (Milli-Q, Millipore, >18.2 mΩ cm^{-1}) to cover the surface of the filter and then turning on the pump to suck the de-ionised water through the filter. This process was repeated several times to remove any seawater that may evaporate to form salt crystals. This is necessary in-order to clearly observe the sampled particles using microscopy, which can become difficult if a significant number of salt crystals form. After rinsing SAPS filters were frozen at -20 °C.

Hydrothermal plumes were located using the CTD profiler, LSS and Eh detector to look for deviations in temperature, particulates, and Eh from background seawater. The buoyant part of the hydrothermal plume (BP) was identified by negative Eh anomalies and positive temperature and LSS anomalies. The neutrally buoyant plume (NBP) was detected by a positive particle anomaly and negative Eh anomalies. The direction of NBP dispersal is controlled by of ambient deep water currents. Above the VDVF, the NBP is dispersed in a west north west direction, whilst NBP from the BVF is dispersed in a north north west direction at the time of sampling.

Sampling depths ranged from 1849 to 2296 m at the VDVF and 3911 to 4952 m at the BVF, and all samples were collected within 2 km distance of the vent sites. These samples spanned the depth-range of BP and NBP signals that were observed during this study, and that are previously reported for these sites (German et al., 2010, Connelly et al., 2012, Bennett et al., 2013).

All water samples were collected into Low Density Polyethylene (LDPE) bottles, which were pre-cleaned using the following procedure: submerge in 2% Decon 90 (Decon, UK) for 2 days, submerge in 6M HCl (analytical grade, Fisher UK) for 1 week, submerge in 8 M HNO_3 (analytical grade, Fisher UK) for 1 week. Bottles were rinsed 3 times with deionised water (Milli-Q, Millipore, >18.2 mΩ cm^{-1}) between each cleaning step, with the final rinse conducted in a class 1000 clean laboratory. Sample bottles were filled with 0.015 M sub-boiled (S.B.) HNO_3 for storage. Filters, Teflon filter housing and sampling tubes were cleaned in the clean lab on board the ship in 1.6 M HNO_3 for a minimum of five days before being moved to a bath of deionised water where they were left until required.

Prior to every seawater sample, clean LDPE sample bottles were emptied, rinsed with de-ionised water, and then pre-conditioned by rinsing an aliquot of the sample water and discarding it to waste. Unfiltered seawater was collected for its total dissolvable metals (TDMe). Polycarbonate membrane filters (0.2 µm pore size, 47 mm diameter, Whatman) were connected to Niskins using all-Teflon filter housings and used to filter 125 ml seawater samples for dissolved trace metals (dMe). A separate 125 ml LDPE bottle was filled with unfiltered sample water for separating the soluble fraction. Unfiltered sample was passed through a 0.2 µm cellulose acetate syringe filter (Whatman) and a 0.02 µm aluminium oxide syringe filter (Anotop; Whatman) connected in series at a rate of 1 ml/min using a peristaltic pump and polyvinyl chloride tubing (Elkay). All syringe filters were acid cleaned and rinsed through with de-ionised water before use. The connected filtration set-up was then rinsed through with 40 ml 0.015M ultra-pure HCl followed by a 4 hour circulation of 200 ml of deionised water prior to use. The first 20 ml of sample water passed through the soluble filtration system was used to rinse a sample bottle and discarded to waste. A final minimum of 40 ml was then collected for soluble trace metals (sMe). All water samples for trace metal analysis were acidified using 1 µl of ultra-pure HNO_3 (ROMIL UpA) per 1 ml of sample and analysed after 2 years.

The use of unfiltered seawater and seawater filtered through 0.2 and 0.02 µm membranes is used in this study to provide operational distinctions between total dissolvable trace metals (TDMe), particulate trace metals (pMe; >0.2 µm), dissolved trace metals (dMe; <0.2 µm), colloidal trace metals (cMe; >0.02<0.2 µm), and soluble trace metals (sMe; <0.02 µm). Where TDMe, dMe and sMe are measured values, and pMe and cMe are calculated as pMe = TDMe - dMe, and cMe = dMe - sMe. The calculated concentrations of pMe and cMe are assumed to equal zero if they are less than the propagated analytical error from measured values.

3.2.2 Determination of Fe, Mn, Co, Cu, Zn, Cd, Pb in hydrothermal plumes

Trace metal concentrations in sMe, dMe and TDMe samples were measured by pre-concentration of 15 ml sub-sampled aliquots onto a chelating resin (Kagaya et al., 2009). Samples were processed using an offline extraction system similar to that used by Milne et al. (2010) but using the standard addition procedure for trace metals developed by Biller and Bruland (2012) (see Appendix C for further details of extraction set up and procedure). The 1M S.B HNO_3 eluent from this process was measured using an Element XR (Thermo scientific) (Biller and Bruland, 2012, Milne et al., 2010). No correction was applied for Mo-oxide interference due to no difference between counts of Cd^{111} or Cd^{110} in solutions that were and were not spiked with 50 and 100 nM Mo. Drift corrections were applied to data using standard bracketing by measuring a standard solution of intermediate concentration every 10 samples.

The method blank for each element is detailed in Table 3.1 below. The certified reference material NASS-6 (National Research Council Canada) was taken through the same extraction procedure for every set of samples as a check on the recovery of trace metals and reproducibility of the method. NASS-6 was deemed to be the most suitable reference material due to its elevated concentrations of Fe and Mn similar to hydrothermal plume samples (1 to 1000 nM) in comparison to open ocean seawater where Fe and Mn concentrations are significantly lower (0.1 to 1.5 nM). The results for repeat analysis of NASS-6 during the two separate sessions in, which samples were analysed is shown in Table 3.1.

Table 3.1 Comparison of measured and certified metal concentrations in seawater

	Procedural blank (*n* = 12)	m.d.l (3 s.d)	Measured	s.d	Precision % RSD	Certified	U_{CRM}
Fe	0.08	0.09	9.1	0.7	8%	8.65	0.81
Mn	0.004	0.003	8.7	0.6	6%	9.39	0.86
Co	0.003	0.011	0.28	0.03	9%	0.255	*
Cu	0.011	0.008	3.7	0.3	8%	3.81	0.39
Zn	0.1	0.4	4.5	0.3	7%	3.84	0.31
Cd	0.001	0.001	0.32	0.05	16%	0.270	0.02
Pb	0.0004	0.0004	0.026	0.002	9%	0.029	0.01

U_{crm} = expanded uncertainty of the certified value quoted by National Research Council Canada.

* = Information value rather than certified

m.d.l = method detection limit calculated as 3 s.d of blank, blank n = 12 and measured NASS-6 n = 8. All concentrations are in nmol kg^{-1}.

3.2.3 Soluble 0.02 µm filtration blank for Fe, Mn, Co, Cu, Zn, Cd, Pb analysis

So far oceanographic studies have focussed on measuring the separation of Fe into soluble and colloidal fractions and there is no data as of yet for other trace metals. It is therefore important to consider any blank contribution from the soluble filtering process on the other trace metals to be examined.

The blank of the soluble filtering method was measured by passing 10 ml de-ionised water through the filter system (Table 3.2), then evaporating and re-constituting in 1 ml 1M HNO_3 for ICP-MS analysis. The soluble blank concentrations detailed in Table 3.2 are lower than all the concentrations of elements in North Atlantic Deepwater (NADW) except Pb where the blank is equal to the NADW concentration. Deep waters over the MCSC are thought to be derived from NADW due to its similarities in temperature, salinity and oxygen concentration (Connelly et al., 2012). We therefore assume that concentrations of elements in NADW are analogues to what would be expected for deep water in the MCSC with no hydrothermal input.

The soluble blank represents a small fraction (1-5 %) of the concentration of background seawater for Cu, Co and Cd. For elements enriched in hydrothermal plumes such as Mn, Fe and Zn the sample concentrations in this study are much higher than the soluble blank. The filter blank therefore represents a small percentage of measured concentrations for these elements in the plume.

Measured concentrations of soluble Pb in plume samples are as low as 0.004 nmol kg^{-1}, which is lower than the soluble filtering blank value (0.008 nmol kg^{-1}) and open ocean seawater (0.008 nmol kg^{-1}). It is likely that the process of conditioning the filtration system with sample before filtering was the main reason for this and that passing de-ionised water through the system does not have the exact same effect.

Table 3.2: Soluble filtration blank of analysed trace metals (nmol kg^{-1})

	Mn	Fe	Co	Cu	Zn	Cd	Pb
Soluble (<0.02 µm) filter blank (n= 4)	0.036	0.3	0.001	0.09	1.1	0.002	0.008
Open ocean seawater	0.1[a]	0.75[a]	0.08[b]	2[a]	2[a]	0.3[a]	0.008[a]

a = data from GEOTRACES GA02 30° N (D) 3900 m
http://www.egeotraces.org/sections/jpg/300dpi/GA02_Fe_D_CONC_BOTTLE.jpg

b = Milne et al. (2010) BATS 1800 m

As the soluble blank is much lower than the concentrations measured in samples it is assumed that this blank contribution is negligible for Mn, Fe, Co, Cu, Cd. For Pb and Zn however the soluble blank may represent a significant fraction of the lowest measured soluble concentrations in the plume. The data for these elements is presented with the caveat that samples with soluble Pb and Zn concentrations similar to the soluble blank could be lower than the concentrations measured.

3.2.4 Mineralogical composition of plume particles by SEM-EDX

Particulates collected on SAPS filters were analysed for size and element composition from each vent field. Particles on SAPS filters were rinsed off with de-ionised water and filtered onto acid washed polycarbonate filters (Whatman, 0.2 μm pore size, 47 mm diameter). Polycarbonate filters were cut using Milli-Q rinsed ceramic scissors and mounted onto metal stubs with carbon tape.

Morphology and composition of particles was examined using the backscatter detector on a scanning electron microscope (SEM) (Carlseiz LEO 1450VP) and element composition of particles was determined using an energy dispersive x-ray (EDX) detector (Princeton Gamma Technology Light Element Detector) built-in to the SEM.

Mineralogy of particles analysed was determined using relative atomic percent of elements using the mass balance method of Hitch (2012), which was adapted from the method used by Klevenz et al. (2011). Fe bearing particles that did not contain sulphur but showed peaks for oxygen were assumed to be Fe oxyhydroxides. However, the exact mineralogy of these particles cannot be determined due to the uncertainty of EDX analysis for elements as light as oxygen (Goldstein et al., 2003.). Due to the time-scales over which plume dilution occurs it is unlikely that Fe oxides such as hematite or goethite will form and Fe oxyhydroxides have been shown to be the prevailing Fe oxide phase in plumes in other studies (Rudnicki and Elderfield, 1993).

3.3 Results

The temperature, Eh and LSS profiles for two hydrothermal plumes over the VDVF and BVF are shown in Figure 3.1. LSS anomalies were less frequent in the VDVF plume in comparison to the BVF plume due to the lack of plume particles that scatter light effectively in the clear venting fluids observed during ROV dives of JC082 and in previous studies (German et al., 2010, Connelly et al., 2012). Eh and temperature anomalies were detected from 2300 m depth up to 2180 m over the VDVF. Generally the plume over the VDVF was dispersed in multiple directions and was difficult to sample. The strongest Eh and LSS signals detected to the west north west of the vent field at a depth of ~2120 m.

The strongest Eh and temperature signals over BVF coincided at a maximum depth of ~4890 m, indicative of the early BP. These anomalies were persistent up to a minimum depth of ~4480 m - deeper than the extent of previous temperature anomalies that were reported up to ~4000 m (German et al., 2010, Connelly et al., 2012). We detected particle anomalies at BVF at 4080 and 4480 m, which we interpret to be particle dense layers of the NBP.

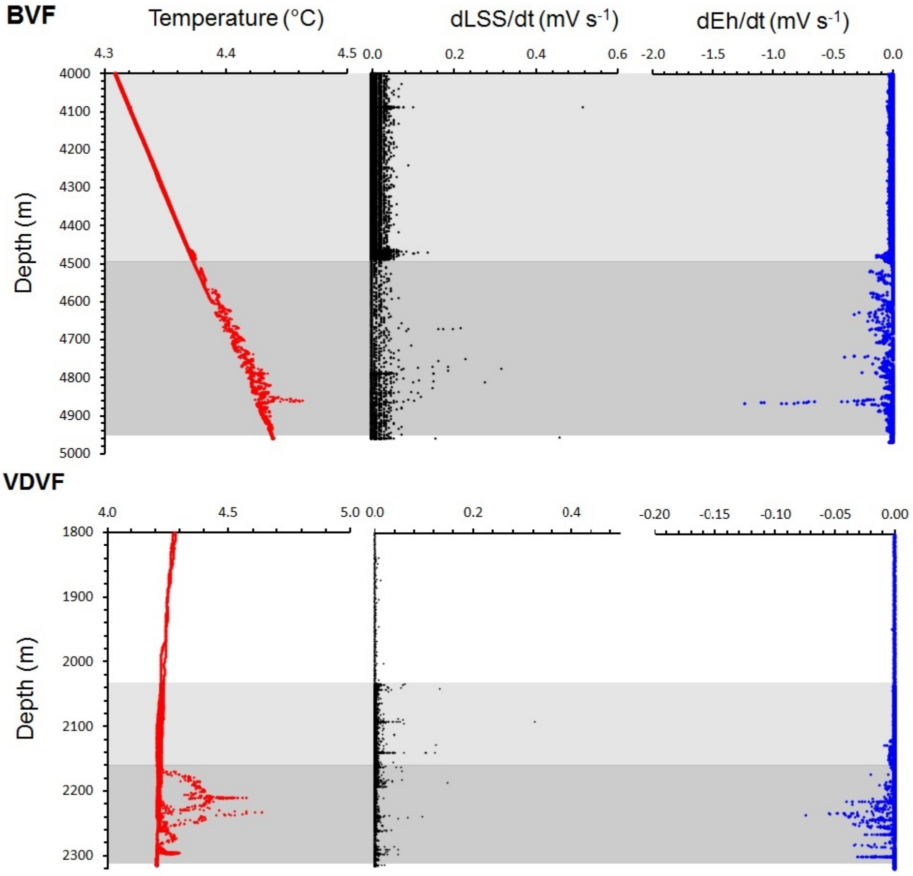

Figure 3.1 The detection of hydrothermal plume anomalies in the water column over the VDVF and BVF. All grey shaded areas indicate the full range of plume depth. Light grey areas indicate particle anomalies only attributed to the NBPs, whereas dark grey areas indicate temperature, Eh and particle anomalies attributed to BPs.

3.3.1 TD trace metal concentrations during hydrothermal plume-seawater mixing

Dissolved Mn is used as a near-conservative tracer to track the dispersal of hydrothermal fluids in BPs and NBPs (James and Elderfield, 1996, Field and Sherrell, 2000). A caveat to such use of dMn, is that we always measured TDMn concentrations higher than dMn at both study sites, indicating a fraction (30 ± 18 % *n* =28) of TDMn was adsorbed or incorporated into particles. Due to the slow oxidation rate (weeks to years) of dMn (Cowen et al., 1990) relative to the time-scale of plume dispersal (m s^{-1}) (Speer and Rona, 1989), we do not consider the oxidation of dMn to invalidate its use as a tracer within our reported samples, and consider it to be the best and most tractable means of evaluating plume dilution in accord with previous studies (James and Elderfield, 1996, Field and Sherrell, 2000).

The difference between sMn and dMn concentrations for the vast majority of samples are indistinguishable, with no Mn present in the colloidal fraction. As a percentage of TDMn, sMn represented 84 ± 15 % across all samples from both sites. This suggests that dMn is almost entirely in the soluble fraction (Figure 3.4, Figure 3.3) and behaves near conservatively over the time scales that samples were taken in this study (Cowen et al., 1990).

Several processes are able to change the TDMe concentration of metals in plumes. Plume dilution between metals enriched in the hydrothermal plume relative to seawater will be the main process lowering concentrations. Such dilution will reduce TDMe concentrations as the plume is dispersed (Field and Sherrell, 2000, James and Elderfield, 1996). Heterogeneous dispersion of plume particles can create particle rich layers of the plume, where TDMe concentrations are elevated relative to the extent of plume dilution (Carazzo et al., 2013). Finally scavenging of trace metals from background seawater or recycled plume waters by plume particles will increase TDMe concentrations during plume dilution. A conceptual model for identifying three different chemical behaviours for metals in the plume profile is presented in Figure 3.2.
To aid our interpretion of data, the BVF is separated into the early plume (>2.5 nmol kg^{-1} dMn) and dispersed plume (<2.5 nmol kg^{-1} dMn) (Figure 3.5), and the VDVF is separated into the early plume (>3.3 nmol kg^{-1} dMn), intermediate plume (0.6-3.3 nmol kg^{-1} dMn) and dispersed plume regions (<0.6 nmol kg^{-1}

dMn) (Figure 3.4). Significant trends throughout the plume were identified by r^2 values >0.4 and p values >0.005 (see Appendix D for full table of values). The t-statistic of regressions was also examined to make sure chosen regressions fell within 95 % confidence intervals determined by the number of samples in the regression (if $n = 20$ then t must be >2.09 or <-2.09 (Miller and Miller, 2000)). Residuals were also examined for sufficient scatter to ensure the appropriate regression (straight line, exponential curve polynomial or power law) was chosen, where patterns in residuals plotted against fitted lines indicates a poor fit. Regressions with a p-value >0.005 typically had r^2 values <0.4, therefore the choice of 0.4 as a cut off for meaningful r^2 is defined by the conservative p value of 0.005.

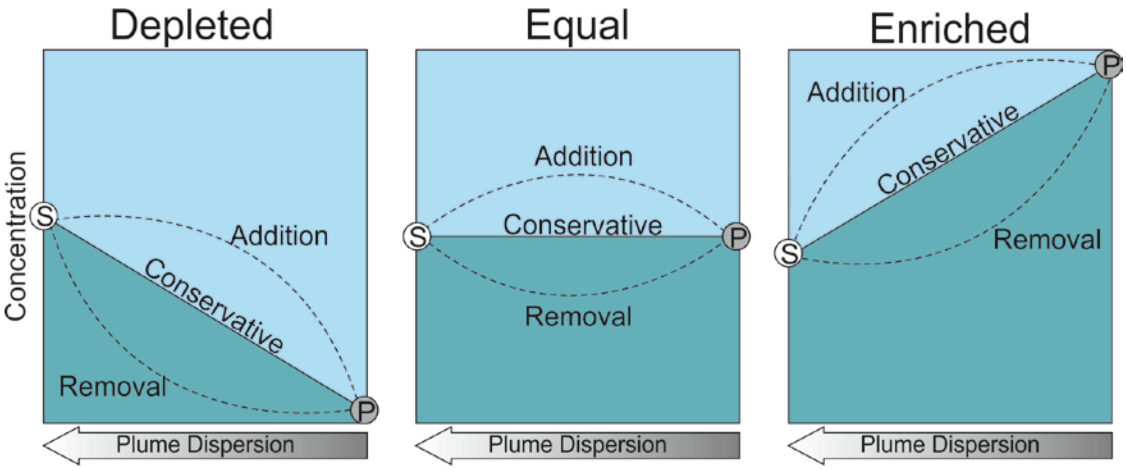

Figure 3.2 Conceptual view of hydrothermal plume dispersion for different dissolved metals that are either depleted, equal-to, or enriched in the early plume (P) relative to seawater (S). Straight solid lines indicate conservative mixing paths. Dashed lines indicate the modified dispersion paths of dissolved elements due to addition (e.g. particle dissolution) or removal (e.g. scavenging) processes during plume dispersion.

3.3.1.1 TD trace metal concentrations in the Beebe Vent Field Plume

Total dissolvable (TD) concentrations of Mn, Fe, Zn and Pb in the plume are all significantly higher than dissolved concentrations of these metals in NADW (Figure 3.3) (Table 3.2). TDFe concentrations in the BVF plume range from 6 to 312 nmol kg^{-1} and decrease linearly ($r^2 = 0.989$) with dMn. Indicating that, during plume dispersion, the high concentrations of dFe and dMn in the vent fluid are diluted by seawater, which contains several orders of magnitude less dFe and dMn.

TDZn and TDPb show little correlation with dMn (Figure 3.3). The highest concentrations of both TDZn and TDPb of 24 and 0.088 nmol kg^{-1} respectively are observed at dMn concentrations <2 nmol kg^{-1}. Unlike TDFe and TDMn, where the largest influence on the change in concentration is dilution of the plume, other process such as the settling and the distribution of particulates must be more important in controlling the total dissolvable budgets of Zn and Pb in the plume.

Total dissolvable concentrations of Cu, Cd and Co in the plume are generally less than dissolved concentrations of NADW. This is probably because NADW is a poor approximation of Cayman deep waters for these elements. TDCu and TDCd show little variation with dMn concentrations (Figure 3.3), with TDCd decreasing slightly during plume dilution ($r^2 = 0.427$). Any hydrothermal input of Cu, Cd and Co to the plume does not significantly increase TD concentrations relative to seawater as markedly as it does for Mn, Fe, Zn and Pb.

3.3.1.2 Von Damm Vent Field Plume

Total dissolvable concentrations of Mn, Fe, Zn, Cd, and Pb in the VDVF plume were all elevated above NADW concentrations suggesting hydrothermal input to the plume from vents on the VDVF (Figure 3.4). TDFe in the VDVF plume ranges from 4 to 196 nmol kg^{-1} with highest concentrations observed in the early plume samples. However TDFe and dMn do not show the typical linear correlation expected of plume dilution (Figure 3.4). This indicates that whilst plume dilution does lower TDFe concentration of the plume, other processes such as scavenging, particle settling and dispersion of pFe are also important controls on the TDFe budget of the VDVF plume.

Total dissolvable concentrations of Cu, Pb and Co in the early plume decrease from highs of 1.9, 0.064 and 0.08 to 1.2, 0.026 and 0.04 nmol kg^{-1}. In the dispersed region of the plume the TD Cu, Pb and Co increases again to 1.7, 0.051 and 0.09 nmol kg^{-1} (Figure 3.4). The initial decrease in the early plume for these elements shows plume dilution of the hydrothermal vent source. The increase in TDCu, TDPb and TDCo in the most dispersed samples maybe from scavenging of these elements by plume particles or sampling a layer of the plume with a high concentration of particles containing these elements. Alternatively the elevated concentrations of Cu, Pb and Co in the most dispersed region of the plume may indicate that the CTD cast has sampled two plumes with different source compositions. This theory is supported by the concurrent spike in dissolved concentrations for these elements in the same samples.

TDZn concentrations in the plume range from 2.9 to 37 nmol kg $^{-1}$ with higher concentrations >9 nmol kg $^{-1}$ in the early and intermediate plume and concentrations <9 nmol kg $^{-1}$ in the dispersed plume with the exception of 1 sample. To a certain extent profiles of TDZn concentrations are similar to Cu, Pb and Co but with much more scatter. Therefore the settling, scavenging and dispersal of pZn is the main control on TDZn concentrations.

TDCd shows little variation throughout the plume. Notably the lowest TDCd concentrations of 0.07 nmol kg^{-1} are observed in the same samples, which also had the lowest TDCu and TDCo concentrations, these low concentrations were also concurrent with decreases in TDFe and TDPb indicating that the depletion of these metals to lower concentrations may be occurring by the same processes at this stage of the plume.

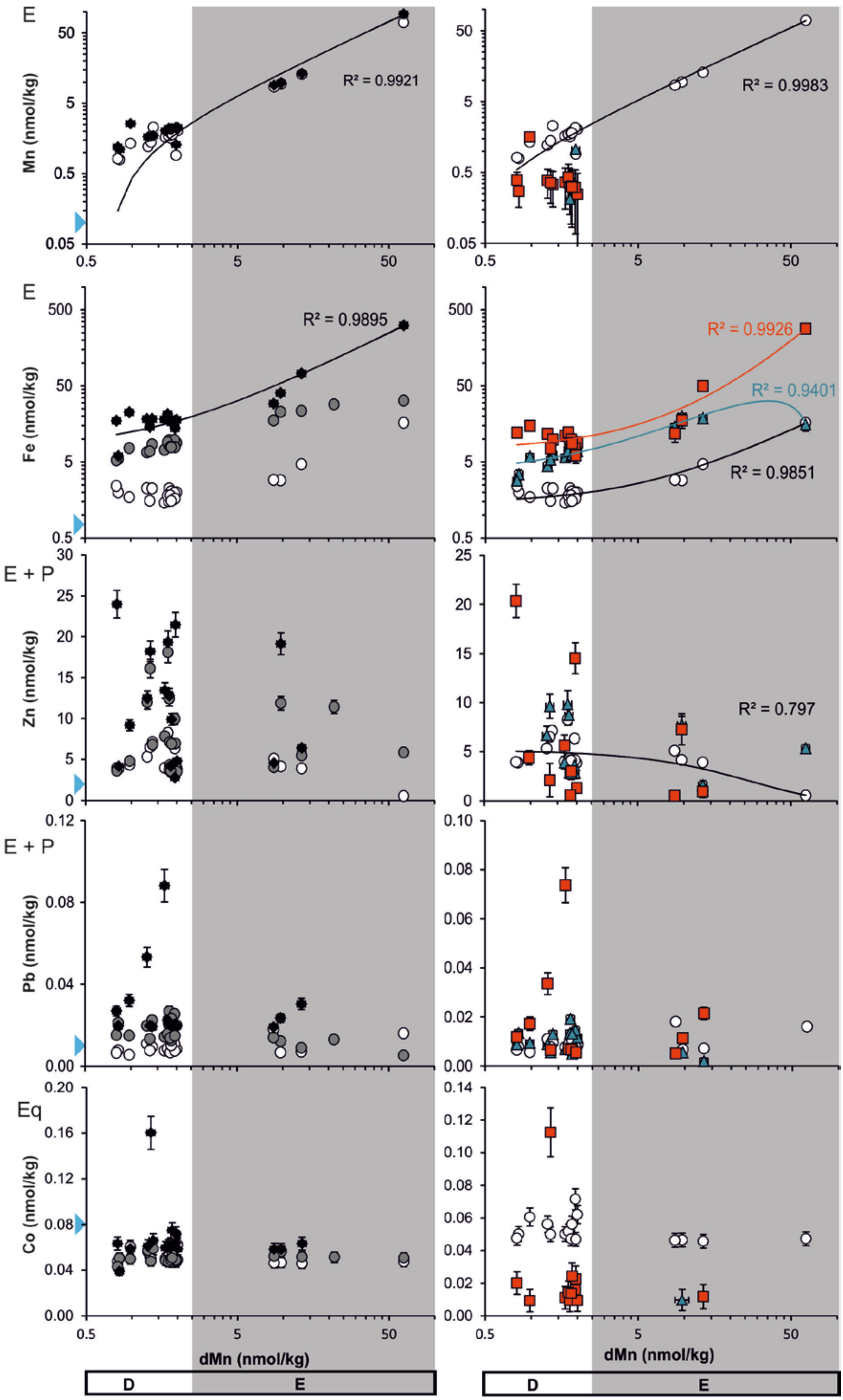
E
Mn (nmol/kg)
50
5
0.5
0.05
R² = 0.9921
R² = 0.9983
E
Fe (nmol/kg)
500
50
5
0.5
R² = 0.9895
R² = 0.9926
R² = 0.9401
R² = 0.9851
E + P
Zn (nmol/kg)
30
25
20
15
10
5
0
R² = 0.797
E + P
Pb (nmol/kg)
0.12
0.08
0.04
0.00
0.10
0.06
0.02
Eq
Co (nmol/kg)
0.20
0.16
0.12
0.08
0.04
0.00
0.14
0.10
0.06
0.02
0.5
5
50
dMn (nmol/kg)
D
E

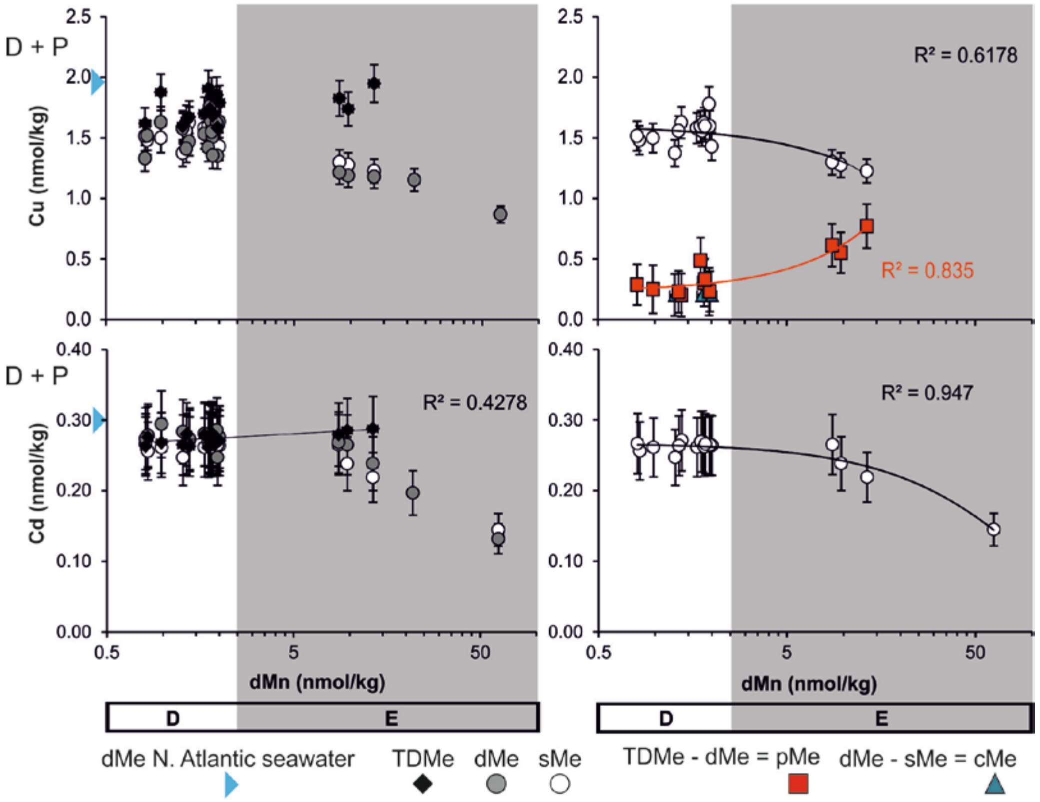

Figure 3.3 BVF plume trace metal concentrations. Grey bar refers to areas of the plume discussed in the text, early (E), dispersed (D). Lines show significant trends (p value >0.005, r^2 >0.4) through concentrations. Blue triangles are NADW seawater concentrations from Table 3.2. Trends through TDMn, sMn and sFe are linear, trends through pFe, cFe and pCu are 2nd polynomials and trends through sCd, sCu and sZn are exponential curves (see Appendix D for p values). The letter to the left of each panel E (enriched), E + P (enriched and particle reactive), D + P (depleted and particle reactive) and Eq (equal), describe how elements behave with regards to the conceptual models presented in Figure 3.2.

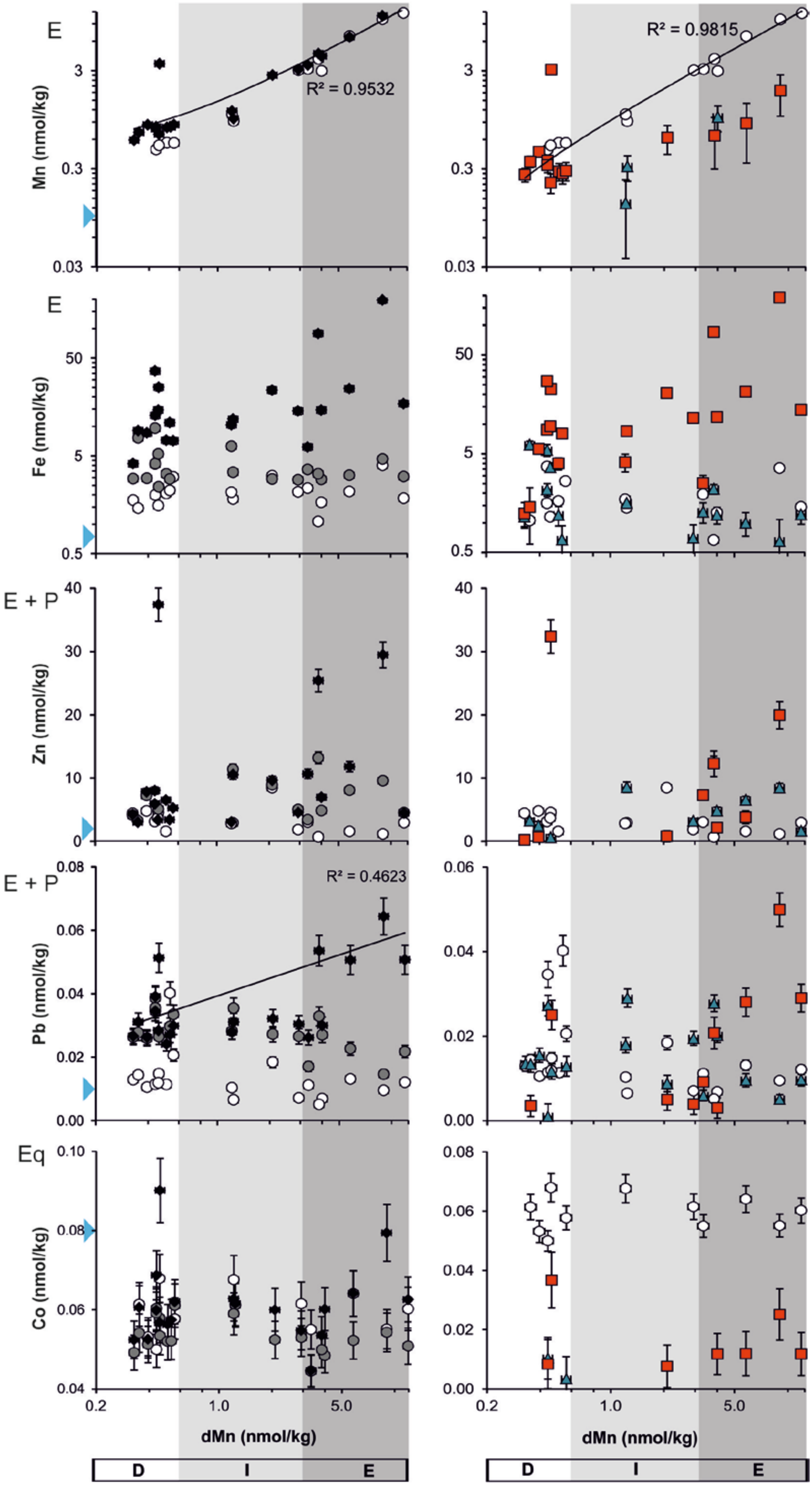
E
Mn (nmol/kg)
3
0.3
0.03
R² = 0.9532
R² = 0.9815
E
Fe (nmol/kg)
50
5
0.5
E + P
Zn (nmol/kg)
40
30
20
10
0
E + P
Pb (nmol/kg)
0.08
0.06
0.04
0.02
0.00
R² = 0.4623
Eq
Co (nmol/kg)
0.10
0.08
0.06
0.04
0.02
0.00
0.2
1.0
5.0
dMn (nmol/kg)
D
I
E

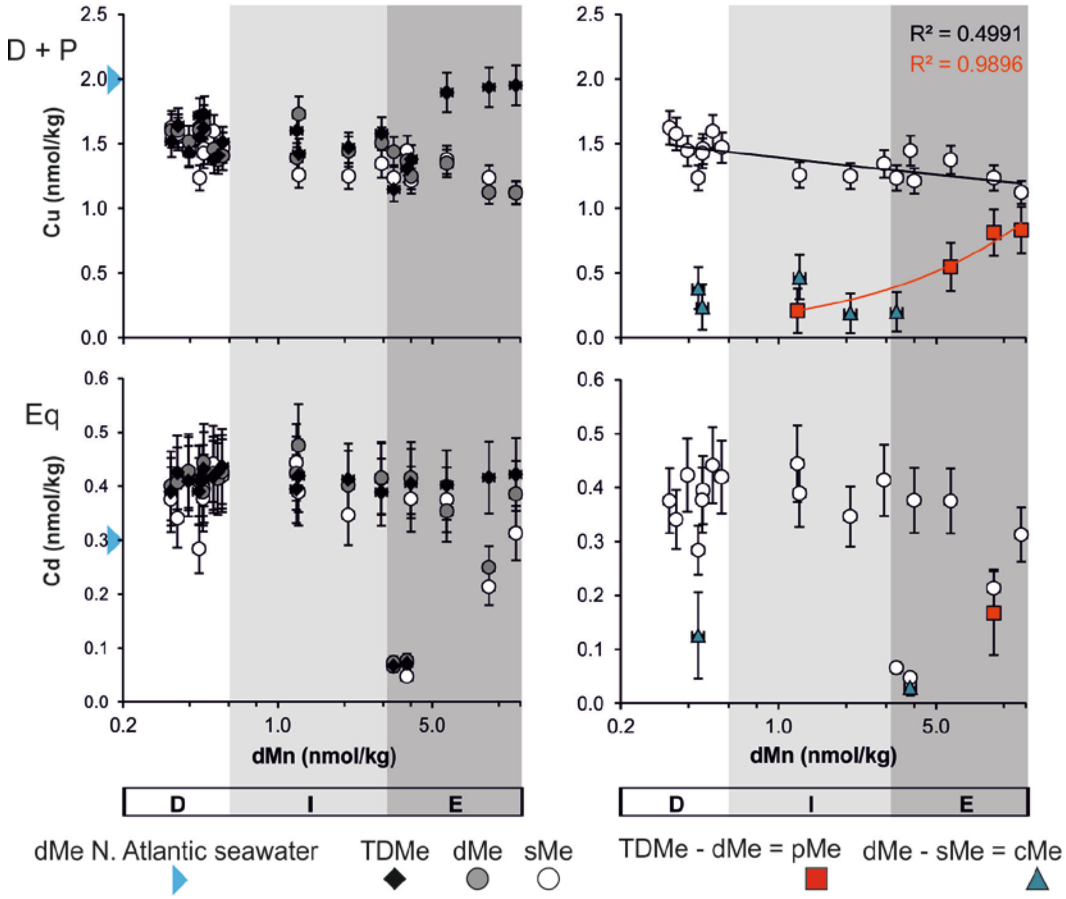

Figure 3.4 VDVF plume trace metal concentrations. Lines show significant trends (p value >0.005, r^2 >0.4) through concentrations except blue lines, which are background seawater concentrations from Table 3.2. All trend lines are linear except those through pCu and sCu, which are power law curves (see Appendix D for p values). The grey bar at the bottom shows sections of the plume discussed in the text, early (E), intermediate (I), and dispersed (D). The letter to the left of each panel E (enriched), E + P (enriched and particle reactive), D + P (depleted and particle reactive) and Eq (equal), describes how the behaviour of elements fits with the conceptual model presented in Figure 3.2.

3.3.2 Size fractioning of metals with hydrothermal plume dispersion

3.3.2.1 Profile of plume enriched elements - Iron and Manganese

TDMn concentrations were higher than dMn at both sites indicating a measurable amount of pMn. In the VDVF plume pMn as a percentage of TDMn varied from 13 to 87 % and in the BVF plume pMn varied from 11 to 62 % of TDMn.

The BVF plume follows a typical plume dilution profile for sFe, cFe and pFe relative to dMn (Figure 3.3). Concentrations of sFe and dFe are 16 and 32 nmol kg^{-1}, respectively, in the early plume and decrease to 1 and 5 nmol kg^{-1} in the dispersed plume. This equates to an even split of Fe between sFe and cFe in the early plume samples with sFe lowered to 20 % of dFe as the plume is further dispersed.

On average 54 ± 18 % of TDFe is present as pFe in the BVF plume with 35 ± 13 % in the cFe fraction and 11± 6 % in the sFe fraction. In almost all samples from the BVF plume the amount of Fe in the cFe fraction was approximately triple the amount of sFe. Two exceptions from this are the two samples collected from the shallowest and deepest depths, which had the highest and lowest Mn concentrations (62 and 0.8 nmol kg^{-1} dMn). In the deepest BVF plume sample sFe and cFe are equal and both represent 5 % of TDFe. However, in the most dispersed plume sample sFe and cFe represent 33 and 58 % of TDFe.

The change in sFe concentration relative to dMn in the BVF plume is described by a linear trend ($r^2 = 0.985$) (Figure 3.3). Changes in pFe and cFe deviate from linearity at lower dMn concentrations. Relative to what would be expected from a linear trend, pFe increases at the lowest dMn concentrations and cFe decreases (Figure 3.5). Trends in both cFe and sFe fractions are best described by 2nd order polynomial ($r^2 = 0.940$) and linear fit ($r^2 = 0.985$).

In contrast to what would be expected from plume dilution, concentrations of dFe and sFe were highest in the dispersed region of VDVF plume. The lowest concentrations of sFe and dFe in the early plume are 1.0 and 2.8 nmol Kg^{-1} respectively with concentrations as high as 4.2 and 9.6 nmol Kg^{-1} in more dispersed plume samples (Figure 3.4). Profiles of sFe and dFe in the early and dispersed plume mimic the profile of TDFe where increases and decreases in TDFe are coupled to increases and decreases in sFe and dFe.

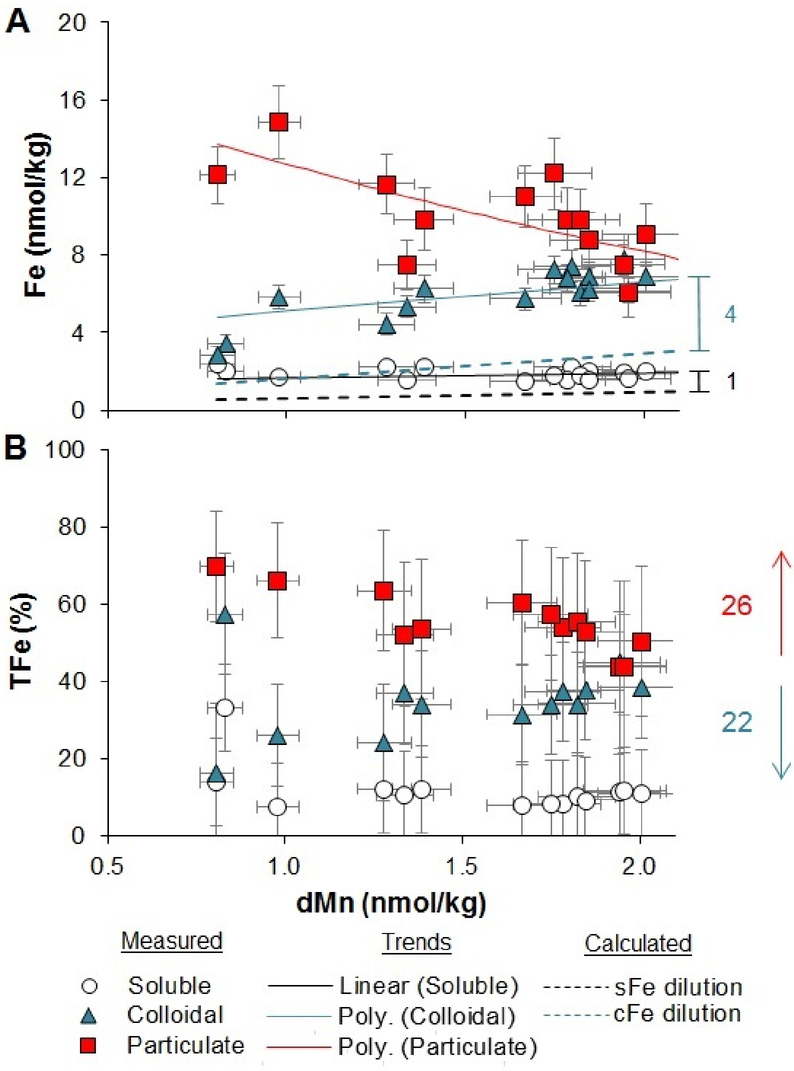

Figure 3.5 The concentration of Fe in different size fractions of BVF dispersed plume samples. Panel A shows concentrations with trend lines, which are the same as in Figure 3.3 except for pFe where the regression is through NBP samples only (dilution factor >10,000). Dashed lines show the expected concentration from conservative mixing of near vent sample concentrations. Brackets in Panel A and adjacent text show the difference between measured cFe and sFe in comparison to the concentration calculated from dilution. Panel B shows size fractions as a percentage of TDFe. Coloured arrows illustrate the observed change in pFe and cFe with plume dilution in this section of the plume. Vertical error bars in panel B are calculated from the error propagation of errors for TDFe, pFe, cFe and sFe.

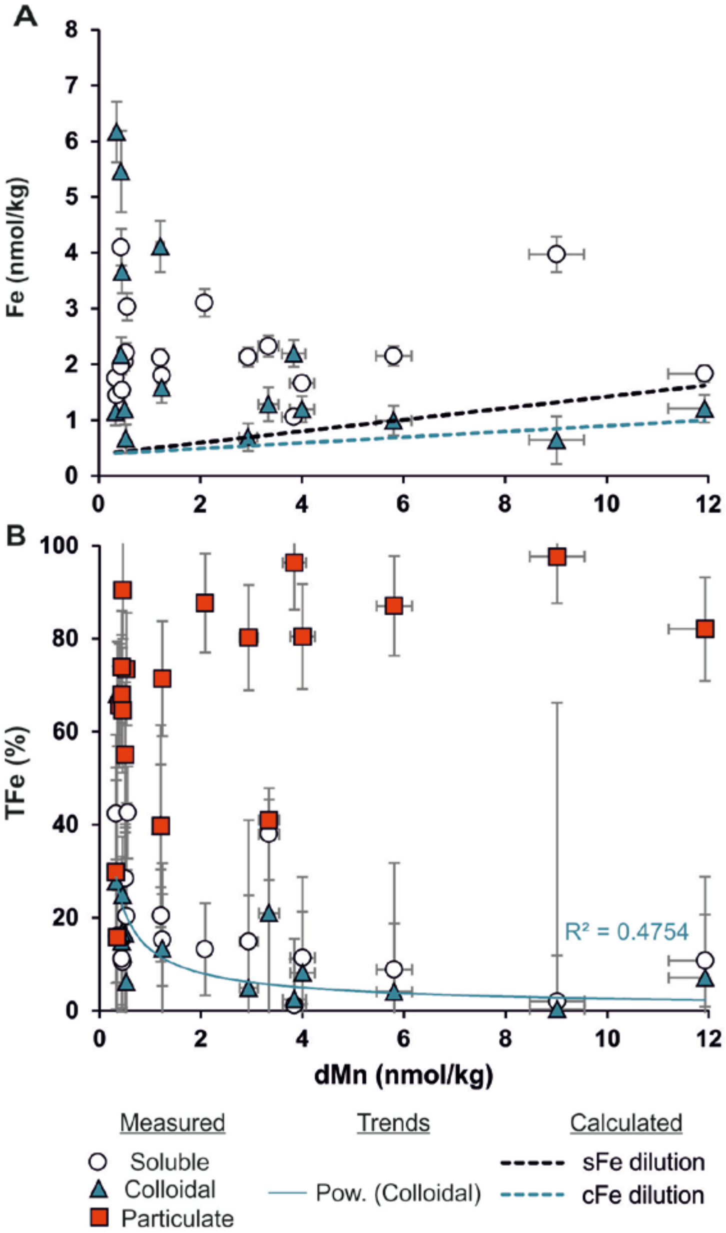

Figure 3.6 Separation of Fe between different size fractions in VDVF plume samples. (A) Concentrations of cFe and sFe in the plume (pFe is not shown in this plot to show the change in cFe and sFe). Dashed lines show the concentration predicted from conservative mixing of near vent samples. Coloured brackets and adjacent text in A show the difference between measured cFe and sFe and those estimated from conservative mixing. (B) Size fractions as a percentage of TDFe. Coloured arrows illustrate the observed change in pFe and cFe with plume dilution. Vertical error bars in panel B are calculated from the error propagation of errors for TDFe, pFe, cFe and sFe.

Average sFe in the VDVF plume as a percentage of TDFe was 18 ± 12 %, higher than that of the BVF plume which was 10 ± 6 %. The amount of Fe in the cFe fraction was 17 ± 17 %, which is lower and more variable than the BVF plume which was 34 ± 12 %. The majority of Fe in the VDVF plume was present in the particulate fraction with pFe making up 68 ± 23 % of TDFe.

3.3.2.2 Profile of plume enriched and particle reactive elements – Zinc and Lead

Zinc was present in the soluble, colloidal and particulate fractions of plume samples from both BVF and VDVF. The distribution of Zn between these different fractions was highly variable within both plumes. Colloidal Zn in the BVF plume follows a similar trend as sZn with concentrations of cZn doubling from 5.3 to 9.6 nmol kg^{-1} between the early and dispersed plume samples. Colloidal Zn in the VDVF early plume shows a general decrease in concentration from 8.4 to 3.2 nmol kg^{-1} with sZn similar throughout the early plume at 2.0 to 2.9 nmol kg^{-1}.

Particulate Zn in the BVF plume generally increased with decreasing with dMn concentrations (Figure 3.3). The VDVF plume showed more scatter in the data so may be similar to BVF but appeared to show a poorly resolved general decrease (Figure 3.4). The highest pZn concentrations of 32 (VDVF) and 20 (BVF) nmol kg^{-1} in both plumes were observed in the more dispersed regions of the plume. This is conceivably the result of pZn being efficiently transported to the NBP height prior to settling, resulting in a pZn rich layer of the plume.

At both sites the lowest sZn concentrations are observed in early plume samples and higher concentrations in more dispersed samples. In the BVF plume the highest sZn concentration in dispersed samples is 8.2 nmol kg^{-1}, which is more than 15 times that of the early plume, where sZn is 0.52 nmol kg^{-1}. Soluble Zn in the VDVF plume increases from 2.9 nmol kg^{-1} to 11.9 nmol kg^{-1} throughout the plume.

Both plumes had measurable Pb concentrations in the soluble, colloidal and particulate fractions. The distribution of Pb between these different fractions was highly variable within both the plumes. In the early stage of the BVF plume (>2 nmol kg^{-1} dMn) pPb decreases and both cPb and sPb increase (not including the initial high sPb concentration in the sample with the highest dMn). The decrease in pPb concentration of 0.016 nmol kg^{-1} is approximate to the increase in sPb of 0.011 nmol kg^{-1} indicating that Pb is transferred from the particulate to the soluble fraction in this stage of the plume. In the more dispersed region (<2 nmol kg^{-1} dMn) of the BVF plume cPb and sPb were approximately equal with concentrations ~0.01 nmol kg^{-1} similar to that of dPb in NADW. The highest pPb concentrations were observed in this region of the plume up to 0.074 nmol kg^{-1} (Figure 3.3). The highest pPb concentrations observed in the same regions as the highest pZn suggest that the concentrations of these elements maybe controlled by reactions with the same particulate species.

Particulate Pb showed a very similar distribution across the VDVF plume to pZn. This similarity was not re-produced in the colloidal and soluble fractions where a range of concentrations of colloidal Pb in the VDVF plume were observed from 0.001 to 0.029 nmol kg^{-1} with no trend as the plume is progressively diluted.

3.3.2.3 Plume equal elements showing some particle reactivity - Cobalt

Dissolved Co is entirely in the soluble fraction throughout the BVF and VDVF plumes. Most samples in the BVF plume were ~0.05 nmol kg^{-1} sCo except for several samples in the more dispersed region of the plume with concentrations up to 0.07 nmol kg^{-1}. The concentration of Co in the BVF plume particulate fraction was less than that of sCo ranging from 0.01 to 0.02 nmol kg^{-1}.

The VDVF plume had a constant concentration of 0.06 ± 0.01 nmol kg^{-1} sCo. Disimilarly pCo ranged from 0.01 to 0.04 nmol kg^{-1}. The highest pCo being observed in the most dispersed region of the plume. Particulate Co in the VDVF plume shows excellent linear correlation with pZn and pMn (r^2 >0.98) (Figure 3.7). This likely indicates that these elements are precipitating in or are scavenged by the same types of plume particles.

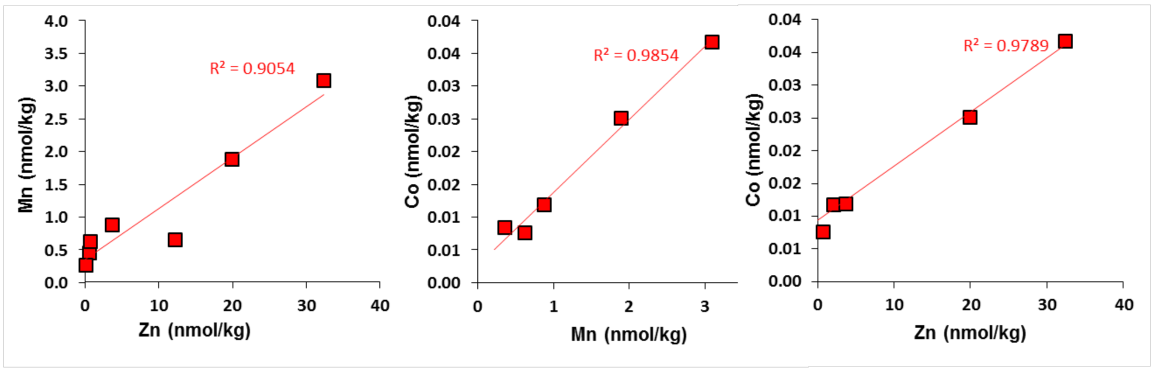

Figure 3.7 Correlation of particulate Mn, Co and Zn in VDVF plume particles

3.3.2.4 Plume depleted and particle reactive elements – Copper

Both sites show similar distributions for Cu where sCu increases with plume dispersion and the increase in sCu is roughly proportional to a decrease in pCu. Several samples at both sites had low but measurable concentrations of colloidal Cu. At BVF the only measurable concentrations of cCu were in 2 to 3 samples in the more dispersed region of the plume all with ~0.2 nmol kg^{-1}. Where as in the VDVF plume the cCu occurred throughout the 3 defined sections of the plume ranging from 0.2 to 0.5 nmol kg^{-1}.

3.3.2.5 Elements exhibiting different profiles in different plumes - Cadmium

Cd was predominantly in the soluble fraction for both plumes studied. Soluble Cd in the BVF plume increased from 0.14 to 0.27 nmol kg^{-1} with a plume dispersion profile the same as sCu, which is shown by the similarity of trend lines in Figure 3.3. Curved trends indicate sCd in the BVF plume is behaving as a plume depleted element (Figure 3.2 & Figure 3.3) with some addition. Soluble Cd in the VDVF plume was ~0.4 nmol kg^{-1} throughout the plume with more scatter in data to values lower than 0.4. This shows that generally sCd is equal in both the plume and surrounding seawater possibly with some sCd removal during dispersion.

3.3.3 Particle composition

Along with a large number of metallic mineral particles other types of particles from both sites included a large amount of biological detritus and barite, which could be hydrothermal or detrital in origin. Out of all the trace metals of interest in this study only Fe, Zn, Cu and Mn showed significant peaks in EDX spectra of the plume particles. The SEM-EDX method can therefore only attempt to identify the mineralogy of particles that Fe, Zn, Cu and Mn were associated with.

In BVF plume particles Zn was only present as ZnS and Fe was present as both FeS_2 and Fe oxyhydroxide. Mn was most likely present as Mn oxyhydroxide associated with a cluster of other non-metal bearing particles. Trace peaks for Cu and Mn were observed in particles identified as ZnS, Fe oxyhydroxide and FeS_2 (Figure 3.8). Large ~10 µm metal sulphide particles (FeS_2, ZnS) were aggregates composed of smaller particles <2 µm (Figure 3.8).

Only 1 Zn sulphide was identified in the VDVF plume and no FeS_2. One Cu bearing particle was observed but there were no peaks for S or Fe so this falls under the category of other (Table 3.3). Four of the particles analysed that are assumed to be Fe oxyhydroxide were ~1 µm in size and embedded within a larger particle ~16 µm (Figure 3.9). The composition of the larger particle could not be identified quantitatively as it only showed peaks for lighter elements C, O and trace Si, which give high uncertainties on EDX spectra (Goldstein et al., 2003.).

Table 3.3 Inventory of particle compositions >1 μm analysed by SEM-EDX.

Site	Depth (m)	No. of particles analysed	Identified mineral particles				Other	
			ZnS	FeS_2	FeOOH*	MnOOH*	Unidentified mineral with trace amounts of Fe, Mn, Cu, Zn	Non trace metal bearing
BVF	4090	51	11	8	9	1	7	15
VDVF	2140	22	1	0	7	0	2	12

*Assumed to be amorphous Fe oxyhydroxide and Mn oxyhydroxide but cannot determine exact composition due to limitations of SEM-EDX.

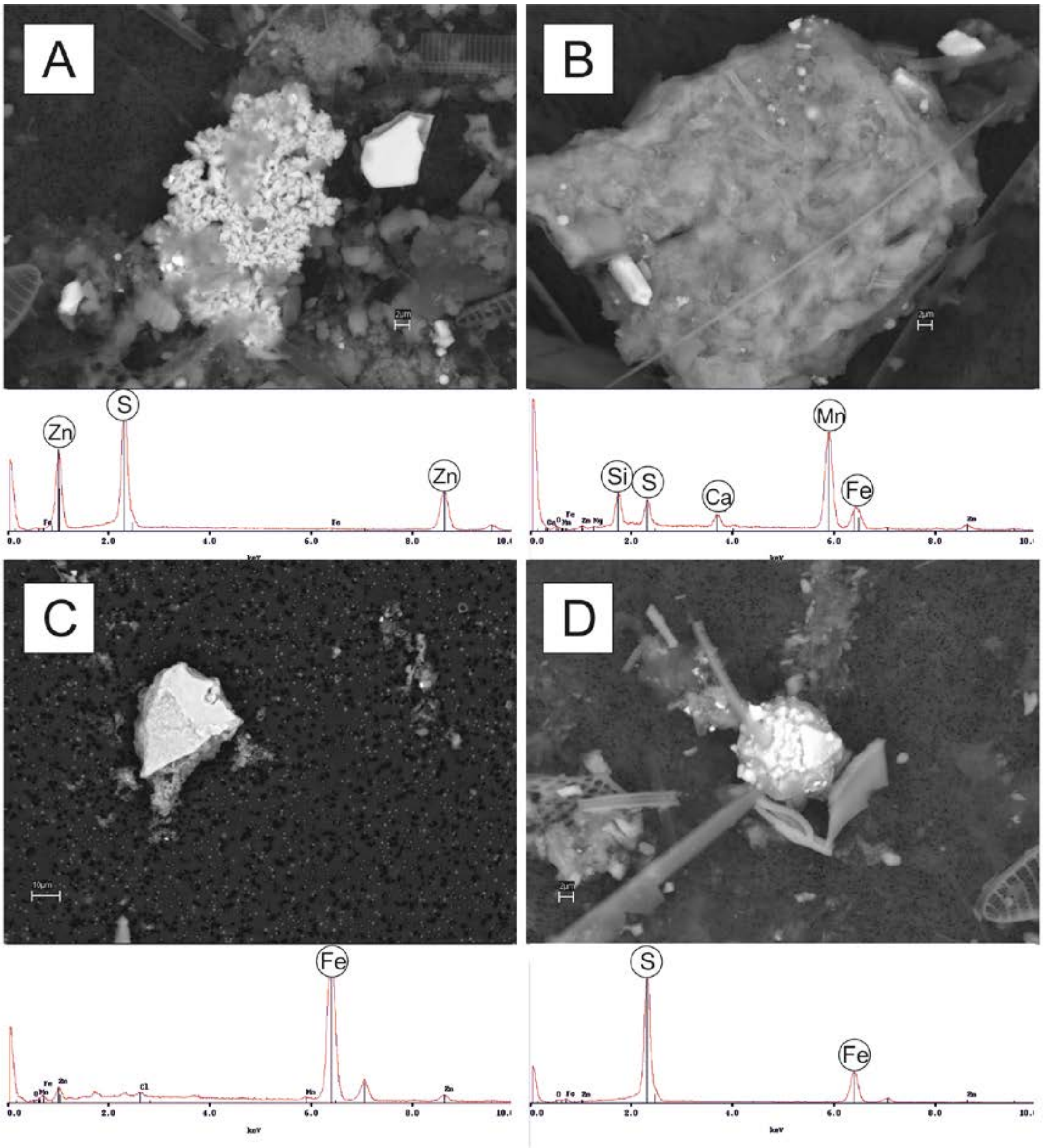

Figure 3.8 BVF plume particles with SEM images and EDX spectra for A. ZnS, B. Mn oxyhydroxide, C. Fe oxyhydroxide and D. FeS_2

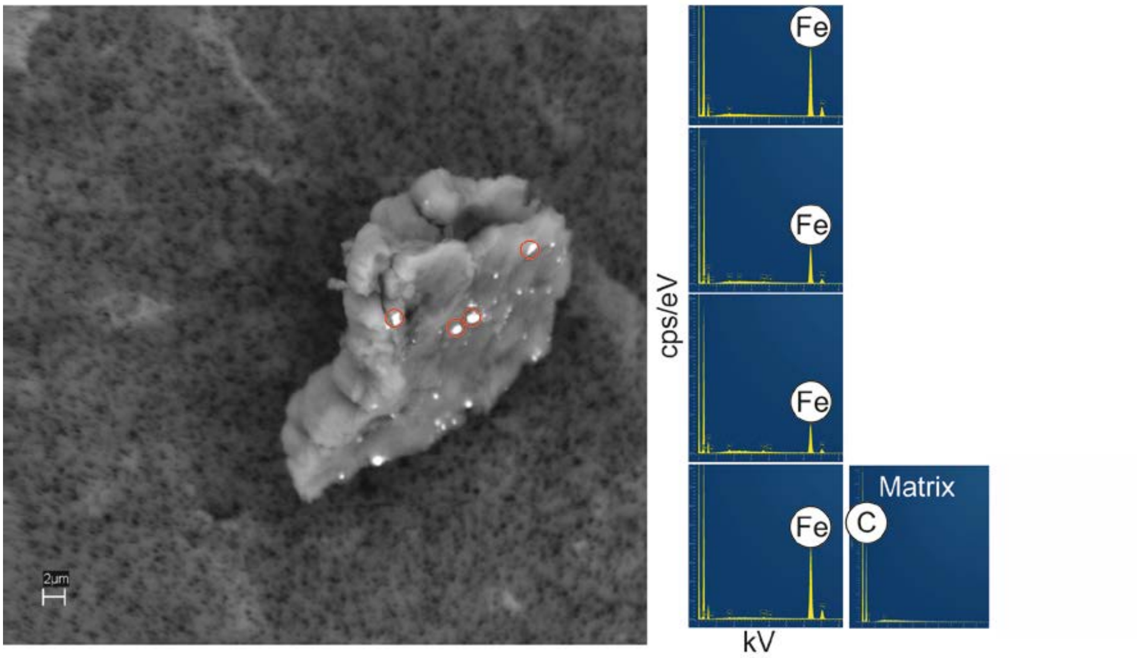

Figure 3.9 Backscatter image of VDVF plume particle. Red circles correspond to points of EDX analysis shown to the right except for the slide labelled matrix, which is the analysis of the particle matrix in, which Fe rich grains are embedded in.

3.4 Discussion

3.4.1 Fe(II) oxidation rates in the Cayman Basin

In order to examine the form of pFe at both sites it is important to consider the rate that vent Fe(II) will be oxidised to Fe(III) as this controls the rate of Fe oxyhydroxide particle formation. The oxidation half time of Fe(II) from deep water masses in the Cayman Basin is calculated as 27 mins for deep waters mixing with the VDVF plume and 17 mins for the BVF plume (Table 3.4). These Fe(II) oxidation rates are nearly identical to those calculated for North Atlantic deep water masses of 17 to 29 minutes (Field and Sherrell, 2000). Such similarity in oxidation rates is somewhat expected, given that deep waters in the Cayman basin are sourced from North Atlantic Intermediate Water (Connelly et al., 2012). These rates allow for near quantitative oxidation of Fe (II) within the sampling bottle between the time of water column sampling and filtering on deck, which was approximately 2 to 3 hours.

The precipitation of Fe in the Niskin bottles is analogous to mineralisation reactions occurring in the plume itself. The only difference being that the dispersion of the sample would continue in the plume, which will enhance the formation of colloids and decrease the possibility of larger particles forming from colloid aggregation. Therefore dFe in the plume at the time of sampling is likely to be higher than measured dFe as the sample has been enclosed within the fixed volume of the sampling bottle for 2 to 3 hours. This change is expected to be minimal given the fast oxidation rates and experimental evidence which shows time scales of >10 hrs are required before 0.1 µm sized Fe oxyhydroxide particles begin aggregate to form larger particles at room temperature (Stegemeier et al., 2015).

Table 3.4 Calculation of Fe (II) oxidation rates for Cayman deep waters compared to Atlantic

Depth (*m*)	Temp. (°C)	Salinity	O_2 (µmol kg^{-1})	pH_{sws}[c]	pK_w[c]	pOH[d]	K_1[e]	Fe (II) half life (h)
*Von Damm**								
2327	4.3	34.98	220	7.900	14.011	6.111	0.0259	0.45
*Beebe**								
5069	4.5	34.98	220	7.900	13.910	6.010	0.0416	0.28
Rainbow[d]								
1942	3.75	34.97	269	7.993	14.050	6.057	0.04	0.29
TAG[d]								
3326	2.59	34.91	255	7.938	14.069	6.131	0.026	0.45

*Cayman deep water salinity, pH, O_2 from Connelly et al. (2012), P, Si and Alkalinity for oxidation calculation taken from WOCE 15N A22 2000m.

[a] pH and pKw calculated using Lewis, E., and D. W. R. Wallace. 1998. Program Developed for CO2 System Calculations. ORNL/CDIAC-105. Information Analysis Center, Oak Ridge National Laboratory, U.S. Department of Energy, Oak Ridge, Tennessee.

[b] $pOH = pK_w - pH$.

[c] $\log k = 21.56 - 1545/T - 3.29 I^{1/2} + 1.521$ where $I = 19.9201 \times S/(10^3 - 1.00488 \times S)$, where, S is salinity and T is temperature in Kelvin (Millero et al., 1987), $k_1 = k[OH^-]^2[O_2]$.

[d] Data from Field and Sherrell (2000).

Other trace metals are enriched in vent fluids to a lesser extent than Fe and it is expected that the majority of metals enriched in the vent fluid are rapidly consumed by sulphide faster than any oxidation process. The exception to this rule being Mn, which is enriched in vent fluids to the same extent as Fe but is slow to oxidise and does not typically react with sulphide.

3.4.2 Particle formation during plume dispersion

The compilation of results for different trace metals in different size fractions gives a unique insight into how particles are formed during hydrothermal plume rise and dispersion. The range of trace metal concentrations in the particulate fraction is similar at both sites, which is surprising given that Beebe vents are typical black smokers and Von Damm vents emit clear fluids. The chemistry of fluids venting from the VDVF results in low particle anomalies in the water column in comparison to the BVF plume, which is filled with metal sulphides, which are easily detected by LSS due to the optical properties of metal sulphide minerals (Figure 3.1) (German et al., 2010, Connelly et al., 2012, Bennett et al., 2013, Estapa et al., 2015). The lack of any black smoke and less frequent particle anomalies in the VDVF plume would initially suggest metal sulphides make up a smaller fraction of particulate metal concentrations in the plume in comparison to BVF.

The distribution of pFe with plume dispersion (Figure 3.3) in the BVF BP can be explained by formation of FeS_2 and Fe oxyhydroxide particles in the early plume, which are diluted by seawater during dispersion with some particles settling out of the water column. This trend has been observed previously in buoyant hydrothermal plumes over the MAR (James and Elderfield, 1996) but is different from the linear trend observed in BP samples over the EPR (Field and Sherrell, 2000). Dilution is the main control on pFe concentrations consistent with what has been inferred from optical sensors in the same plume (Estapa et al., 2015). Also the range of particles sizes analysed in the plume by SEM-EDX was in the range of 1 to 20 µm, this is similar to what has been inferred previously from optical sensors used to measure particle size in-situ (Estapa et al., 2015).

The increase in pFe as the plume becomes more dispersed is similar to that observed (Figure 3.5) in a NBP over the EPR (Field and Sherrell, 2000). The increase in pFe in the EPR NBP was concurrent with a decrease in the percentage of dFe relative to TDFe. Field and Sherrell (2000) hypothesised that this increase in pFe was due to aggregation of colloidal Fe oxyhydroxides in the dFe fraction. Consistent with this hypothesis the increase in pFe in the BVF plume is concurrent with a decrease in colloidal Fe (Figure 3.5). As a percentage of the TDFe, pFe in the most dispersed section of the plume increases by 26 % with a concomitant decrease in cFe of 22 % (Figure 3.5). This is the result of aggregation of smaller colloids forming larger particles. This could be a result of the aggregation of FeS_2 or Fe oxyhydroxide colloids. SEM images (Figure 3.8) confirmed larger 10 µm particles are composed of smaller particles. Conversely the observed increase in pFe could be due to aggregation of Fe oxyhydroxide colloids. If this pFe formation from cFe was the result of aggregation of FeS_2 colloids a similar trend in concentrations of Zn between the colloidal and particulate fraction should be observed as ZnS particles are also aggregates of smaller particles like FeS_2 (Figure 3.8). Unlike Fe however, cZn and pZn do not show a similar trend indicating there is little or no aggregation of cZnS to form pZnS in this late stage of the plume. From this it can be concluded that these larger sulphide aggregates of Fe and Zn are likely to have formed in an earlier stage of the plume and the addition of cFe to pFe in more dispersed plume samples is the result of aggregation of colloidal Fe oxyhydroxides. This supports the hypothesis initially suggested by Field and Sherrell (2000) that vent derived Fe (II) is oxidised to Fe (III), which forms colloidal Fe oxyhydroxides, which aggregate in the NBP to from particulate Fe oxyhydroxides.

In contrast to the above argument neither site shows a correlation between pFe and other metals scavenged by pFe oxyhydroxide such as Cu, Mn and Pb in either plume. The particulate fraction is composed of many different types of particles in both plumes that will incorporate these trace metals and as a result the association of trace metals usually observed due to scavenging by Fe oxyhydroxide may not be apparent. Particulate studies where the association between Fe oxyhydroxide and scavenged elements is apparent filter large volumes of plume waters >1 L and it maybe that the association of these scavenged elements is not apparent in this study as only small 15 ml volumes of sample were pre-concentrated.

The only Fe bearing particles observed in the VDVF plume by SEM-EDX are assumed to be Fe oxyhydroxide. If a significant fraction of Fe oxyhydroxide are incorporated or scavenged by detrital organic material (Figure 3.9) along with free floating pFe oxyhydroxides differences in settling and dispersion could explain the scatter in pFe concentrations relative to plume dilution (Figure 3.4). Another possible explanation for this scatter is that the VDVF plume samples represent mixing of two plumes from different vent fluid end members on the vent field. The concentration of dMn in all vent fluids from the VDVF is similar (11 ± 4 µmol/kg n = 12 (Figure 2.18) however the concentrations of other metals can differ by 3 orders of magnitude between different vents (6 to 2543 µmol/kg Fe *n* = 12 (Figure 2.18). Therefore if plumes from two different vent sources mix there may be an increase in other dissolved metal concentrations but not dMn. Whilst vent fluid concentrations of dMn are consistently lower across the VDVF the concentration of pMn in near vent particulates varies 3 to 2301 µmol/kg (Figure 2.19). The spike in metal concentrations for TD and dFe, dCo, dPb, dZn, in the dispersed VDVF plume samples is concomitant with one sample which had increased pMn (Figure 3.4). This could indicate that the increase in metals in the most dispersed plume samples maybe from mixing of plumes sourced from different vent end members. This process would be encouraged by the alignment of active vents in a north-westerly direction, which is the same direction of prevailing deep water currents (Figure 2.3).

Profiles of pCu with plume dispersion are similar at both sites and are consistent with the mixing and settling of Cu sulphide particles formed in the early plume (German et al., 1991). This is consistent with element concentrations from near vent samples (Figure 2.8 & Figure 2.13) and studies of the chimney mineralogy of BVF and VDVF, which identified chalcopyrite and other Cu bearing sulphides in the vent chimneys, which precipitated from vent fluids (Hodgkinson et al., 2015, Webber et al., 2015).

Correlation between pMn, pZn and pCo (Figure 3.7) in the VDVF plume could be explained either by the presence of Mn sulphide particles or Mn oxides that have been observed in hydrothermal plumes (Cowen et al., 1986, Breier et al., 2012). The scavenging of Mn by Fe oxyhydroxides is ruled out due to the lack of correlation between pFe and pMn. Also out of 7 Fe oxyhydroxide plume particles analysed by EDX only one had trace peaks for Mn. Zn is known to form discrete sulphide phases, which incorporate Pb due to similar water exchange rates however they do not incorporate Co. Co is incorporated into pyrite or chalcopyrite (Findlay et al., 2015) due to a slower water exchange rate and Mn does not readily form MnS therefore it is unlikely that correlation between pMn, pZn and pCo can be explained by metal sulphides (Morse and Luther, 1999).

Zn and Co are known to be associated with Mn oxyhydroxides formed via biologically mediated oxidation of Mn (Zeng et al., 2012) and this mechanism could explain the association of these metals in the VDVF plume. This would be consistent with previous work on hydrothermal plumes that shows bacteria oxidise Mn (II) to Mn (III) with Mn incorporated into extracellular capsules (Cowen et al., 1986, Cowen et al., 1990, Cowen and Li, 1991)

3.4.3 Fe stabilization in the dissolved fraction

The stabilisation of dFe concentrations as Fe (II) at the different sampling depths can be calculated and compared to measured concentrations. Assuming a BP rise velocity of 0.1 m s^{-1} (Speer and Rona, 1989) and that dFe samples proximal to both vents were 100 % Fe (II) (Sedwick et al., 2015) and using the Fe (II) oxidation half-lives from Table 3.4. In the VDVF plume Fe(II) was calculated as 12 to 105 % of measured dFe. In the BVF plume 0.4 to 66 % of measured dFe could be present as Fe (II). Calculated Fe (II) concentrations did not include time for Fe (II) to be oxidised within the sampling bottle so calculated dFe (II) concentrations are maximum estimates. It is clear from previous studies that dFe concentrations cannot be simply explained by oxidation kinetics of Fe (II) alone (Statham et al., 2005), removal of Fe from the dissolved fraction by particle formation and Fe stabilization of the dissolved fraction are important processes. In both plumes sFe and cFe are elevated above open ocean deep water and concentrations that would be expected from dilution alone (Figure 3.5 & Figure 3.6). Understanding the speciation of Fe in these fractions is key to understanding why these elevated concentrations of dFe persist and the process of stabilising dFe in hydrothermal plumes.

The difference between plume profiles of cFe and sFe at both sites indicates that the process by which dFe is stabilised is different between the two hydrothermal plumes. In the BVF plume dilution of vent derived cFe and sFe is clearly a key process in decreasing concentrations throughout plume dispersion. However cFe and sFe in the BVF dispersed plume regions are both higher than what would be expected from conservative dilution of cFe and sFe created proximal to the vent (Figure 3.5). It is therefore likely that another secondary process is occurring in the BVF plume that increases the concentration of cFe and sFe in the distal plume relative to dilution alone. The increased cFe and sFe with plume dispersion relative to the expected concentration from dilution of cFe and sFe created in the near vent environment must result from the addition of Fe to the colloidal and soluble fractions as the plume is dispersed by recycling of the plume waters possibly promoting dissolution of some particulates.

The percentage of dFe composed of cFe throughout the BVF plume (74 ± 11 % cFe) is similar to that measured in plumes in the Pacific ~100 km away from the EPR (76 % cFe) (Fitzsimmons et al., 2014) and lower than that measured in plumes over the MAR (82 to 96 % cFe) ~500 km from TAG (Fitzsimmons et al., 2015). The fraction of cFe in the VDVF plume (45 ± 19 % cFe) was similar to that observed for a plume in the Scotia Sea from the E9 vent field (47 ± 25 % cFe) (Hawkes et al., 2013a). Colloidal Fe in both plumes was higher than that observed by Nishioka et al. (2013) in a plume in the Indian Ocean (23 % cFe) where the majority of hydrothermal dFe is in the soluble fraction. The differences in the separation of dFe between cFe and sFe at different sites is further indication that processes generating cFe are different between hydrothermal plumes. Fe (II) oxidation half-lives are similar for both the BVF and VDVF plumes but the percentage of cFe is different between both sites indicating that Fe (II) oxidation kinetics alone cannot explain the formation of cFe in plumes.

Determining the speciation of cFe and sFe throughout plume dispersion is important in order to understand the processes that stabilize Fe in these fractions. Recent studies suggest cFe and sFe is composed of FeS_2 (Gartman et al., 2014, Yucel et al., 2011), organic complexed Fe (Hawkes et al., 2013a, Bennett et al., 2008) and/or other Fe (II) species (Sedwick et al., 2015). In order to determine the process of dFe stabilisation in the plume the possibility of each of these species making up a significant portion of dFe is considered based on the plume profiles and associations of different trace metals in the different size fractions.

3.4.3.1 Nano-FeS_2

FeS_2 nanoparticles can range from 4 to 200 nm in size, which is small enough to pass through both types of filters used in this study and be present in the sFe or cFe fractions. Nano-FeS_2 are formed instantaneously as vent fluid mixes with seawater and due to the kinetic stability of these particles, it has been suggested that they could remain in the dissolved fraction and account for most of the dFe export from hydrothermal plumes (Yucel et al., 2011, Gartman et al., 2014, Findlay et al., 2015). This theory is consistent with the profile of cFe and sFe observed in the BVF plume where the increase in concentrations of cFe in early plume samples could be attributed to nano-FeS_2 formation (Figure 3.3). However if cFe was predominantly composed of nano-FeS_2 or nano-$FeCuS_2$ it is predicted that other chalcophile elements that are known to be incorporated into pyrites such as Cu and Co would also be present in the colloidal fraction (Findlay et al., 2015), particularly in samples with high dMn concentrations in the near vent plume where concentrations of nano-metal sulphides should be highest. This is inconsistent with our results from both sites where only 1 to 5 out of 20 samples had measurable concentrations of Co or Cu in the colloidal fraction in intermediate to dispersed plume samples (Figure 3.4 and Figure 3.3). The lack of any correlation between colloidal concentrations of Fe, Cu and Co suggests nano particles of pyrite do not make up a large fraction of cFe. Similar if a significant fraction of sFe was present as nano FeS_2 it would be expected that soluble Co and Cu should show the same general trend as sFe, decreasing from high concentrations in the early plume to lower values in the dispersed plume. This was not the case as both sCu and sCo have different plume profiles to sFe.

3.4.3.2 Colloidal Fe oxyhydroxide

The presence of inorganic Fe oxyhydroxide colloids has been suggested previously (Field and Sherrell, 2000) and the pFe data discussed in the previous section from the BVF plume supports this hypothesis. However if cFe was present as mostly Fe oxyhydroxide it might be reasonable to assume these colloids would also scavenge elements such as Cu, Pb and Mn. As has been observed for larger Fe oxyhydroxide particles >0.2 µm in hydrothermal plumes (German et al., 1991, Feely et al., 1994k, Edmonds and German, 2004) and experimentally for colloids (Madden and Hochella, 2005, Madden et al., 2006, Waychunas et al., 2005). Of these three metals only Pb has measurable concentrations in the colloidal fraction throughout the plume at both sites. The lack of any correlation (r^2 <0.4 and p <0.005) between colloidal Pb and Fe at both sites contradicts the theory that a large fraction of cFe is composed of Fe oxyhydroxide. This is based on the assumption that cFe oxyhydroxides will scavenge metals at constant molar ratios in a similar manner to pFe oxyhydroxides. It is possible that cFe oxyhydroxides do not scavenge elements in a similar fashion to pFe oxyhydroxides as colloidal Fe will have a smaller volume to surface area ratio with more of an amorphous structure. Differences in the reactivity of the surface of cFe oxyhydroxides in comparison to larger particulate pFe oxyhydroxides may result in preferential scavenging of some elements relative to others (Waychunas et al., 2005, Hochella et al., 2012). Differences in scavenging behaviour between pFe oxyhydroxides and cFe oxyhydroxides could explain the presence of other particle reactive elements such as Pb and Zn in the colloidal fraction and lack of correlation between the colloidal concentrations of these elements and cFe.

3.4.3.3 Ligand complexation

Ligands that form Fe complexes are small enough to be present in the soluble and colloidal fractions. In the surface ocean, transition metal ligand complexation is a mechanism by which micro-organisms obtain metals such as Fe, Zn, Cd, Cu and Co (Barbeau et al., 2001, Ellwood and Van den Berg, 2000, Coale and Bruland, 1990, Saito and Moffett, 2001, Wells et al., 1998). Metal ligand complexation in the surface ocean is therefore dependant on the biological demand for these metals and there is a defined pathway for metal complexation and biological uptake. The demand for metals by micro-organisms in hydrothermal plumes and the deep ocean is less clear and ligands in the deep ocean could come from a number of different sources.

It is possible that vent-derived Fe at both sites could be complexed in the early plume by either organic ligands entrained from adjacent diffuse areas (Hawkes et al., 2013a, Kleint et al., 2016), organic ligands entrained from deep ocean waters (Bennett et al., 2008), organic ligands formed by abiotic processes during venting (Hawkes et al., 2015) or by sulphide ligands (Gartman et al., 2014, Yucel et al., 2011).

Complexation by ligands could explain the elevated concentrations of sFe and cFe at both sites. Previous studies have identified Fe ligand complexation as an important mechanism of dFe stabilisation (Bennett et al., 2008, Hawkes et al., 2013a, Kleint et al., 2016). This could explain why cFe and sFe in the dispersed plume samples at both sites are higher than would be expected from plume dilution of near vent samples. Recycling of particle rich plume waters during BP rise could also facilitate metal complexation increasing the concentrations of dFe relative to dMn.

Vent fluids from both sites have dissolved organic carbon concentrations higher (VDVF = 310 μM, BVF = 132 μM) than background seawater (35 to 48 μM) (Hawkes et al., 2015) and it is therefore possible that Fe binding organic ligands could be sourced from the vents themselves or from the surrounding diffuse areas stabilising Fe in the early plume. If this is the case then a linear profile of Fe would be observed with plume dispersion between plume samples proximal and distal to the vent assuming most of the dFe is complexed by organic ligands and once these complexes form they are unreactive. This linear trend is only observed for sFe in the BVF plume (Figure 3.3) suggesting another possible explanation for the stability of sFe at this site other than FeS_2 nanoparticles. Alternatively the same profile could also be observed if sFe was complexed by sulphide ligands in the early plume. However stability constants of $FeSH^+$ (Luther and Ferdelman, 1993) are weaker than those measured for organic ligands in hydrothermal plumes (Bennett et al., 2008, Hawkes et al., 2013a). Sulphide complexes may also be oxidised during plume dispersion. If sulphide ligands were complexing Fe then we would also expect sulphide complexes for other chalcophile elements Cu, Zn, Cd and Pb. The low soluble concentrations of chalcophile elements in near vent samples suggests that formation of kinetically stable metal sulphide complexes are an unlikely mechanism for stabilizing Fe in the plume. Sulphide complexes are likely an intermediate phase during the process of forming more stable FeS_2 nanoparticles in the early plume (Gartman and Luther, 2014).

The process of ligand complexation may also be facilitated by microbes in the plume, either by the release of siderophores or by the breakdown of dead microbes and release of intracellular Fe (Li et al., 2014). Previously the work of Bennett et al. (2013) has measured concentrations of elevated carbon in the VDVF plume and proposed that chemoautotrophy in the plume supports heterotrophic organisms. Uptake and subsequent dispersal of dFe by microbes could explain why TDFe, dFe and sFe concentrations in the VDVF plume do not form a typical plume dilution profile (Figure 3.4). The lack of any Fe sulphides in VDVF NBP plume particles means that less pFe will be removed by the settling of these dense particles. If the particle investigated by SEM-EDX (Figure 3.9) is assumed to be organic and representative of particles in the VDVF plume then the remineralization of these Fe bearing particles could increase the concentrations of cFe and sFe in the dispersed region of the plume and would also explain lower pFe concentrations. This is consistent with effective breakdown of POC in the NBP resulting in a minimal flux of carbon to ocean sediments from NBPs (Roth and Dymond, 1989). This is consistent with the microbial Fe pump theory (Li et al., 2014) assuming that the decrease in pFe is from the breakdown of particles and settling rather than settling on its own.

3.4.4 Potential for the stabilisation of other trace metals within hydrothermal plumes

The presence of Zn and Pb colloids was a feature throughout profiles of both hydrothermal plumes despite the differences in the chemistry of these two sites. It is therefore possible that this is common feature of hydrothermal plumes. The presence of colloidal Zn could explain elevated concentrations of dZn observed in the TAG plume over the MAR (Conway and John, 2014a); concentrations of dZn in the TAG plume showed greater variability than Fe concentrations, similar to both plumes in this study (Conway and John, 2014g, Conway and John, 2014a). Using Zn isotope measurements Conway and John (2014a) suggest that elevated concentrations of dZn in the TAG plume maybe the result of hydrothermal ZnS nanoparticles (cZn or sZn) and truly aqueous Zn (sZn). This is congruent with our results, which show concentrations of cZn and sZn throughout the plume. The observation of ZnS particles at NBP height in the BVF plume indicates that these particles are stable over plume dispersion times and it is therefore plausible that smaller nano ZnS could also be present. However (for the same reasons discussed above for FeS_2 nanoparticles) nano ZnS would be expected to form in the early plume and therefore dZn would be high in the early plume decreasing with plume dispersion. This is inconsistent with dZn at BVF where the highest concentrations of cZn and sZn are observed in the most dispersed plume samples (Figure 3.2). A possible explanation for the increased dZn in the dispersed BVF plume is the rate that ZnS particles are injected to NBP height from the BP is faster than the settling rate out of the NBP. This would result in an accumulation of ZnS in the NBP, which would be aided by the stratified water column of the Cayman trench, which will be slow to disperse the NBP laterally. There is a general decrease in dZn at VDVF and this could partly be attributed to the presence of nano ZnS (Figure 3.3).

Pb precipitates with ZnS due to similar water exchange rates upon initial vent fluid, seawater mixing (Findlay et al., 2015, Hsu-Kim et al., 2008, Morse and Luther, 1999). If ZnS is the predominant form of dZn and dPb then a correlation between Zn and Pb in these fractions would be expected. Linear correlation between colloidal and soluble fractions of Zn and Pb was observed in the dispersed and intermediate VDVF plume but not in the BVF plume (Figure 3.10) where ZnS particles were observed (Figure 3.8). The trend in the VDVF plume could be due to the lower Zn/H_2S ratios in the Von Damm vents (Hotter than Hole vent Zn/H_2S 0.08) in comparison to the Beebe vents (Beebe Woods Zn/H_2S 0.15). The higher Zn/H_2S ratio of the Von Damm vents makes it more likely that a larger fraction of Zn and Pb from the vents would react with sulphide to form ZnS.

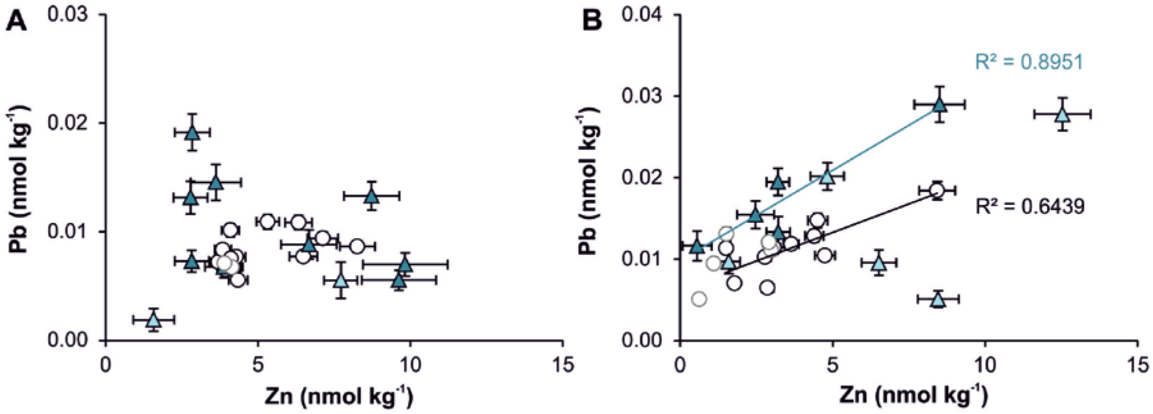

Figure 3.10 Concentrations of Pb and Zn in colloidal and soluble fractions in the (A) BVF and (B) the VDVF plume. Significant linear trend is only observed in the VDVF plume with dispersed plume samples. Early plume samples (light green colloidal and light grey outline for soluble) are excluded from regression.

The lack of an overall trend between Zn and Pb throughout both plumes shows that the presence of ZnS nanoparticles alone cannot fully explain the observed concentrations of these elements in the soluble and colloidal fractions and other factors such as scavenging by other particulate species are also likely to be important.

Complexation of Zn by ligands could also explain the elevated concentrations of Zn in the soluble and colloidal fractions at both sites. Zn is known to be complexed by organic ligands in seawater (Ellwood and Van den Berg, 2000, Boye et al., 2001, Lohan et al., 2005) but as of yet there have been no similar studies examining Zn ligand complexation in hydrothermal plumes. Assuming concentrations of Zn binding ligands in hydrothermal plumes are similar to that of Fe and Cu at 3 to 4 nM (Jacquot and Moffett, 2015, Buck et al., 2015) then Zn binding ligands cannot fully explain the results from both sites where sZn and cZn was >5 nmol kg^{-1}.

Measurable concentrations of colloidal Cu are also observed in the 3 to 5 samples from both plumes and this may also be associated with metal sulphide particles or organic complexation (Sander and Koschinsky, 2011, Jacquot and Moffett, 2015). Unlike Zn the concentrations of cCu are sufficiently low that they could be explained by Cu binding ligands and strong Cu binding ligands (log K >14) have been measured in hydrothermal plumes (Jacquot and Moffett, 2015). The observation of cCu in both plumes suggests this maybe a consistent feature of hydrothermal plumes globally.

3.4.5 Export of Fe from hydrothermal plumes to the deep ocean

The data presented suggest that a significant portion of vent derived Fe is present in the plume as colloidal and soluble species that can be exported to the deep ocean. The flux of Fe from both sites is calculated using equation 3.2 where *n* is the number of samples in the plume, and *f* is the flow of water venting from the sea floor calculated from an exit velocity of 1.5 m/s at both sites and a vent area of 0.2 m^2 for BVF vents and 0.325 m^2 for VDVF vents to accommodate larger venting orifices (Figure 2.4) (Connelly et al., 2012, Hodgkinson et al., 2015). The fraction of vent fluid Fe (*vFe*) added to the plume as sFe or cFe (*xFe*) is represented by the terms in brackets. A background seawater value (*swFe*) is subtracted assuming that the shallowest and/or most dispersed plume sample is representative of background concentrations. The fraction of TDFe present as *xFe* is multiplied by the fraction of TDMn present as dMn. This is in order to account for the near-consevative behaviour of dMn where older recycled plume waters will have a dMn/TDMn <1 as they contain particulate Mn as a result of slow Mn oxidation (James and Elderfield, 1996, Field and Sherrell, 2000).

$$Mean\ vent\ Fe\ added\ to\ plume\ (\%) = \left(\sum_n \left(\frac{xFe - swFe}{TDFe} \times \frac{dMn}{TDMn}\right)/n\right) \times 100 \tag{3.1}$$

$$Mean\ Fe\ Flux = \left(\sum_n \left(\frac{xFe - swFe}{TDFe} \times \frac{dMn}{TDMn}\right)/n\right) \times vFe\ \times f \tag{3.2}$$

One of the limitations of equation 1 is that venting (*f*) is assumed to be from a single point source, however the venting from the VDVF covers a wide area and includes diffuse venting from cracks as well as from holes 0.1 to 1.5 m in diameter. Similarly whilst venting styles are less varied at BVF there are many vents of differing morphology, which add Fe to the overlying plume. Therefore *f* is a highly conservative estimate of the amount of water flowing from vents. The other limitation is that background values of *swFe* are likely to be higher than true background seawater concentrations as even the most dispersed dFe values of 3 to 5 nmol kg^{-1} are higher than typical deep ocean values of 0.6 to 1.2 nmol kg^{-1}. This approach is used to be consistent with fluxes calculated for other elements in the next section (3.4.6) where there is no data from the deep ocean on the separation between colloidal and soluble fractions. This means that the Fe fluxes presented are the most conservative estimate possible.

Individual vent fluxes are calculated based on the fraction of hydrothermal vent end member Fe stabilised in the plume. End member vent fluid Fe concentrations cannot be calculated for VDVF by extrapolation to Mg = 0 mmol kg^{-1} due to a non-linear relationship between Mg and trace metals (2.4.2). The average vent fluid Fe concentrations from all vents located in the VDVF vent field is used as was used for thermodynamic modelling in the previous chapter (2.4.10). The limitation of this being that there is a large amount of variation in the Fe concentrations of these fluids (250 ± 268 µmol kg^{-1}, n = 7). The calculated fluxes from VDVF are dependent on the concentration of Fe in vent fluids and the values presented in Table 3.5 are the best approximation based on available vent fluid data. Despite this variability the vent concentrations at VDVF are still lower than that of BVF vents and therefore the initial vent flux (*vFe* x *f*) from BVF is greater.

The Fe flux from the VDVF field is found to be lower for dFe (Table 3.5), which is as expected given the Fe concentration of the fluids venting from chimneys at this vent field are lower than those of BVF by an order of magnitude. The mean amount of vent dFe added to the plume (equation 3.1) is similar at both sites (VDVF:19 % and BVF:14 %). The percentage of sFe added at VDVF (11 %) is greater than BVF (0.1 %). This suggests that the VDVF plume was more effective at stabilising sFe whilst the BVF plume was more effective at forming colloids. The lower flux from VDVF is therefore a result of lower vent fluid Fe concentrations rather than more dFe being removed by particle formation or scavenging.

Global vent fluxes were calculated using equation 3.2 but the *f* term is changed to apply to hydrothermal vents globally rather than individual vent fields. The global flux of seawater passing through high temperature venting calculated from chemical and isotopic mass balance of thalium is 7.2×10^{12} kg yr^{-1} (Nielsen et al., 2006), which is multiplied by the global average vent fluid Fe (*vFe*) concentration calculated as 2.5 mM (*n* = 157) (range = 0.8 to 24 mM (Elderfield, 1996, Douville et al., 2002, Bennett et al., 2008, Beaulieu et al., 2013) from available end-member vent fluid data in the inter-ridge data base (Beaulieu et al., 2013). For calculating a global flux from off axis venting like VDVF *vFe* is corrected for the lower concentrations in off axis vent fluids by normalising *vFe* to the percent difference between average VDVF and BVF end member vent fluid concentrations.

Table 3.5 Estimating global soluble and colloidal Fe fluxes from plume mass balance

	Mean vent Fe added to plume (%)		Fe Flux (mol yr^{-1})							
			Near Vent study					Open Ocean Study		
			MCSC		ESR[a]	MAR[b]	MAR, EPR, LB[c]	EPR[d]	EPR[e]	Model[f]
	VDVF	BVF	VDVF	BVF	E2	Red Lion				
sFe	11	0.1	4x10^{-4}	6x10^{-5}	-	-	-	-	-	-
cFe	8	14	3x10^{-4}	9x10^{-3}	-	-	-	-	-	-
dFe	19	14	7x10^{-4}	2x10^{-2}	4x10^{-5}	8x10^{-6}	-	-	-	-
Global dFe			2x10^{8}	3x10^{9}	1x10^{9}	7x10^{8}	9x10^{8}	7x10^{8}	4x10^{9}	9x10^{8}

a, b and c fluxes are calculated by plume mass balance based on stabilization of 8, 4 and 5 % dFe respectively as stated in [a]Hawkes *et al.*(2013) [b]Bennett *et al.*(2009) [c]Gartman *et al.* (2014). Estimate from d, e and f are calculated from δ^3He:dFe ratios and are copied from [d]Fitzsimmons *et al.* (2014) [e]Resing *et al.* (2015) [f]Tagliabue *et al.* (2010).

The global flux of dFe from VDVF and BVF cover the range of those calculated from previous "near vent" plume studies. Global flux estimates for E2 and Red Lion are based on studies that measured ligand complexation (Bennett et al., 2008, Hawkes et al., 2013a) whereas the flux estimate from vents on the MAR, EPR and Lau Basin (LA) are calculated based on the amount of nanoparticulate pyrite measured. The higher global fluxes from BVF suggest that by only considering inorganic nanoparticles or organic complexes these previous studies may have underestimated plume dFe fluxes. Plume dFe stabilisation is likely to be controlled by a combination of both organic ligand and inorganic nanoparticle chemistry.

Fluxes from individual vent fields on the EPR could not be calculated due to the lack of any vent fluid data in individual studies (Fitzsimmons et al., 2014, Resing et al., 2015) and annual variability of vent fluid chemistry of vents on the EPR (Yucel and Luther, 2013). The most recent effort to calculate the global flux of dFe based on plume δ^3He:dFe ratios gives an estimate of 4x10^9 (Resing et al., 2015) mol yr^{-1} similar to the global flux calculated using BVF data but higher than those predicted from previous near vent studies. This may be further evidence that considering plume dFe stabilisation in a purely inorganic or organic context is not enough to account for the entire global hydrothermal dFe flux.

In previous global flux estimates (Table 3.5) the flux of stabilised dFe is assumed to be conservative during plume dispersion. This study shows that only sFe behaves conservatively in one of the plumes investigated and an attempt has been made to average the change in cFe throughout two plumes in order to show how differences in the chemistry of vent Fe sources can influence dFe exported from plumes to the deep ocean. In the case of all studies flux calculations assume that the process of Fe stabilisation is the same in every plume, however plume profiles (Figure 3.3 & Figure 3.4) and the average vent sFe and cFe added to the plume (Table 3.5) show that the process of Fe stabilisation is likely to be different between plumes originating from vents with different chemistry. In order to improve flux estimates further an understanding of how Fe stabilisation varies between vent sites due to differences in vent and deep ocean chemistry needs to be incorporated into models of hydrothermal Fe fluxes.

Due to the low light scattering profile of the VDVF plume and the wide spread occurrence of ocean core complexes it has been suggested that venting similar to that occurring at the VDVF could be occurring at other slow to ultra-slow spreading ridges (Hodgkinson et al., 2015, D'Orazio et al., 2004). It is possible that these types of vent fields remain undetected due to a combination of the low level of particle anomalies, unexplored areas of the deep sea and the bias towards searching ridge axis for plume signals rather than off axis areas (German et al., 2011). The flux calculations for VDVF (Table 3.5) are presented for comparison with BVF and to demonstrate differences between the two sites. In order to get a true global estimate of how important off-axis venting maybe for Fe fluxes more information is required on the global occurrence of off-axis vent sites. Importantly these off axis sites would not be included in models of hydrothermal dFe input based on spreading rate of ridge axis (Tagliabue, 2010). This therefore supports the idea that initial models of hydrothermal dFe input are likely to be a conservative minimum estimate (Saito et al., 2013).

The similarity between our calculated global dFe fluxes based on the BVF plume and that calculated for the EPR (Resing et al., 2015) using samples up to 4300 km from the vent site indicates that a large portion of plume dFe within several km's of the vent site must be transported 1000's of km's away in order to reproduce observations from the deep ocean. Whilst these calculations have their limitations the similarity between the global dFe flux calculated in these two studies by two different methods demonstrates the importance of processes in the plume within 1 km of the vent field controlling the amount of dFe transported to the deep ocean.

3.4.6 Implications of soluble, colloidal and dissolved metals for global ocean inventories

There are a limited number of studies that have investigated the change in dissolved concentrations of trace metals (other than Fe) in hydrothermal plumes (James and Elderfield, 1996, Sands et al., 2012) and as a result it is unknown as to whether hydrothermal plumes represent a global sink or source of other trace metals such as Cd, Cu, Mn, Zn, Pb and Co. The hydrothermal vents at the source of plumes in this study book end the global range of vent fluid chemistries and therefore cover the possible range of fluxes that may add or remove these metals from the deep ocean in different ocean basins. In a first attempt to identify, which other trace metals maybe added or removed from the deep ocean from hydrothermal plumes a similar flux calculation used for Fe in the previous section is applied to the other metals measured in the plume.

In several cases the plume budget of metals (equation 3.2) gave a negative number where concentrations in the plume were depleted relative to seawater. In these cases this indicates that the plume is removing this element from the deep ocean and acting as a sink. Therefore where the plume budget is negative, the flux term is changed to account for the volume of seawater passing through plumes globally (*pf*) and multiplied by N.Atlantic seawater concentrations (*naMe*) (Table 3.2) to calculate the net removal from deep ocean seawater by plume particle scavenging. The volume of seawater passing through BP's in the global ocean is calculated by multiplying the volume of seawater passing through high temperature venting by 10^4, which is the amount of dilution it takes for BP to become neutrally buoyant. This gives a volume of 7.2×10^{16} kg y^{1} of deep ocean water passing through BP's. This ensures that global flux calculations are representative of the effect of hydrothermal plumes on metal concentrations in the deep ocean.

$$Mean\ Me\ added\ or\ removed\ (\%) = \left(\sum_n \left(\frac{xMe-swMe}{TDMe} \times \frac{dMn}{TDMn}\right)/n\right) \times 100 \tag{3.2}$$

$$Mean\ Source\ Me\ Flux = \left(\sum_n \left(\frac{xMe-swMe}{TDMe} \times \frac{dMn}{TDMn}\right)/n\right) \times vMe\ \times vf \tag{3.3}$$

$$Mean\ Sink\ Me\ Flux = \left(\sum_n \left(\frac{xMe-swMe}{TDMe} \times \frac{dMn}{TDMn}\right)/n\right) \times naMe\ \times pf \tag{3.4}$$

Given there are no open ocean colloidal or soluble measurements of the other metals investigated assumptions must be made as to how dMe is partitioned between sMe and cMe in the open ocean with regards to *swMe* in equations 3.2, 3.3 and 3.4. This is done by taking the distribution of metals between colloidal and soluble fractions in the most diluted plume samples and assuming this is representative of the deep ocean. At both sites the distribution of dFe between cFe and sFe in the most plume diluted samples is 46:54 % in the BVF plume and 60:40 % in the VDVF plume, which is similar to the average distribution of dFe between cFe and sFe in the open N.Atlantic ocean of 50:50 (Fitzsimmons et al., 2015). For the most dilute plume samples from both sites 97 to 100 % of dMn, dCd, dCu, dZn is in the soluble fraction. Pb is the exception to this where 42 to 49 % of dPb is in the soluble fraction and 51 to 58 % in the colloidal fraction. It is therefore assumed that for *swMe* 100 % of deep ocean dMn, dCd, dCu, dZn and dCo is present entirely in the soluble fraction and that for dPb deep ocean concentrations are split 50:50 between the soluble and colloidal fractions like Fe.

The plume budgets of metals added or removed from the deep ocean with plume dispersion (Table 3.6) agree between both sites that there is a net addition of dMn, dZn, dCo and net removal of dCd and dPb. The only element where the two sites disagree is Cu where there is net removal of dCu in the VDVF plume and net addition in the BVF plume.

Table 3.6 Estimating global fluxes of Mn, Zn, Pb, Co, Cu and Cd

	Me (%) added/removed with plume dispersion				*Global Hydrothermal Flux (mol yr^{-1})		
	VDVF	±	BVF	±	Mean	Min	Max
sMn	41	42	39	29	$1x10^9$	$4x10^8$	$3x10^9$
cMn	6	11	5	11	$2x10^8$	$-5x10^5$	$6x10^8$
dMn	47	53	44	40	$2x10^9$	$1x10^8$	$3x10^9$
sZn	-12	20	9	19	$8x10^7$	$-1x10^7$	$2x10^8$
cZn	28	29	26	32	$2x10^8$	$-9x10^6$	$5x10^8$
dZn	17	49	36	52	$3x10^8$	$-2x10^7$	$7x10^8$
sPb	-3	15	4	13	$1x10^5$	$-7x10^4$	$6x10^5$
cPb	2	20	-18	23	$-6 x10^9$	$-3x10^5$	$1x10^5$
dPb	-2	35	-14	36	$-4 x10^9$	$-4x10^5$	$7x10^5$
sCo	14	9	2	10	$7x10^4$	$-4x10^5$	$4x10^5$
cCo	1	3	1	4	$3x10^4$	$-2x10^5$	$2x10^5$
dCo	15	12	3	14	$1x10^5$	$-6x10^5$	$6x10^5$
sCu	-12	10	-1	8	$-2x10^{10}$	$-1x10^7$	$1x10^7$
cCu	5	9	2	4	$3x10^6$	$-3 x10^6$	$1x10^7$
dCu	-7	19	1	12	$1x10^6$	$-2x10^7$	$2x10^7$
sCd	-55	146	-6	5	$-1x10^9$	$-2x10^6$	$-2x10^8$
cCd	3	9	0	0	0	0	0
dCd	-52	155	-6	5	$-1 x10^9$	$-2 x10^6$	$-2x10^8$

*Global hydrothermal flux based on BVF plume (%)
Plume budget = Me (%) vent fluid added (+ve) or seawater removed (-ve) with plume dispersion

Global flux calculations are based on BVF plume budgets for the same reason that global Fe flux calculations from BVF were compared to other studies in the previous section. Black smoker type vents like BVF are known to be present on all ocean ridges whereas the distribution of off-axis vent systems like VDVF is unknown. For all elements a possible minimum and maximum flux estimate was calculated based on the standard deviation of the plume budget (±) in order to account for the limitations of this method. Therefore the variation between mean, maximum and minimum fluxes reflects variation of element profiles within the BVF plume. Given that there have been no other previous attempts to quantify the dissolved fluxes of these metals from plumes the global fluxes in Table 3.6 serve as a first attempt at this in order to provide values, which can be used to test any biogeochemical models attempting to incorporate these elements. The flux ranges also highlight the limited understanding of the processes controlling other trace metals.

The mean global fluxes estimate a net addition of all metals to the deep ocean except for Cd and Pb. However only dMn has positive fluxes for mean, minimum and maximum calculations therefore it can only be said definitively that of these metals hydrothermal vents are a source of dMn to the deep ocean and this is in agreement with large plumes of elevated dMn throughout the deep ocean (Hatta et al., 2015, Resing et al., 2015). Similar plumes of dZn have been observed over ridge axis in the Atlantic and in agreement with our mean flux estimate Conway and John (2014b) conclude that hydrothermal plumes are likely to be a small source of dZn to the deep ocean. However, very recently an extensive hydrothermal plume of dZn emanating from the EPR covering a distance of >4000 km suggests hydrothermal dZn is more important than previously recognised (Roshan et al., 2016). This new data estimates a global hydrothermal dZn flux of 1.75×10^9 mol yr^{-1} which is one order of magnitude greater than the mean dZn flux presented here of 3×10^8 mol yr^{-1}.

For the other metals hydrothermal vents could be a source or a sink. Recent studies measuring dCu and dPb in the N.Atlantic (Roshan and Wu, 2015, Noble et al., 2015) conclude that hydrothermal plumes are probably a sink for these elements due to scavenging by Fe oxyhydroxide particles and this agrees with our minimum flux estimates. Even though there is net removal of dCu and dPb in hydrothermal plumes the discovery of measurable concentrations of cCu and cPb is an important consideration for the cycling of these elements. For example if plumes are scavenging sCu and sPb but adding cCu and cPb this will control the overall separation of these elements between these two size fractions in the deep ocean. This effect is likely to be more important for cCu as a large fraction of cPb may be derived from background seawater as the most dispersed plume samples contained ~50 % cPb. Any changes in speciation are likely to have implications for the biological role of these elements where deep waters are upwelled into the surface ocean.

For metals that show the widest variation in min and max flux estimates this reflects the variation in these elements throughout the plume profile. The largest variation in soluble and colloidal metal concentrations is observed in the particulate rich layers of the plume for Zn, Pb Cu and Cd. The main issue with trying to resolve if hydrothermal plumes are sinks or sources of Zn, Cu, Cd or Co metals is that unlike cFe in the BVF plume it is not clear from the plume profile whether or not there is net addition or loss of metals from the particulate to the dissolved fraction. This could be assessed in future studies by simply sub-sampling plume waters trapped in Niskin bottles over a period of time to see if the dissolved concentration of these elements decreases or increases.

3.5 Conclusions

The two hydrothermal plumes studied herein contain both colloidal and soluble Fe, Zn, Cu and Pb. Despite the difference in Fe concentrations in the hydrothermal sources (BVF = 6807 µmol kg^{-1}, VDVF = 250 µmol kg^{-1}) at each site both plumes have a similar range of concentrations of TdFe throughout (BVF = 5 to 312 nmol kg^{-1}, VDVF = 4 to 196 nmol kg^{-1}). This result is counterintuitive to the appearance of the two plumes as it was expected that the BVF black smoker plume would contain far more pFe than the clear plume over the VDVF. The plume profiles of sFe, cFe and pFe along with particle compositions indicate that the BVF plume is relatively consistent with current theory of hydrothermal plume chemistry. This being that the formation of pFe is controlled by the reaction of H_2S with Fe (II) to form FeS_2 and Fe oxyhydroxides form subsequently after Fe (II) oxidation to Fe (III). The results presented here for BVF add to this current theory by showing that pFe in the NBP is formed by colloid aggregation. This is likely to be an intermediate step between Fe (II) oxidation and particulate Fe oxyhydroxide formation. Furthermore the BVF plume profiles demonstrate that sFe behaves near-conservatively (same as dMn) indicating that sFe is the most chemically stable form of Fe in the plume.

Despite the VDVF plume having similar Fe concentrations to BVF it is clear from the plume profile that the processes of Fe (II) oxidation, Fe oxyhydroxide formation and colloid formation/aggregation are not expressed in the same way. The VDVF plume has more conserved dFe concentrations throughout plume dispersion and this indicates that there may be additional stabilisation processes, particularly for sFe (Table 3.5). It cannot be said definitely what these processes may be from the results presented here but the influence of FeS_2 nanoparticle formation, Fe oxyhydroxide colloid formation and Fe ligand complexation on the concentrations of Fe in the VDVF plume are discussed. The most likely explanation being that biologically mediated process (such as incorporation of Fe into particulate organic matter with subsequent release of organic complexed cFe and sFe) play a more significant role in the VDVF plume resulting in more dFe ligand complexation.

In order to confirm these theories and the composition of cFe and sFe future detailed analysis is required based on direct speciation studies of the cFe and sFe fractions. This could be done by synchrotron methods similar to those that have been used to analyse ocean and hydrothermal particles in detail (Toner et al., 2009a, von der Heyden et al., 2014) as well as voltammetry methods (Hawkes et al., 2013ab).

The VDVF plume represents a previously unrecognised source of off axis hydrothermal dFe, which could be present in other ocean basins. The formation sFe and cFe in the VDVF plume could also be analogous to that occurring in diffuse areas of venting around black smoker vents. This diffuse venting is also mixed into the plume and therefore could be an important mechanism for stabilising dFe globally.

The Fe/H_2S ratio, pH and temperature of vents at both sites covers a wide range of the chemistry reported for vents globally and these vent fluids mix with background deep waters of similar chemistry as they are located in the same ocean basin. The differences in Fe plume profiles at both sites indicates that in order to improve models of the hydrothermal dFe flux to the deep ocean the influence of vent chemistry on the formation of sFe and cFe must be incorporated into future models.

Whilst recent calculated hydrothermal Fe fluxes from different studies agree to within one order of magnitude (Table 3.5) the range of fluxes presented in Table 3.6 show that the current understanding of other metals is similar to that of dFe >7 years ago when hydrothermal flux estimates ranged from 0 (German and Von Damm, 2004) to $3x10^8$ (Bennett et al., 2008).

Out of all the other metals measured it is only clear that hydrothermal vents are a source of dMn with a hydrothermal dMn flux similar in size to that of dFe. It is suggested that hydrothermal vents may also be a source of dZn and dCo to the deep ocean and in the case of Zn this is supported by recent measurements of dZn and Zn isotopes in the N.Atlantic and Pacific (Conway and John, 2014b, Roshan et al., 2016). Flux estimates for both sites also indicate that there is net removal of dCd and dPb and this is consistent with scavenging of these elements onto plume particles which has been observed previously (German et al., 1991, Feely et al., 1994k). Hydrothermal plumes over the MAR are depleted in dPb relative to the deep the N.Atlantic which is attributed to adsorption onto Fe oxyhydroxides and co-precipitation in metal sulphides (Noble et al., 2015).

Only Zn, Pb and Cu were found to have measurable concentrations in the colloidal fraction in both hydrothermal plumes. Plume budgets indicate that that cZn and cCu may be a feature of hydrothermal plumes globally where as cPb could be from background seawater. This could have important implications for the cycling of these elements globally as our global flux estimates indicate that hydrothermal plumes may be a sink for sCu and cPb whilst being a source of sPb and cCu. This discrepancy between soluble and colloidal fluxes could act to alter the separation of these elements between soluble and colloidal fractions in the deep ocean. This is likely to have important implications for the biogeochemical cycling of these elements in the ocean possibly by changing their overall speciation. Assuming that soluble and colloidal fractions are likely to represent different species rather than a size continuum of the same species.

Chapter 4: Opposing controls on the isotopic signature of dissolved iron in hydrothermal plumes

ABSTRACT

Iron is a scarce but essential micronutrient in the oceans that limits primary productivity in many regions of the surface ocean. The mechanisms and rates of Fe supply to the ocean interior are still poorly understood and quantified. Fe isotope ratios of different Fe pools can potentially be used to trace sources and sinks of the global Fe biogeochemical cycle if these boundary fluxes have distinct signatures. Seafloor hydrothermal vents emit metal rich fluids from tectonic margins into the deep ocean. Fe isotope ratios have the potential to be used to trace the input of hydrothermal dissolved Fe to the oceans if the local controls on the fractionation of Fe isotopes during plume dispersal in the deep ocean are understood. In this study the behaviour of Fe isotopes is assessed in a Southern Ocean hydrothermal plume using a sampling program of Total Dissolvable Fe (TDFe), particulate Fe (pFe) and dissolved Fe (dFe). δ^{56}Fe values of dFe (δ^{56}dFe) within the hydrothermal plume change dramatically during early plume dispersal, ranging from -2.39 ± 0.05 ‰ to -0.13 ± 0.06 ‰ (2 SD). The isotopic composition of TDFe (δ^{56}TDFe) was consistently heavier than dFe values, ranging from -0.31 ± 0.03 ‰ to 0.78 ± 0.05 ‰, consistent with Fe oxyhydroxide precipitation as the plume samples age. The dFe present in the hydrothermal plume includes stabilised dFe species with potential to be transported to the deep ocean. Estimates based on our measurements predict that stable dFe exported from the plume will have a δ^{56}Fe of -0.28 ± 0.17 ‰. Further, the proportion of authigenic Fe-sulfide and Fe-oxyhydroxide minerals in the buoyant plume exert opposing controls on the resultant isotope composition of dissolved Fe passed into the neutrally buoyant plume. Such controls yield variable dissolved Fe isotope signatures under the authigenic conditions reported from modern vent sites elsewhere, and so ought to be considered during Fe isotope reconstructions of past hydrothermalism from ocean sediment records.

4.1 Introduction

Iron (Fe) is a key micronutrient that often limits primary productivity in high nutrient low chlorophyll zones of the surface ocean and therefore has an indirect influence on the biological carbon pump (Martin, 1990). For this reason it is important to understand the biogeochemical cycle of Fe in the marine environment. Iron exhibits very low solubility in seawater and hence is only present in pico- to nano-molar concentrations (Fitzsimmons et al., 2015). A consequence of this is that Fe is a limiting nutrient in areas where other key nutrients are abundant, such as the Southern Ocean (Moore et al., 2013).

In contrast, the Fe content of hydrothermal vent fluids is in the µM to mM range. The recent basin-scale sampling of the GEOTRACES program highlighted areas of increased dissolved Fe (dFe) concentration (>1 nM) extending for thousands of km away from mid-ocean ridges (Nishioka et al., 2013, Conway and John, 2014f, Fitzsimmons et al., 2015, Resing et al., 2015). Hydrothermal vents had long been considered to have a negligible impact on ocean dFe due to extensive Fe mineral precipitation in the stock work, chimney features and hydrothermal plume (Elderfield, 1996). On the other hand recent work suggests that 4-7.5% of hydrothermal Fe may be prevented from precipitating as Fe minerals by complexation with organic ligands (Bennett et al., 2008, Hawkes et al., 2013a, Kleint et al., 2016). The distributions of dFe observed in the deep ocean are better reproduced in models by including a relatively significant flux of hydrothermal Fe to the deep ocean (Tagliabue, 2010). These observations suggest that hydrothermal vents represent an important and previously overlooked source of dFe to the oceans.

4.1.1 Fe in hydrothermal systems

As seawater circulates through the crust and undergoes alteration, Fe is leached from host rocks and the sea water becomes enriched with Fe contents of 2 to 24,000 µM (Mottl and McConachy, 1990, German and Von Damm, 2004). The hot hydrothermal fluid rises up through the crust and vents at the sea floor. The vent fluid mixes with the oxic deep water and rises up through the water column under its own buoyancy. The plume becomes neutrally buoyant once it is diluted 8000-10,000 times and the plume density equals that of the surrounding seawater (McDuff, 1995).

In initial studies of mid-ocean ridge axial high temperature, and diffuse low temperature, hydrothermal sites it was estimated that the gross flux of Fe to the ocean was 2.3-19 x10^{10} mol y^{-1}, approximately equal in size to the estimated flux from rivers of 2.3x10^{10} mol y^{-1} (Elderfield, 1996). The net input of hydrothermal Fe to deep waters, however, was considered to be negligible due to Fe oxide and Fe sulphide mineral precipitation close to the vents (Mottl and McConachy, 1990, Elderfield, 1996).

Where substantial sulphide exists relative to Fe in the vent fluid, Fe sulphides precipitate as the buoyant fluids cool and mix with seawater. During this buoyant plume rise dFe remaining in the plume undergoes further mixing with entrained oxic seawater and Fe(II) is oxidised to form Fe(III)-bearing oxyhydroxide precipitates (Mottl and McConachy, 1990). On the other hand, where low sulphide concentrations exist in the vent fluid, such as in ultramafic geological settings, there is little Fe sulphide formation and Fe precipitates principally as Fe oxyhydroxides (Douville *et al.*, 2002).

The rate at which Fe(II) is oxidised to Fe(III) is an important control on particulate Fe oxyhydroxide formation and hence the concentration of dFe in the hydrothermal plume. The pseudo first order oxidation half-life of Fe(II) varies with changes in oxygen and pH between deep ocean basins from 2.1 mins in the relatively oxygenated high pH Atlantic to 6 hours in the lower oxygen levels and lower pH observed in the Pacific (Millero *et al.*, 1987; Field and Sherrell 2000).

Fe sulphide minerals have been identified as colloidal constituents within the dissolved phase of some vent fluids (Yucel et al., 2011, Sands et al., 2012), while in other studies, the complexation of Fe with dissolved organic ligands has also been reported in hydrothermal plumes (Bennett et al., 2008, Hawkes et al., 2013a, Kleint et al., 2016). In many cases, Fe-rich colloids are seen to be transported many hundreds to thousands of kilometres from their hydrothermal source (Klunder et al., 2011, Wu et al., 2011a, Klunder et al., 2012, Nishioka et al., 2013, Fitzsimmons et al., 2014, Resing et al., 2015).

4.1.2 Fe isotopes in hydrothermal vents and plumes

Natural variations in stable Fe isotope compositions are caused by biological and abiotic redox processes with either kinetic or equilibrium fractionation effects (Welch et al., 2003, Johnson et al., 2004, Anbar et al., 2005). If hydrothermal sources of dFe to the ocean have a distinct δ^{56}Fe signature, they could be used to constrain isotope mass-balance quantifications of Fe sources to the ocean (Conway and John, 2014f) or help to reconstruct past oceanic Fe cycles (Horner et al., 2015). However, this utility requires a fully resolved knowledge of the biogeochemical processes that fractionate Fe isotopes as they transition between hydrothermal vents and the open ocean.

The Fe isotope composition of hydrothermal vent fluids is not uniform and several studies report a range from -0.69 ± 0.16 to -0.13 ± 0.06 ‰ (2 SD) (Sharma et al., 2001, Beard et al., 2003, Severmann et al., 2004, Rouxel et al., 2008, Bennett et al., 2009). So far the fractionation of Fe isotopes in hydrothermal plumes has been examined in just two studies (Severmann et al., 2004, Bennett et al., 2009). In both cases, the particulate Fe (pFe) fraction (>0.4 µm) collected on filters was measured and showed that the Fe isotope composition of dFe from the vent source is likely to be modified in the hydrothermal plume by precipitation of Fe oxyhydroxide and/or Fe sulphide mineral particles (Severmann et al., 2004, Bennett et al., 2009). However the influence of these processes on the δ^{56}Fe composition of dFe in hydrothermal plumes has not yet been directly measured. Severmann et al. (2004) sampled the sediments, vent fluid and plume particles derived from the Rainbow hydrothermal vent on the Mid-Atlantic Ridge. Neutrally buoyant plume (NBP) particles collected *in-situ* had an average Fe isotope composition (δ^{56}pFe = -0.09 ± 0.03 ‰ relative to IRMM-14) similar to the surrounding Fe-Mn rich sediments (δ^{56}Fe = -0.11 ± 0.10 ‰) and the hydrothermal vent fluid (δ^{56}dFe = -0.14 ± 0.02 ‰). Only the Fe isotope composition of samples collected in the buoyant plume varied significantly at this site, where δ^{56}pFe ranged from +0.24 to +1.29 ‰. Due to its ultramafic host rock the Rainbow vent fluids contain abundant Fe and a very high Fe/H_2S ratio (Douville et al., 2002). Consequently, they precipitate almost exclusively as Fe oxyhydroxides in the plume, with no more than 4% of Fe forming sulphide minerals (Severmann et al., 2004). Therefore the Fe isotope signature of the vent fluid is preserved in the NBP by the near quantitative conversion of vent fluid Fe to Fe oxyhydroxide particles, and the isotopically heavy buoyant plume particles result from partial oxidation of vent fluid Fe(II) (Severmann *et al.*, 2004). The high Fe/H_2S ratio at Rainbow makes this site unusual in comparison to the more widespread basalt hosted hydrothermal vents, where vent fluids have more sulphide relative to Fe, and as much as half of Fe from the vent fluid may form Fe sulphide minerals (Rudnicki and Elderfield, 1993).

Bennett et al. (2009) sampled buoyant plume particles and vent fluids from basalt-hosted hydrothermal vents in the South Atlantic and revealed contrasting results to Severmann et al. (2004). Particles in the buoyant plume appeared isotopically lighter (-0.31 ± 0.06 to -0.70 ± 0.14 ‰, 2 SD) than the vent fluids (-0.29 ± 0.05 ‰, 2SD), which the authors attributed to the influence of Fe sulphide precipitation. Using isotope mass-balance, Bennett et al. (2009) reasoned the dissolved Fe fraction of the hydrothermal plume would be isotopically heavier than the vent fluid, but its isotope composition was never measured.

The aim of this study is to determine the effective isotope composition of dissolved Fe that is dispersed into the deep-ocean interior from a hydrothermal vent source, and to resolve the mechanisms responsible for isotope fractionation between dissolved and particulate phases during plume mixing and dispersal. Samples were collected from a hydrothermal site in the East Scotia Sea to determine the concentrations of Fe and Mn in the Total Dissolvable (TD), dissolved (d) and particulate (p) size fractions as well as the Fe isotope composition of TDFe and dFe. This work provides new constraints on the nature of plume particle interactions and the impact on the deep ocean, which have implications for Fe isotopic mass-balance studies of the present and past oceans.

4.2 Materials and Methods

4.2.1 Study area

The East Scotia Ridge (ESR) is located in the Southern Ocean sector of the South Atlantic, southeast of South Georgia and west of the South Sandwich Island Arc (Figure 4.1). The ESR separates the Scotia Plate and Sandwich Plate and is a back arc spreading centre. Spreading at the ESR has been occurring for a minimum of 9 Ma and currently proceeds at an intermediate rate of 65-70 mm yr^{-1} (Bruguier and Livermore, 2001). The ridge is split into nine spreading segments, E1-E9. The E2 and E9 segments are topographically distinct from the E3-E8 segments and evidence from seismic reflection shows that E2 and E9 are or have been in the past underlain by axial magma chambers (Bruguier and Livermore, 2001). Hydrothermal plume signals indicative of seafloor hydrothermal venting were initially detected over the E2 segment in 1999 (German et al., 2000). High temperature black smoker chimneys have now been observed and sampled at E2 where the plume signals were first observed (Rogers et al., 2012).

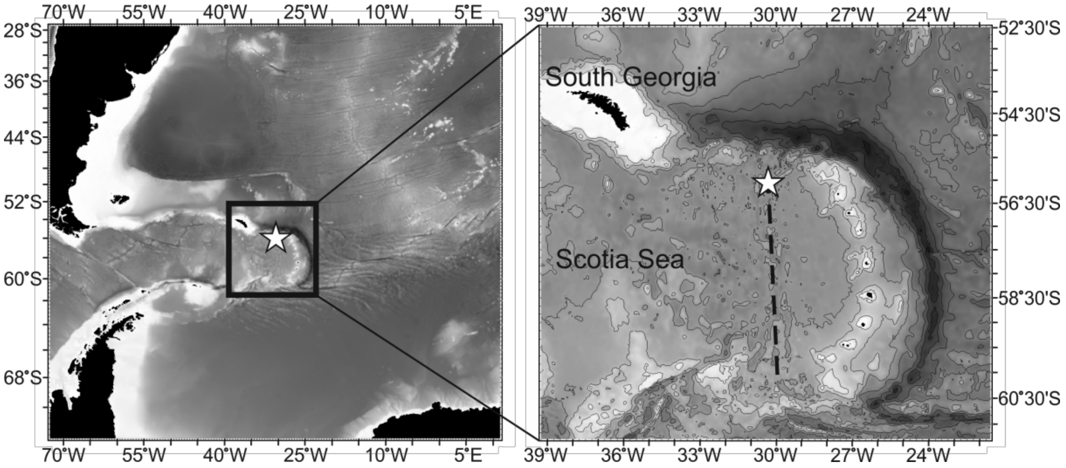

Figure 4.1 Study map showing the location of the E2 vent field (star). The dashed line represents the approximate location of the East Scotia Ridge.

The E2 site is located at 56.089°S, 30.317°W (Figure 4.1). BP and vent fluid samples were collected at the Dog’s Head site located at a water depth of 2600 m. Dog’s Head is a group of three 10 m tall chimneys spaced 1 to 2 m apart, actively venting hydrothermal fluids at temperatures up to 351 °C, which form the characteristic “black smoke” upon mixing with seawater (James et al., 2014, Rogers et al., 2012). Cooler water from depth is entrained up to the height of neutral buoyancy (~2360 mbsl) in the Scotia Sea (German et al., 2000). Deep waters at this site are Weddell Sea Deep Water partially mixed with Lower Circumpolar Deep water (Naveira Garabato et al., 2002, Hawkes et al., 2013a). With no local topographic features to confine the plume, the direction of plume dispersal is controlled by ambient deep water currents (German et al., 2000, Walter et al., 2000, Hawkes et al., 2013a), which at the time of sampling transported the plume in an easterly.

4.2.2 Hydrothermal Plume detection and sampling

Seawater samples from the BP were collected, filtered and preserved on the RRS *James Cook* during expedition JC080. Samples were analysed for trace metal concentrations and Fe isotopes at the National Oceanography Centre in Southampton. The pH and oxygen concentration of several samples were measured on board the ship.

Detection and sampling of the hydrothermal plumes was conducted using a Seabird +911 conductivity, temperature and depth (CTD) profiler system that was attached to a titanium frame that holds 24 externally sprung 10 litre OTE (Ocean Test Equipment) water sampling bottles. These bottles were cleaned at the start of the cruise by filling each bottle with freshwater and an aliquot of HCl. The Niskin bottles are Teflon lined with Teflon taps and non-metallic parts to prevent any contamination during sampling of waters with low concentrations of trace metals. A light scattering sensor (LSS), Eh detector and Stand Alone Pumping System (SAPS) were also mounted on the titanium frame.

The hydrothermal plume was located using the CTD profiler, LSS and Eh detectors to look for deviations in temperature, particulates, and Eh from background seawater. The buoyant part of the hydrothermal plume (BP) was identified by negative Eh anomalies and positive temperature and LSS anomalies. The NBP was detected by positive LSS anomalies and negative Eh and temperature anomalies. These anomalies were evidenced by relative changes in sensor signals in real time whilst towing the CTD rosette across the vent field and simultaneously profiling the water-column (so-termed 'tow-yoing').

During JC80 vent fluid samples were taken from the chimney orifices using a set of titanium syringes (Von Damm et al., 1985) with a temperature probe attached, which was aligned with the snorkel of the syringe for simultaneously measuring fluid temperature during sampling. The temperature probe measured temperatures of 320-343 ˚C during sampling of Dog's Head vents.

Six 1.2 L Niskin bottles were attached to the Remotely Operated Vehicle (ROV) *Isis* for sampling the buoyant plume. *Isis* was manoeuvred until the black smoke from the vent was observed flowing through the bottles on a camera pointed at the Niskin rosette. Once the black smoke was observed the temperature was recorded using the CTD on *Isis* and the bottles were closed.

4.2.3 Sample filtration and preservation

All bottles used for sampling were low-density polyethylene (LDPE) and pre-cleaned using the following procedure: 2 days soaked in 2 % Decon 90; rinsed 3 times with deionised water (Milli-Q, Millipore, >18.2 MΩ cm); 1 week soaked in 6 M HCl; rinsed 3 times with deionised water; 1 week soaked in 8 M HNO_3; transferred to Class 1000 clean laboratory and rinsed 3 times with deionised water; filled with 0.015 M sub boiled (S.B.) HNO_3. Filters, Teflon filter housings and sampling tubes were soaked in 1.6 M HNO_3 for at least 5 days before being moved to a bath of deionised water where they were stored until required. Filter housings used for samples from the 1.2 L Niskin bottles on *Isis* were cleaned in a separate 1.6 M HNO_3 bath and rinsed 3 times with deionised water prior to use.

Before sub-sampling Niskin bottles were shaken in order to re-homogenize fluid and particles within the bottle. Samples were transferred from the Niskin bottles under 0.5 bar of pressure using oxygen free nitrogen. 125 ml of unfiltered water sample was sub-sampled from each Niskin for total dissolvable metals. Polycarbonate membrane filters (0.2 µm, Whatman) were used to filter 125 ml of water from Niskin bottles to collect the dissolved metal size fraction for trace metal analysis. Clean sample bottles were rinsed 3x with de-ionised water then rinsed with an aliquot of sample water before filling.

Vent fluid samples were transferred directly from titanium syringes (Von Damm *et al.*, 1985) to pre-cleaned LDPE bottles for trace metal analysis.

All samples for trace metal analysis were acidified at the end of the cruise using 1 µl of ultra-pure conc. HNO_3 (ROMIL UpA) per 1 ml of sample to achieve a pH <2, and stored for a minimum of 6 months prior to analysis.

4.2.4 Determination of trace metal concentrations in plume samples

Concentration measurements of dissolved and total dissolvable metals followed a three step procedure: (1) diluting samples to evaluate the range of concentrations sampled, (2) identifying any samples from step (1) with concentrations below the limit of detection (l.o.d) or with a high blank contribution for pre-concentration and re-analysis, (3) repeat analyses of Fe concentration by isotope dilution - a useful by product of Fe isotope analyses by double spike (Lacan et al., 2010, Conway et al., 2013).

Initially samples were diluted 21-fold in 1M S.B. HNO_3. Several samples were doped with a Mn and Fe standard to determine concentrations by standard addition. Dilute sample-spike solutions were analysed using an Element 2 (Thermo Scientific) Inductively Coupled Plasma-Mass Spectrometer (ICP-MS). Procedural blanks for Fe and Mn calculated from the analysis of 1M S.B. HNO_3 were 2 and 0.2 nmol kg^{-1} respectively, with corresponding instrument limits of detection (3σ of blanks, $n = 15$) of 0.5 and 0.2 nmol kg^{-1}. Two reference materials were analysed to assess accuracy. The measured Fe and Mn content of SLRS-4 (National Research Council, Canada) was 1812 ± 49 nmol kg^{-1} Fe and 66 ± 5 nmol kg^{-1} Mn ($n = 8$), which compares well to certified values of 1844 ±90 nmol kg^{-1} Fe and 61.3 ± 0.2 nmol kg^{-1} Mn. Good agreement was also demonstrated at lower concentrations; measured values of Fe and Mn (14 ± 10 nmol kg^{-1} and 48 ± 3 nmol kg^{-1}, $n = 8$) in CASS-4 (National Research Council, Canada) compare well to certified values (12 ± 1, 50.60 ± 0.34 nmol kg^{-1} respectively).

Samples with measured Fe concentrations <400 nmol kg^{-1} (i.e. where the blank contribution was >10 %) were re-analysed by pre-concentration (Milne et al., 2010, Biller and Bruland, 2012) onto a chelating resin that uses carboxymethylated pentaethylenehexamine (CM-PEHA resin) (Kagaya et al., 2009). Fe concentrations determined for CASS-4 (11.1 ± 0.5 nmol kg^{-1}, $n = 3$) and NASS-6 (9.0 ± 0.7 nmol kg^{-1}, $n = 6$) had excellent agreement with their certified values (12 ± 1 nmol kg^{-1} and 8.6 ± 0.8 nmol kg^{-1}, respectively), with a corresponding Fe blank of 0.2 nmol kg^{-1} and limit of detection (3σ of blanks, *n* = 6) of 0.1 nmol kg^{-1}.

Initial ICP-MS determinations of TDFe and dFe in diluted and pre-concentrated samples were used to estimate the volume required for ~200 ng of Fe used in the isotope analysis described below. The reported sample concentrations of dFe and TDFe were determined by isotope dilution using Multi-Collector (MC) ICP-MS, as has been used elsewhere (Conway and John, 2014f, Lacan et al., 2010). For accurate determination of concentrations, the double spike Fe isotope composition was calibrated by inverse deconvolution of a 3.6 µmol kg^{-1} spike-reference material (IRMM 14) mix with Fe concentration determined by inverse isotope dilution of a spike-certified Fe standard mix (Inorganic Ventures) of known concentration with a relative standard deviation (RSD) of ± 0.3 %. The maximum RSD on repeat Fe measurements by double spike MC-ICP-MS was ± 0.1 % (*n* = 2), and is an improvement on the precision of Fe concentrations initially measured by ICP-MS where the RSD was up to ± 6 % (*n* = 17). The accuracy of Fe measurements by MC-ICP-MS was assessed by inter-comparison with the previous measurements by ICP-MS and all values agreed within 11 % (*n* = 38). Subsequently Fe concentration data reported herein were determined by MC-ICP-MS because it provides sufficient accuracy with the best precision available.

Particles collected from 0.6 to 3 L of sample passed through 0.2 µm filters were dissolved in concentrated nitric acid at 150 °C for 3 days following the method of German et al. (1991). Dissolution efficiency was assessed using the RTS-1 sulphide ore mill tailings reference material. This reference material was deemed the most likely to have similar Fe mineralogy to hydrothermal plume particles in comparison to other reference materials. Recoveries of Fe, Zn and Cu from a weighed amount of RTS-1 were 94 ± 2, 126 ± 9 and 110 ± 10 %. Particles collected on SAPS filters were also characterised using scanning electron microscope energy dispersive x-ray (SEM-EDX) as described in the Appendix E.

Concentrations of TD Cu, Zn, V, and Mg in the vent fluid samples were measured by dilution in 0.3 M S.B. HNO_3 and analysis on a X-Series 2 quadrupole ICP-MS (Thermo Scientific). TD vent fluid concentrations of Fe and Mn were diluted in the same way but measured by ICP Atomic Emission

Spectroscopy (AES) (Thermo Scientific iCAP 6000 Plus Series). The concentration of chloride in the vent fluids was measured by ion chromatography (IC; Dionex ICS2500).

Oxygen concentration and alkalinity were measured at sea as soon as possible after sampling. Oxygen was measured using the Winkler Titration (Hansen, 2007) with a standardised iodate solution (1.667mM) (OSIL) and alkalinity by the Gran titration method (Kaeding, 1973).

4.2.5 Fe isotope analysis

The Fe isotope composition of samples was determined using a ^{57}Fe and ^{58}Fe double spike method adapted from Lacan et al. (2010). All sample handling was carried out under laminar flow hoods, set within a Class 1000 clean laboratory to minimise the potential for airborne sample contamination.

Initial matrix removal and pre-concentration of spiked samples was carried out using nitriloacetic acid (NTA Superflow, Quiagen) resin packed into a ~5 cm^3 volume of a 12 cm long handmade column constructed from Perfluoroalkoxy alkane (PFA) tubing with the resin retained by Teflon frits with 20 μm pores. Samples were prepared by acidifying to a pH between 1.7 and 1.8 several days before adding the double spike in equi-molar concentration to the sample. After adding the double spike 1 μl of 0.1 M H_2O_2 (Upa ROMIL) was added per 1 ml of sample 1 hour prior to loading the sample onto the NTA columns. Prior to sample loading NTA columns were cleaned using 75 ml 1.5 M S.B. HCl and 80 ml de-ionised water (18.2 MΩ cm, Milli-Q) checking that the pH was neutral after the de-ionised water rinse. Samples were loaded onto the columns and rinsed with 80 ml de-ionised water to remove salts. Fe was then eluted from the NTA columns using 10 ml of 1.5 M S.B. HCl. The eluate was collected in 15 ml PFA vials (Savillex), dried down and reconstituted in 0.5 ml 6 M S.B. HCl + 0.001 % v/v H_2O_2, in preparation for a secondary purification step.

AG1-X8 anion-exchange resin with 100-200 dry mesh size (Bio Rad) was used to further purify Fe in the samples. Handmade polyethylene columns (~9 cm length and ~0.4 mm diameter) were filled with the AG1-X8 resin and pre-cleaned once with 5 ml of 0.1 M ultrapure HF; four times filling the columns with 6 M S.B. HCl followed by 7 M S.B. HNO_3 then with 2 ml of 1 M S.B. HCl (all acids had a concentration of 0.001 % v/v H_2O_2). The resin was then conditioned with 1 ml 6 M S.B. HCl + 0.001% v/v H_2O_2 before the sample was loaded onto the columns in 0.5 ml 6 M S.B. HCl + 0.001 % v/v H_2O_2 and rinsed using 3.5 ml of 6 M S.B. HCl + 0.001 % v/v H_2O_2. Fe was eluted from the resin using 4 mL of 1 M HCl + 0.001% v/v H_2O_2 and collected in a 7 ml Teflon vial. The procedural blank was estimated as 0.9 ± 0.3 ng Fe (n = 5) by taking de-ionised water through the entire procedure.

All purified samples were evaporated on a hotplate and re-dissolved in 1 to 2 ml of 0.3 M S.B. HNO_3 for isotopic analysis by MC-ICP-MS (Thermo Fisher Neptune or Neptune Plus) with aluminium skimmer and sample cones. Samples were introduced using an Aridus II (CETAC) or Apex-Q (ESI) desolvator and masses ^{54}Fe, ^{56}Fe, ^{57}Fe, ^{58}Fe, ^{53}Cr and ^{60}Ni were measured. Fe concentrations for isotope analysis were 200 ng/ml introduced at 75 µl min^{-1} using a PFA nebuliser. Analysis by MC-ICP-MS was conducted in high-resolution mode in order to resolve polyatomic interferences on ^{54}Fe, ^{56}Fe and ^{57}Fe. Sample analysis consisted of 50 repeat measurements of 4.2 s. A blank (the same 0.3 M S.B HNO_3 samples were dissolved in) solution was measured before and after every sample/standard, with 20 repeat measurements of 4.2 s. Sample and blank uptake time was 80 s. Wash time before each sample/standard was 60 s. The wash time before blanks was 300 s when using the Apex-Q and increased to 900 s when using the Aridus. The instrument was tuned until the mass resolution was >8000 with a plateau >200 ppm. The centre mass for measurements was 2/5ths along the length of the signal plateau and a sequence of standards were analysed before measuring any samples in order to assess instrument performance. Isotopes ^{53}Cr and ^{60}Ni were monitored in order to correct for any isobaric interferences from ^{54}Cr on ^{54}Fe and ^{58}Ni on ^{58}Fe. Detectors measuring ^{53}Cr and ^{60}Ni used 10^{12} ohm resistors to improve the accuracy of low intensities from these isotopes. All other detectors used 10^{11} ohm resistors. Sequences were set up on the instrument with a standard bracketing approach in the repeating order reference material (IRMM), internal standard (ETH), Sample 1, Sample 2. The mean beam intensity of blanks bracketing each sample/standard is subtracted from the sample/standard analysis. Mass bias on sample/standard measurements is corrected for by iteratively deconvolving the spike-sample mix following the data reduction methodology of Bonnand et al. (2011). ^{54}Cr and ^{58}Ni interferences were corrected based on beam intensity (Albarede and Beard, 2004).This correction procedure assumes instrumental mass bias is the same for Fe, Cr and Ni with $^{53}Cr/^{54}Cr$ and $^{58}Ni/^{60}Ni$ equal to natural abundances (Dauphas et al., 2009). Instrument accuracy was assessed by repeat measurements of IRMM-14 and Eidgenössische Technische Hochschule (ETH) Zürich standards. The precision of Fe isotope measurements was ±0.07 ‰, 2 SD, based on repeat analysis of IRMM-14 (0.00 ± 0.07, 2SD, n = 40), samples (mean error ± 0.07, 2SD, from 2 repeats of n = 11 samples) and ETH standard (0.51 ± 0.07, 2SD, n = 32). To assess accuracy and precision of the entire method de-ionised water doped with the ETH standard and taken through the full procedure gave values of 0.52 ± 0.10 (2SD, n = 5). Both instrument and method analysis of the ETH standard were in agreement with the consensus value of 0.53 ± 0.06 (2SD, n = 6) (Lacan et al., 2008, Lacan et al., 2010, Levasseur et al., 2004, Poitrasson and Freydier, 2005, Teutsch et al., 2005).

All isotope values reported here are in delta notation relative to the standard reference material IRMM-14:

$$\delta^{56}Fe\ (‰) = ((^{54}Fe/^{56}Fe)_{sample}/(^{54}Fe/^{56}Fe)_{IRMM-14} - 1) \times 1000 \qquad (4.1)$$

4.3 Results

4.3.1 Vent fluid composition

The mean temperature of vent fluids issuing from several different chimneys was 333 °C, which is typical of black smoker type hydrothermal vents (Table 4.1) (Ishibashi, 1995). Measured chloride concentrations were slightly higher than background seawater (540 mM), which is typical of vents in back arc basins (Gamo et al., 2006). A vent fluid Mg content of 0.9 to 1.6 mM was highly depleted relative to a Scotia Sea bottom water concentration of 53.5 mM (James et al., 2014), and showed that only a negligible proportion of background seawater (1.9 to 3.1%) was entrained with the vent fluid during sampling.

Table 4.1 Hydrothermal vent fluid composition at E2, Dog's Head. Temp. is the maximum temperature recorded during sampling from a temperature probe attached to the snorkel of the titanium sampler.

Sample	Temp. (°C)	Cl^- (mM)	Fe (mM)	Mn (mM)	Cu (mM)	Zn (mM)	V (mM)	Mg (mM)
B1-02	343	555	1.41	1.96	0.0420	0.258	0.485	1.51
B1-03	343	556	1.41	1.97	0.0394	0.265	0.543	1.65
B2-08	320	550	1.40	1.99	0.0386	0.268	0.596	1.68
Y1-06	346	558	1.25	2.00	0.0367	0.295	0.611	1.00
Y2-01	324	553	1.37	1.99	0.0370	0.280	0.570	1.25
Y2-04	324	556	1.37	2.03	0.0373	0.280	0.562	1.41
Mean	333	555	1.37	1.99	0.0385	0.274	0.561	1.42
RSD (%)	4%	1%	5%	1%	5%	5%	8%	18%
End-member		555	1.40	2.00	0.0396	0.282	0.577	0

Concentrations of dFe, dMn, dCu, dZn and dV in the vent fluids were similar in all samples, with relative standard deviations (RSD) typically <8% of mean values. The RSD of Mg concentrations across all samples was higher (18%), but still only reflects minor seawater entrainments up to 3.1%, which result in negligible differences between observed values and predicted mean end-member element concentrations (Table 1).

Hydrothermal end-member Fe and Mn concentrations of 1.4 to 2.0 mM are relatively high compared to the global range measured for back arc basin vents of 0.4 to 6.8 mM for Mn and 0.02 to 1.7 mM for Fe (Ishibashi, 1995), but comparable to end-member vent fluid concentrations reported previously for this site (James et al., 2014). The end-member Cu concentrations observed (0.0396 mM) were also at the high end of previously reported values from vents in a back arc basin, which varied from 3×10^{-6} to 0.034 mM (Ishibashi, 1995). Whereas Zn concentrations of 0.282 mM were intermediate in this respect, compared to values between 7 x 10^{-3} to 7 mM (Ishibashi, 1995). Both Cu and Zn are approximately double the end-member values calculated previously of 0.146 mM and 0.0185 mM (James et al., 2014) indicating an increase of Zn and Cu in the three years between sampling.

The end-member molar ratio of chalcophile elements to Fe in the vent fluids was 0.028 for Cu/Fe and 0.201 for Zn/Fe. In comparison to previous Fe isotope studies from hydrothermal vents, the Cu/Fe and Zn/Fe ratios at Dog's Head were higher than at Red Lion in the South Atlantic, which had ratios of <0.01 for Cu/Fe and 0.13 for Zn/Fe (Bennett *et al.*, 2009). The ratios from Dog's Head were also much higher than those reported from Rainbow, in the North Atlantic, which were <0.01 for Cu/Fe and <0.01 for Zn/Fe (Douville *et al.*, 2002).

Herein the Fe isotope composition of the vent source is considered the same as the plume sample with dMn maxima of 11.2 µmol kg^{-1} collected directly above Dog's Head chimney (5 m) to be representative of the end-member vent-fluid. Our assumption of TDFe conservation within 5 m of buoyant plume rise is supported by the *in situ* observations that particles do not attain settleable size within the immediate plume over the vent orifice (Estapa et al., 2015). Further, the δ^{56}TDFe of the plume sample that is assumed to equate to the vent fluid had an Fe isotope composition of -0.31 ± 0.03 ‰ (Figure 4.6b), which is centred within the range of δ^{56}Fe values reported previously for vent fluids sampled from other sites of -0.69 to -0.13 ‰ (Sharma et al., 2001, Beard et al., 2003, Rouxel et al., 2008, Severmann et al., 2004, Bennett et al., 2009).

4.3.2 Buoyant plume detection

Negative anomalies in Eh and positive anomalies in temperature and LSS at a depth of 2600 m indicated that the buoyant plume was sampled by the CTD rosette very close to if not directly over the Dog's Head chimney, which is known to be at 2600 m depth (Figure 4.2).

The influence of other nearby venting edifices from E2 can be ruled out as they do not generate significant particulate plumes (James et al., 2014).

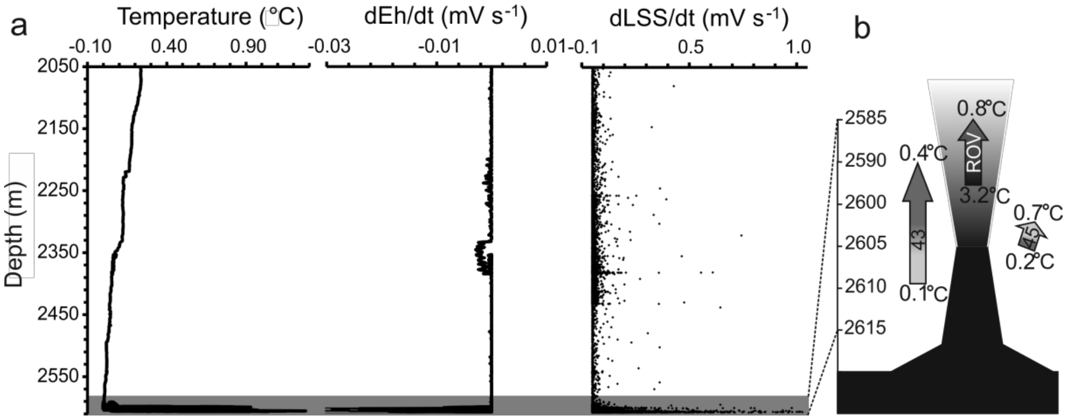

Figure 4.2 Tow-yo profile of main sampling cast (CTD 45) showing temperature, delta Eh/ delta time, and delta light scattering signal/ delta time (a). The depth of buoyant plume samples collected for Fe isotope analyses is represented by the grey bar. Further details of sampling are provided by the schematic diagram (b) where arrows represent the path of the sampling equipment relative to depth (m) on the y-axis. Corresponding *in-situ* temperature (˚C) range of samples is noted at either end of the arrows. Numbers on arrows correspond to designated CTD cast numbers with ROV representative of samples taken using ISIS in the black smoke of the plume.

4.3.3 Fe and Mn concentrations in the buoyant Plume

Dissolved Mn (dMn) has been used as a near-conservative tracer of plume dilution as in previous plume studies (James and Elderfield, 1996, Field and Sherrell, 2000) as the oxidation rates of reduced Mn are considered to be negligible compared to the time scales of plume dispersal at our study site (Cowen et al.1990b) . The TDFe, dFe and dMn content of the buoyant plume was 2 to 3 orders of magnitude higher than background Scotia Seawater (Fe and Mn = 0.4 and 2.8 nM) (Loscher et al., 1997, Klunder et al., 2011, Hawkes et al., 2013a). The concentration of TDFe was 13.6 µmol kg^{-1} in black smoke above the hydrothermal vent and dropped to 0.49 µmol kg^{-1} during dispersal in the buoyant plume (Figure 4.3). Similarly, dFe concentrations decreased from 9.20 to 0.05 µmol kg^{-1} and were always less than the corresponding TDFe concentration (Figure 4.3). Dissolved Mn was 11.2 µmol kg^{-1} in near vent samples, and down to 0.6 µM in more dispersed samples further away from the vents. Dissolved Mn was consistently more abundant than dFe in the buoyant plume, where dFe/dMn ranged from 0.81 in near vent samples down to 0.07 in more distal samples, and was mainly lower than the mean vent fluid ratio of 0.69. The TDFe/dFe ratio ranged from 1.11 to 6.56 in the buoyant plume, with higher ratios in more dispersed samples reflecting a greater proportion of particulate Fe in the TDFe samples.

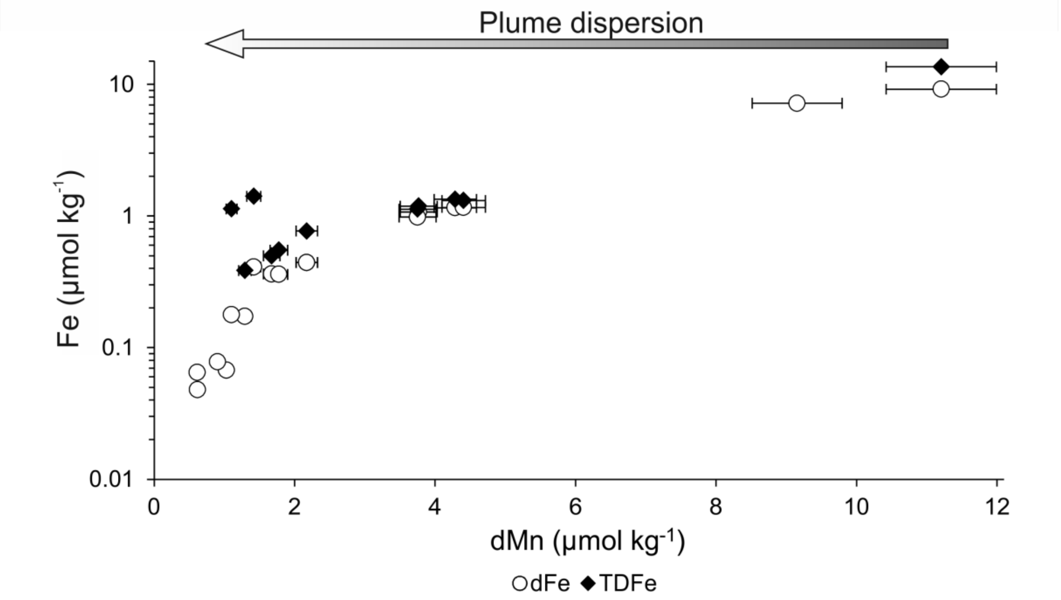

Figure 4.3 Concentrations of TDFe (black diamonds) and dFe (open circles) plotted against the near-conservative tracer dMn. Error bars represent 6 % RSD error on dMn measurements. Error bars on Fe concentrations are smaller than the size of data point markers.

4.3.4 Sample aging within Niskin bottles

Metal concentrations in the ‘dissolved’ and ‘total dissolvable’ fractions represent their partition at the time of filtering rather than in the water column at the time of sampling. In the case of Fe, the formation of pFe from dFe is rapid enough that consideration must be given to the likely artefacts that arise from the delay between sampling and filtering times.

Samples were stored in the Niskin bottles for between 2 to 7 hours before they were filtered. Samples were filtered in the order that they had been collected, to minimise the storage time before filtration.

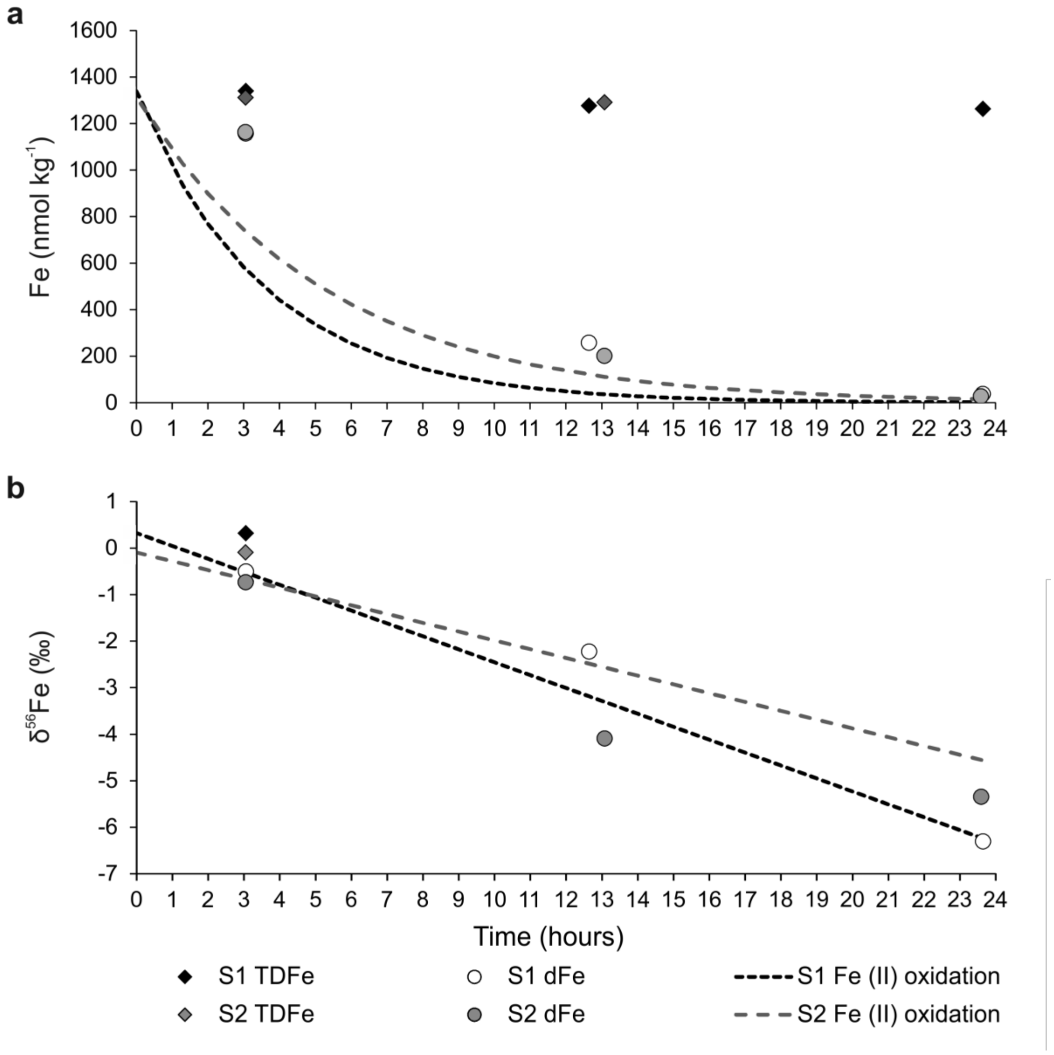

Figure 4.4 Observed and predicted behaviour of (a) dFe and TDFe concentration and (b) dFe isotope composition (δ56dFe) for two samples (S1 and S2) sub-sampled intermittently from their Niskin bottles over 24 hours. Predicted concentrations (dashed lines) assume dFe is comprised of Fe(II), Fe (II) oxidation half-life is 2.50 (S1) and 3.67 (S2) hours (Appendix E, Table E1). It is also assumed that all TDFe was present as dFe at the time of sampling (t = 0), so predicted dFe concentrations are a maximum possible estimate. The predicted trends in δ56dFe (dashed lines) assume dFe is comprised of Fe(II) and follows the same oxidation rates using a Rayleigh equation and fractionation factor of 1.0009 between ferrihydrite and Fe(aq) (Bullen et al., 2001).

Several samples were taken sequentially from two recovered Niskin bottles over a period of 24 hours to study the rate of Fe precipitation within the sampling bottles and its influence on δ^{56}dFe (Figure 4.4). The measured dFe concentration in both samples decreased significantly over 24 hours from 1160 nM to 27-37 nM, while TDFe concentrations were quasi-stable between 1350 and 1200 nM (Figure 4.4a). The stability of TDFe over time confirms only minor loss of TDFe from the system over time. This is likely to be the result of particles becoming trapped in or beneath tap fittings on the Niskin bottle.

Following the approach of Field and Sherrell (2000) and Bennett et al. (2009), the average Fe(II) oxidation half-life in the plume at E2 was calculated to be 3.67 hrs (Appendix E, Table E1). However, this may range from 1.45-5.63 hours, if input parameters from background Scotia seawater (Hawkes et al., 2013a) or samples taken directly over the vent chimney are used instead. Measured dFe concentrations in the two Niskin bottles were always higher than the Fe(II) concentrations predicted from Fe(II) oxidation kinetics (Figure 4.4a), which may result from a partial presence of Fe(III) oxyhydroxide nanoparticles or colloids in the dFe pool. In accord with dFe oxidation to Fe(III), δ^{56}dFe also decreased from -0.50 and -0.74 ± 0.05 ‰ to -6.30 ± 0.05 ‰ and -5.35 ± 0.08 ‰, compared to δ^{56}TDFe compositions of 0.32 and -0.10 ± 0.05 ‰.

A delay of 2 to 7 hrs between sampling and filtration corresponds to roughly one to two Fe(II) oxidation half-lives. For the purposes of our discussion, it is assumed that sample aging within the Niskin bottles is analogous to plume aging in the water column with the caveat that oxidation of Fe in the water column may occur more quickly as plume waters are continuously mixed with oxic seawater. Furthermore the dFe isotope composition can be compared to the mineralogical composition of pFe filtered from the Niskin bottles in order to assess how precipitation of Fe mineral particles influences dFe isotope composition and how this relates to the dFe isotope composition of the *in-situ* plume.

4.3.5 Hydrothermal particle composition

The mineralogy of hydrothermal particles can be examined indirectly using chalcophile elements that also form sulphides, and the particle-reactive element vanadium (V), which is sensitive to scavenging by Fe oxyhydroxides. The oxyanion VO_4H^{2-} is co-precipitated and scavenged at constant molar ratios by Fe oxyhydroxides depending on the local phosphate concentration (Feely et al., 1998) and this relationship can be used calculate the fraction of pFe present as Fe oxyhydroxides.

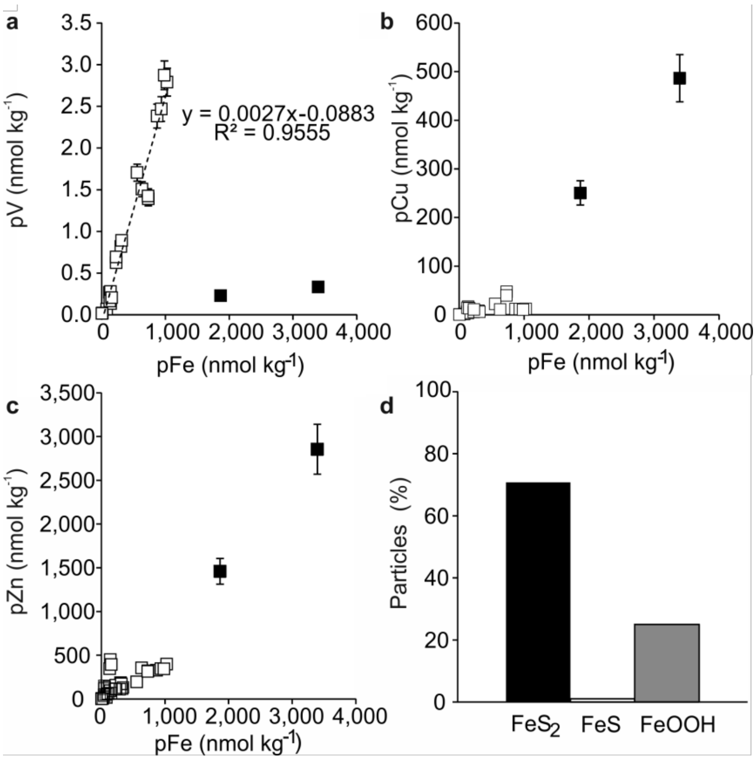

Figure 4.5 Concentration of (a) pV, (b) pCu and (c) pZn relative to pFe in the buoyant plume above the E2. Outliers (excluded from the linear regression) are highlighted in black, and are consistent with the presence of Fe sulphide minerals in an otherwise Fe oxyhydroxide dominated hydrothermal plume. Composition of particles (n = 24) collected on SAPS filters directly over the vent (similar depth and temperature as black points in a, b and c) show (d) that the main Fe sulphide mineral is pyrite (FeS_2); see Appendix E for further details.

Concentrations of particulate V (pV) and Fe (pFe) were positively correlated in the buoyant plume (r^2 = 0.955), for all but two of the highest concentration samples near the vent chimney (Figure 4.5a), indicating the widespread occurrence of Fe oxyhydroxides. The outliers in Figure 4.5a also contained the highest concentrations of particulate chalcophile elements (Figure 4.5b and 5c), suggesting that the particle contained significant Fe sulphides.

The ratio of pV/pFe in the E2 buoyant plume was 3.0 x10^{-5}, and much lower in the sulphide dominated outliers (0.1 x10^{-5}). The pV/pFe ratio observed in other Atlantic hydrothermal plumes is highly variable, 1.0-30 x10^{-5} (Feely et al., 1998, Bennett et al., 2009), whereas similar values (2.9-3.0 x10^{-5}) are observed over the East Pacific Rise (EPR) and also Juan de Fuca Ridge (JdFR; 2.3-2.8 x10^{-5}) (Feely *et al.*, 1998). Thus the pV/pFe ratios measured in particles over E2 are more similar to plumes from the EPR and JdFR than sites in the Atlantic Ocean, perhaps indicative of the similarity of Fe particle-forming processes between these regions. Alternatively, such similarities could result from the V/Fe ratios in vent fluids from these regions, although variable input of V is not considered to have a significant effect on pV/pFe in the plume (Trefry and Metz, 1989). Overall the strong correlation between pV/pFe suggests that the formation of Fe oxyhydroxides is the main Fe particle forming process throughout the rising plume over E2. This study observed higher ratios of pCu/pFe and pZn/pFe than previously observed in a hydrothermal plume. The E2 plume has pCu/pFe of 8-14 x10^{-2}, compared to previous observations in the Atlantic and Pacific Oceans of 0.3-8 x10^{-2} (German et al., 1996, James and Elderfield, 1996, Edmonds and German, 2004, Bennett et al., 2009, Feely et al., 1994a). Particulate Zn was also enriched with respect to pFe at E2, where pZn/pFe was 19-310 x10^{-2}, compared to 0.1-29 x10^{-2} from Atlantic and Pacific Ocean sites (Bennett et al., 2009, German et al., 1991, Edmonds and German, 2004, Feely et al., 1994a). The abundance of chalcophile elements at E2 means they serve as a particularly sensitive indicator of sulphide precipitation in the near vent region of the buoyant plume to support our interpretation of the Fe particle forming processes during plume mixing and dispersal.

4.3.6 Fe isotope composition of TDFe and dFe

Dissolved Mn concentrations can be used to trace the dilution of hydrothermal vent fluids by seawater because its behaviour is quasi-conservative on the time-scales of plume rise, except for a minor amount of scavenging to Fe oxyhydroxide particles (Cowen et al., 1990, James and Elderfield, 1996, Field and Sherrell, 2000). In general, as the plume becomes more dispersed (and hence the dMn concentrations decrease) δ^{56}TDFe values become heavier, with the vent-proximal plume containing δ^{56}TDFe of -0.31 ± 0.03 ‰ and the more dispersed plume containing δ^{56}TDFe of 0.78 ± 0.05 ‰ (Figure 4.6b.).

The δ^{56}Fe of dFe (δ^{56}dFe) in plume samples ranged from -2.39 ± 0.05 ‰ to -0.13 ± 0.05 ‰, and indicates dFe was fractionated towards lighter values during plume dilution and dispersal (Figure 4.6b.). The difference between δ^{56}dFe and δ^{56}TDFe (here after referred to as $\Delta^{56}\mathrm{Fe}_{d\text{-}T}$) is consistently negative because δ^{56}dFe was always lighter than the corresponding δ^{56}TDFe (Figure 4.6b). $\Delta^{56}\mathrm{Fe}_{d\text{-}T}$ ranged from -0.11 ± 0.04 in the vent-proximal plume to -2.13 ± 0.07 ‰ in the dispersed plume (Figure 4.6c). Hence the degree to which Fe isotopes were fractionated between the dFe and TDFe samples was also a function of plume dispersal.

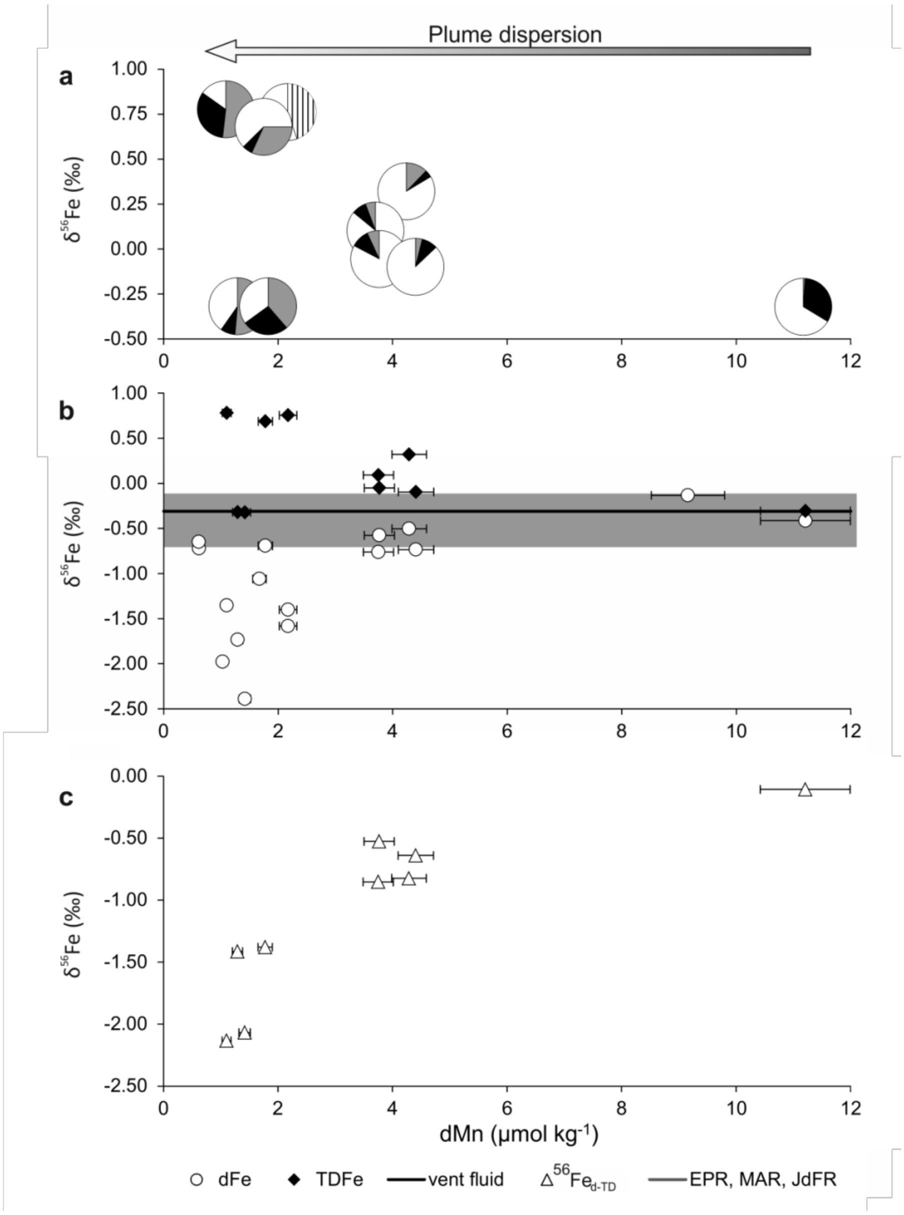

Figure 4.6 (a) abundances of dFe (white) pX_{FeS2} (black) and pX_{FeOOH} (grey) within TDFe, vertical lines indicate no data for composition of particle fraction (see section 4.4.2 equations (4.2) and (4.3)), (b) isotopic composition of dFe and TDFe, (c) difference in isotopic composition of dFe and TDFe ($\Delta^{56}Fe_{d\text{-}TD}$), as a function of plume dMn, which can be used as a proxy of plume dispersion. Position of pie charts in A corresponds to position of TDFe in b. The grey line in panel B represents the range of δ^{56}TDFe values of vent fluids measured in previous studies (Sharma et al., 2001, Beard et al., 2003, Severmann et al., 2004, Rouxel et al., 2008, Bennett et al., 2009). The black line represents the δ^{56}TDFe value of the hydrothermal vent source at the Dog’s Head chimney on the E2 vent field.

4.4 Discussion

4.4.1 Fe(II) oxidation and isotope fractionation in the buoyant plume

The main process by which dFe is removed from hydrothermal plumes is the oxidation of Fe(II) to Fe(III), where the resultant precipitation of Fe oxyhydroxides will contribute to the pFe and TDFe phases. Redox transformations impart a significant isotopic fractionation to Fe (Bullen et al., 2001), hence the oxidation of dissolved Fe(II) is expected to be the main process that controls the isotope composition of dissolved and particulate Fe fractions in hydrothermal plumes.

The rate of Fe oxyhydroxide formation in the plume is controlled by the production of Fe(III) from Fe(II) supplied from the highly-reducing vent fluids. Fe(III) forms Fe oxyhydroxide colloids (<0.2 μm), which subsequently aggregate to form Fe oxyhydroxide particles (>0.2 μm) that are collected on the filter during filtration (Schwertmann *et al.*, 1999). Experimental and theoretical studies show that oxidation of $Fe(II)_{(aq)}$ favours production of isotopically heavier $Fe(III)_{(aq)}$ (Anbar et al., 2005, Bullen et al., 2001, Welch et al., 2003, Wu et al., 2011c). Precipitation of $Fe(III)_{(aq)}$ as Fe oxyhydroxides also favours the heavier isotopes of Fe via a kinetic isotope fractionation mechanism, which depends on the rate of mineral precipitation (Skulan *et al.*, 2002) and the exchange of Fe on the mineral surface (Icopini et al., 2004, Mikutta et al., 2009, Teutsch et al., 2005). Due to rapid equilibration between $Fe(II)_{(aq)}$ and $Fe(III)_{(aq)}$ within 150-300 seconds (Welch et al., 2003), and the instability of $Fe(III)_{(aq)}$ it is expected that oxidation of $Fe(II)_{(aq)}$ will contribute isotopically heavier Fe oxyhydroxides to the pFe fraction leaving the remaining Fe(II) in the dFe fraction isotopically light.

The assumption of an entirely ferrous and aqueous dFe fraction, however, is a simplification of reality. In the 24 hour plume aging experiment, this study recorded a slower drop in dFe concentration over time than predicted by the oxidation kinetics of Fe(II) (Figure 4.4a). Additionally, the range of oxidation half-lives calculated throughout the plume (Appendix E, Table E1) is slow compared to previous observations from the Atlantic Ocean, which ranged from 17 to 27 min (Field and Sherrell, 2000), meaning our reported discrepancy between observed and predicted dFe is probably conservative. Clearly, the assumed aqueous Fe(II) oxidation to form particulate Fe oxhydroxides is unable to fully account for our observed concentrations of dFe.

Recent work has shown that 80 % of the dFe in a hydrothermal plume over the MAR was indeed present as Fe(II) (Sedwick *et al.*, 2015), however up to 82-96 % of dFe was present as colloids (Fitzsimmons et al., 2014). Previous work on the E2 plume has also shown that 47 ± 26 % of Fe is present as colloids and 7.5 % of all hydrothermal Fe is stabilised by organic ligands (Hawkes et al., 2013a). Therefore, using Fe(II) oxidation half-life from the bottle experiments it can be reasoned that $Fe(II)_{(aq)}$ was likely to represent just 50-63 % of the initial dFe measured in our bottle experiments (Figure 4.4a). This suggests that the dFe comprises of a mixture of aqueous Fe(II), Fe complexed by organic ligands, and colloidal Fe(III) oxyhydroxides.

Nonetheless, δ^{56}dFe in our 24 hour bottle experiments is similar to the Fe isotope composition predicted from the Rayleigh equation and fractionation factors attributable to Fe oxyhydroxide formation after Bullen et al. (2001) (Figure 4.4b). A good fit to the Rayleigh equations indicates any Fe sulphide nanoparticles or organic ligands present in the dFe pool were apparently of little significance for shifting the isotopic composition of dFe in the early plume samples used in these experiments at E2.

4.4.2 TDFe isotope composition and FeS_2 precipitation in the buoyant plume

Values of δ^{56}TDFe represent the mass balance of both particulate and dissolved fractions in the water column. Therefore, δ^{56}TDFe is insensitive to internal isotope fractionations between dFe and pFe pools, unless one of these pools is physically separated from the other. In this instance, δ^{56}TDFe will reflect the revised isotopic composition of its modified mass. Physical mixing processes in the plume are capable of inducing changes to δ^{56}TDFe, e.g., loss of pFe from the buoyant plume by particle aggregation and gravitational settling or more complex dispersion of particles according to their densities within the buoyant plume. A loss of isotopically light pFe from the buoyant plume is required to explain our observed values of δ^{56}TDFe, which become isotopically heavier relative to the plume source during dispersal (Figure 4.6b).

Fe oxidation does not provide the required fractionation, but low temperature experimental studies demonstrate there is a kinetic isotope fractionation during Fe sulphide precipitation, which favours reaction with lighter Fe isotopes (Butler et al., 2005, Polyakov et al., 2007, Rouxel et al., 2008), and produces isotopically light Fe sulphide particles. Large (>20μm) Fe sulphide aggregates (Carazzo et al., 2013, Feely et al., 1994k, Mottl and McConachy, 1990, Yucel et al., 2011) are more likely to settle out of the water column during buoyant plume rise and remove isotopically light pFe to nearby sediments.

The fraction of pFe present as sulphides and oxyhydroxides can be estimated from the relationship between pV/pFe and dissolved phosphate (Bennett et al., 2009) in order to re-construct how the change in sample composition influences δ^{56}TDFe. Dissolved phosphate scavenges onto Fe oxyhydroxides at constant molar ratios (Feely et al., 1996, Sands et al., 2012). The concentration of dissolved phosphate in the East Scotia Sea is 2.15 μM (Hawkes et al., 2013a). Using the linear relationship in Feely et al. (1998) an expected P/Fe ratio of 0.16 can be calculated. The inverse relationship between P/Fe and V/Fe in Feely *et al.* (1998) for Fe oxyhydroxide particles from different vents can be used to calculate the expected pV/pFe for the Fe oxyhydroxide particles in the plume over Dog's Head. The fraction of Fe oxyhydroxide (pX_{FeOOH}) and Fe sulphide particles (pX_{FeS2}) collected on filters is then calculated from equations (4.2) and (4.3):

$$pX_{FeOOH} = (pV/pFe)_{measured} / (pV/pFe)_{expected} \tag{4.2}$$

$$pX_{FeS2} = 1 - pX_{FeOOH} \tag{4.3}$$

As pX_{FeS2} decreases and pX_{FeOOH} increases δ^{56}TDFe moves from -0.31 ± 0.03 ‰ to 0.69 ± 0.05 ‰ with the exception of the two TDFe samples with the lightest δ^{56}TDFe (Figure 4.6a dMn <2 nmol kg^{-1}), which are offset by the lightest δ^{56}dFe values. Samples taken in the black smoke of the hydrothermal plume using the ROV *Isis* had an average pX_{FeS2} of 0.31 ± 0.03 ($n = 4$) when normalised to TDFe concentrations. This suggests that in the early stages of buoyant plume rise 31 % of the Fe from the hydrothermal vent precipitates as FeS_2. Assuming that most of this FeS_2 is removed by settling to sediments, the isotopic fractionation can be calculated using the Fe isotope fractionation factor of $\alpha_{FeS\text{-}Fe(II)}$ 0.9992 from Butler et al. (2005). Removal of 31 % of initial TDFe in the vent fluid as FeS_2 would shift the vent proximal plume from δ^{56}TDFe -0.31 ± 0.03 ‰ towards δ^{56}TDFe of 0.06 ‰. This predicted value is broadly intermediate within the range of observed δ^{56}TDFe values in the buoyant plume (Figure 4.6b). In summary the δ^{56}TDFe of the plume generally shifts towards heavier values, which are dependent on the balance between the amount of particulate FeS_2 and FeOOH. Isotopically light FeS_2 particles are denser than FeOOH and therefore more likely to settle out of the water column faster as the plume is dispersed. As a result the δ^{56}TDFe of the plume becomes isotopically heavier relative to the vent source.

4.4.3 Isotope composition of dFe and effects of Fe oxyhydroxide precipitation

The presence of Fe oxyhydroxides in particulate samples (equation 4.2) is used to evaluate controls on δ^{56}dFe in the buoyant plume during mixing and dispersal. Our buoyant plume samples will represent both lateral and vertical patchiness inherently attributed to the rapid and dynamically mixing plume environment. As such, even simple and well-defined reaction pathways are likely to be observed with a degree of scatter in vertical transects derived from *in-situ* hydrothermal plume sampling. Nonetheless, the wide range of pX_{FeOOH} (<0.05 to >0.95) indicates sampling by the ROV *Isis* successfully resolved the onset and almost full extent of particle formation and the corresponding influence on δ^{56}Fe during buoyant plume dispersal.

The decrease in δ^{56}dFe (-0.41 ‰ to -1.98 ‰) accompanied by increasing pX_{FeOOH} (Figure 4.7) is consistent with the decreasing δ^{56}dFe during plume dispersal as described by dMn (Figure 4.6b), where more dispersal equates to longer timescales of oxidation and the formation of more Fe oxyhydroxides. The trend in decreasing δ^{56}dFe is evaluated using a Rayleigh equation and the $\alpha_{ferrihydrite\text{-}(aq)Fe}$ value of 1.0009 calculated from experiments by Bullen et al. (2001), and derive three mineral precipitation scenarios for comparison to our observations presented in Figure 4.7.

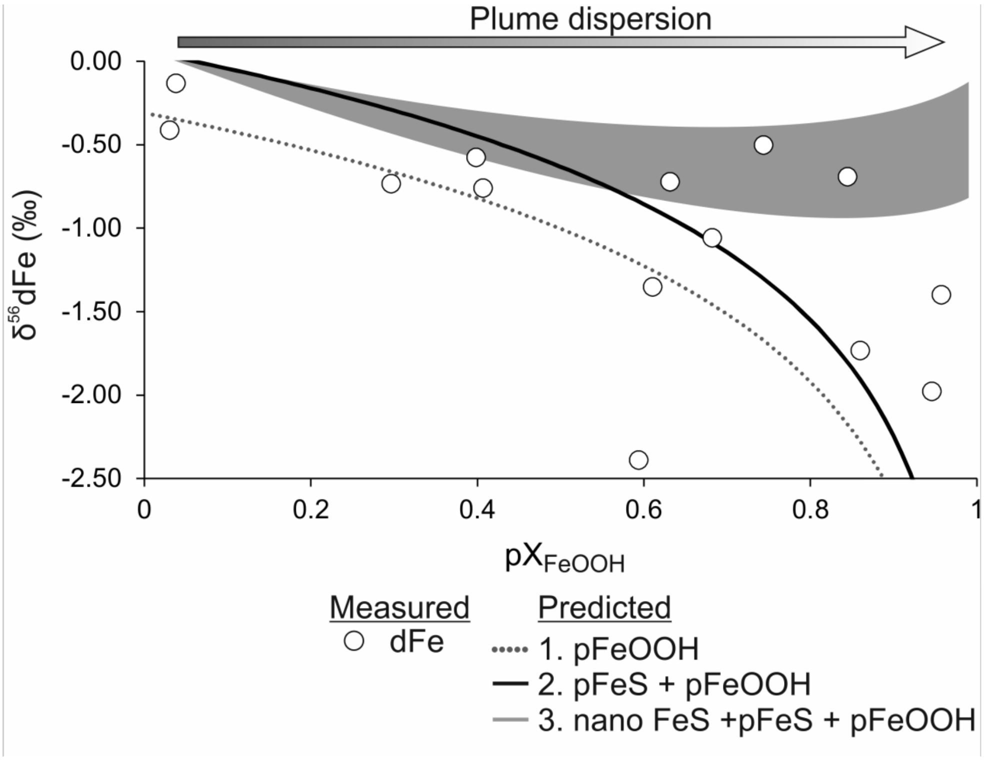

Figure 4.7 Isotope composition of dFe (circles) relative to the proportion of Fe oxyhydroxides (pX_{FeOOH}) in the particulate fraction. The evolution of the isotopic composition of dFe due to precipitation of different minerals is also plotted for comparison. Scenario 1 (grey dotted line) is the calculated Rayleigh fractionation curve for precipitation of dFe as Fe oxyhydroxide particles from a vent end-member δ^{56}TDFe of -0.31 ‰, and fractionation factor ($\alpha_{ferrihydrite\text{-}(aq)Fe}$) of 1.0009 from Bullen et al. (2001) (equation E1). Scenario 2 (black solid line) is the same as 1 except a source composition of 0.06 ‰ that accounts for removal of 31 % of the vent fluid Fe as FeS_2 particles (see section 4.2) (equation E2 and E3). Scenario 3 (black dashed line) is calculated from mass balance assuming that Fe isotopes are fractionated the same as in scenario 2 but a fraction of dFe is present as stablilised dFe with an isotope composition of -0.09 to -0.79. Stabalised dFe is initially only 1% of dFe but as pX_{FeOOH} increases and dFe (III) is consumed by production of pFeOOH the inert stable dFe fraction increases to 99 % of dFe (equation S4). See Appendix E for full details.

In the first scenario, precipitation of Fe oxyhydroxides from the vent source provides a reasonable fit to the lower bounds of δ^{56}dFe observed (Figure 4.7 & equation S1). The second scenario provides an improved fit to the observed data. Vent-proximal plume dFe was partially (31%) precipitated as Fe sulphide and served to shift δ^{56}TDFe of the vent-proximal plume towards an isotopically heavier value of 0.06 ‰ before the onset of Fe oxyhydroxide formation (equation E2 & E3). These comparisons suggest that the early and partial removal of isotopically light dFe to Fe sulphides is needed to account for our observations of δ^{56}dFe at E2.

In the third scenario, consideration is given to the influence of FeS_2 nanoparticle formation in the plume, which might also be analogous to other kinetically stable forms of dFe. Scenario three assumes the same sulphide and oxyhydroxide reactions as scenario two. Fe isotopes are also fractionated as they are in scenario two, however, a portion of dFe is now present as a stable FeS_2 nanoparticle with an δ^{56}dFe between -0.09 to -0.79 ‰ (equation S4). These values of -0.09 to -0.79 ‰ were chosen as -0.09 ‰ was the isotope composition calculated from mass balance of δ^{56} TDFe and δ^{56}dFe in the near vent sample where the pFe was entirely FeS_2 particles (Figure 4.6a) and -0.79 ‰ the FeS_2 isotope composition expected from kinetic fractionation of the vent fluid end-member value of -0.31 ‰ with 31 % pyrite formation. This range is within the breadth of δ^{56}Fe values measured for pyrite in high temperature and low temperature hydrothermal samples (Rouxel et al., 2008, Bennett et al., 2008). Given that the mechanics of FeS_2 nanoparticle formation are not fully understood this range covers the possibility that FeS_2 nanoparticles may have a δ^{56} Fe that reflects equilibrium fractionation as a result of formation at high temperature at the point of venting (Rouxel et al., 2008, Syverson et al., 2013) or a δ^{56}Fe that reflects low temperature kinetic fractionation (Bennett et al., 2009).

In scenario three, the fraction of dFe present as FeS_2 nanoparticles is set to increase from 1 to 100 % to mimic the buoyant plume evolution. In the early stages of mixing, FeS_2 nanoparticles represent a small fraction of dFe, but as Fe minerals continue to precipitate from dFe and settle out of the plume, other species are continually removed from the dFe pool, until only the stable FeS_2 nanoparticles remain. The isotope composition predicted by scenario three forms an envelope, which is isotopically heavier than most of the measured

δ^{56}dFe values, yet it provides a good description of upper bounds of the δ^{56}dFe values in the buoyant plume, and suggests the partial presence of FeS_2 nanoparticles may account for the deviations towards heavier values of δ^{56}dFe than predicted in scenario two.

Consistent with experimental work (Bullen et al., 2001, Welch et al., 2003, Butler et al., 2005) and the isotope composition of particulate Fe in hydrothermal plumes (Bennett et al., 2009, Severmann et al., 2004), our results show that Fe oxyhydroxide precipitation produces lighter values for residual δ^{56}dFe, while the respective δ^{56}TDFe is isotopically heavier due to the preferential settling of isotopically light Fe sulphide minerals from the TDFe pool during plume dispersal (Figure 4.6a,b). This means that after the isotope composition of the vent fluid is offset by FeS_2 precipitation, the isotope composition of dFe exported from the plume is largely dictated by the extent to, which Fe oxyhydroxide particles form. Due to the amount of scatter in measured dFe isotope composition relative to the modelled fractionation curves it cannot be said definitively whether or not complexation of dFe by organic ligands or the formation of nanoparticles have an influence on δ^{56}dFe. Based on the residuals of δ^{56}dFe relative to calculated fractionation lines (scenario 1 and 2 in Figure 4.7 and Figure 4.4b), between 14 to 27 % of the Fe isotope fractionation may result from the formation of nanoparticle/ligand complexed species and/or re-dissolution of particles relative to the overall effect from Fe oxyhydroxide and pyrite formation.

4.4.4 dFe exported to the neutrally buoyant plume and deep ocean

The trends in δ^{56}dFe are explained best by precipitation of Fe sulphides and Fe oxyhydroxides in the buoyant plume (scenario two, Figure 4.7). This suggests that the formation of Fe sulphide particles has an influence on the δ^{56}dFe of the hydrothermal plume by immediately offsetting the δ^{56}Fe of the vent fluid source in the initial stages of plume rise.

The δ^{56}Fe of pFe in buoyant plumes studied previously ranges from -0.31 to -0.7 ‰ for pFe sourced from the Red Lion vent (Bennett et al., 2009) and 0.24 to 1.28 ‰ for pFe sourced from the Rainbow hydrothermal vent (Severmann et al., 2004). In both cases the δ^{56}pFe was heavier than the δ^{56}dFe measured in this study, which is in the range -0.13 to -2.39 ‰. There was some overlap between the δ^{56}dFe results of this study and δ^{56}pFe measured by Bennett et al. (2009) but particles measured in their study covered a smaller range of pX_{FeOOH} from 0.34 to 0.69 whereas pX_{FeOOH} in this study ranged from 0.03 to 0.95. If δ^{56}pFe from Bennett et al. (2009) is compared to δ^{56}dFe from this study across the same range of pX_{FeOOH} then the range of δ^{56}dFe is narrowed to -0.58 to -2.39 ‰, which is isotopically lighter than δ^{56}pFe in the Red Lion plume.

Bennett et al. (2009) also calculated δ^{56}dFe from mass balance using δ^{56}pFe and estimate that during buoyant plume dispersion δ^{56}dFe would increase from the vent fluid end-member of -0.29 ± 0.05 towards a value of 0.8 ± 2.2 ‰. These estimates are contrary to our results that show δ^{56}dFe getting isotopically lighter as the plume is dispersed and not heavier. The estimates made by Bennett et al. (2009) also assume that the δ^{56}TDFe of the plume remains constant during plume dispersion whereas our results show δ^{56}TDFe varies significantly in the buoyant plume most likely due to heterogeneous dispersion and settling of pFe. This is the reason why our observed δ^{56}dFe differ from the calculated δ^{56}dFe of Bennett et al. (2009).

A transect of δ^{56}dFe measurements through the North Atlantic intersected a hydrothermal plume over the Mid-Atlantic Ridge with δ^{56}dFe in this region ranging from -0.92 to -1.35 ± 0.03 ‰ (n = 5) (Conway and John, 2014f). This observation of isotopically light dFe is in agreement with our conclusions that hydrothermal δ^{56}dFe is isotopically light relative to the bulk silicate Earth. This study shows a greater range of values than the ocean section data, due to the greater sampling resolution of the hydrothermal plume in this study where for δ^{56}dFe n = 17. Using a mass balance approach and a hydrothermal end-member of -1.35 ‰ Conway and John (2014f) successfully re-produced observed δ^{56}dFe in the N. Atlantic and estimate that 2.3 % of dFe in the N. Atlantic is derived from hydrothermal vents. The controls on plume Fe isotope fractionation revealed from the results presented in this study indicate that the isotopically light hydrothermal end-member needed to reproduce the observed δ^{56}dFe in the N. Atlantic is the result of Fe oxyhydroxide precipitation in the buoyant plumes of the N. Atlantic (Conway and John, 2014f).

The difference between the range of δ^{56}dFe from the E2 plume and the N. Atlantic (Conway and John, 2014f) could also be explained by the higher Cu/Fe (0.028) and Zn/Fe (0.02) ratios in the Dogs Head vent fluid relative to those of vents found on the MAR (0.005, 0.01 and 0.006-0.13) (Bennett et al., 2009, Edmonds and German, 2004, German et al., 1991). Lower concentrations of Cu and Zn in MAR vent fluids may result in more Fe sulphide precipitation in the overlying plume, which would shift the δ^{56}dFe exported from the buoyant plume towards heavier δ^{56}dFe values. In contrast, higher concentrations of Cu and Zn relative to Fe in vent fluids from Dog's Head may result in less Fe sulphide precipitation and therefore, more Fe is converted to Fe oxyhydroxides resulting in a lighter δ^{56}dFe in the E2 plume. This suggests that differences in chemistry of vent fluids and Fe(II) oxidation rates in ocean basins influence the degree to, which Fe isotopes are fractionated between pFe and dFe in plumes. This would result in unique Fe isotope signatures of dFe exported from hydrothermal plumes in different ocean basins.

The δ^{56}dFe values measured in this study demonstrate that Fe isotopes in the hydrothermal plume are fractionated initially by precipitation of FeS_2 particles and subsequently by continual oxidation of Fe(II) to Fe(III) and the formation of Fe oxyhydroxides. Enclosing the plume samples within Niskin bottles is likely to slow Fe(II) oxidation compared to the *in-situ* plume but the aggregation of colloidal Fe oxyhydroxides may have been encouraged as the turbulent mixing of plume waters are continually dispersed *in-situ* making the aggregation of Fe oxyhydroxide colloids less likely. Based on the observations of how δ^{56}dFe is fractionated in samples, the *in-situ* Fe isotope composition of dFe exported to the NBP at E2 can be calculated from the measured δ^{56}TDFe of the vent proximal plume. Such a calculation uses known fractionation factors (Bullen et al., 2001, Butler et al., 2005), an estimated plume rise time and the calculated Fe(II) oxidation half-life (Appendix E Table E1 and E4). The plume rise time is important as this dictates the amount of time for vent fluid Fe(II) to be oxidised to Fe(III) in the buoyant plume. Speer and Rona (1989) calculated that the rate of plume rise for both Pacific and Atlantic hydrothermal plumes was 0.1 m s^{-1}. Assuming this is also the same at E2, which rises 245 m (Figure 4.2), a rise time of 0.68 hrs can be estimated. Using the Fe(II) oxidation half time calculated for Scotia Sea deep water (1.38 hrs, Appendix E, Table E1) it is predicted that 71 % of dFe may still be present as Fe(II) when the hydrothermal plume reaches a height of neutral buoyancy. If 31 % of vent-derived dFe is precipitated as Fe sulphide particles during BP rise (as described in section 4.2), a residual 69 % of vent-derived dFe remains as dFe(II). From our Fe(II) NBP calculation 29 % of the remaining vent derived dFe is oxidised to Fe(III) during plume rise a large fraction of which is removed from the dissolved fraction by formation of Fe oxyhydroxide particles with potentially a small amount persisting as colloids.

Using the Rayleigh equations and fractionation factors from scenario two (Figure 4.7) the *in-situ* δ^{56}dFe supplied to the NBP will have a δ^{56}dFe composition of -0.28 ± 0.17 ‰ (represented schematically in Figure 4.8). The predicted δ^{56}dFe is similar to the δ^{56}TDFe of the vent proximal plume of -0.31 ± 0.03 ‰ as the processes of Fe sulphide and Fe oxyhydroxide formation have opposing, and in this instance, largely balanced effects during the course of BP dispersal. Such balanced isotope-fractionation processes may not occur in other ocean basins and at different vents where the extent of Fe sulphide and Fe oxyhydroxide formation will vary. Furthermore, continual physiochemical processing of Fe in the NBP may impart further changes on the isotope composition of Fe in the dissolved pool.

The same prediction can be made for other vents to consider the implications of Fe-sulphide and Fe-oxyhydoxide authigenesis on the dissolved Fe isotope composition. Following our treatment of the E2 plume, the δ^{56}dFe of the NBP for Rainbow and TAG (N. Atlantic), Red Lion (S. Atlantic) and 9 to 10°N (E. Pacific) are estimated to be -1.37 ± 0.22 ‰, -0.73 ± 0.77 ‰, -0.30 ± 0.25 ‰, 0.36 ± 0.84 ‰ respectively. These estimates vary between similar and very dissimilar and isotopically lighter values than their hydrothermal end-members (δ^{56}dFe of -0.14 ± 0.09 ‰, n = 10, -0.15 ± 0.07 ‰, n = 3 (Severmann et al., 2004); -0.29 ± 0.10 ‰, n = 6 (Bennett et al., 2009); -0.40 ± 0.14 ‰, n = 7 (Rouxel et al., 2008) (Appendix E, Table E4).

Further, pronounced changes in the authigenic mineral sinks of Fe released from hydrothermal vents may have occurred during perturbations in ambient ocean redox chemistry of the past ocean. These changes may be reflected in the δ^{56}Fe of hydrothermal sediments.

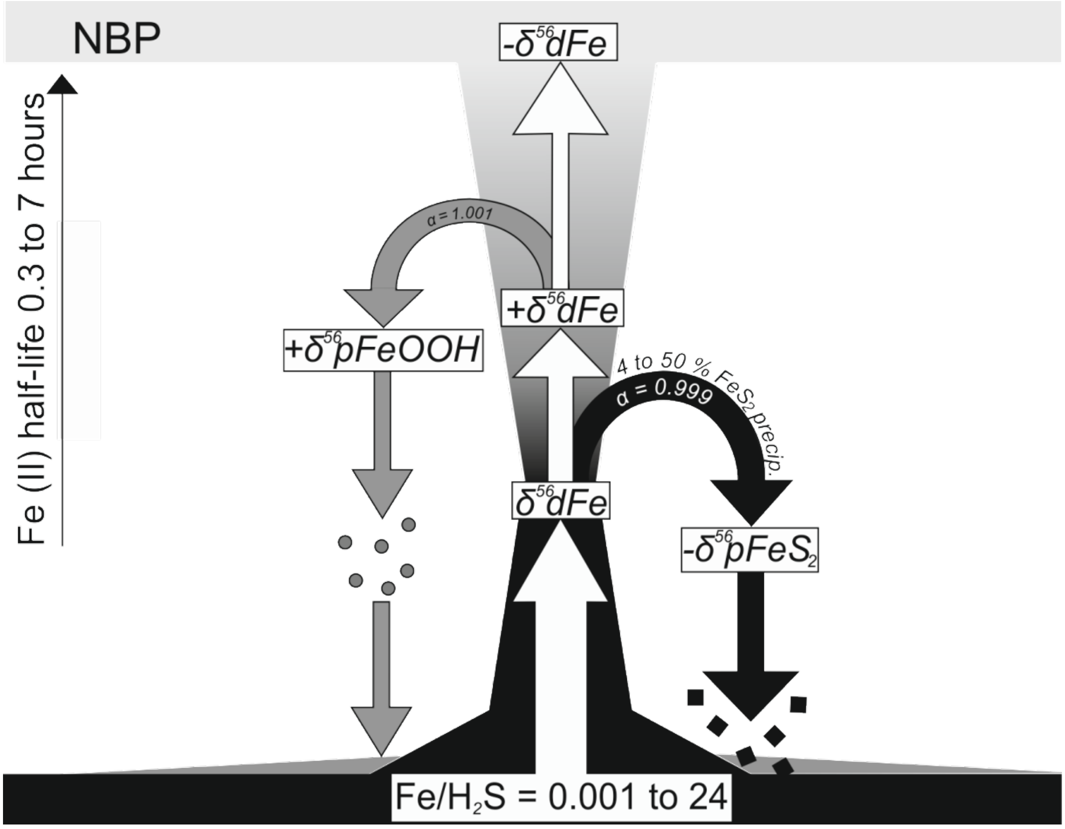

Figure 4.8 Schematic diagram of Fe isotope fractionation described in text and Appendix E. Positive and negative signs indicate enrichment in the heavier or lighter Fe isotope. The range of Fe (II) half-lives represents the global range for different oceans basins as calculated by Field & Sherrell (2000). Shapes represent mineral particles of FeOOH (grey) and FeS_2 (black). Arrows with fractionation factors (α) are associated with mineral particles of the same colour. Fe/H2S values represent the global range and the amount of FeS_2 precipitating is dependent on this (Bennett et al., 2009, Douville et al., 2002, Mottl and McConachy, 1990, Rudnicki and Elderfield, 1993, Severmann et al., 2004)

4.5 Conclusions

Published studies of Fe isotopes in hydrothermal plumes have only determined the isotope composition of pFe, which is expected to eventually settle out of the water column to hydrothermal sediments. The conclusion of previous studies was that Fe isotopes are fractionated during particle precipitation in the dispersing plume, which alters the plume δ^{56}pFe relative to the hydrothermal source.

In this study the Fe isotope composition of both δ^{56}dFe, and δ^{56}TDFe fractions was determined and compared to the bulk chemical composition of Fe particles in order to assess the processes leading to Fe isotope fractionation in a hydrothermal plume. If the vent fluid source and local seawater values are well constrained, the isotopically light δ^{56}dFe signature of hydrothermal plumes can be used to trace hydrothermal input in different ocean basins.

Evidence for Fe isotope fractionation by Fe sulphide precipitation was only observed in δ^{56}TDFe samples that were isotopically heavier than the δ^{56}TDFe of the vent fluid source, indicating that a fraction of isotopically light pFe must have been removed from the plume, most likely by rapid settling of large Fe sulphide particles.

After an initial offset to heavier values in early plume mixing, the δ^{56}dFe decreased during buoyant plume rise to values isotopically lighter than the δ^{56}Fe of the hydrothermal vent source, with δ^{56}TDFe getting heavier with plume dispersion as a result of continuous particle mixing and settling. The shift to isotopically lighter δ^{56}dFe during further dispersion and aging of the plume can be explained by precipitation of Fe oxyhydroxides. The isotopically light δ^{56}dFe values presented here are in agreement with the basin scale studies of δ^{56}dFe (Conway and John, 2014f) but they are not concordant with previous estimates of δ^{56}dFe calculated from plume mass balance and δ^{56}pFe (Bennett et al., 2009). This is because Bennett et al. (2009) base their prediction of δ^{56}dFe on the assumption that δ^{56}TDFe remains constant. This study shows that δ^{56}TDFe is highly variable due to complex mixing and settling of plume particles.

At the E2 hydrothermal site, δ^{56}dFe of stabilised dFe exported from the buoyant plume and further into the deep ocean has an inferred Fe isotope composition that is coincidentally isotopically similar to that of the initial hydrothermal vent fluid. If the balance of sulphide and oxide formation changes then the net impact on the Fe isotope composition will shift accordingly. This study highlights the need to resolve Fe isotopes fractionation at the boundary between the ocean and Fe source regions as the isotope signature of the Fe exported from the source can be dramatically altered from its source isotope composition upon entering the ocean. This is an important consideration for mass balance of Fe in the modern ocean and for using Fe isotopes to infer changes in the Fe cycle throughout past Earth history.

Chapter 5: Final conclusions & future work

5.1 Conclusions

This thesis has helped to further constrain the impact of hydrothermal venting on the biogeochemistry of the ocean-climate system. The role that trace metals play in regulating the draw-down of CO_2 from the atmosphere via the biological carbon pump remains a difficult aspect of global biogeochemistry to reproduce in global ocean climate models (Tagliabue et al., 2016). The uncertainty in future predictions of climate change can therefore be decreased by improving our knowledge of trace metal cycling. The work presented in this study has improved our understanding of the role hydrothermal vents play in global trace metal cycles. This was done by examining the processes that transform Fe as it is transported away from vents and the processes controlling the isotope signature of hydrothermal dFe so Fe isotopes can be used to quantify hydrothermal dFe input on an ocean basin scale.

The transition metal chemistry of vents along the MCSC is described in detail for the first time. Studying high temperature off-axis venting at sites such as the VDVF has improved our understanding of how off axis venting sites could be an important and previously unrecognised source of dissolved and particulate metals to the deep ocean. Sub-surface hydrothermal-seawater mixing is identified as an important controlling factor on the segregation of metals between venting fluid and particle fractions that add metals to the overlying plume. The importance of off-axis venting for global trace metal cycles depends on how widespread these types of vents are relative to “black smoker type” vents and to determine this more sensor transects are needed that search for plume signals away from the ridge axis. The use of novel redox sensors will also help detect the overlying plumes from these vent sites where the density of particles in the plume is too low to be easily detectable by particle sensors. The BVF site is one of the few sites with ultramafic lithologies to be investigated for its vent chemistry. Me/H_2S ratios of 5 were higher than basalt hosted vents (Me/H_2S ~1) but less than that of other ultramafic hosted vent sites such as rainbow ($Me/H_2S = 24$). The higher Me/H_2S ratio of BVF did not result in similar near vent particle compositions in comparison to rainbow, which suggests other factors such as venting temperature and rates of particle formation maybe just as important in dictating the composition of particles formed in the immediate stages of venting.

The differences in sFe, cFe and pFe separation between two hydrothermal plumes show that the processes controlling the separation of Fe between these different size fractions are different between vent sites. This could be a result of differences in the chemistry of the hydrothermal source. Current models of global hydrothermal dFe fluxes do not consider how any variations in the chemistry of the vent source will impact vent fluxes. The approach used in these models of assuming that a fixed percentage of hydrothermal dFe is stabilised by organic ligands in the ocean globally is similar to the mass balance approach used in section 3.4.5. The issue with this (as is discussed in section 3.4.5) is that at different vent sites the percentage of hydrothermal vent Fe exported to the deep ocean as colloidal and soluble Fe is very likely to be different depending on plume chemistry. Therefore assuming that the same percentage of hydrothermal dFe is stabilised by ligands throughout all hydrothermal plumes in the global ocean will cause systematic regional errors when trying to re-produce the distribution of dFe on a global scale. This issue can only be resolved by understanding the common chemical processes between vent sites that control the extent of colloid formation and ligand complexation. By examining the dispersion of sFe in the BVF hydrothermal plume this work has revealed that sFe behaves near-conservatively during dispersion of a "black smoker type plume". To date it is thought that Black smoker type plumes will make up the largest proportion of the hydrothermal dFe flux and are therefore the most important to constrain. If the near-conservative behaviour observed for sFe at BVF is similar across all "black smoker type plumes" then it makes the sFe flux from hydrothermal vents simple to constrain using current modelling techniques that determine dFe fluxes based on conservative hydrothermal tracers such as δ^3He. This also indicates that any variability in the flux of dFe from black smoker plumes is due to differences in non-conservative colloid behaviour between different sites during plume dispersion.

Previous to the work presented in this thesis there has been no data presented on how other trace metals maybe separated between soluble and colloidal fractions in a hydrothermal plume. One study examined the separation of Cu, Mn and Fe between 0.1µm and 0.4 µm size fractions (Sands *et al.* 2012) but this is not consistent with the size fractions typically used in oceanography of 0.02 µm and 0.2 µm used here to be consistent with other oceanographic and sedimentary studies of dFe (Homoky et al., 2011, Hawkes et al., 2013a, Fitzsimmons et al., 2014, Fitzsimmons et al., 2015). Other trace metals examined such as Zn, Cd, Co, Cu, Pb are all enriched in hydrothermal fluids to a lesser extent than Fe and removed in the early plume preferentially by metal-sulphide particle formation. This smaller difference between plume and seawater concentrations makes it more difficult to examine the processes controlling these metals from plume profiles alone. What is clear from this work is that a significant quantity of Zn and Pb appears to be present as colloids in hydrothermal plumes and the processes controlling the fluxes of all these metals will be strongly controlled by particle forming and scavenging processes. From the variability in plume profiles in these elements it is difficult to tell weather hydrothermal plumes will act as a source or sink of these metals in the ocean. The only other metal to show the similar "hot spots" of Fe and Mn in basin scale transect of the GEOTRACES program was Zn (Conway and John, 2014b, Roshan et al., 2016). Similar to Fe the presence of Zn and Fe sulphide nanoparticles in vent fluids is one possible mechanism that would explain the "hot spots" of Fe and Zn observed over the MAR (Conway and John, 2014f, Conway and John, 2014b). However other mechanisms including complexation of Zn by organic ligands could also explain this. To understand the role of metal sulphide nanoparticles in hydrothermal fluxes, the degree to which nanoparticles aggregate to form larger particles that then settle out of the water column needs to be quantified; however this is incredibly difficult to measure without new types of sensors sensitive to changes in particle size (Estapa et al., 2015). It is important to bear in mind that even if the flux of dissolved metals from vents to the ocean is equal to the removal by plume particles, differences in the soluble and colloidal fluxes could still have important implications for the speciation of metals in the ocean. For example if the flux of colloidal Zn-sulphide from vents is equal to the removal of sZn by plume particle scavenging then there would be no net gain or loss of dZn to the ocean but a net loss of sZn and a net gain of cZn-sulphide. Such a process could change the overall ratio of colloidal to soluble metals in the deep ocean without dramatically changing dissolved concentrations observed in a basin scale ocean profile. Changing the separation of metals between colloidal and soluble fractions in the deep ocean would likely impact its bioavailability to phytoplankton in the surface ocean therefore influencing nutrient limitation and carbon drawdown.

By measuring the Fe isotope composition of dFe and TDFe in a hydrothermal plume the processes that control the Fe isotope signature of hydrothermal dFe to the ocean have been identified. The Fe isotope signature of the hydrothermal plume was predominantly controlled by the balance between precipitation of Fe oxyhydroxides and Fe sulphide mineral particles in the plume. Using what was learned from the Fe isotope fractionation of the E2 plume I was able to use the published data from other vent sites to predict what the Fe isotope signature from hydrothermal plumes in different ocean basins might be. This will now make it much easier to identify hydrothermal inputs of dFe to the deep ocean using Fe isotopes. This will further improve our understanding of hydrothermal dFe fluxes in the modern ocean and over geological time.

These findings build upon on previous work that stresses the importance of the role hydrothermal vents play in the cycling of trace metals in the ocean. Based on this evidence all future global biogeochemical models should look to incorporate a hydrothermal dFe flux if they are to accurately simulate the relationship between dFe limitation and primary productivity in the ocean over decadal to millennial time scales. This will improve our understanding of how the global climate system has developed over geological time and how it may change in the future as a result of anthropogenic forcing.

5.2 Future work

There are several questions raised by this work that I was unable to address during the course of the PhD and should be the focus of future research. There is still a lot of uncertainty with regards to the role that biological processes in the plume that influence trace metal fluxes. This could be by direct uptake of metals by microorganisms in the plume or by the scavenging of metals from biological detritus. Quantifying the impact of biological processes on plume trace metal fluxes remains a key question, which may be of particular importance for plumes where the chemistry is not dominated by precipitation of inorganic mineral particles. This includes all areas of on and off-axis diffuse venting that likely covers a wider area of the seafloor compared to focused black smoker vents. Ligand speciation and incubations of organic matter recovered from diffuse sites could help further constrain how important biological processes are to the flux of metal from hydrothermal vents.

Speciation also remains a key question not only for hydrothermal settings but for sediments and freshwater inputs also. There are currently two methods used to investigate speciation of dFe in hydrothermal plumes. One is competitive ligand exchange cathodic stripping voltammetry, which is used to investigate ligand complexation (CLE-CSV). The other examines sulphide speciation by separating samples into acid volatile sulphide (AVS = H_2S, FeS) and chromium reducible sulphide (CRS = FeS_2). Studies using AVS-CRS have focussed on the near vent environment (Yucel et al., 2011) whilst studies using CLE-CSV focus on BP and NBP samples. It is still unclear as to how the presence of FeS_2 or Fe (oxy)hydroxide nanoparticles may influence results from CLE-CSV and likewise studies exclusively examining sulphide speciation do not take into account any organic ligand complexation. As a result the current conceptual models of dFe stabilisation in hydrothermal plumes are either one based on organic ligand chemistry or the inorganic chemistry of FeS_2 nanoparticles. What is needed is a method that bridges the gap between these two conceptual models as in reality there is likely to be an interplay between organic ligand complexation and inorganic nanoparticles. Organic carbon coatings and incorporation into the structure Fe (oxy)hydroxides studied in soils and sediments has shown that these processes can alter the physiochemistry of Fe (oxy)hydroxides and their reactivity with trace metals (Moon & Peacock 2013). Similar processes could be important in hydrothermal plumes and synchrotron x-ray methods used to examine larger particles (Toner *et al.* 2009) could be used to examine finer nano-particles. Finally the metal bearing dissolved species generated in plumes maybe further transformed during the processes of transport to the surface ocean and this will alter the bioavailability of any hydrothermal cFe and sFe. Bioavailability of any hydrothermal dFe species needs to be assessed to determine if the Fe in species such as FeS_2 is available as a micronutrient. This is crucial to further constrain how important hydrothermal dFe is as a nutrient and what impact it has on fertilizing the surface ocean.

The global flux of Fe estimated from hydrothermal plumes in Chapter 3 is in agreement with previous estimates with all estimates in broad agreement ± 10 mol yr^{-1}. This broad agreement in a hydrothermal dFe flux gives a mean global hydrothermal dFe flux of 2 x 10^9 mol yr^{-1} (n = 7) which is lower than the range of hydrothermal dFe fluxes currently used in biogeochemical models of 11 x 10^{9} to 17 x 10^9. It is clear from comparing current models to observations that a global average flux for Fe is not sufficient information to resolve the regional differences in hydrothermal dFe fluxes (Tagliabue et al., 2016). This is particularly important for constraining the impact of hydrothermal dFe on Southern Ocean primary productivity which will have the largest impact on export of atmospheric C to the deep ocean. Models using dFe/δ^3He that consider an amount of Fe ligand stabilization are better able to reproduce dFe ocean observations but globally this still leads to an overestimation of deep ocean dFe (Resing et al., 2015).

From the work presented in this thesis it is clear that the variability in plume processes between different vent sites will result in regional variations in the hydrothermal dFe flux. Future simulations of hydrothermal dFe should look to incorporate the regional variability in plume processes in order to further improve our estimates of how hydrothermal dFe impacts primary production in the surface ocean. In the first instance this could be done by making more measurements of dFe/δ^3He in plumes over ridges spreading at different rates in order to incorporate variability dFe of vent sources into current models of hydrothermal dFe based on δ^3He. Rather than assuming a mean dFe/δ^3He for vents on all ridges which ignores the range in vent fluid Fe concentrations possible from different geological settings. Furthermore, differences in the trends for sFe, cFe and pFe that are observed here we interpret to be a result of vent specific differences in particle aggregation and ligand stabilization. In order to improve simulations these processes need to be incorporated into models. The key to this is further detailed investigation into how colloidal aggregation rates and ligand stabilization varies between sites. Only after the biogeochemical controls on these processes has been parameterized can these processes be incorporated into models to resolve regional differences in the hydrothermal dFe fluxes. This will also apply to future attempts to simulate and better constrain hydrothermal Zn and Mn fluxes, with scavenging and ligand stabilization being more important for Mn fluxes as this is predominantly in the soluble fraction.

Appendices

Appendix A

Acid Cleaning Procedures at NOCS

Within the ocean the concentrations of trace metals are typically very low, and therefore a number of precautions must be taken during the sampling and analysis of the samples to avoid contamination. Any containers and equipment should be acid cleaned and when dealing with the samples a clean laboratory suit, gloves and hair net should be worn.

LDPE (Low density polyethylene) and Teflon bottles and Teflon vials

1. Soaked in Decon 90 for three days followed by a thorough rinse (3 times) with RO (reverse osmosis) water
2. A week long soak in 50% HCl, followed by a MQ rinse (3 times) (Ultra pure deionised water (>18.2 MΩ cm-1) dispensed from a Millipore Milli-Q system)
3. A week long soak in 50% HNO3 followed by a MQ rinse (3 times) and left to dry in a laminar flow hood

Teflon vials had an additional cleaning step, which was carried out after each use:

1. Soaked in 50% HNO3 and refluxed for 24 hours, followed by a rinse with MQ water
2. Filled with 3 M HCl and refluxed for 24 hours, followed by a rinse with MQ water and left to dry in a laminar flow hood.

Pipette Tips

1. Before use all pipette tips were rinsed 3 times with 40% HCl and then 3 times with MQ water.
2. After use all pipette tips were rinsed 3 times with MQ water.
3. All tips were saved for pipetting reagents, becoming cleaner over time the more they were rinsed. Tips used for samples were disposed of after use.

Appendix B

Regression statistics for vent fluids and particles

Significant trends identified by an r^2 >0.6 and a p value <0.05 as stated in text. The residuals from each regression were plotted to check for any patterns that would indicate a poor fit. The t-statistic for all regressions was also checked to ensure it was always within the 95 % confidence limit for the number of samples in the regression based on the values in (Miller and Miller, 2000). Any regressions with a t-statistic outside the 95 % confidence limit are rejected. Grey fill in tables below shows non-significant trends, bold text shows significant trends, which are presented in figures in Chapter 2. Where r^2 values are similar for two different regression types (e.g linear or exponential) the trend shown in figures was decided by selecting the regression with the lowest p-value. If r^2 and p-value were similar for different regressions a decision was made as to, which is presented in figures based on trends observed for other elements however this was rarely the case.

Vent fluid seawater mixing

Elements	r^2	p	Hypothesis: Mg and metal correlation from plume dilution	r^2	p	Hypothesis: Mg and metal correlation from plume dilution
	VDVF			BVF		
Ca/Mg*	**0.943**	**0.000**	**Accept**	**0.987**	**0.000**	**Accept**
Mn/Mg	0.065	0.478	Reject	**0.998**	**0.000**	**Accept**
Fe/Mg†	0.057	0.507	Reject	**0.995**	**0.000**	**Accept**
Ni/Mg	0.021	0.692	Reject	0.250	0.118	Reject
Co/Mg†	0.008	0.810	Reject	**0.899**	**0.000**	**Accept**
Cu/Mg†	0.057	0.505	Reject	0.732	0.007	Reject
Zn/Mg	0.066	0.622	Reject	**0.770**	**0.000**	**Accept**
Cd/Mg	0.075	0.443	Reject	**0.643**	**0.003**	**Accept**
Pb/Mg	0.078	0.435	Reject	**0.745**	**0.001**	**Accept**

*Samples not lying on conservative Ca/Mg Cl/Mg mixing line excluded as a result of chimney material contamination.

†Regression for BVF through Beebe 125 samples only

Association of metals in BVF vent fluids

		Linear		
BVF	Elements	r^2	p	Hypothesis: metals associated with same mineral phase
	Cu/Co	**0.996**	**0.000**	**Accept**
	Zn/Pb	**0.911**	**0.000**	**Accept**
	Zn/Cd	**0.936**	**0.000**	**Accept**

		Linear			exponential			log			2nd polynomial			power		
		r^2	p	H*	r^2	p	H*	r^2	p	H*	r^2	p	H*	r^2	p	H*
BVF	Mn/Fe*	**0.986**	**9E-08**	**A**	0.456	3E-02	R	0.385	6E-02	R	0.324	3E-01	R	0.570	1E-02	R
	Cu/Fe	0.314	1E-01	R	**0.726**	**2E-03**	**A**	0.156	3E-01	R	0.803	3E-03	R	0.630	6E-03	R
	Zn/Fe	0.629	6E-03	R	0.793	5E-04	R	0.677	3E-03	R	0.749	8E-03	R	**0.884**	5E-05	**A**
	Co/Fe	0.299	1E-01	R	**0.826**	**3E-04**	**A**	0.185	2E-01	R	0.818	3E-03	R	0.744	1E-03	R
	Pb/Fe	0.458	3E-02	R	0.662	4E-03	R	0.508	2E-02	R	0.614	4E-02	R	**0.762**	**1E-03**	**A**
	Cd/Fe	0.611	0E+00	R	0.823	3E-04	R	0.620	7E-03	R	0.649	3E-02	R	**0.883**	**5E-05**	**A**

*Beebe Woods excluded from regression as outlier for Mn/Fe due to diff. between r2 (0.53) and p-value (0.01) with this sample included in regression.

T-statistic outside 95 % confidence for 2nd poly through Zn/Pb, Zn/Cd, Cu/Co and for power through Cu/Co.

H* = Hypothesis: metals associated with same mineral phase as Fe and/or dilution effect, A = accept, R = reject

Association of metals in VDVF vent fluids

		Linear		
VDVF	Elements	r^2	p	Hypothesis: metals associated with same mineral phase
	Cu/Co	**0.943**	**0.000**	**Accept**
	Zn/Pb*	**1.000**	**0.000**	**Accept**
	Zn/Cd*	**0.999**	**0.000**	**Accept**

*less observations for Zn as some samples <l.o.d (n = 5)

		Linear			exponential			log			2nd polynomial			power		
		r^2	p	H*	r^2	p	H*	r^2	p	H*	r^2	p	H*	r^2	p	H*
VDVF	Mn/Fe	0.698	5E-03	R	0.484	4E-02	R	0.817	8E-04	A	0.723	2E-02	R	**0.865**	**3E-04**	**A**
	Cu/Fe	**0.983**	**2E-07**	**A**	0.460	4E-02	A	0.513	3E-02	A	0.986	3E-06	R	0.775	2E-03	A
	Zn/Fe	**0.994**	**2E-04**	**A**	0.844	3E-02	R	0.810	4E-02	R	0.996	4E-03	R	0.954	4E-03	A
	Co/Fe	**0.919**	**5E-05**	**A**	0.750	3E-03	R	0.329	1E-01	R	0.964	4E-05	R	0.263	2E-01	A
	Pb/Fe	**0.980**	**4E-07**	**A**	0.716	4E-03	A	0.426	6E-02	A	0.991	7E-07	A	0.730	3E-03	A
	Cd/Fe	**0.986**	**9E-08**	**A**	0.595	1E-02	R	0.445	5E-02	R	0.998	2E-08	A	0.876	2E-04	A

*less observations for Zn as some below l.o.d (n = 5)

T-statistic outside 95 % confidence for 2nd poly through Cu/Fe, Zn/Fe and Co/Fe

H* = Hypothesis: metals associated with same mineral phase as Fe and/or dilution effect, A = accept, R = reject

Particle seawater mixing

		Linear			exponential			log			2nd polynomial			power		
BVF	Elements	r^2	p	H*	r^2	p	H*	r^2	p	H*	r^2	p	H*	r^2	p	H*
	Mg/p(Fe+Cu+Zn) %	0.045	0.6	R	0.007	8E-01	R	0.102	4E-01	R	0.404	2E-01	R	0.007	8E-01	R

		Linear			exponential			log			2nd polynomial			power		
VDVF	Elements	r^2	p	H*	r^2	p	H*	r^2	p	H*	r^2	p	H*	r^2	p	H*
	Mg/p(Fe+Cu+Zn) %	0.050	0.6	R	0.050	6E-01	R	0.060	5E-01	R	0.061	8E-01	R	0.311	1E-01	R

H* = Amount of metals in particulate fraction increases with mixing, A = accept, R = reject.

Association of metals in BVF particles

		Linear			exponential			log			2nd polynomial			power		
	Elements	r^2	p	H*	r^2	p	H*	r^2	p	H*	r^2	p	socia	r^2	p	H*
BVF	Mn/Fe	0.160	2E-01	R	0.151	2E-01	R	0.375	2E-02	R	0.324	1E-01	R	0.528	3E-03	R
	Cu/Fe	0.944	7E-09	A	0.581	2E-03	**R**	0.573	2E-03	R	0.944	1E-07	A	**0.962**	**7E-10**	A
	Zn/Fe	0.736	2E-04	A	0.679	5E-04	A	0.426	2E-02	R	0.766	7E-04	A	**0.927**	**1E-07**	**A**
	Co/Fe	**0.959**	**3E-08**	**A**	0.648	2E-03	A	0.659	1E-03	A	0.963	3E-07	A	0.954	5E-08	A
	Pb/Fe	0.287	6E-02	R	0.405	2E-02	R	0.297	5E-02	R	0.386	9E-02	R	**0.691**	**4E-04**	**A**
	Cd/Fe	0.798	9E-05	A	0.737	3E-04	R	0.580	4E-03	R	0.801	7E-04	R	**0.951**	**7E-08**	**A**

H* = metals are associated with the same mineral phase

		Linear			exponential			log			2nd polynomial			power		
	Elements	r^2	p	H*	r2	p	H*	r2	p	H*	r2	p	H*	r2	p	H*
BVF	Cu/Co	0.992	8E-12	A	0.600	3E-03	A	0.625	2E-03	A	0.996	2E-11	A	**0.999**	**3E-17**	**A**
	Zn/Pb	0.365	3E-02	R	0.483	8E-03	A	0.403	2E-02	R	0.529	2E-02	R	**0.842**	**1E-05**	**A**
	Zn/Cd	0.976	2E-09	A	0.583	4E-03	A	0.780	1E-04	A	**0.990**	**9E-10**	**A**	**0.968**	**8E-09**	**A**

H* = metals are associated with the same mineral phase

Association of metals in VDVF particles

		Linear			exponential			log			2nd polynomial			power		
	Elements	r^2	p	H*	r^2	p	H*	r^2	p	H*	r^2	p	H*	r^2	p	H*
VDVF	Mn/Fe	0.966	2E-06	A	0.689	6E-03	R	0.558	2E-02	R	0.989	1E-06	R	0.915	5E-05	A
	Cu/Fe	0.843	5E-04	A	0.464	4E-02	R	0.413	6E-02	R	0.980	8E-06	R	**0.850**	**4E-04**	**A**
	Zn/Fe	0.932	4E-04	A	0.467	9E-02	R	0.687	2E-02	R	0.932	5E-03	A	0.797	7E-03	R
	Co/Fe	0.419	4E-01	R	0.402	3E-01	R	0.489	3E-01	R	0.454	7E-01	R	0.693	2E-01	R
	Pb/Fe	0.086	4E-01	R	0.317	1E-01	R	0.347	1E-01	R	0.399	2E-01	R	**0.801**	**1E-03**	**A**
	Cd/Fe	**0.918**	**7E-04**	**A**	0.648	3E-02	R	0.465	9E-02	R	0.999	2E-06	A	0.850	3E-03	A

H* = metals are associated with the same mineral phase

T-statistic outside 95 % confidence limit for 2nd poly through Mn/Fe, Cu/Fe and Cd/Fe

		Linear			exponential			log			2nd polynomial			power		
	Elements	r^2	p	H*	r^2	p	H*	r^2	p	H*	r^2	p	H*	r^2	p	H*
VDVF	Cu/Co	0.550	3E-01	R	0.725	1E-01	R	0.332	4E-01	R	0.803	4E-01	R	0.724	1E-01	R
	Zn/Pb	0.199	3E-01	R	0.476	6E-02	R	0.421	8E-02	R	0.738	4E-02	R	**0.950**	**4E-05**	**A**
	Zn/Cd	0.869	2E-03	A	0.707	2E-02	R	0.343	2E-01	R	0.993	5E-05	R	**0.881**	**2E-03**	**A**

H* = metals are associated with the same mineral phase

T-statistic outside 95 % confidence limit for 2nd poly through Zn/Cd

Appendix C

Trace metal analysis by inductively coupled plasma mass spectrometry (ICP-MS).

Analysis of high salinity samples by ICP-MS

The high salinity of hydrothermal plume samples prevents direct analysis using ICP-MS. Direct analysis of samples with high salinity and total dissolved solids (TDS) causes salt precipitation within the instrument decreasing its sensitivity and overall performance (Hutton and Eaton, 1988). The high salinity of samples also causes isobaric interferences, which can mask the analyte signal. Therefore prior to analysis it is necessary to remove the high salinity matrix of samples either by sample dilution or analyte extraction/separation.

Concentrations of trace metals in a hydrothermal plume can range from mM concentration to nM concentration. This wide range of concentrations makes it difficult to use a single sample preparation technique to prepare samples for ICP-MS analysis.

Near vent samples with higher concentrations of trace metals can be analysed by diluting the sample. Samples can be diluted by a factor of 20 this is sufficient to lower the salinity of the solution to prevent problems during analysis. Near vent samples were diluted in 1M sub-boiled (s.b) HNO_3 solution with 10 ppb Rh, Bi, Sc internal standards for instrument sensitivity correction post analysis. A standard and blank were analysed every 10 samples to monitor error and blank derived from the ICP-MS (Thermo Element XR magnetic sector). All samples were analysed for Fe, Mn, V, Co, Ni, Zn, Cu in medium resolution and Pb, Cd in low resolution. In all near vent samples Co, Cd, Ni and Pb were below detection limit as these elements were not sufficiently enriched in vent fluids to be above the instrument limit of detection (l.o.d) after sample dilution.

Two reference materials as well as an in-house standard were analysed to assess accuracy of sample dilutions. Reference river water standard SLRS-4 from the National Research Council, Canada (NRCC) has a higher concentration of Fe similar to hydrothermal plume samples but the sample matrix will differ from hydrothermal samples. Near shore seawater CASS-5 (NRCC) is closer to a matrix matched reference material and was expected to have similar concentrations to some of the most dilute plume samples however concentrations of most elements will be close to the detection limit after 20x dilution.

Table C.1. Measured and certified values for reference materials diluted and analysed by ICP-MS using standard addition.

	$\text{CASS-5}_{\text{measured}}$		$\text{CASS-5}_{\text{certified}}$		$\text{SLRS-4}_{\text{measured}}$		$\text{SLRS-4}_{\text{certified}}$	
Fe	< 33		25	± 1.9	1868	± 19	1844	± 89
Mn	56	± 0.03	48	± 3.6	61.6	± 0.03	61.3	±3.28

As the hydrothermal vent fluid is diluted by seawater during plume rise the concentration of trace metals enriched in the vent fluid source are lowered. In samples that are more distal relative to the vent source with lower concentrations of trace metals dilution of the sample results in a concentration below the instrument l.o.d or less than the method blank concentration. For example Table C.1 show that an accurate measurement for Fe in the CASS-5 reference material could not be obtained. The instrument blank calculated from standard additions was 1.6 nM. After 21 x dilution of the CASS-5 reference material the concentration would have been 1.1 nM and therefore less than that of the blank.

For these samples an offline analyte extraction procedure is necessary to separate the trace metals of interest from the high salinity sample matrix.

Standard addition vs isotope dilution

Analyte extraction was performed offline prior to ICP-MS analysis using a chelating resin. The method of standard additions was used similar to Biller and Bruland (2012) however an extraction set up similar to that used by Milne et al. (2010) was used.

Standard additions were preferred to the isotope dilution method (Milne, Landing et al. 2010) for three reasons: lowering error over the wide range of sample concentrations, practicality and expense. For the most accurate analysis using isotope dilution, a rough estimate of sample concentration is required so the isotope spike solution can be added to the sample at a similar concentration. Higher sample to spike ratios reduce accuracy and increase the error of the isotope dilution method (Figure C.1) (Van Heuzen et al., 1989, Lee et al., 2011). Ideally the sample to spike ratio should be 1 and no higher than 5.

The concentration of open ocean seawater is typically between 0.1 to 1 nM for Fe (Worsfold et al., 2014) and does not vary as dramatically as it does in hydrothermal plumes, which vary in trace metal concentrations over several orders of magnitude. Thus the isotope dilution method is more appropriate for open ocean seawater samples as it is easier to get an ideal sample to spike ratio without any knowledge of the specific sample concentration. Furthermore labs, which use this method often analyse Fe concentration during cruises by flow injection techniques (Lohan et al., 2006). Then re-analyse samples on shore by isotope dilution ICP-MS (ID-ICP-MS) to get a more accurate and precise result for Fe and analysis additional results for other trace metals (Schlosser pers. Comm.). It is possible to get accurate and precise measurements shipboard by flow injection chemiluminescence but no analysis of trace metals was conducted on the ship during JC80 or JC82 therefore plume samples could have an Fe concentration anywhere between 10,000 to 1 nM making it difficult to obtain the ideal sample to spike ratio without time consuming repeat analysis of samples.

Mn and Co are both mono-isotopic elements therefore it is impossible to measure these elements by isotope dilution. Milne et al. (2010) measure Mn and Co by standard addition and other trace metals by isotope dilution. Using two methods of standardisation increases the amount of time it takes to prepare samples and to process ICP-MS data. Therefore it is more efficient to use one method of standardisation for all elements.

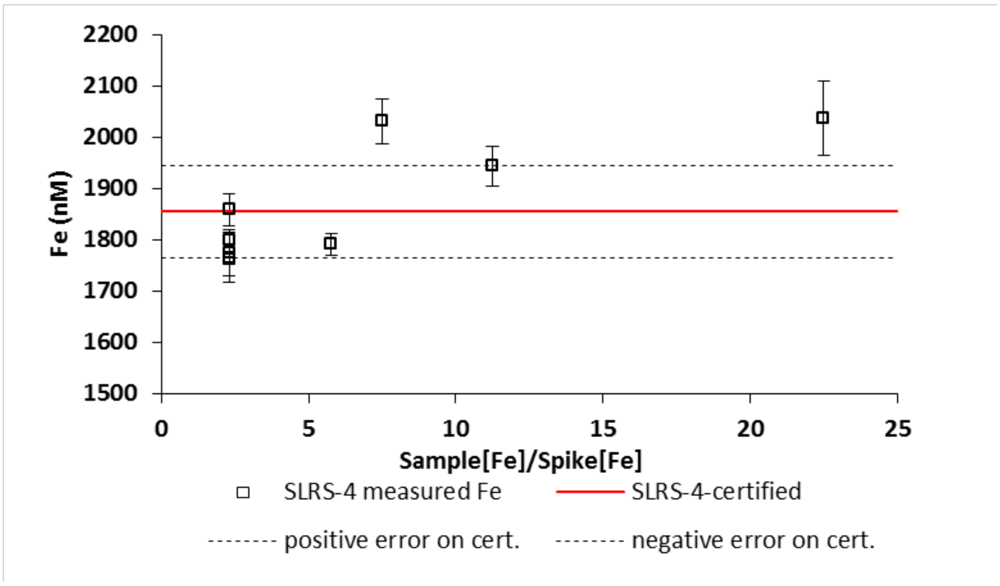

Figure C.1. Analysis of the certified reference material SLRS-4 using isotope dilution with increasing sample to spike ratio. Dashed lines are the error quoted by the distributor the National Research Council of Canada.

Preparing a multi element isotope spike solution is a time consuming and expensive process. Solid metals enriched in trace metal isotopes of low abundance are expensive. These metals then have to be dissolved in solution and the concentration of trace metals and isotope ratios in the solution accurately quantified by repeat analysis on a MC-ICP-MS. By comparison standards in matrix matched seawater can be prepared by simple dilution of a standard with all elements of interest in less than a day.

Experimental

Reagents

All reagents were prepared in >18 MΩ de-ionised water in LDPE or FEP bottles that had been cleaned using the acid cleaning procedure at NOCS (Appendix A). Trace metal grade nitric acid (Fisher Scientific) was purified by sub-boiling (s.b) quartz distillation. Elution acid of 1M s.b HNO_3 and 2M s.b HNO_3 column wash were prepared from concentrated s.b HNO_3. The elution acid was spiked with 10 ppb Rh, Bi, Sc internal standards. A 2M Ammonium acetate buffer solution was prepared from ammonium hydroxide (optima grade, Fisher Scientific), acetic acid (optima grade, Fisher Scientific) and de-ionised water. The pH was increased to 9 by adding small aliquots of ammonia hydroxide. A 0.05M ammonium acetate solution for conditioning the column before sample loading was also prepared from the 2M solution.

Standards

A multi-element stock standard solution of V, Mn, Fe, Co, Ni, Cd, Cu and Pb was made from dilution of commercial ICP-MS individual element standards (inorganic ventures). This stock solution was used to prepare 2 sets of standards. One set of acid standards (A_{sTD}) were prepared by dilution of the stock standard in the 1M S.B HNO3 elution acid. Another set of matrix-matched standards were prepared by spiking several aliquots of seawater with the stock standard. For these seawater standards (S_{sTD}) a 2 L of coastal seawater was taken through the extraction procedure to remove trace metals and produce a matrix matched solution with low concentrations (0.8 ± 0.3 nmol kg^{-1} $n = 6$) of trace metals that could be used for standard additions. These seawater standards were treated exactly the same as samples during the extraction procedure. The comparison of the slope between A_{sTD} and S_{sTD} was used to check the recovery of elements during the extraction procedure. If the recovery of the extraction procedure is 100 % then the slope of A_{sTD} will be the same as the slope of S_{sTD}.

S_{sTD} was also used to check the precision and accuracy of each run of samples along with another low metal seawater in-house standard (LMSW) and the NASS-6 seawater certified reference material (NRCC).

Two LMSW standards were spiked with increasing concentrations of Mo and taken through the extraction procedure. This was in order to monitor and correct for any isobaric interference from MoO+ on Cd110 or Cd111 (Wu and Boyle, 1997, Milne et al., 2010, Biller and Bruland, 2012).

Extraction set-up

An amino carboxylic acid type chelating resin (CM-PEHA) was used for pre-concentration and matrix separation of samples (Kagaya et al., 2009). This resin was used instead of the commercially available nobias chelate PA-1 resin as the CM-PEHA resin showed better recovery for Mn with less resin conditioning required and a lower blank (Appendix C.2). A batch of the resin was cleaned in 3 changes of 3M s.b HNO3. Cleaned resin was then packed into two separate columns with an internal volume of 27 µl (Global FIA) and immobilized with polypropylene frits with 20 µm pore size. The columns were set up in a flow manifold (prep lab, Fisons instruments) (Figure C. 2). All tubing used was FEP except for peristaltic pump tubing, which was silicone (grey-grey, Cole Parmer).

The use of a closed flow manifold was deemed the most suitable method in comparison to dripping samples through columns or performing a bulk extraction by adding resin to a bottle containing the sample and leaving it on a shaker table. Generally blanks from these methods were significantly higher and the recovery of trace metals was lower. These methods involve more sample handling and the resin cannot be cleaned as extensively as it can be in a closed system, which is likely to increase blank concentrations.

A multi-port injector valve allowed switching between different pump lines to pass different solutions through the resin column. Electric valves were used on individual sample lines to switch between buffered sample solution and 0.05 M rinse/condition solution. Valve selection and timing were automated using the LabVIEW software (National Instruments). This extraction set-up allowed for pre-concentration of two samples simultaneously.

Prior to sample extraction samples were irradiated using a low power UV (119 mW cm^{-2} ; 254 nm) system. This consisted of a box with 2 15 W UV lamps inside facing each other. A trip switch for the UV lamps was connected to the lid of the box to prevent accidental exposure. Acid cleaned 30 ml FEP bottles (Fisher Scientific) containing samples were placed 2 cm from the UV lamps.

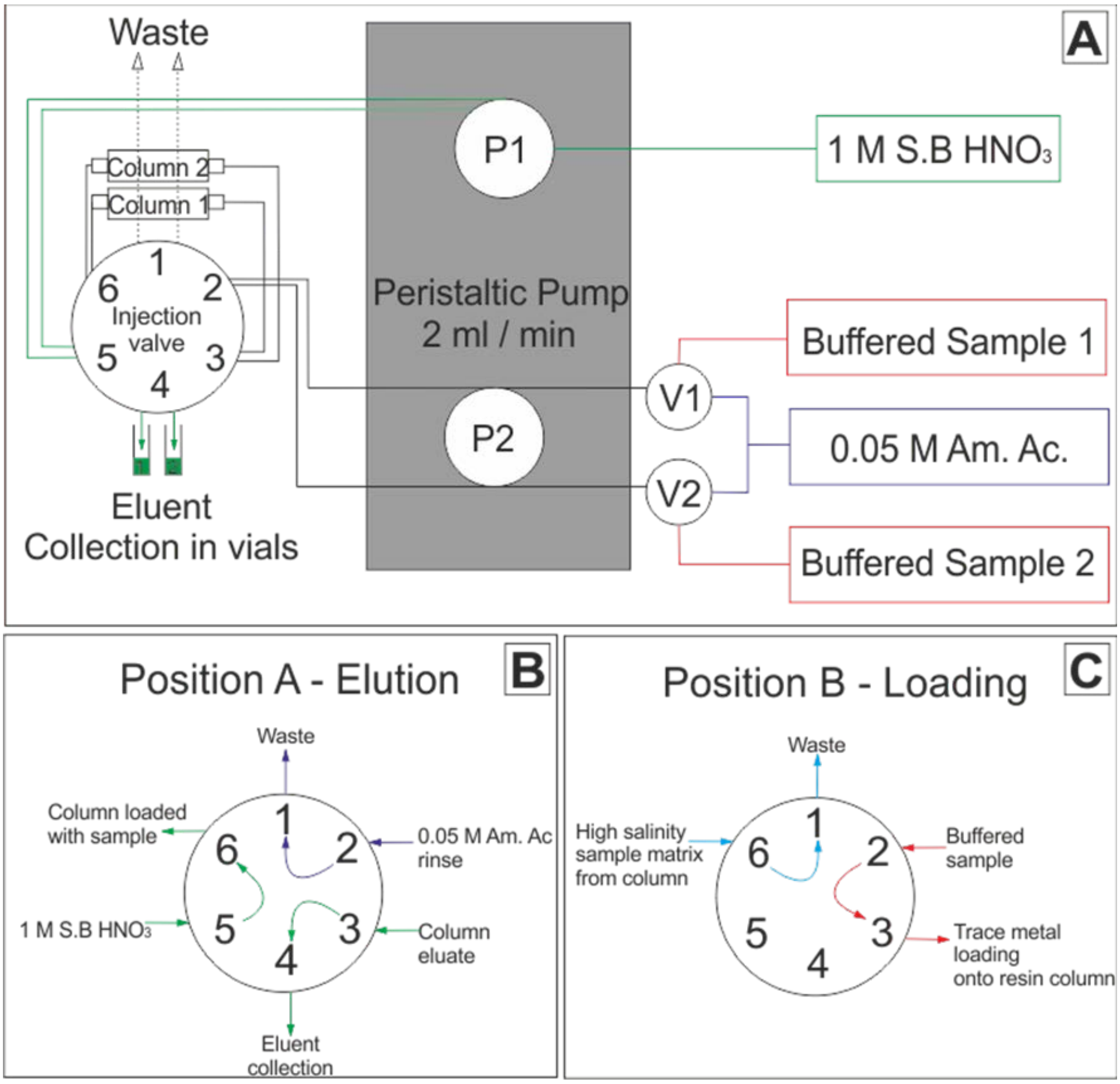

Figure C. 2. A, Extraction set up for pre-concentration of trace metals and separation of high salinity sample matrix. P1 and P2 are two separate peristaltic pumps, V1 and V2 are valves for switching between 0.05 M ammonium acetate rinse/condition solution and buffered samples. B, injection valve position A for eluting trace metals from the resin column. C, injection valve position B for loading the sample onto the resin column and separation of saline matrix.

Extraction Procedure

15 ml aliquots of acidified samples were sub-sampled into 30 ml FEP bottles. Sub-samples were exposed to UV for 3 hours, which has proved to be long

enough to dissociate Co and Cu from organic ligand complexes (Biller and Bruland, 2012, Milne et al., 2010, Queroue et al., 2014)

The flow manifold was cleaned before use with 2 M s.b HNO3 at a flow rate of 0.5 ml/min for 2 hours. Six blanks were taken before processing samples to quantify the blank contribution from the flow manifold as well as reagents and bottles. The flow manifold sample lines and columns were rinsed through with 0.05 M NH_4Ac solution before extraction of the first sample.

Acidified 15 ml sub samples were adjusted to pH 6.2 +/- 0.3 by adding 650 µl of the 2 M NH_4Ac buffer immediately before extraction. This was to minimise the time sample solutions were at high pH to reduce the chance of any colloids forming. Sub-samples were weighed before and after extraction to calculate an exact pre-concentration factor.

Table C. 2: Extraction procedure of flow manifold for matrix separation and pre-concentration of trace metals.

Step	Time (sec)	P1	P2	Sample valves V1 and V2	Injection valve	Action
0	270	Off	On	On	B	Loading
1	15	Off	Off	On	B	Pause to remove tubing from sample bottles
1	15	Off	On	On	B	Sample line flush
1	120	Off	On	Off	B	Rinse
2	45	On	On	On	A	Elution and condition
3	45	On	On	On	A	wash and condition

The sample extraction process through the flow manifold is outlined in Table 3. Buffered sample solutions were loaded onto the columns at a rate of 2 ml/min. The sample lines up to valves 1 and 2 (V1 and V2 in Figure C. 2) were then flushed with de-ionised water (Milli-Q) to ensure all the sample solution was loaded onto the column and prevent carry over when loading the next sample. Columns were then rinsed with 0.05 M NH_4Ac to remove major ions (Na^+, K^+, Mg^{2+} and Ca^{2+}) and residual sample matrix. The 1 M s.b HNO3 eluent was then passed across the columns to elute trace metals, 1.5 ml was collected. The eluent was passed over the columns in the opposite direction to sample loading to prevent the resin becoming packed down in one end of the column.

The collected eluent was weighed post extraction and the 15 ml sub-sample was weighed before extraction in order to calculate the exact pre-concentration factor for each sample and S_{sTD}.

ICP-MS

Samples were analysed using a Thermo Element XR magnetic sector ICP-MS at NOCS. Ni sample and skimmer cones were used and a ESI-PC3 Peltier cooled spray chamber. The sample gas rate was 0.75 ml/min and the additional gas was optimized during tuning before each run. Low resolution mode was used to measure ^{110}Cd, ^{111}Cd, ^{208}Pb, and ^{95}Mo. Medium resolution mode was used to measure ^{55}Mn, ^{56}Fe, ^{66}Zn, ^{63}Cu, ^{65}Cu, ^{59}Co and ^{51}V. Internal standards of ^{103}Rh, ^{209}Bi, ^{45}Sc were measured in both low and high resolution. To account for the change in sensitivity over the course of a run the counts per second (cps) of isotopes measured in low resolution were normalized to the cps of ^{103}Rh measured in low resolution except for ^{208}Pb, which was normalized using ^{209}Bi measured in low resolution. All isotopes measured in medium resolution were normalized to ^{103}Rh except ^{51}V, which was normalized to ^{45}Sc. An acid blank and standard were run every 10 samples to monitor precision and the blank associated with the instrument.

Procedure blank and error

The procedural blank calculated from buffered de-ionised water (Milli-Q) for V, Mn, Fe, Co, Ni, Cu, Zn, Cd and Pb was 5, 55, 371, 6, 426, 123, 677, 50, 2 pmol kg^{-1} respectively. The blank contribution to analysis of the NASS-6 CRM was <3 % for all elements except for Ni, Zn, Cd, and Pb where the blank contribution was 8, 15, 16 and 6 % respectively. Accuracy and precision of the analysis of 8 ml of the NASS-6 CRM is shown in Table C.3. Element concentration and recovery is estimated from the slope of A_{sTD}. A comparison between this method and other published methods is given in Appendix B for all elements.

Table C.3. Certified values for NASS-6 seawater (NRCC) shown with values measured using the method described and the associated error (s.d is standard deviation). Value for Co is not certified. U_{CRM} is the expanded uncertainty of the certified value.

	NASS-6 certified		Measured		
	nM	U_{CRM}	nM	s.d	Recovery %
Fe	8.649	0.806	8.910	1.186	103%
Mn	9.392	0.856	10.468	1.536	111%
V	27.875	3.141	16.713	2.646	60%
Co	0.255	*	0.332	0.047	130%
Ni	5.009	0.426	3.932	0.775	78%
Cu	3.808	0.393	3.712	0.588	97%
Zn	3.839	0.306	4.094	1.256	107%
Cd	0.270	0.017	0.377	0.061	140%
Pb	0.029	0.010	0.030	0.004	103%

Table C.4. Comparison of nobias resin and CM-PEHA resin (wako resin). The extraction processes were done twice, once where the resin was conditioned with de-ionised water the other where it was conditioned with 0.05 M Am.Ac. All results are the average of 2 samples taken through procedures.

	De-ionised water (Milli-Q) condition/rinse						**0.05M AmAc condition/rinse**					
NASS 6	nobias resin			wako resin			nobias resin			wako resin		
	ppb	s.d	recovery %	ppb	s.d	recovery %	ppb	s.d	recovery	ppb	s.d	recovery %
Fe	0.361	0.033	93%	0.402	0.039	112%	0.510	0.139	106%	0.515	0.069	107%
Mn	0.225	0.005	44%	0.307	0.040	96%	0.493	0.117	95%	0.575	0.084	111%
V	0.991	0.005	70%	1.194	0.145	84%	0.709	0.136	50%	0.851	0.135	61%
Co	0.016	0.000	109%	0.018	0.002	120%	0.021	0.005	139%	0.020	0.003	133%
Ni	0.255	0.007	92%	0.320	0.040	94%	0.251	0.066	117%	0.246	0.045	102%
Cu	0.232	0.005	98%	0.264	0.030	103%	0.236	0.070	112%	0.238	0.037	104%
Zn	0.193	0.011	98%	0.261	0.024	118%	0.275	0.098	122%	0.286	0.056	121%
Cd	0.036	0.000	124%	0.046	0.007	128%	0.038	0.010	172%	0.042	0.007	141%
Pb	0.004	0.001	95%	0.006	0.001	107%	0.006	0.002	113%	0.006	0.001	108%

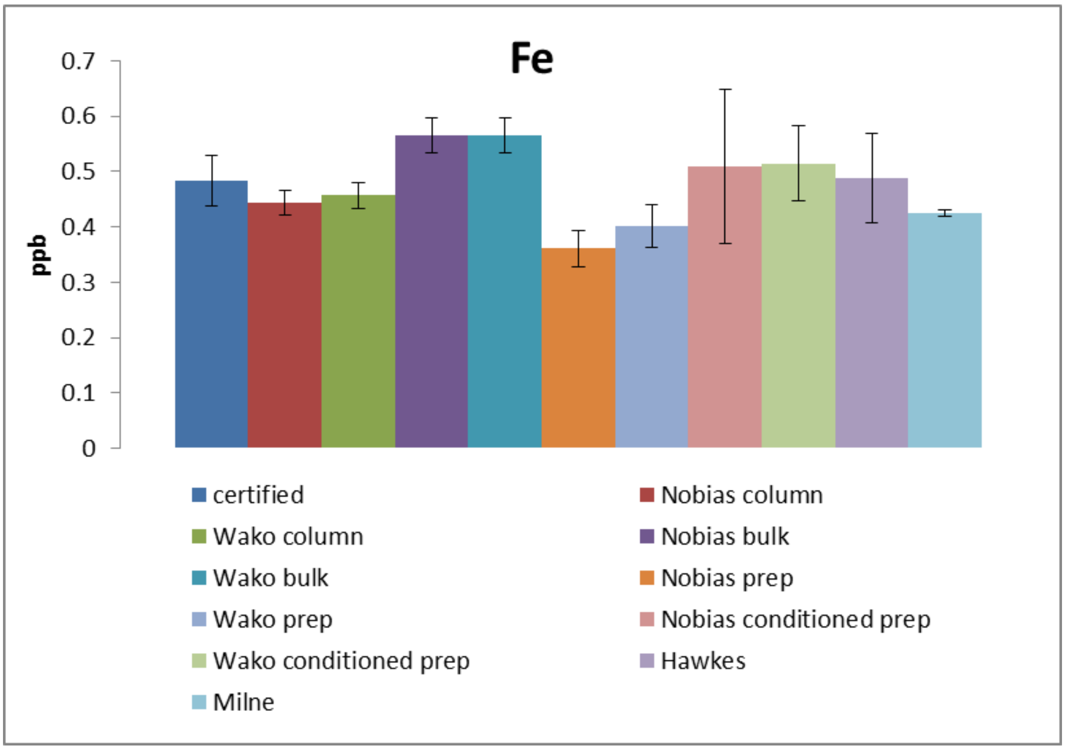

Figure C.3. Comparison of Fe analysis on NASS-6 for different methods using different resins. Where other studies measured NASS-5 or CASS-4 recovery of these CRMs was calculated and then used to estimate the measured NASS-6 concentration using this method. This is done for all the graphs below also.

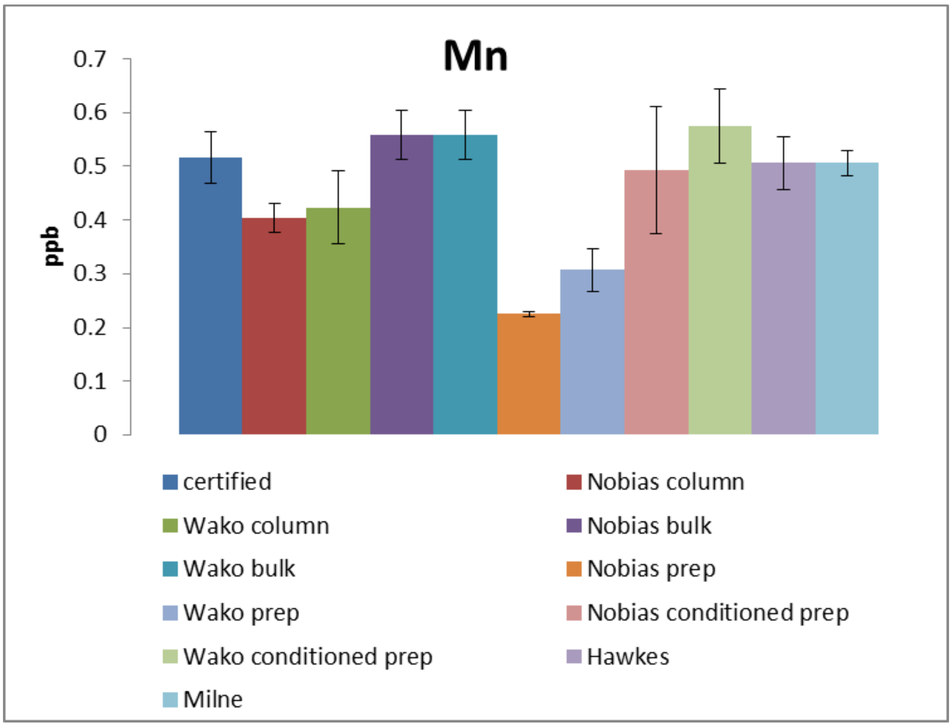

Figure C.4. Comparison of Mn analysis for different methods using different resins.

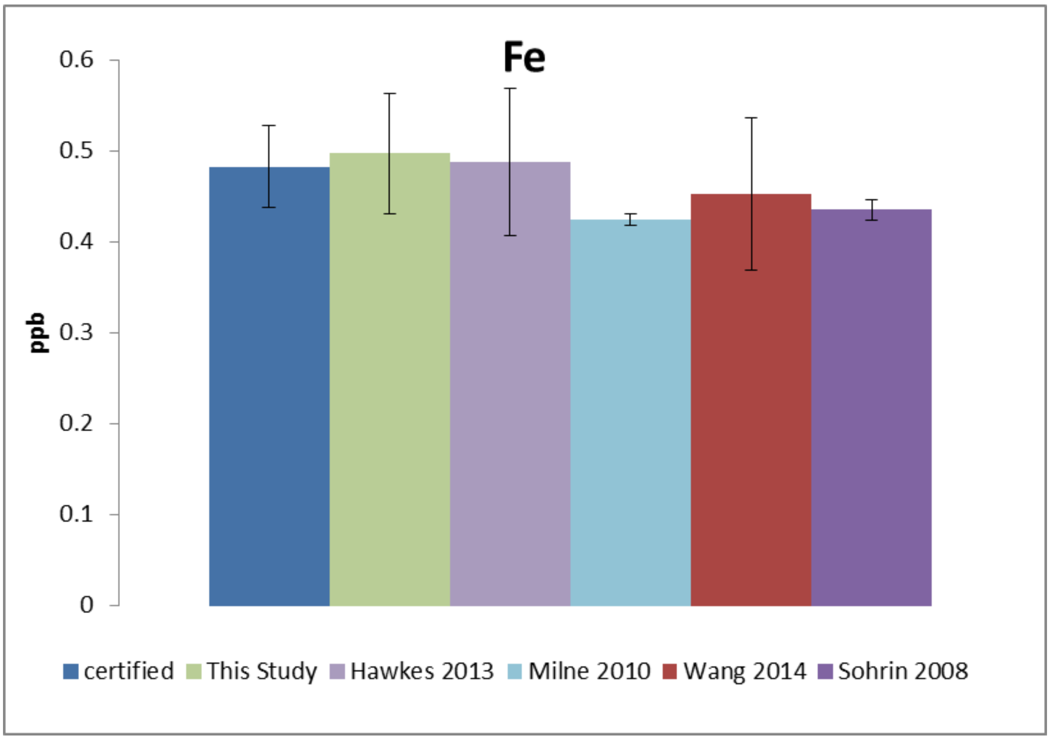

Figure C.5. Comparison of extraction method to other published methods for Fe

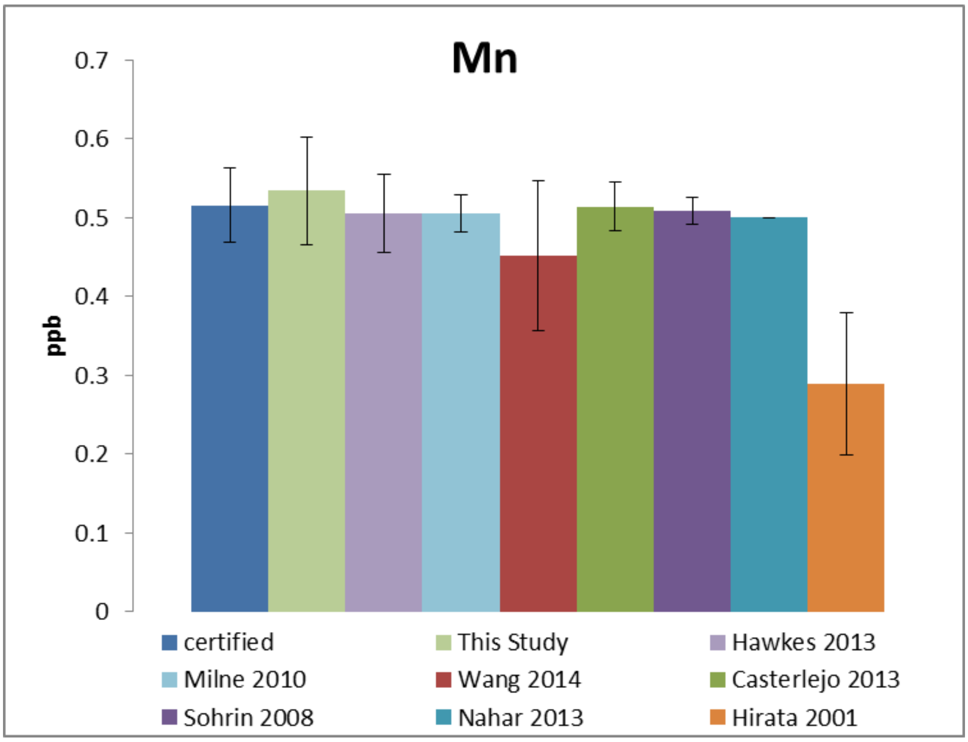

Figure C.6. Comparison of extraction method to other published methods for Mn.

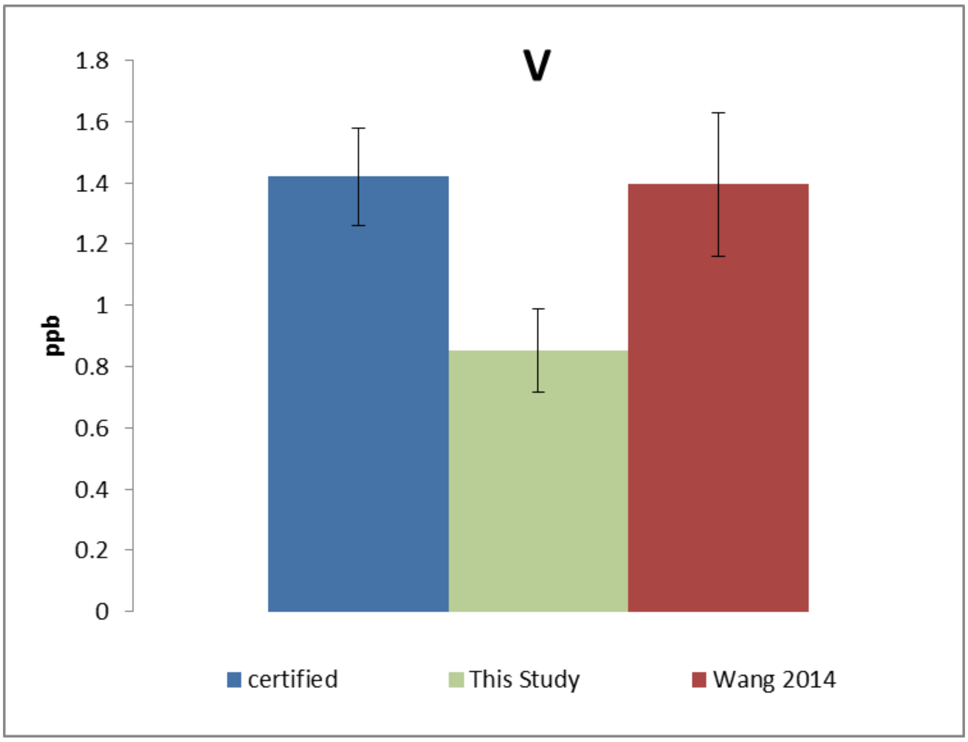

Figure C.7. Comparison of extraction method to other published methods for V.

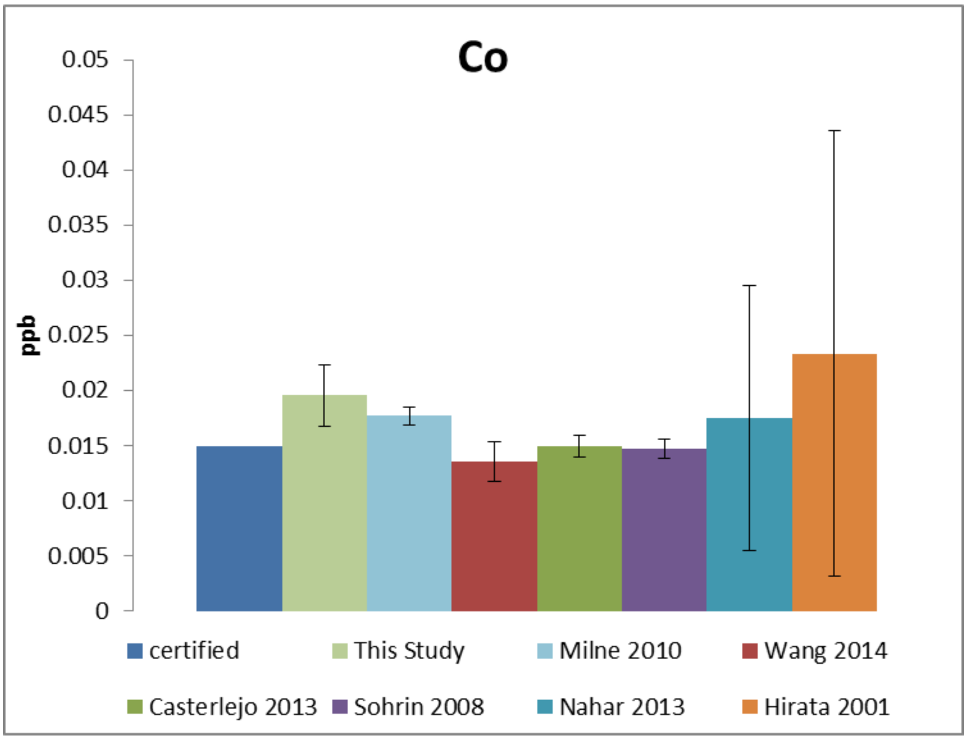

Figure C.8. Comparison of extraction method to other published methods for Co.

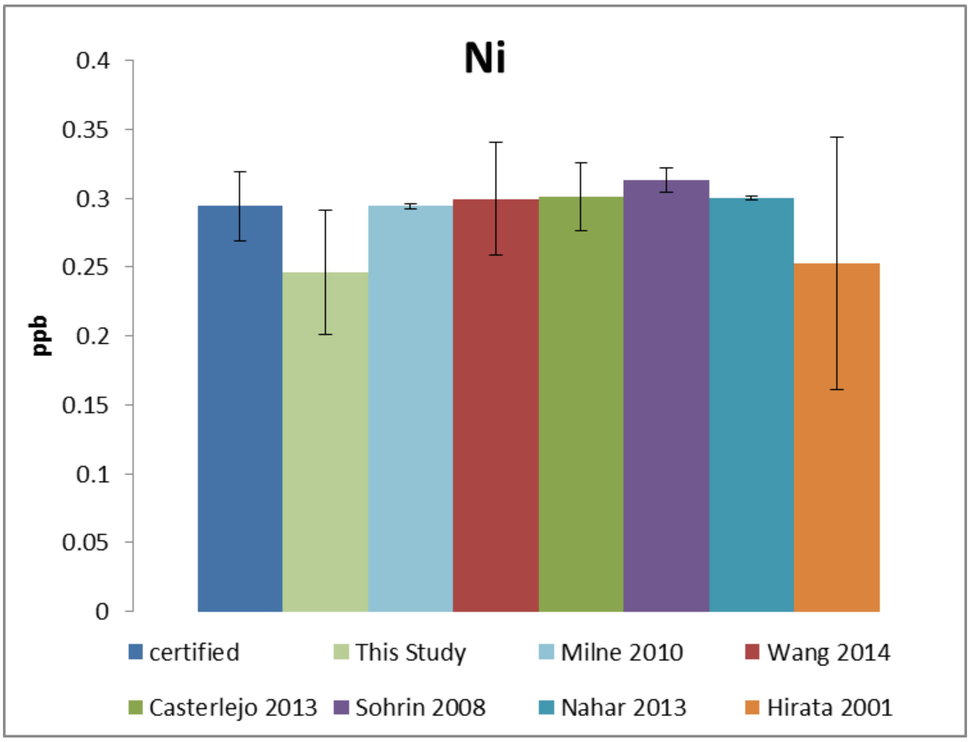

Figure C.9. Comparison of extraction method to other published methods for Ni.

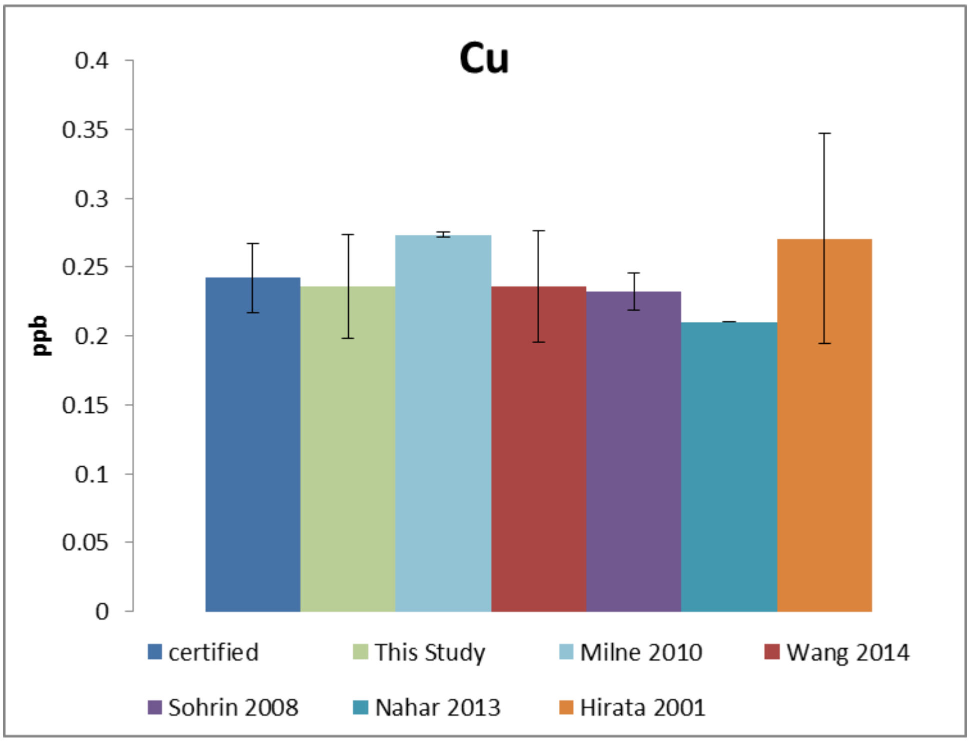

Figure C.10. Comparison of extraction method to other published methods for Cu.

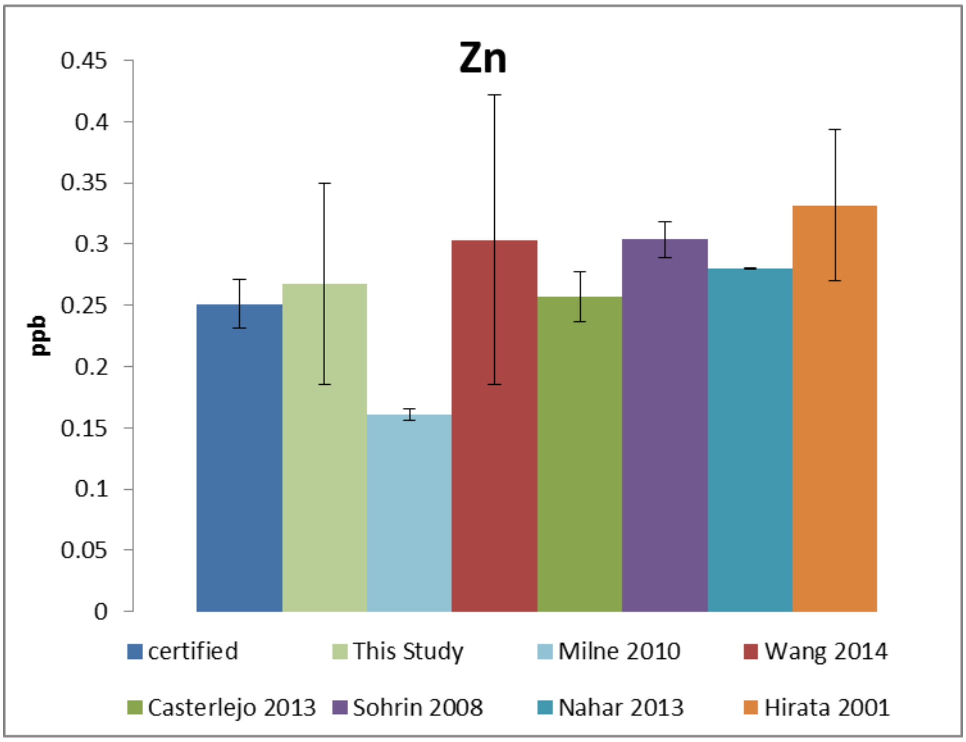

Figure C.11. Comparison of extraction method to other published methods for Zn.

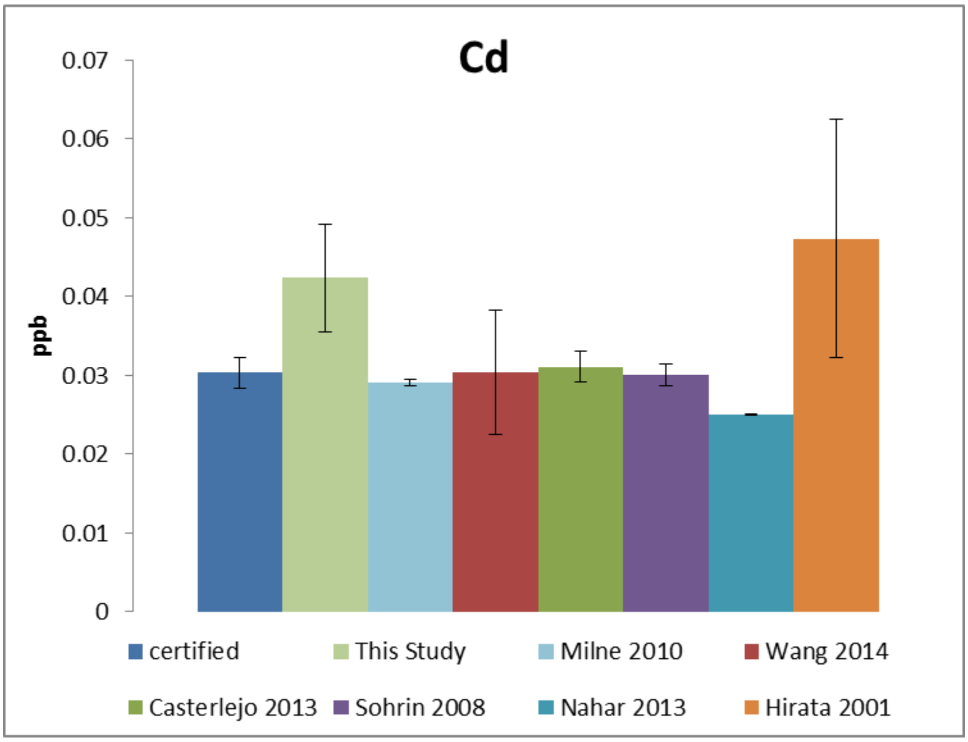

Figure C.12. Comparison of extraction method to other published methods for Cd.

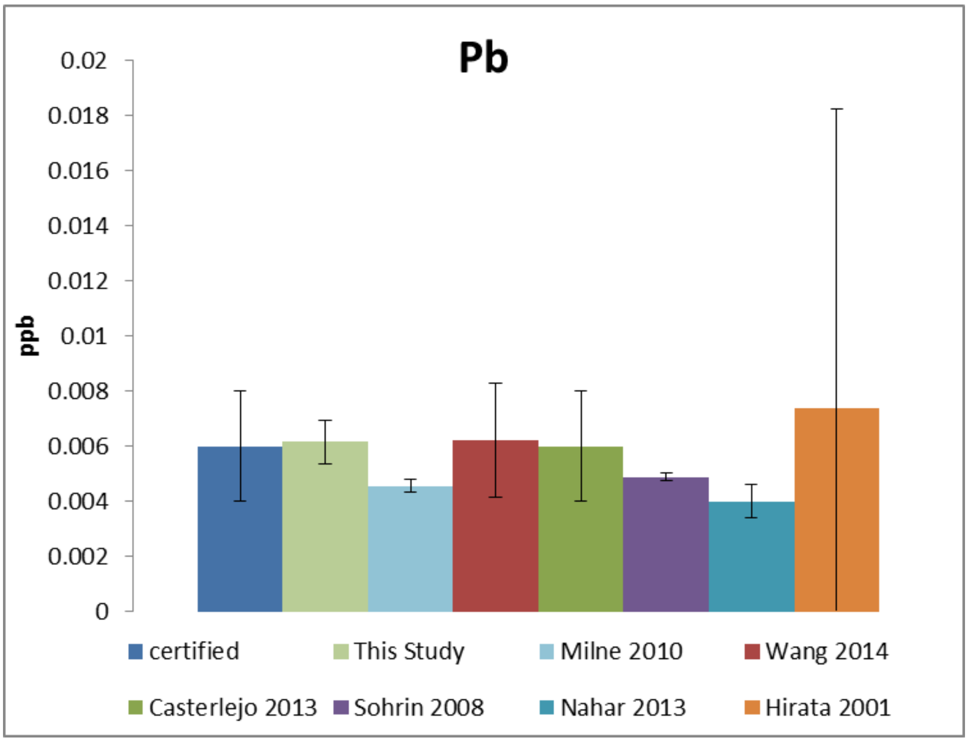

Figure C.13. Comparison of extraction method to other published methods for Pb.

Appendix D

Regression statistics for plume profiles

TD metals and dMn

		Linear		
	Elements	r^2	p	H*
BVF	TDMn/dMn	0.992	0.000	A
	TDFe/dMn	0.989	0.000	A
	TDZn/dMn	0.024	0.566	R
	TDPb/dMn	0.006	0.764	R
	TDCo/dMn	0.014	0.648	R
	TDCu/dMn	0.094	0.231	R
	TDCd/dMn	0.428	0.004	A

		Linear		
	Elements	r^2	p	H*
VDVF	TDMn/dMn	0.953	0.000	A
	TDFe/dMn	0.262	0.021	R
	TDZn/dMn	0.055	0.320	R
	TDPb/dMn	0.462	0.001	A
	TDCo/dMn	0.030	0.468	R
	TDCu/dMn	0.271	0.019	R
	TDCd/dMn	0.013	0.638	R

H^* = conservative trend of TD element budget. A = significant trend, R = non-significant.

Size fractioned metals and dMn

		Linear			exponential			log			2nd polynomial			power		
	Elements	r^2	p	H*	r^2	p	H*	r^2	p	H*	r^2	p	H*	r^2	p	H*
VDVF	sMn/dMn	0.981	7E-11	A	0.838	1E-05	A	0.791	5E-05	A	0.982	2E-09	A	0.984	3E-11	A
	sCu/dMn	0.397	7E-03	R	0.417	5E-03	R	0.496	2E-03	A	0.420	2E-02	R	0.499	2E-03	A
	pCu/dMn	0.942	3E-02	R	0.896	5E-02	R	0.958	2E-02	R	0.981	1E-01	R	0.990	5E-03	A
BVF	sMn/dMn	0.998	2E-26	A	0.738	1E-06	A	0.700	4E-06	A	1.000	4E-29	A	0.957	9E-14	A
	sFe/dMn	0.985	7E-18	A	0.877	1E-09	A	0.653	2E-05	A	0.988	4E-17	A	0.744	1E-06	A
	sZn/dMn	0.384	5E-03	R	0.797	3E-07	A	0.247	3E-02	R	0.384	2E-02	R	0.455	2E-03	A
	cFe/dMn	0.319	9E-03	R	0.300	1E-02	R	0.791	2E-07	A	0.940	4E-17	A	0.775	3E-07	A
	pFe/dMn	0.975	2E-13	A	0.867	6E-08	A	0.601	3E-04	A	0.993	1E-15	A	0.697	3E-05	A
	pCu/dMn	0.835	3E-05	A	0.744	3E-04	A	0.777	2E-04	A	0.835	3E-04	A	0.715	5E-04	A

H^* = trend of element fraction with dMn. A = significant trend, R = non-significant.

Association of metals in different size fractions

	Linear			
	Elements	r^2	p	H*
VDVF	pCo/pZn	0.9964	2E-03	A
	pCo/pMn	0.9854	8E-04	A
	pZn/pMn	0.9054	1E-03	A
	Linear			
	Elements	r^2	p	H*
VDVF	cPb/cZn	0.1701	2E-01	R
	cPb/cZn*	0.8951	1E-02	A
	sPb/sZn	0.2233	2E-01	R
	sPb/sZn*	0.5607	1E-03	A
	Elements	r^2	p	H*
BVF	cPb/cZn	0.0355	6E-01	R
	cPb/cZn*	0.2105	2E-01	R
	sPb/sZn	0.2233	6E-02	R
	sPb/sZn*	0.1957	1E-01	R

H* = elements in fractions correlated and maybe associated with same species. A = significant trend, R = non-significant. * = near vent samples excluded from Zn/Pb regression.

Appendix E

Fe(II) oxidation rate calculations for E2 plume samples

Table E1. Calculated of Fe(II) oxidation half-lives in the E2 buoyant plume and background seawater (Scotia Sea) compared to Fe(II) half-lives for deep waters surrounding Atlantic sites 5˚S (Red Lion) and TAG

Depth (*m*)	Temp. (˚C)	Salinity	O_2 (µmol kg^{-1})	pH_{sws}[a]	pK_w[a]	pOH[b]	K_1[c]	Fe(II) half life (h)
E2[d]								
2605	0.3	34.66	223	7.694	14.188	6.501	0.0036	3.18
2605	0.5	34.66	217	7.560	14.179	6.625	0.0020	5.71
2605	0.5	34.66	223	7.745	14.179	6.434	0.0050	2.31
2605	0.3	34.66	224	7.681	14.189	6.508	0.0036	3.25
2605	0.6	34.66	221	7.674	14.174	6.501	0.0037	3.15
2605	0.6	34.66	219	7.644	14.175	6.531	0.0032	3.66
2605	0.7	34.66	216	7.727	14.172	6.446	0.0046	2.50
2605	0.7	34.66	217	7.546	14.169	6.624	0.0021	5.63
Average								3.67
Scotia Sea[d]	0.1	34.66	210	7.894	14.199	6.305	0.0084	1.38
5˚S (Red Lion)[e]								
2700	2.5	34.91	242	7.965	14.081	6.117	0.026	0.45
TAG[f]								
2985	2.8	34.94	255	7.945	14.057	6.112	0.028	0.41

[a] pH and pKw calculated using Lewis, E., and D. W. R. Wallace. 1998. Program Developed for CO2 System Calculations (CO2SYS). ORNL/CDIAC-105. Information Analysis Center, Oak Ridge National Laboratory, U.S. Department of Energy, Oak Ridge, Tennessee.

[b] $pOH = pK_w - pH$

[c] $\log k = 21.56 \qquad T + 1545\ 3.29 I^{1/2} + 1.521$ where $I = 19.9201 \times S/(10^3 - 1.00488 \times S)$, where, S is salinity and T is temperature in Kelvin (Millero et al., 1987), $k_1 = k[OH^-]^2[O_2]$.

[d] Phosphate, Silica and TCO_2 for pH and pKw calculations taken from Hawkes et al. (2013a). Oxygen data is the mean from 6 Niskins closed at 2319, 2271, 2221 m depth from CTD1 near South Georgia (55˚26.66'S 38˚25.63'W) during JC080.

[e] Oxygen data sourced from WOCE hydrographic program line number AR15, 316 N142_3, station 55. Other data sourced from CD169 CTD station 10 as described in Bennett et al. (2008).

[f] Data sourced from WOCE hydrographic program line number A05, 29HE06_1, station 73 as described in Bennett et al. (2008).

Particle characterisation using Scanning Electron Microscope-Energy Dispersive X-ray (SEM-EDX)

Particles from the BP were collected by in situ filtering of >100 L of plume water through SAPS filters (1 μm pore size, Whatman, 293 mm) at a depth of 2605 m. Recovered filter membranes were stored at -20°C prior to analyses.

Filter membranes were thawed at room temperature and cut in half using ceramic scissors. These were rinsed with pH 8 Milli-Q® water (pH adjusted using optima grade NH_4OH) and filtered onto an acid (10% HNO_3) washed polycarbonate filter membrane (Whatman, 0.2 μm).

Samples were mounted for SEM analysis in two ways, either on metal studs or in resin blocks, as the polished surface of resin blocks allows a higher resolution to be achieved. For metal studs, a 5 mm^2 sample was cut from the filter using Milli-Q® water-rinsed ceramic scissors. This filter sample was mounted onto a metal (Al with 5 % Cu) stub using carbon tape, and coated with 20 nm of C (Edwards Auto 306). For resin blocks, an approximately 1 cm^2 portion of the filter was rinsed with Milli-Q® water to transfer particles onto a glass disk. This disk was mounted in a resin block and the glass polished down and then coated with 20 nm of C (Edwards Auto 306).

Particle analysis was performed using a Carlseiz LEO 1450VP SEM located at The National Oceanography Centre, Southampton, with operating conditions of 19 mm working distance, 20 kV Beam Energy and a nominal probe current of 700 pA. The samples were analysed for sulfides and oxides containing Fe, Zn and Cu. These were identified using the SEM's Backscatter Detector; backscattered electrons are a function of atomic number, therefore, a brighter image is produced for a particle of higher atomic number (Carleton College, 2012). Using this technique it was possible to distinguish the metallic sulfides and oxides (brighter particles) from the biological debris, to identify particles of interest for further elemental analysis. The filters were studied systematically (Fig. S1.a) to enable representative results of the whole sample, and the brighter particles were chosen for spot analysis (Comer, 2013).

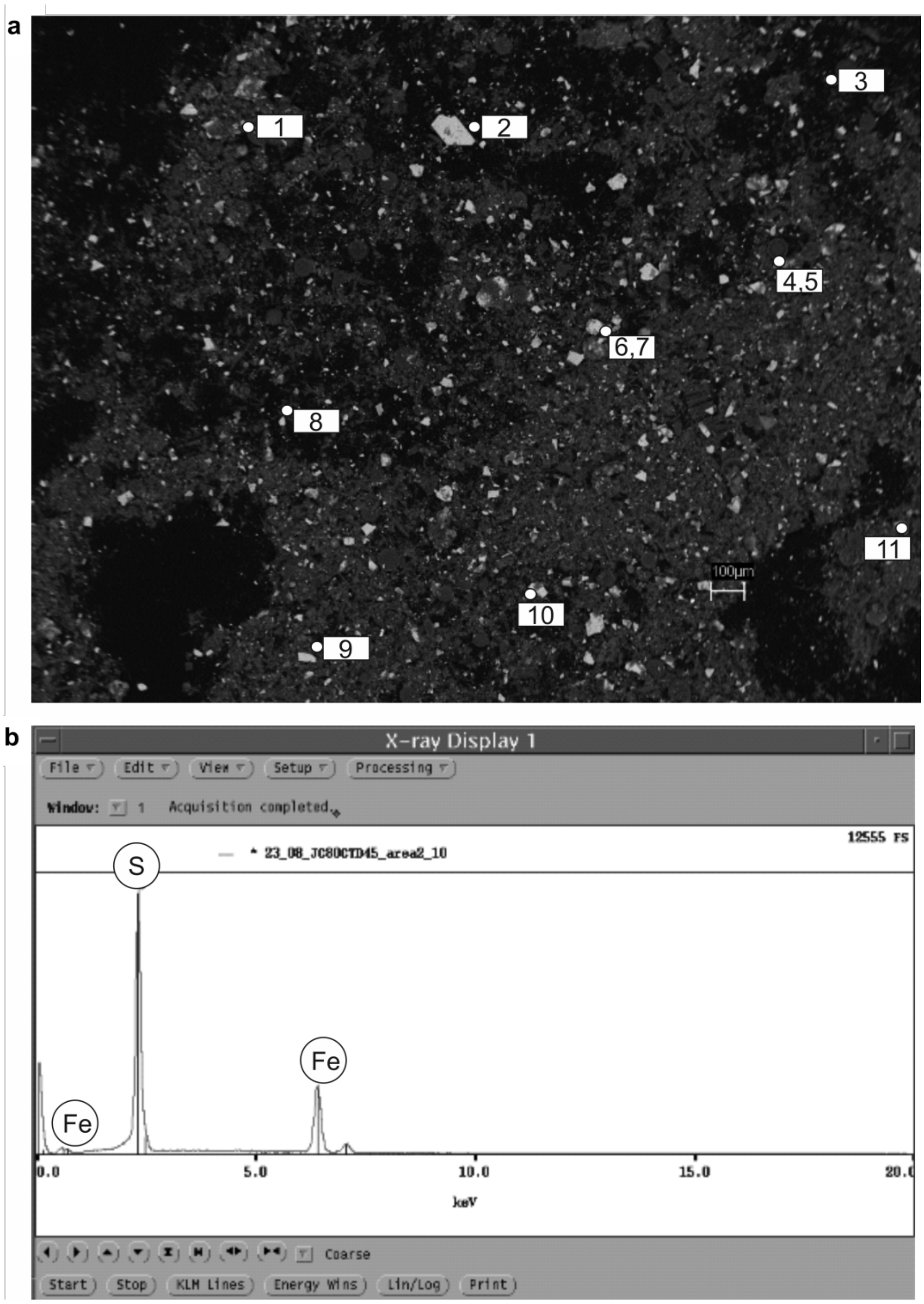

Acquisition completed.

Figure E1 (a) An image of an analysed area from the SAPS filter collected from JC80 CTD45 showing the systematic grid of particles analysed (Comer, 2013), and (b) an example spectra showing the presence of Fe and sulphur in the particle analysed.

Elemental analysis was performed on the selected particles using a Princeton Gamma Technology Light Element Detector EDX analyser built-in to the SEM. This produced qualitative spectra allowing spectra peaks and subsequently the composition of the particle to be identified (Fig. S1.b), and semi-quantitative analysis identifying the relative abundance of each element present.

The mineralogy of each analysed particle was determined from the relative atomic percentage of elements present adapted from Klevenz et al. (2011). Cu was considered first, and was assumed to be present as chalcopyrite ($FeCuS_2$), therefore Cu, Fe and S were removed in a 1:1:2 ratio, if there was a S deficit then CuS was removed instead. Zn was considered next, and was assumed to be ZnS, with Fe considered last as FeS_2 or FeS, depending on the available S budget. If metals remained then these were paired with oxygen as oxides, which reflects the formation of metal sulphides prior to metal oxides in the plume. Fe oxide was considered to be FeOOH due to the short time scales over, which Fe oxide particles form in the plume making more stable Fe oxides such as hematite unlikely.

The analysis of pyrite and pyrrhotite standards (Table S2) resulted in errors from the EDX that were too small to significantly affect the Fe to S ratios and subsequent particle mineralogy. The mineralogy of particles analysed is shown in Table S2.

Table E2. The relative atomic abundance of pyrite and pyrrhotite standards, and the errors associated with these.

Standard	Fe (Atomic %)	Standard Deviation	S (Atomic %)	Standard Deviation
Pyrite	37.7	0.29	62.3	0.29
Pyrrhotite	52.0	0.15	48.0	0.14

Using the mineralogy assignment, Fe particles (*n* = 24) were identified from the total number of analysed particles (*n* =58). The remaining particles found were ZnS (*n* = 21) with other minerals such as $BaSO_4$ and SiO_2. The contribution of each Fe mineral to the total number of Fe particles was calculated as a percentage (Table S2 and Figure 4.4). These percentages are without a stated error because the EDX error is too small to vary the mineralogy assignment.

Fe particles were aggregates composed of smaller particles. Of the Fe aggregate particles analysed 50% were between 1 to 10 μm in size with the other 50% being >10 μm.

Table E3. The number of Fe particles analysed in near-vent plume samples at E2 and the number (N) and percentages of these particles that were observed as $CuFeS_2$, FeS, FeS_2 and FeOOH.

Depth (m)	Total Fe Particles	$CuFeS_2$		FeS		FeS_2		FeOOH	
		N	% of Total Fe	N	% of Total Fe	N	% of Total Fe	N	% of Total Fe
2605	24	0	0	1	4.2	17	70.8	6	25.0

Fe isotope fractionation equations

Scenario 1: Precipitation of FeOOH

$$\delta^{56}dFe = \delta^{56}vFe + \alpha_{ferrihydrite-Fe(aq)} \cdot \ln fdFe \tag{E1}$$

Where $\delta^{56}dFe$ is the resulting Fe isotope composition of dissolved Fe, $\delta^{56}vFe$ is the initial Fe isotope composition of the vent fluid of -0.31 ± 0.03 ‰, $\alpha_{ferrihydrite-Fe(aq)}$ is the fractionation factor of 1.001 for ferrihydrite precipitation determined experimentally by Bullen et al. (2001), and *fdFe* is the fraction of dissolved Fe remaining, which changes from 1 (all Fe dissolved in vent fluid) to 0 (all dFe precipitated as FeOOH) as the reaction proceeds.

Scenario 2: 31 % FeS_2 precipitation (S2) followed by FeOOH precipitation.

$$\delta^{56}vFe_{-pFeS2} = \delta^{56}vFe - \alpha_{FeS-Fe(II)} \cdot \ln fvFe \tag{E2}$$

Where $\delta^{56}vFe_{-pFeS2}$ is the resulting Fe isotope composition of $\delta^{56}vFe$ after 31 % of the vent fluid Fe has precipitated as pyrite. $\delta^{56}vFe$ is the initial Fe isotope composition of the vent fluid of -0.31 ± 0.03 ‰. $\alpha_{FeS-Fe(II)}$ is the fractionation factor of 0.9992 for FeS precipitation determined experimentally by Butler et al. (2005), this is used for lack of a fractionation factor for pyrite precipitation and previous studies of hydrothermal vent particles have shown that this fractionation factor successfully predicts the Fe isotope composition of pyrite (Rouxel et al., 2008, Bennett et al., 2009) and therefore, is appropriate for these calculations. *fvFe* is the fraction of vent fluid Fe remaining after precipitation of 31 % pyrite (therefore *fvFe* = 0.69).

$$\delta^{56}dFe_{S2} = \delta^{56}vFe_{-pFeS2} + \alpha_{ferrihydrite-Fe(aq)} \cdot \ln fdFe \qquad \text{(E3)}$$

Equation S3 is the same as S1 only the initial Fe isotope composition (*fdFe* = 1) is defined by $\delta^{56}vFe_{-pFeS2}$ instead of $\delta^{56}vFe$.

Scenario 3: Scenario 2 + FeS_2 nanoparticles mass balance

$$\delta^{56}dFe = (\delta^{56}nanoFeS_2 \cdot fnanoFeS_2) + (\delta^{56}dFe_{S2} \cdot fdFe_{S2}) \qquad \text{(E4)}$$

Where $\delta^{56}nanoFeS_2$ (the isotope composition of nanoparticulate pyrite) between -0.09 to -0.79 ‰. The upper limit of -0.09 is based on mass balance of δ^{56}TDFe and δ^{56}dFe in the sample with the highest percentage particulate FeS_2. The lower limit of -0.79 is based on kinetic FeS_2 isotope fractionation of the hydrothermal endmember (-0.31 ± 0.03 ‰) after 31 % pyrite precipitation. In both cases this assumes that the $\delta^{56}nanoFeS_2$ is the same as larger FeS_2 particles. $\delta^{56}dFe_{S2}$ is the Fe isotope composition from scenario 2 and $fdFe_{S2}$ is the fraction of dFe from this process. $fnanoFeS_2$ is the fraction of dFe present as FeS_2 nanoparticles, which increases from 0.01 to 0.99 as other dFe species precipitate as pFeOOH until dFe is almost entirely composed of FeS_2 nanoparticles.

Fe isotope composition of the NBP exported to the deep ocean

The dFe exported to the neutrally buoyant plume and deep ocean presented in section 4.5 is calculated using the same method as scenario 2 described above. The fraction of vent dFe still present as Fe(II) at NBP height was calculated based on the plume rise and the Fe(II) oxidation half-lives calculated by Field and Sherrell (2000). The plume rise from vents was calculated from the difference between the seafloor depth and the depth that the NBP was detected in individual studies (Figure 4.2) (Bennett et al., 2009, Mottl and McConachy, 1990, Rudnicki and Elderfield, 1993, Severmann et al., 2004). Once the plume rise distance was calculated a plume rise time was derived from this based on a constant plume rise velocity of 0.1 m s^{-1} (Speer and Rona, 1989). Plume rise times are assigned a 10 % error based on the 10 % difference in plume rise velocity between Pacific and Atlantic plumes (Speer and Rona, 1989). The amount of vent fluid TDFe that precipitates as Fe sulphide particles is taken from the literature (Bennett et al., 2009, Douville et al., 2002, Mottl and McConachy, 1990, Rudnicki and Elderfield, 1993, Severmann et al., 2004). It is assumed that the main Fe sulphide minerals precipitating are either pyrite or pyrrhotite and that the fractionation associated with any chalcopyrite precipitation is small in comparison to FeS_x minerals. The error associated with the amount of Fe-sulphide precipitation is higher for the EPR and TAG and as a result the propagated error of NBP δ^{56}dFe is higher than that of the other sites. Vent end member δ^{56}TDFe of different sites is taken from the literature (Bennett et al., 2009, Rouxel et al., 2008, Severmann et al., 2004) and the vent end member for the EPR is the mean from 7 different vents.

Table E4. Data for calculating dFe exported to the NBP from the BP at different vent sites in different ocean basins.

Input Data

Site	vent end member δ^{56}TDFe (‰)	2SD	X_{FeS}	error	Fe(II) half life (hrs)[a,b]	Vent depth (m)	NBP depth (m)
E2	-0.31	0.03	0.31	0.03	1.38	2605	2360
TAG[c,d]	-0.15	0.07	0.50	0.30	0.41	3645	3375
Rainbow[c]	-0.14	0.09	0.04	0.03	0.29	2400	2050
Red Lion[b]	-0.29	0.10	0.25	0.04	0.45	3045	2775
EPR[e,f]	-0.40	0.14	0.50	0.30	3.49	2500	2000

Calculated Values

	NBP δ^{56}Fe (‰)	error prop.	$X_{dFe} = 1 - X_{FeS}$	error	Rise height (m)	Rise time (hrs)	Rise time 10 % error
E2	-0.28	0.17	0.69	0.03	245	0.68	0.07
TAG	-0.73	0.77	0.50	0.30	270	0.75	0.08
Rainbow	-1.37	0.22	0.96	0.03	350	0.97	0.10
Red Lion	-0.30	0.25	0.75	0.04	270	0.75	0.08
EPR	0.36	0.84	0.50	0.30	500	1.39	0.14

[a] Fe(II) half-lives from Field and Sherrell (2000).

[b] TAG and Red Lion Fe(II) half-lives from Bennett et al. (2008), Red Lion data Bennett et al. (2009) .

[c] Fe isotope data for TAG and Rainbow and X_{FeS} for Rainbow from Severmann et al. (2004).

[d] TAG depths and X_{FeS} from Rudnicki and Elderfield (1993)

[e] EPR Fe isotope data from Rouxel et al. (2008)

[f] EPR depths and X_{FeS} Mottl and McConachy (1990)

List of References

Bibliography

ALBAREDE, F. & BEARD, B. 2004. Analytical methods for non-traditional isotopes. *In:* JOHNSON, C. M., BEARD, B. L. & ALBAREDE, F. (eds.) *Geochemistry of Non-Traditional Stable Isotopes.* Chantilly: Mineralogical Soc Amer.

ANBAR, A. D. 2004. Iron stable isotopes: beyond biosignatures. *Earth and Planetary Science Letters,* 217**,** 223-236.

ANBAR, A. D., JARZECKI, A. A. & SPIRO, T. G. 2005. Theoretical investigation of iron isotope fractionation between Fe(H2O)63+ and Fe(H2O)62+: Implications for iron stable isotope geochemistry. *Geochimica et Cosmochimica Acta,* 69**,** 825-837.

AQUILINA, A., HOMOKY, W. B., HAWKES, J. A., LYONS, T. W. & MILLS, R. A. 2014. Hydrothermal sediments are a source of water column Fe and Mn in the Bransfield Strait, Antarctica. *Geochimica et Cosmochimica Acta,* 137**,** 64-80.

BAKER, E. T., RESING, J. A., HAYMON, R. M., TUNNICLIFFE, V., LAVELLE, J. W., MARTINEZ, F., FERRINI, V., WALKER, S. L. & NAKAMURA, K. 2016. How many vent fields? New estimates of vent field populations on ocean ridges from precise mapping of hydrothermal discharge locations. *Earth and Planetary Science Letters,* 449**,** 186-196.

BALISTRIERI, L., BREWER, P. G. & MURRAY, J. W. 1981. Scavenging residence times of trace metals and surface chemistry of sinking particles in the deep ocean. *Deep Sea Research Part A. Oceanographic Research Papers,* 28**,** 101-121.

BARBEAU, K., RUE, E. L., BRULAND, K. W. & BUTLER, A. 2001. Photochemical cycling of iron in the surface ocean mediated by microbial iron(iii)-binding ligands. *Nature,* 413**,** 409-413.

BAUMGARTNER, J. & FAIVRE, D. 2015. Iron solubility, colloids and their impact on iron (oxyhydr)oxide formation from solution. *Earth-Science Reviews,* 150**,** 520-530.

BEARD, B. L., JOHNSON, C. M., VON DAMM, K. L. & POULSON, R. L. 2003. Iron isotope constraints on Fe cycling and mass balance in oxygenated Earth oceans. *Geology,* 31**,** 629-632.

BEAULIEU, S. E., BAKER, E. T., GERMAN, C. R. & MAFFEI, A. 2013. An authoritative global database for active submarine hydrothermal vent fields. *Geochemistry Geophysics Geosystems,* 14**,** 4892-4905.

BENNETT, S. A., ACHTERBERG, E. P., CONNELLY, D. P., STATHAM, P. J., FONES, G. R. & GERMAN, C. R. 2008. The distribution and stabilisation of dissolved Fe in deep-sea hydrothermal plumes. *Earth and Planetary Science Letters,* 270**,** 157-167.

BENNETT, S. A., COLEMAN, M., HUBER, J. A., REDDINGTON, E., KINSEY, J. C., MCINTYRE, C., SEEWALD, J. S. & GERMAN, C. R. 2013. Trophic regions of a hydrothermal plume dispersing away from an ultramafic-hosted vent-system: Von Damm vent-site, Mid-Cayman Rise. *Geochemistry Geophysics Geosystems,* 14, 317-327.

BENNETT, S. A., ROUXEL, O., SCHMIDT, K., GARBE-SCHONBERG, D., STATHAM, P. J. & GERMAN, C. R. 2009. Iron isotope fractionation in a buoyant hydrothermal plume, 5 degrees S Mid-Atlantic Ridge. *Geochimica Et Cosmochimica Acta,* 73, 5619-5634.

BETHKE, C. M. 1996. *Geochemical Reaction Modelling,* New York, Oxford Univ. Press.

BILLER, D. V. & BRULAND, K. W. 2012. Analysis of Mn, Fe, Co, Ni, Cu, Zn, Cd, and Pb in seawater using the Nobias-chelate PA1 resin and magnetic sector inductively coupled plasma mass spectrometry (ICP-MS). *Marine Chemistry,* 130, 12-20.

BIRCHILL, A., LOHAN, M., MILNE, A., USSHER, S., WOODWARD, M., 2016. Seasonal cycling of dFe in the Celtic Sea. *Challenger society conference 2016.* Liverpool University.

BISCHOFF, J. L. & DICKSON, F. W. 1975. Seawater basalt interactions at 200 degrees C and 500 bars - implications for the origin of seafloor heavy metal deposits and regulation of seawater chemistry. *Earth and Planetary Science Letters,* 25, 385-397.

BISCHOFF, J. L. & PITZER, K. S. 1985. Phase-Relations and Adoabats in Boiling Seafloor Geothermal systems. *Earth and Planetary Science Letters,* 75, 327-338.

BONNAND, P., PARKINSON, I. J., JAMES, R. H., KARJALAINEN, A. M. & FEHR, M. A. 2011. Accurate and precise determination of stable Cr isotope compositions in carbonates by double spike MC-ICP-MS. *Journal of Analytical Atomic Spectrometry,* 26, 528-535.

BOSTROM, K. & PETERSON, M. N. A. 1966. Precipitates from hydrothermal exhalations on the East Pacific rise. *Economic Geology,* 61, 1258-1265.

BOYD, P. W., WATSON, A. J., LAW, C. S., ABRAHAM, E. R., TRULL, T., MURDOCH, R., BAKKER, D. C. E., BOWIE, A. R., BUESSELER, K. O., CHANG, H., CHARETTE, M., CROOT, P., DOWNING, K., FREW, R., GALL, M., HADFIELD, M., HALL, J., HARVEY, M., JAMESON, G., LAROCHE, J., LIDDICOAT, M., LING, R., MALDONADO, M. T., MCKAY, R. M., NODDER, S., PICKMERE, S., PRIDMORE, R., RINTOUL, S., SAFI, K., SUTTON, P., STRZEPEK, R., TANNEBERGER, K., TURNER, S., WAITE, A. & ZELDIS, J. 2000. A mesoscale phytoplankton bloom in the polar Southern Ocean stimulated by iron fertilization. *Nature,* 407, 695-702.

BOYE, M., VAN DEN BERG, C. M. G., DE JONG, J. T. M., LEACH, H., CROOT, P. & DE BAAR, H. J. W. 2001. Organic complexation of iron in the Southern Ocean. *Deep-Sea Research Part I-Oceanographic Research Papers,* 48, 1477-1497.

BREIER, J. A., TONER, B. M., FAKRA, S. C., MARCUS, M. A., WHITE, S. N., THURNHERR, A. M. & GERMAN, C. R. 2012. Sulfur, sulfides, oxides and organic matter aggregated in submarine hydrothermal plumes at 9 degrees 50 ' N East Pacific Rise. *Geochimica et Cosmochimica Acta,* 88, 216-236.

BROWNING, T. J., BOUMAN, H. A., HENDERSON, G. M., MATHER, T. A., PYLE, D. M., SCHLOSSER, C., WOODWARD, E. M. S. & MOORE, C. M. 2014. Strong responses of Southern Ocean phytoplankton communities to volcanic ash. *Geophysical Research Letters,* 41, 2851-2857.

BRUGUIER, N. J. & LIVERMORE, R. A. 2001. Enhanced magma supply at the southern East Scotia Ridge: evidence for mantle flow around the subducting slab? *Earth and Planetary Science Letters,* 191, 129-144.

BRULAND, K. W., RUE, E. L., SMITH, G. J. & DITULLIO, G. R. 2005. Iron, macronutrients and diatom blooms in the Peru upwelling regime: brown and blue waters of Peru. *Marine Chemistry,* 93, 81-103.

BUCK, K. N., SOHST, B. & SEDWICK, P. N. 2015. The organic complexation of dissolved iron along the US GEOTRACES (GA03) North Atlantic Section. *Deep-Sea Research Part Ii-Topical Studies in Oceanography,* 116, 152-165.

BULLEN, T. D., WHITE, A. F., CHILDS, C. W., VIVIT, D. V. & SCHULZ, M. S. 2001. Demonstration of significant abiotic iron isotope fractionation in nature. *Geology,* 29, 699-702.

BUTLER, I. B., ARCHER, C., VANCE, D., OLDROYD, A. & RICKARD, D. 2005. Fe isotope fractionation on FeS formation in ambient aqueous solution. *Earth and Planetary Science Letters,* 236, 430-442.

BUTTERFIELD, D. A. & MASSOTH, G. J. 1994. Geochemistry of North Cleft Segment Vent Fluids- Temporal Changes in Chlorinity and their Possible Relation to Recent Volcanism. *Journal of Geophysical Research-Solid Earth,* 99, 4951-4968.

CAMPBELL, A. C., PALMER, M. R., KLINKHAMMER, G. P., BOWERS, T. S., EDMOND, J. M., LAWRENCE, J. R., CASEY, J. F., THOMPSON, G., HUMPHRIS, S., RONA, P. & KARSON, J. A. 1988. Chemistry of Hot Springs on the Mid-Atlantic Ridge. *Nature,* 335, 514-519.

CARAZZO, G., JELLINEK, A. M. & TURCHYN, A. V. 2013. The remarkable longevity of submarine plumes: Implications for the hydrothermal input of iron to the deep-ocean. *Earth and Planetary Science Letters,* 382, 66-76.

COALE, K. H. & BRULAND, K. W. 1990. Spatial and temporal variability in copper complexation in the North Pacific. *Deep Sea Research Part A. Oceanographic Research Papers,* 37, 317-336.

COMER, S. 2013. *The Comparison of Iron Speciation and Transport between Two Hydrothermal Vent Fields, E2, East Scotia Ridge and Beebe, Mid-*

Cayman Spreading Centre. M.Sc Dissertation, University of Southampton.

CONNELLY, D. P., COPLEY, J. T., MURTON, B. J., STANSFIELD, K., TYLER, P. A., GERMAN, C. R., VAN DOVER, C. L., AMON, D., FURLONG, M., GRINDLAY, N., HAYMAN, N., HUHNERBACH, V., JUDGE, M., LE BAS, T., MCPHAIL, S., MEIER, A., NAKAMURA, K., NYE, V., PEBODY, M., PEDERSEN, R. B., PLOUVIEZ, S., SANDS, C., SEARLE, R. C., STEVENSON, P., TAWS, S. & WILCOX, S. 2012. Hydrothermal vent fields and chemosynthetic biota on the world's deepest seafloor spreading centre. *Nat Commun,* 3, 620.

CONWAY, T. M. & JOHN, S. G. 2014a. The biogeochemical cycling of zinc and zinc isotopes in the North Atlantic Ocean. *Global Biogeochemical Cycles,* 28, 2014GB004862.

CONWAY, T. M. & JOHN, S. G. 2014b. The biogeochemical cycling of zinc and zinc isotopes in the North Atlantic Ocean. *Global Biogeochemical Cycles,* 28, 1111-1128.

CONWAY, T. M. & JOHN, S. G. 2014f. Quantification of dissolved iron sources to the North Atlantic Ocean. *Nature,* 511, 212-215.

CONWAY, T. M., ROSENBERG, A. D., ADKINS, J. F. & JOHN, S. G. 2013. A new method for precise determination of iron, zinc and cadmium stable isotope ratios in seawater by double-spike mass spectrometry. *Analytica Chimica Acta,* 793, 44-52.

COTTE, L., WAELES, M., PERNET-COUDRIER, B., SARRADIN, P.-M., CATHALOT, C. & RISO, R. D. 2015. A comparison of in situ vs. ex situ filtration methods on the assessment of dissolved and particulate metals at hydrothermal vents. *Deep Sea Research Part I: Oceanographic Research Papers,* 105, 186-194.

COWEN, J. P. & LI, Y. H. 1991. The influence of changing bacterial community on trace metal scavenging in a deep sea particle plume. *Journal of Marine Research,* 49, 517-542.

COWEN, J. P., MASSOTH, G. J. & BAKER, E. T. 1986. Bacterial scavenging of Mn and Fe in a Mid Field to Far Field hydrothermal particle plume. *Nature,* 322, 169-171.

COWEN, J. P., MASSOTH, G. J. & FEELY, R. A. 1990. Scavenging rates of dissolved manganese in a hydrothermal vent plume. *Deep Sea Research Part A. Oceanographic Research Papers,* 37, 1619-1637.

D'ORAZIO, M., BOSCHI, C. & BRUNELLI, D. 2004. Talc-rich hydrothermal rocks from the St. Paul and Conrad fracture zones in the Atlantic Ocean. *European Journal of Mineralogy,* 16, 73-83.

DAUPHAS, N., POURMAND, A. & TENG, F. Z. 2009. Routine isotopic analysis of iron by HR-MC-ICPMS: How precise and how accurate? *Chemical Geology,* 267, 175-184.

DOUVILLE, E., CHARLOU, J. L., OELKERS, E. H., BIENVENU, P., COLON, C. F. J., DONVAL, J. P., FOUQUET, Y., PRIEUR, D. & APPRIOU, P. 2002. The rainbow vent fluids (36 degrees 14 ' N, MAR): the influence of ultramafic rocks and phase separation on trace metal content in Mid-Atlantic Ridge hydrothermal fluids. *Chemical Geology,* 184**,** 37-48.

DUPONT, C. L., BUTCHER, A., VALAS, R. E., BOURNE, P. E. & CAETANO-ANOLLÉS, G. 2010. History of biological metal utilization inferred through phylogenomic analysis of protein structures. *Proceedings of the National Academy of Sciences,* 107**,** 10567-10572.

EDMOND, J. M., MEASURES, C., MCDUFF, R. E., CHAN, L. H., COLLIER, R., GRANT, B., GORDON, L. I. & CORLISS, J. B. 1979. RIDGE CREST HYDROTHERMAL ACTIVITY AND THE BALANCES OF THE MAJOR AND MINOR ELEMENTS IN THE OCEAN - GALAPAGOS DATA. *Earth and Planetary Science Letters,* 46**,** 1-18.

EDMONDS, H. N. & GERMAN, C. R. 2004. Particle geochemistry in the Rainbow hydrothermal plume, Mid-Atlantic Ridge. *Geochimica et Cosmochimica Acta,* 68**,** 759-772.

ELDERFIELD, H. & SCHULTZ, A. 1996. Mid-ocean ridge hydrothermal fluxes and the chemical composition of the ocean. *Annual Review of Earth and Planetary Sciences,* 24**,** 191-224.

ELDERFIELD, H., SCHULTZ, A. 1996. Mid-ocean ridge hydrothermal fluxes and chemical composition of the ocean. *Annu. Rev. Earth Planet. Sci.,* 24**,** 191-224.

ELLWOOD, M. J. & VAN DEN BERG, C. M. G. 2000. Zinc speciation in the Northeastern Atlantic Ocean. *Marine Chemistry,* 68**,** 295-306.

ELROD, V. A. 2004. The flux of iron from continental shelf sediments: A missing source for global budgets. *Geophysical Research Letters,* 31.

ESCOUBE, R., ROUXEL, O. J., SHOLKOVITZ, E. & DONARD, O. F. X. 2009. Iron isotope systematics in estuaries: The case of North River, Massachusetts (USA). *Geochimica Et Cosmochimica Acta,* 73**,** 4045-4059.

ESTAPA, M. L., BREIER, J. A. & GERMAN, C. R. 2015. Particle dynamics in the rising plume at Piccard Hydrothermal Field, Mid-Cayman Rise. *Geochemistry Geophysics Geosystems,* 16**,** 2762-2774.

FAN, S. M., MOXIM, W. J. & LEVY, H. 2006. Aeolian input of bioavailable iron to the ocean. *Geophysical Research Letters,* 33**,** 4.

FEELY, R. A., BAKER, E. T., MARUMO, K., URABE, T., ISHIBASHI, J., GENDRON, J., LEBON, G. T. & OKAMURA, K. 1996. Hydrothermal plume particles and dissolved phosphate over the superfast-spreading southern East Pacific Rise. *Geochimica Et Cosmochimica Acta,* 60**,** 2297-2323.

FEELY, R. A., GENDRON, J. F., BAKER, E. T. & LEBON, G. T. 1994a. Hydrothermal plumes along the east pacific rise, 8-degrees-40' to 11-degrees-50'N -

particle distribution and composition. *Earth and Planetary Science Letters,* 128**,** 19-36.

FEELY, R. A., LEWISON, M., MASSOTH, G. J., ROBERTBALDO, G., LAVELLE, J. W., BYRNE, R. H., VONDAMM, K. L. & CURL, H. C. 1987. Composition and dissolution of black smoker particulates from active vents on the Jaun de Fuca ridge. *Journal of Geophysical Research-Solid Earth and Planets,* 92**,** 11347-11363.

FEELY, R. A., MASSOTH, G. J., TREFRY, J. H., BAKER, E. T., PAULSON, A. J. & LEBON, G. T. 1994k. Composition and sedimentation of hydrothermal plume particles from North Cleft Segment, Juan De Fuca Ridge. *Journal of Geophysical Research-Solid Earth,* 99**,** 4985-5006.

FEELY, R. A., TREFRY, J. H., LEBON, G. T. & GERMAN, C. R. 1998. The relationship between P/Fe and V/Fe ratios in hydrothermal precipitates and dissolved phosphate in seawater. *Geophysical Research Letters,* 25**,** 2253-2256.

FIELD, C. B., BEHRENFELD, M. J., RANDERSON, J. T. & FALKOWSKI, P. 1998. Primary Production of the Biosphere: Integrating Terrestrial and Oceanic Components. *Science,* 281**,** 237-240.

FIELD, M. P. & SHERRELL, R. M. 2000. Dissolved and particulate Fe in a hydrothermal plume at 9 degrees 45 ' N, East Pacific Rise: Slow Fe (II) oxidation kinetics in Pacific plumes. *Geochimica et Cosmochimica Acta,* 64**,** 619-628.

FINDLAY, A. J., GARTMAN, A., MACDONALD, D. J., HANSON, T. E., SHAW, T. J. & LUTHER III, G. W. 2014. Distribution and size fractionation of elemental sulfur in aqueous environments: The Chesapeake Bay and Mid-Atlantic Ridge. *Geochimica et Cosmochimica Acta,* 142**,** 334-348.

FINDLAY, A. J., GARTMAN, A., SHAW, T. J. & LUTHER, G. W. 2015. Trace metal concentration and partitioning in the first 1.5 m of hydrothermal vent plumes along the Mid-Atlantic Ridge: TAG, Snakepit, and Rainbow. *Chemical Geology,* 412**,** 117-131.

FITZSIMMONS, J. N., BOYLE, E. A. & JENKINS, W. J. 2014. Distal transport of dissolved hydrothermal iron in the deep South Pacific Ocean. *Proceedings of the National Academy of Sciences of the United States of America,* 111**,** 16654-16661.

FITZSIMMONS, J. N., CARRASCO, G. G., WU, J. F., ROSHAN, S., HATTA, M., MEASURES, C. I., CONWAY, T. M., JOHN, S. G. & BOYLE, E. A. 2015. Partitioning of dissolved iron and iron isotopes into soluble and colloidal phases along the GA03 GEOTRACES North Atlantic Transect. *Deep-Sea Research Part Ii-Topical Studies in Oceanography,* 116**,** 130-151.

GAMO, T., ISHIBASHI, J., TSUNOGAI, U., OKAMURA, K. & CHIBA, H. 2006. Unique geochemistry of submarine hydrothermal fluids from arc-back-arc settings of the western pacific. *In:* CHRISTIE, D. M., FISHER, C. R., LEE, S. M. & GIVENS, S. (eds.) *Back-Arc Spreading Systems: Geological,* *Biological, Chemical, and Physical Interactions.* Washington: Amer Geophysical Union.

GARTMAN, A., FINDLAY, A. J. & LUTHER, G. W. 2014. Nanoparticulate pyrite and other nanoparticles are a widespread component of hydrothermal vent black smoker emissions. *Chemical Geology,* 366**,** 32-41.

GARTMAN, A. & LUTHER, G. W. 2013. Comparison of pyrite (FeS2) synthesis mechanisms to reproduce natural FeS2 nanoparticles found at hydrothermal vents. *Geochimica Et Cosmochimica Acta,* 120**,** 447-458.

GARTMAN, A. & LUTHER, G. W. 2014. Oxidation of synthesized sub-micron pyrite (FeS2) in seawater. *Geochimica Et Cosmochimica Acta,* 144**,** 96-108.

GERMAN, C. 2016. GEOTRACES Royal Society meeting on ocean boundary fluxes. *in prep.*

GERMAN, C. & VON DAMM, K. L. 2004. Hydrothermal Processes. *In:* ELDERFIELD, H. (ed.) *The Oceans and Marine Geochemistry. Treatise on Geochemistry.* Oxford: Elsevier-Pergamon.

GERMAN, C. R., BOWEN, A., COLEMAN, M. L., HONIG, D. L., HUBER, J. A., JAKUBA, M. V., KINSEY, J. C., KURZ, M. D., LEROY, S., MCDERMOTT, J. M., DE LEPINAY, B. M., NAKAMURA, K., SEEWALD, J. S., SMITH, J. L., SYLVA, S. P., VAN DOVER, C. L., WHITCOMB, L. L. & YOERGER, D. R. 2010. Diverse styles of submarine venting on the ultraslow spreading Mid-Cayman Rise. *Proceedings of the National Academy of Sciences of the United States of America,* 107**,** 14020-14025.

GERMAN, C. R., CAMPBELL, A. C. & EDMOND, J. M. 1991. Hydrothermal scavenging at the Mid-Atlantic Ridge - modification of trace-element dissolved fluxes. *Earth and Planetary Science Letters,* 107**,** 101-114.

GERMAN, C. R., KLINKHAMMER, G. P. & RUDNICKI, M. D. 1996. The Rainbow hydrothermal plume, 36 degrees 15'N, MAR. *Geophysical Research Letters,* 23**,** 2979-2982.

GERMAN, C. R., LIVERMORE, R. A., BAKER, E. T., BRUGUIER, N. I., CONNELLY, D. P., CUNNINGHAM, A. P., MORRIS, P., ROUSE, I. P., STATHAM, P. J. & TYLER, P. A. 2000. Hydrothermal plumes above the East Scotia Ridge: an isolated high-latitude back-arc spreading centre. *Earth and Planetary Science Letters,* 184**,** 241-250.

GERMAN, C. R., PETERSEN, S. & HANNINGTON, M. D. 2016. Hydrothermal exploration of mid-ocean ridges: Where might the largest sulfide deposits be forming? *Chemical Geology,* 420**,** 114-126.

GERMAN, C. R., RAMIREZ-LLODRA, E., BAKER, M. C., TYLER, P. A. & CHESS SCI STEERING, C. 2011. Deep-Water Chemosynthetic Ecosystem Research during the Census of Marine Life Decade and Beyond: A Proposed Deep-Ocean Road Map. *Plos One,* 6**,** 16.

GOLDSTEIN, J., NEWBURY, D. E., JOY, D. C., LYMAN, C. E., ECHLIN, P., LIFSHIN, E., SAWYER, L. & MICHAEL, J. R. 2003. *Scanning Electron microscopy and X-ray Microanalysis.,* New York., Springer.

GUO, X., ZHANG, S., SHAN, X.-Q., LUO, L., PEI, Z., ZHU, Y.-G., LIU, T., XIE, Y.-N. & GAULT, A. 2006. Characterization of Pb, Cu, and Cd adsorption on particulate organic matter in soil. *Environmental Toxicology and Chemistry,* 25**,** 2366-2373.

HANSEN, H. P. 2007. Determination of oxygen. *In:* GRASSHOFF, K., KREMLING, K. & EHRHARDT, M. (eds.) *Methods of Seawater Analysis.* Wiley Online Library: Wiley-VCH Verlag GmbH.

HATTA, M., MEASURES, C. I., WU, J. F., ROSHAN, S., FITZSIMMONS, J. N., SEDWICK, P. & MORTON, P. 2015. An overview of dissolved Fe and Mn distributions during the 2010-2011 US GEOTRACES north Atlantic cruises: GEOTRACES GA03. *Deep-Sea Research Part Ii-Topical Studies in Oceanography,* 116**,** 117-129.

HAWKES, J. A., CONNELLY, D. P., GLEDHILL, M. & ACHTERBERG, E. P. 2013a. The stabilisation and transportation of dissolved iron from high temperature hydrothermal vent systems. *Earth and Planetary Science Letters,* 375**,** 280-290.

HAWKES, J. A., CONNELLY, D. P., RIJKENBERG, M. J. A. & ACHTERBERG, E. P. 2014. The importance of shallow hydrothermal island arc systems in ocean biogeochemistry. *Geophysical Research Letters***,** 2013GL058817.

HAWKES, J. A., GLEDHILL, M., CONNELLY, D. P. & ACHTERBERG, E. P. 2013ab. Characterisation of iron binding ligands in seawater by reverse titration. *Analytica Chimica Acta,* 766**,** 53-60.

HAWKES, J. A., ROSSEL, P. E., STUBBINS, A., BUTTERFIELD, D., CONNELLY, D. P., ACHTERBERG, E. P., KOSCHINSKY, A., CHAVAGNAC, V., HANSEN, C. T., BACH, W. & DITTMAR, T. 2015. Efficient removal of recalcitrant deep-ocean dissolved organic matter during hydrothermal circulation. *Nature Geoscience,* 8**,** 856-+.

HAWKINGS, J. R., WADHAM, J. L., TRANTER, M., RAISWELL, R., BENNING, L. G., STATHAM, P. J., TEDSTONE, A., NIENOW, P., LEE, K. & TELLING, J. 2014. Ice sheets as a significant source of highly reactive nanoparticulate iron to the oceans. *Nature Communications,* 5**,** 8.

HAYMON, R. M. 1983. Growth History of Hydrothermal Black Smoker Chimneys. *Nature,* 301**,** 695-698.

HENDERSON, G. M., ANDERSON, R. F., ADKINS, J., ANDERSSON, P., BOYLE, E. A., CUTTER, G., DE BAAR, H., EISENHAUER, A., FRANK, M., FRANCOIS, R., ORIANS, K., GAMO, T., GERMAN, C., JENKINS, W., MOFFETT, J., JEANDEL, C., JICKELLS, T., KRISHNASWAMI, S., MACKEY, D., MEASURES, C. I., MOORE, J. K., OSCHLIES, A., POLLARD, R., VAN DER LOEFF, M. R. D., SCHLITZER, R., SHARMA, M., VON DAMM, K., ZHANG, J., MASQUE, P. & GRP, S. W. 2007. GEOTRACES - An international study of the global marine biogeochemical cycles of trace elements and their isotopes. *Chemie Der Erde-Geochemistry,* 67, 85-131.

HITCH. 2012. *Spectroscopic Analysis of Hydrothermal Plume Particles from the Scotia Sea.* M.Sc, University of Southampton, National Oceanography Centre Southampton (NOCS).

HOCHELLA, M. F., ARUGUETE, D., KIM, B. & MADDEN, A. S. 2012. Naturally Occurring Inorganic Nanoparticles: General Assessment and a Global Budget for One of Earth's Last Unexplored Major Geochemical Components. *Nature's Nanostructures*, 1-42.

HOCHELLA, M. F., LOWER, S. K., MAURICE, P. A., PENN, R. L., SAHAI, N., SPARKS, D. L. & TWINING, B. S. 2008. Nanominerals, Mineral Nanoparticles, and Earth Systems. *Science,* 319, 1631-1635.

HODGKINSON, M. R. S., WEBBER, A. P., ROBERTS, S., MILLS, R. A., CONNELLY, D. P. & MURTON, B. J. 2015. Talc-dominated seafloor deposits reveal a new class of hydrothermal system. *Nature communications,* 6, 10150.

HOMOKY, W. B., HEMBURY, D. J., HEPBURN, L. E., MILLS, R. A., STATHAM, P. J., FONES, G. R. & PALMER, M. R. 2011. Iron and manganese diagenesis in deep sea volcanogenic sediments and the origins of pore water colloids. *Geochimica et Cosmochimica Acta,* 75, 5032-5048.

HOMOKY, W. B., JOHN, S. G., CONWAY, T. M. & MILLS, R. A. 2013. Distinct iron isotopic signatures and supply from marine sediment dissolution. *Nature Communications,* 4, 10.

HOMOKY, W. B., SEVERMANN, S., MCMANUS, J., BERELSON, W.M., RIEDEL T.E, STATHAM, P.J, MILLS R.A., 2012. Dissolved oxygen and suspended particles regulate the benthic flux of iron from continental margins. *Marine Chemistry,* 134-135, 59-70.

HORNER, T. J., WILLIAMS, H. M., HEIN, J. R., SAITO, M. A., BURTON, K. W., HALLIDAY, A. N. & NIELSEN, S. G. 2015. Persistence of deeply sourced iron in the Pacific Ocean. *Proceedings of the National Academy of Sciences of the United States of America,* 112, 1292-1297.

HSU-KIM, H., MULLAUGH, K. M., TSANG, J. J., YUCEL, M. & LUTHER, G. W. 2008. Formation of Zn- and Fe-sulfides near hydrothermal vents at the Eastern Lau Spreading Center: implications for sulfide bioavailability to chemoautotrophs. *Geochemical Transactions,* 9, 14.

HUTTON, R. C. & EATON, A. N. 1988. Analysis of solutions containing high levels of dissolved solids by inductively coupled plasma mass spectrometry. *Journal of Analytical Atomic Spectrometry,* 3, 547-550.

ICOPINI, G. A., ANBAR, A. D., RUEBUSH, S. S., TIEN, M. & BRANTLEY, S. L. 2004. Iron isotope fractionation during microbial reduction of iron: The importance of adsorption. *Geology,* 32, 205-208.

ISHIBASHI 1995. Backarc Basins: Tectonics and Magmatism. *In:* TAYLOR, B. (ed.) *Hydrothermal activity related to arc-backarc magmatism in the western Pacific.* NY: Plenum.

ISHIBASHI, J., TSUNOGAI, U., TOKI, T., EBINA, N., GAMO, T., SANO, Y., MASUDA, H. & CHIBA, H. 2015. Chemical composition of hydrothermal fluids in the central and southern Mariana Trough backarc basin. *Deep-Sea Research Part Ii-Topical Studies in Oceanography,* 121, 126-136.

JACQUOT, J. E. & MOFFETT, J. W. 2015. Copper distribution and speciation across the International GEOTRACES Section GA03. *Deep-Sea Research Part Ii-Topical Studies in Oceanography,* 116, 187-207.

JAMES, R. H. & ELDERFIELD, H. 1996. Dissolved and particulate trace metals in hydrothermal plumes at the Mid-Atlantic Ridge. *Geophysical Research Letters,* 23, 3499-3502.

JAMES, R. H., ELDERFIELD, H. & PALMER, M. R. 1995. The chemistry of hydrothermal fluids from the broken spur site, 29 degrees N Mid Atlantic Ridge. *Geochimica et Cosmochimica Acta,* 59, 651-659.

JAMES, R. H., GREEN, D. R. H., STOCK, M. J., ALKER, B. J., BANERJEE, N. R., COLE, C., GERMAN, C. R., HUVENNE, V. A. I., POWELL, A. M. & CONNELLY, D. P. 2014. Composition of hydrothermal fluids and mineralogy of associated chimney material on the East Scotia Ridge back-arc spreading centre. *Geochimica Et Cosmochimica Acta,* 139, 47-71.

JANECKY, D. R. & SEYFRIED, W. E. 1984. Formation of massive sulfide deposits on oceanic ridge crests: Incremental reaction models for mixing between hydrothermal solutions and seawater. *Geochimica et Cosmochimica Acta,* 48, 2723-2738.

JICKELLS, T. D., AN, Z. S., ANDERSEN, K. K., BAKER, A. R., BERGAMETTI, G., BROOKS, N., CAO, J. J., BOYD, P. W., DUCE, R. A., HUNTER, K. A., KAWAHATA, H., KUBILAY, N., LAROCHE, J., LISS, P. S., MAHOWALD, N., PROSPERO, J. M., RIDGWELL, A. J., TEGEN, I. & TORRES, R. 2005. Global iron connections between desert dust, ocean biogeochemistry, and climate. *Science,* 308, 67-71.

JOHN, S. G. & ADKINS, J. 2012. The vertical distribution of iron stable isotopes in the North Atlantic near Bermuda. *Global Biogeochemical Cycles,* 26, 10.

JOHNS, W. E., TOWNSEND, T. L., FRATANTONI, D. M. & WILSON, W. D. 2002. On the Atlantic inflow to the Caribbean Sea. *Deep-Sea Research Part I-Oceanographic Research Papers,* 49, 211-243.

JOHNSON, C. M., BEARD, B. L., RODEN, E. E., NEWMAN, D. K. & NEALSON, K. H. 2004. Isotopic constraints on biogeochemical cycling of Fe. *In:* JOHNSON, C. M., BEARD, B. L. & ALBAREDE, F. (eds.) *Geochemistry of Non-Traditional Stable Isotopes.* Washington: Mineralogical Soc America.

JOHNSON, K. S., GORDON, R. M. & COALE, K. H. 1997. What controls dissolved iron concentrations in the world ocean? Authors' closing comments. *Marine Chemistry,* 57, 181-186.

KAEDING, J. 1973. W. Stumm und J. J. Morgan: Aquatic Chemistry An Introduction Emphasizing Chemical Equilibria in Natural Waters. New York, London, Sydney, Toronto, Wiley-Interscience, 1970, 583 S., zahlr. Abb. und Tab. *Acta hydrochimica et hydrobiologica,* 1, 117-117.

KAGAYA, S., MAEBA, E., INOUE, Y., KAMICHATANI, W., KAJIWARA, T., YANAI, H., SAITO, M. & TOHDA, K. 2009. A solid phase extraction using a chelate resin immobilizing carboxymethylated pentaethylenehexamine for separation and preconcentration of trace elements in water samples. *Talanta,* 79, 146-152.

KEELING, R. F., KÖRTZINGER, A. & GRUBER, N. 2010. Ocean Deoxygenation in a Warming World. *Annual Review of Marine Science,* 2, 199-229.

KELLEY, D. S., KARSON, J. A., BLACKMAN, D. K., FRUH-GREEN, G. L., BUTTERFIELD, D. A., LILLEY, M. D., OLSON, E. J., SCHRENK, M. O., ROE, K. K., LEBON, G. T., RIVIZZIGNO, P. & PARTY, A. T. S. 2001. An off-axis hydrothermal vent field near the Mid-Atlantic Ridge at 30 degrees N. *Nature,* 412, 145-149.

KELLEY, D. S., KARSON, J. A., FRUH-GREEN, G. L., YOERGER, D. R., SHANK, T. M., BUTTERFIELD, D. A., HAYES, J. M., SCHRENK, M. O., OLSON, E. J., PROSKUROWSKI, G., JAKUBA, M., BRADLEY, A., LARSON, B., LUDWIG, K., GLICKSON, D., BUCKMAN, K., BRADLEY, A. S., BRAZELTON, W. J., ROE, K., ELEND, M. J., DELACOUR, A., BERNASCONI, S. M., LILLEY, M. D., BAROSS, J. A., SUMMONS, R. T. & SYLVA, S. P. 2005. A serpentinite-hosted ecosystem: The lost city hydrothermal field. *Science,* 307, 1428-1434.

KLEINT, C., HAWKES, J. A., SANDER, S. G. & KOSCHINSKY, A. 2016. Voltammetric Investigation Of Hydrothermal Iron Speciation. *Frontiers in Marine Science,* 3.

KLEVENZ, V., BACH, W., SCHMIDT, K., HENTSCHER, M., KOSCHINSKY, A. & PETERSEN, S. 2011. Geochemistry of vent fluid particles formed during initial hydrothermal fluid–seawater mixing along the Mid-Atlantic Ridge. *Geochemistry Geophysics Geosystems,* 12.

KLINKHAMMER, G., ELDERFIELD, H. & HUDSON, A. 1983. Rare-Earth Elements in Seawater Near Hydrothermal Vents. *Nature,* 305, 185-188.

KLUNDER, M. B., LAAN, P., DE BAAR, H. J. W., MIDDAG, R., NEVEN, I. & VAN OOIJEN, J. 2014. Dissolved Fe across the Weddell Sea and Drake Passage: impact of DFe on nutrient uptake. *Biogeosciences,* 11, 651-669.

KLUNDER, M. B., LAAN, P., MIDDAG, R., DE BAAR, H. J. W. & BAKKER, K. 2012. Dissolved iron in the Arctic Ocean: Important role of hydrothermal sources, shelf input and scavenging removal. *Journal of Geophysical Research-Oceans,* 117, 17.

KLUNDER, M. B., LAAN, P., MIDDAG, R., DE BAAR, H. J. W. & VAN OOIJEN, J. C. 2011. Dissolved iron in the Southern Ocean (Atlantic sector). *Deep-Sea Research Part Ii-Topical Studies in Oceanography,* 58**,** 2678-2694.

LABATUT, M., LACAN, F., PRADOUX, C., CHMELEFF, J., RADIC, A., MURRAY, J. W., POITRASSON, F., JOHANSEN, A. M. & THIL, F. 2014. Iron sources and dissolved-particulate interactions in the seawater of the Western Equatorial Pacific, iron isotope perspectives. *Global Biogeochemical Cycles,* 28**,** 1044-1065.

LACAN, F., RADIC, A., JEANDEL, C., POITRASSON, F., SARTHOU, G., PRADOUX, C. & FREYDIER, R. 2008. Measurement of the isotopic composition of dissolved iron in the open ocean. *Geophysical Research Letters,* 35**,** 5.

LACAN, F., RADIC, A., LABATUT, M., JEANDEL, C., POITRASSON, F., SARTHOU, G., PRADOUX, C., CHMELEFF, J. & FREYDIER, R. 2010. High-Precision Determination of the Isotopic Composition of Dissolved Iron in Iron Depleted Seawater by Double Spike Multicollector-ICPMS. *Analytical Chemistry,* 82**,** 7103-7111.

LEE, J.-M., BOYLE, E. A., ECHEGOYEN-SANZ, Y., FITZSIMMONS, J. N., ZHANG, R. & KAYSER, R. A. 2011. Analysis of trace metals (Cu, Cd, Pb, and Fe) in seawater using single batch nitrilotriacetate resin extraction and isotope dilution inductively coupled plasma mass spectrometry. *Analytica Chimica Acta,* 686**,** 93-101.

LEROY, S., MAUFFRET, A., PATRIAT, P. & DE LEPINAY, B. M. 2000. An alternative interpretation of the Cayman trough evolution from a reidentification of magnetic anomalies. *Geophysical Journal International,* 141**,** 539-557.

LEVASSEUR, S., FRANK, M., HEIN, J. R. & HALLIDAY, A. 2004. The global variation in the iron isotope composition of marine hydrogenetic ferromanganese deposits: implications for seawater chemistry? *Earth and Planetary Science Letters,* 224**,** 91-105.

LI, M., TONER, B. M., BAKER, B. J., BREIER, J. A., SHEIK, C. S. & DICK, G. J. 2014. Microbial iron uptake as a mechanism for dispersing iron from deep-sea hydrothermal vents. *Nature Communications,* 5**,** 8.

LOHAN, M. C., AGUILAR-ISLAS, A. M. & BRULAND, K. W. 2006. Direct determination of iron in acidified (pH 1.7) seawater samples by flow injection analysis with catalytic spectrophotometric detection: Application and intercomparison. *Limnology and Oceanography: Methods,* 4**,** 164-171.

LOHAN, M. C. & BRULAND, K. W. 2008. Elevated Fe(II) and dissolved Fe in hypoxic shelf waters off Oregon and Washington: An enhanced source of iron to coastal upwelling regimes. *Environmental Science & Technology,* 42**,** 6462-6468.

LOHAN, M. C., CRAWFORD, D. W., PURDIE, D. A. & STATHAM, P. J. 2005. Iron and zinc enrichments in northeast subarctic Pacific: Ligand production and zinc availibility in response to phytoplankton growth. *Limnology and Oceanography,* 50**,** 1427-1437.

LOSCHER, B. M., DEBAAR, H. J. W., DEJONG, J. T. M., VETH, C. & DEHAIRS, F. 1997. The distribution of Fe in the Antarctic Circumpolar Current. *Deep-Sea Research Part Ii-Topical Studies in Oceanography,* 44**,** 143-187.

LUTHER, G. W. & FERDELMAN, T. G. 1993. Voltammetric characterisation of iron (II) sulfide complexes in laboratory solutions and in marine waters and porewaters. *Environmental Science & Technology,* 27**,** 1154-1163.

LUTHER, G. W., FINDLAY, A. J., MACDONALD, D. J., OWINGS, S. M., HANSON, T. E., BEINART, R. A. & GIRGUIS, P. R. 2011. Thermodynamics and Kinetics of Sulfide Oxidation by Oxygen: A Look at Inorganically Controlled Reactions and Biologically Mediated Processes in the Environment. *Frontiers in Microbiology,* 2**,** 62.

MADDEN, A. S. & HOCHELLA, M. F. 2005. A test of geochemical reactivity as a function of mineral size: Manganese oxidation promoted by hematite nanoparticles. *Geochimica Et Cosmochimica Acta,* 69**,** 389-398.

MADDEN, A. S., HOCHELLA, M. F. & LUXTON, T. P. 2006. Insights for size-dependent reactivity of hematite nanomineral surfaces through Cu2+ sorption. *Geochimica Et Cosmochimica Acta,* 70**,** 4095-4104.

MAHOWALD, N. M., MUHS, D. R., LEVIS, S., RASCH, P. J., YOSHIOKA, M., ZENDER, C. S. & LUO, C. 2006. Change in atmospheric mineral aerosols in response to climate: Last glacial period, preindustrial, modern, and doubled carbon dioxide climates. *Journal of Geophysical Research-Atmospheres,* 111.

MANN, E. L., AHLGREN, N., MOFFETT, J. W. & CHISHOLM, S. W. 2002. Copper toxicity and cyanobacteria ecology in the Sargasso Sea. *Limnology and Oceanography,* 47**,** 976-988.

MARTIN, J. H. 1990. Glacial-interglacial CO2 change: the iron hypothesis. *Paleoceanography,* 5**,** 1-13.

MCCARTHY, K. T., PICHLER, T. & PRICE, R. E. 2005. Geochemistry of Champagne Hot Springs shallow hydrothermal vent field and associated sediments, Dominica, Lesser Antilles. *Chemical Geology,* 224**,** 55-68.

MCCOLLOM, T. M. 2000. Geochemical constraints on primary productivity in submarine hydrothermal vent plumes. *Deep Sea Research Part I: Oceanographic Research Papers,* 47**,** 85-101.

MCDUFF, R. E. 1995. Physical dynamics of deep sea hydrothermal plumes. *In:* HUMPHRIS, S. E., ZIERENBERG, R. A., MULLINEAUX, L. S. & THOMSON, R. E. (eds.) *Saefloor Hydrothermal Systems: Physical, Chemical, Biological and Geological Interactions.* Washington D.C: American Geophysical Union.

METZ, S. & TREFRY, J. H. 2000. Chemical and mineralogical influences on concentrations of trace metals in hydrothermal fluids. *Geochimica Et Cosmochimica Acta,* 64**,** 2267-2279.

METZ, S. A. T., JOHN H., 1993. Field and laboratory studies of metal uptake and release by hydrothermal precipitates. *Journal of Geophysical Research: Solid Earth,* 98, 2156-2202.

MICHARD, A., ALBAREDE, F., MICHARD, G., MINSTER, J. F. & CHARLOU, J. L. 1983. Rare-Earth Elements and Uranium in High Temperature Solutions from East Pacific Rise Hydrothermal Vent Field (13-Degrees-N) *Nature,* 303, 795-797.

MIDDAG, R., DE BAAR, H. J. W., LAAN, P. & KLUNDER, M. B. 2011. Fluvial and hydrothermal input of manganese into the Arctic Ocean. *Geochimica Et Cosmochimica Acta,* 75, 2393-2408.

MIKUTTA, C., WIEDERHOLD, J. G., CIRPKA, O. A., HOFSTETTER, T. B., BOURDON, B. & VON GUNTEN, U. 2009. Iron isotope fractionation and atom exchange during sorption of ferrous iron to mineral surfaces. *Geochimica Et Cosmochimica Acta,* 73, 1795-1812.

MILLER, J. N. & MILLER, J. C. 2000. *Statistics and Chemometrics for Analytical Chemistry*, Prentice Hall.

MILLERO, F. J., SOTOLONGO, S. & IZAGUIRRE, M. 1987. The Oxidation Kinetics of Fe(II) in Seawater. *Geochimica et Cosmochimica Acta,* 51, 793-801.

MILLS, R., ELDERFIELD, H. & THOMSON, J. 1993. A dual origin for the metalliferous sediment core from the Mid-Atlantic Ridge. *Journal of Geophysical Research-Solid Earth,* 98, 9671-9681.

MILLS, R. A., THOMSON, J., ELDERFIELD, H., HINTON, R. W. & HYSLOP, E. 1994. Uranium enrichment in metalliferous sediments from the Mid-Atlantic Ridge. *Earth and Planetary Science Letters,* 124, 35-47.

MILNE, A., LANDING, W., BIZIMIS, M. & MORTON, P. 2010. Determination of Mn, Fe, Co, Ni, Cu, Zn, Cd and Pb in seawater using high resolution magnetic sector inductively coupled mass spectrometry (HR-ICP-MS). *Analytica Chimica Acta,* 665, 200-207.

MOORE, C. M., MILLS, M. M., ARRIGO, K. R., BERMAN-FRANK, I., BOPP, L., BOYD, P. W., GALBRAITH, E. D., GEIDER, R. J., GUIEU, C., JACCARD, S. L., JICKELLS, T. D., LA ROCHE, J., LENTON, T. M., MAHOWALD, N. M., MARANON, E., MARINOV, I., MOORE, J. K., NAKATSUKA, T., OSCHLIES, A., SAITO, M. A., THINGSTAD, T. F., TSUDA, A. & ULLOA, O. 2013. Processes and patterns of oceanic nutrient limitation. *Nature Geosci,* 6, 701-710.

MOORE, J. K., DONEY, S. C. & LINDSAY, K. 2004. Upper ocean ecosystem dynamics and iron cycling in a global three-dimensional model. *Global Biogeochemical Cycles,* 18, 21.

MOREL, F. M. M. & PRICE, N. M. 2003. The Biogeochemical Cycles of Trace Metals in the Oceans. *Science,* 300, 944-947.

MOREL, F. M. M., REINFELDER, J. R., ROBERTS, S. B., CHAMBERLAIN, C. P., LEE, J. G. & YEE, D. 1994. Zinc and Carbon Co-Limitation of Marine-Phytoplakton. *Nature,* 369, 740-742.

MORSE, J. W. & LUTHER, G. W. 1999. Chemical influences on trace metal-sulfide interactions in anoxic sediments. *Geochimica Et Cosmochimica Acta,* 63, 3373-3378.

MOTTL, M. J. & MCCONACHY, T. F. 1990. Chemical processes in buoyant hydrothermal plumes on the East Pacific Rise near 21^{0}N. *Geochimica et Cosmochimica Acta,* 54, 1911-1927.

MYLON, S. E., CHEN, K. L. & ELIMELECH, M. 2004. Influence of Natural Organic Matter and Ionic Composition on the Kinetics and Structure of Hematite Colloid Aggregation: Implications to Iron Depletion in Estuaries. *Langmuir,* 20, 9000-9006.

NAVEIRA GARABATO, A. C., MCDONAGH, E. L., STEVENS, D. P., HEYWOOD, K. J. & SANDERS, R. J. 2002. On the export of Antarctic Bottom Water from the Weddell Sea. *Deep-Sea Research, Part II (Topical Studies in Oceanography),* 49, 4715-4742.

NIELSEN, S. G., REHKAMPER, M., TEAGLE, D. A. H., BUTTERFIELD, D. A., ALT, J. C. & HALLIDAY, A. N. 2006. Hydrothermal fluid fluxes calculated from the isotopic mass balance of thallium in the ocean crust. *Earth and Planetary Science Letters,* 251, 120-133.

NISHIOKA, J., OBATA, H. & TSUMUNE, D. 2013. Evidence of an extensive spread of hydrothermal dissolved iron in the Indian Ocean. *Earth and Planetary Science Letters,* 361, 26-33.

NOBLE, A. E., ECHEGOYEN-SANZ, Y., BOYLE, E. A., OHNEMUS, D. C., LAM, P. J., KAYSER, R., REUER, M., WU, J. F. & SMETHIE, W. 2015. Dynamic variability of dissolved Pb and Pb isotope composition from the US North Atlantic GEOTRACES transect. *Deep-Sea Research Part Ii-Topical Studies in Oceanography,* 116, 208-225.

NOBLE, A. E., LAMBORG, C. H., OHNEMUS, D. C., LAM, P. J., GOEPFERT, T. J., MEASURES, C. I., FRAME, C. H., CASCIOTTI, K. L., DITULLIO, G. R., JENNINGS, J. & SAITO, M. A. 2012. Basin-scale inputs of cobalt, iron, and manganese from the Benguela-Angola front to the South Atlantic Ocean. *Limnology and Oceanography,* 57, 989-1010.

NYE, V., COPLEY, J. T. & TYLER, P. A. 2013. Spatial Variation in the Population Structure and Reproductive Biology of Rimicaris hybisae (Caridea: Alvinocarididae) at Hydrothermal Vents on the Mid-Cayman Spreading Centre. *Plos One,* 8, 15.

PAKHOMOVA, S. V., HALL, P. O. J., KONONETS, M. Y., ROZANOV, A. G., TENGBERG, A. & VERSHININ, A. V. 2007. Fluxes of iron and manganese across the sediment–water interface under various redox conditions. *Marine Chemistry,* 107, 319-331.

PAWLAK, Z. & PAWLAK, A. S. 1999. Modification of iodometric determination of total and reactive sulfide in environmental samples. *Talanta,* 48, 347-353.

POITRASSON, F. & FREYDIER, R. 2005. Heavy iron isotope composition of granites determined by high resolution MC-ICP-MS. *Chemical Geology,* 222**,** 132-147.

POLYAKOV, V. B., CLAYTON, R. N., HORITA, J. & MINEEV, S. D. 2007. Equilibrium iron isotope fractionation factors of minerals: Reevaluation from the data of nuclear inelastic resonant X-ray scattering and Mossbauer spectroscopy. *Geochimica Et Cosmochimica Acta,* 71**,** 3833-3846.

QUEROUE, F., TOWNSEND, A., VAN DER MERWE, P., LANNUZEL, D., SARTHOU, G., BUCCIARELLI, E. & BOWIE, A. 2014. Advances in the offline trace metal extraction of Mn, Co, Ni, Cu, Cd, and Pb from open ocean seawater samples with determination by sector field ICP-MS analysis. *Analytical Methods,* 6**,** 2837-2847.

RAISWELL, R., BENNING, L. G., TRANTER, M. & TULACZYK, S. 2008. Bioavailable iron in the Southern Ocean: the significance of the iceberg conveyor belt. *Geochemical Transactions,* 9**,** 9.

RAISWELL, R., CANFIELD D., 2012. The iron biogeochemical cycle past and present. *Geochemical Perspectives,* 1**,** 1-232.

RAWLS, R. L. 1998. Some like it hot. *Chemical and Engineering News* [Online], 76. [Accessed 27.08.2015].

REED, M. H. & PALANDRI, J. 2006. Sulfide Mineral Precipitation from Hydrothermal Fluids. *Reviews in Mineralogy and Geochemistry,* 61**,** 609-631.

RESING, J. A., SEDWICK, P. N., GERMAN, C. R., JENKINS, W. J., MOFFETT, J. W., SOHST, B. M. & TAGLIABUE, A. 2015. Basin-scale transport of hydrothermal dissolved metals across the South Pacific Ocean. *Nature,* 523**,** 200-U140.

REVELS, B. N., OHNEMUS, D. C., LAM, P. J., CONWAY, T. M. & JOHN, S. G. 2015. The isotopic signature and distribution of particulate iron in the North Atlantic Ocean. *Deep-Sea Research Part Ii-Topical Studies in Oceanography,* 116**,** 321-331.

RICKARD, D. 1995. KINETICS OF FES PRECIPITATION .1. COMPETING REACTION-MECHANISMS. *Geochimica Et Cosmochimica Acta,* 59**,** 4367-4379.

RICKARD, D. & LUTHER, G. W. 1997. Kinetics of pyrite formation by the H2S oxidation of iron(II) monosulfide in aqueous solutions between 25 and 125 degrees C: The mechanism. *Geochimica Et Cosmochimica Acta,* 61**,** 135-147.

ROGERS, A. D., TYLER, P. A., CONNELLY, D. P., COPLEY, J. T., JAMES, R., LARTER, R. D., LINSE, K., MILLS, R. A., GARABATO, A. N., PANCOST, R. D., PEARCE, D. A., POLUNIN, N. V., GERMAN, C. R., SHANK, T., BOERSCH-SUPAN, P. H., ALKER, B. J., AQUILINA, A., BENNETT, S. A., CLARKE, A., DINLEY, R. J., GRAHAM, A. G., GREEN, D. R., HAWKES, J. A., HEPBURN, L., HILARIO, A., HUVENNE, V. A., MARSH, L., RAMIREZ-LLODRA, E., REID, W. D.,

ROTERMAN, C. N., SWEETING, C. J., THATJE, S. & ZWIRGLMAIER, K. 2012. The discovery of new deep-sea hydrothermal vent communities in the southern ocean and implications for biogeography. *PLoS Biol,* 10, e1001234.

ROSHAN, S., WU, J. & JENKINS, W. J. 2016. Long-range transport of hydrothermal dissolved Zn in the tropical South Pacific. *Marine Chemistry,* 183, 25-32.

ROSHAN, S. & WU, J. F. 2015. The distribution of dissolved copper in the tropical-subtropical north Atlantic across the GEOTRACES GA03 transect. *Marine Chemistry,* 176, 189-198.

ROTH, S. E. & DYMOND, J. 1989. Transport and settling of organic material in a deep-sea hydrothermal plume: evidence from particle flux measurements. *Deep Sea Research Part A. Oceanographic Research Papers,* 36, 1237-1254.

ROUXEL, O., SHANKS, W. C., BACH, W. & EDWARDS, K. J. 2008. Integrated Fe- and S-isotope study of seafloor hydrothermal vents at East Pacific rise 9-10 degrees N. *Chemical Geology,* 252, 214-227.

RUDNICKI, M. D. & ELDERFIELD, H. 1993. A Chemical-Model of the Buoyant and Neutrally Buoyant Plume Above the TAG Vent Field, 26 Degrees-N, Mid-Atlantic Ridge. *Geochimica et Cosmochimica Acta,* 57, 2939-2957.

SAITO, M. A., GOEPFERT, T. J. & RITT, J. T. 2008. Some thoughts on the concept of colimitation: Three definitions and the importance of bioavailability. *Limnology and Oceanography,* 53, 276-290.

SAITO, M. A. & MOFFETT, J. W. 2001. Complexation of cobalt by natural organic ligands in the Sargasso Sea as determined by a new high-sensitivity electrochemical cobalt speciation method suitable for open ocean work. *Marine Chemistry,* 75, 49-68.

SAITO, M. A., NOBLE, A. E., TAGLIABUE, A., GOEPFERT, T. J., LAMBORG, C. H. & JENKINS, W. J. 2013. Slow-spreading submarine ridges in the South Atlantic as a significant oceanic iron source. *Nature Geoscience,* 6, 775-779.

SANDER, S. G. & KOSCHINSKY, A. 2011. Metal flux from hydrothermal vents increased by organic complexation. *Nature Geoscience,* 4, 145-150.

SANDS, C. M., CONNELLY, D. P., STATHAM, P. J. & GERMAN, C. R. 2012. Size fractionation of trace metals in the Edmond hydrothermal plume, Central Indian Ocean. *Earth and Planetary Science Letters,* 319, 15-22.

SCHMIDT, K., KOSCHINSKY, A., GARBE-SCHÖNBERG, D., DE CARVALHO, L. M. & SEIFERT, R. 2007. Geochemistry of hydrothermal fluids from the ultramafic-hosted Logatchev hydrothermal field, 15°N on the Mid-Atlantic Ridge: Temporal and spatial investigation. *Chemical Geology,* 242, 1-21.

SCHWARZENBACH, R. P., GSCHWEND, P. M. & IMBODEN, D. M. 1993. *Environmental organic chemistry,* New York ; Chichester, Wiley.

SCHWERTMANN, U., FRIEDL, J. & STANJEK, H. 1999. From Fe(III) Ions to Ferrihydrite and then to Hematite. *Journal of Colloid and Interface Science,* 209, 215-223.

SEDWICK, P. N., SOHST, B. M., USSHER, S. J. & BOWIE, A. R. 2015. A zonal picture of the water column distribution of dissolved iron(II) during the U.S. GEOTRACES North Atlantic transect cruise (GEOTRACES GA03). *Deep Sea Research Part II: Topical Studies in Oceanography,* 116, 166-175.

SEVERMANN, S., JOHNSON, C. M., BEARD, B. L., GERMAN, C. R., EDMONDS, H. N., CHIBA, H. & GREEN, D. R. H. 2004. The effect of plume processes on the Fe isotope composition of hydrothermally derived Fe in the deep ocean as inferred from the Rainbow vent site, Mid-Atlantic Ridge, 36°14'N. *Earth and Planetary Science Letters,* 225, 63-76.

SEVERMANN, S., JOHNSON, C. M., BEARD, B. L. & MCMANUS, J. 2006. The effect of early diagenesis on the Fe isotope compositions of porewaters and authigenic minerals in continental margin sediments. *Geochimica et Cosmochimica Acta,* 70, 2006-2022.

SEVERMANN, S., LYONS, T. W., ANBAR, A., MCMANUS, J. & GORDON, G. 2008. Modern iron isotope perspective on the benthic iron shuttle and the redox evolution of ancient oceans. *Geology,* 36, 487-490.

SEYFRIED, W. E. & DING, K. 1993. The effect of redox on the relative solubilities of copper and iron in cl-bearing aqueous fluids at elevated-temperatures and pressures - an experimental-study with application to subseafloor hydrothermal systems. *Geochimica Et Cosmochimica Acta,* 57, 1905-1917.

SEYFRIED, W. E. & DING, K. 2013. Phase Equilibria in Subseafloor Hydrothermal Systems: a Review of the Role of Redox, Temperature, Ph and Dissolved Cl on the Chemistry of Hot Spring Fluids at Mid-Ocean Ridges. *Seafloor Hydrothermal Systems: Physical, Chemical, Biological, and Geological Interactions.* American Geophysical Union.

SHARMA, M., POLIZZOTTO, M. & ANBAR, A. D. 2001. Iron isotopes in hot springs along the Juan de Fuca Ridge. *Earth and Planetary Science Letters,* 194, 39-51.

SIEDLECKI, S. A., MAHADEVAN, A. & ARCHER, D. E. 2012. Mechanism for export of sediment-derived iron in an upwelling regime. *Geophysical Research Letters,* 39, 6.

SKULAN, J. L., BEARD, B. L. & JOHNSON, C. M. 2002. Kinetic and equilibrium Fe isotope fractionation between aqueous Fe(III) and hematite. *Geochimica Et Cosmochimica Acta,* 66, 2995-3015.

SMITH, D. K., CANN, J. R. & ESCARTIN, J. 2006. Widespread active detachment faulting and core complex formation near 13 degrees N on the Mid-Atlantic Ridge. *Nature,* 442, 440-443.

SPEER, K. G. & RONA, P. A. 1989. A model of an Atlantic and Pacific hydrothermal plume. *Journal of Geophysical Research-Oceans,* 94, 6213-6220.

SPRYNSKYY, M., KOWALKOWSKI, T., TUTU, H., CUKROWSKA, E. M. & BUSZEWSKI, B. 2011. Adsorption performance of talc for uranium removal from aqueous solution. *Chemical Engineering Journal,* 171, 1185-1193.

STATHAM, P. J., GERMAN, C. R. & CONNELLY, D. P. 2005. Iron(II) distribution and oxidation kinetics in hydrothermal plumes at the Kairei and Edmond vent sites, Indian Ocean. *Earth and Planetary Science Letters,* 236, 588-596.

STATHAM, P. J., SKIDMORE, M. & TRANTER, M. 2008. Inputs of glacially derived dissolved and colloidal iron to the coastal ocean and implications for primary productivity. *Global Biogeochemical Cycles,* 22, GB3013.

STEGEMEIER, J. P., REINSCH, B. C., LENTINI, C. J., DALE, J. G. & KIM, C. S. 2015. Aggregation of nanoscale iron oxyhydroxides and corresponding effects on metal uptake, retention, and speciation: II. Temperature and time. *Geochimica et Cosmochimica Acta,* 148, 113-129.

SYVERSON, D. D., BORROK, D. M. & SEYFRIED, W. E. 2013. Experimental determination of equilibrium Fe isotopic fractionation between pyrite and dissolved Fe under hydrothermal conditions. *Geochimica Et Cosmochimica Acta,* 122, 170-183.

TAGLIABUE, A., AUMONT, O., DEATH, R., DUNNE, J. P., DUTKIEWICZ, S., GALBRAITH, E., MISUMI, K., MOORE, J. K., RIDGWELL, A., SHERMAN, E., STOCK, C., VICHI, M., VÖLKER, C. & YOOL, A. 2016. How well do global ocean biogeochemistry models simulate dissolved iron distributions? *Global Biogeochemical Cycles,* 30, 149 - 174.

TAGLIABUE, A., *ET AL* 2010. Hydrothermal contribution to the oceanic dissolved iron inventory. *Nature,* 3, 252-256.

TEUTSCH, N., VON GUNTEN, U., PORCELLI, D., CIRPKA, O. A. & HALLIDAY, A. N. 2005. Adsorption as a cause for iron isotope fractionation in reduced groundwater. *Geochimica Et Cosmochimica Acta,* 69, 4175-4185.

TONER, B. M., FAKRA, S. C., MANGANINI, S. J., SANTELLI, C. M., MARCUS, M. A., MOFFETT, J., ROUXEL, O., GERMAN, C. R. & EDWARDS, K. J. 2009a. Preservation of iron(II) by carbon-rich matrices in a hydrothermal plume. *Nature Geoscience,* 2, 197-201.

TONER, B. M., SANTELLI, C. M., MARCUS, M. A., WIRTH, R., CHAN, C. S., MCCOLLOM, T., BACH, W. & EDWARDS, K. J. 2009d. Biogenic iron oxyhydroxide formation at mid-ocean ridge hydrothermal vents: Juan de Fuca Ridge. *Geochimica et Cosmochimica Acta,* 73, 388-403.

TREFRY, J. H., BUTTERFIELD, D. B., METZ, S., MASSOTH, G. J., TROCINE, R. P. & FEELY, R. A. 1994. Trace-Metals in Hydrothermal Solutions from Cleft Segment on the Southern Juan De Fuca Ridge. *Journal of Geophysical Research-Solid Earth,* 99, 4925-4935.

TREFRY, J. H. & METZ, S. 1989. Role of hydrothermal precipitates in the geochemical cycling of Vanadium. *Nature,* 342**,** 531-533.

TROCINE, R. P. & TREFRY, J. H. 1988. Distribution and chemistry of suspended particles from an active hydrothermal vent site on the Mid-Atlantic ridge at 26-degrees-N. *Earth and Planetary Science Letters,* 88**,** 1-15.

VAN HEUZEN, A. A., HOEKSTRA, T. & VAN WINGERDEN, B. 1989. Precision and accuracy attainable with isotope dilution analysis applied to inductively coupled plasma mass spectrometry: theory and experiments. *Journal of Analytical Atomic Spectrometry,* 4**,** 483-489.

VAZQUEZ, F., ZHANG, J. Z. & MILLERO, F. J. 1989. Effect of metals on the rate of oxidation of H2S in seawater. *Geophysical Research Letters,* 16**,** 1363-1366.

VON DAMM, K. L. 1990. Seafloor Hydrothermal Activity - Black Smoker Chemistry and Chimneys. *Annual Review of Earth and Planetary Sciences,* 18**,** 173-204.

VON DAMM, K. L. 1995. Temporal and Compositional Diversity in Sea-Floor Hydrothermal Fluids. *Reviews of Geophysics,* 33**,** 1297-1305.

VON DAMM, K. L., EDMOND, J. M., GRANT, B. & MEASURES, C. I. 1985. Chemistry of submarine hydrothermal solutions at 21-degrees-N, East Pacific Rise. *Geochimica et Cosmochimica Acta,* 49**,** 2197-2220.

VON DER HEYDEN, B. P., HAUSER, E. J., MISHRA, B., MARTINEZ, G. A., BOWIE, A. R., TYLISZCZAK, T., MTSHALI, T. N., ROYCHOUDHURY, A. N. & MYNENI, S. C. B. 2014. Ubiquitous Presence of Fe(II) in Aquatic Colloids and Its Association with Organic Carbon. *Environmental Science & Technology Letters,* 1**,** 387-392.

WADHAM, J. L., DE'ATH, R., MONTEIRO, F. M., TRANTER, M., RIDGWELL, A., RAISWELL, R. & TULACZYK, S. 2013. The potential role of the Antarctic Ice Sheet in global biogeochemical cycles. *Earth and Environmental Science Transactions of the Royal Society of Edinburgh,* 104**,** 55-67.

WALTER, H. J., HEGNER, E., DIEKMANN, B., KUHN, G. & VAN DER LOEFF, M. M. R. 2000. Provenance and transport of terrigenous sediment in the South Atlantic Ocean and their relations to glacial and interglacial cycles: Nd and Sr isotopic evidence. *Geochimica Et Cosmochimica Acta,* 64**,** 3813-3827.

WAYCHUNAS, G. A., KIM, C. S. & BANFIELD, J. F. 2005. Nanoparticulate Iron Oxide Minerals in Soils and Sediments: Unique Properties and Contaminant Scavenging Mechanisms. *Journal of Nanoparticle Research,* 7**,** 409-433.

WEBBER, A. P., ROBERTS, S., MURTON, B. J. & HODGKINSON, M. R. S. 2015. Geology, sulfide geochemistry and supercritical venting at the Beebe Hydrothermal Vent Field, Cayman Trough. *Geochemistry Geophysics Geosystems,* 16**,** 2661-2678.

WELCH, S. A., BEARD, B. L., JOHNSON, C. M. & BRATERMAN, P. S. 2003. Kinetic and equilibrium Fe isotope fractionation between aqueous Fe(II) and Fe(III). *Geochimica Et Cosmochimica Acta,* 67**,** 4231-4250.

WELHAN, J. A. 1988. Origins of Methane in Hydrothermal Systems. *Chemical Geology,* 71**,** 183-198.

WELLS, M. L., KOZELKA, P. B. & BRULAND, K. W. 1998. The complexation of `dissolved' Cu, Zn, Cd and Pb by soluble and colloidal organic matter in Narragansett Bay, RI. *Marine Chemistry,* 62**,** 203-217.

WILKIN, R. T. & BARNES, H. L. 1997. Formation processes of framboidal pyrite. *Geochimica et Cosmochimica Acta,* 61**,** 323-339.

WORSFOLD, P. J., LOHAN, M. C., USSHER, S. J. & BOWIE, A. R. 2014. Determination of dissolved iron in seawater: A historical review. *Marine Chemistry,* 166**,** 25-35.

WU, J. F. & BOYLE, E. A. 1997. Low blank preconcentration technique for the determination of lead, copper, and cadmium in small-volume seawater samples by isotope dilution ICPMS. *Analytical Chemistry,* 69**,** 2464-2470.

WU, J. F., WELLS, M. L. & REMBER, R. 2011a. Dissolved iron anomaly in the deep tropical-subtropical Pacific: Evidence for long-range transport of hydrothermal iron. *Geochimica et Cosmochimica Acta,* 75**,** 460-468.

WU, L. L., BEARD, B. L., RODEN, E. E. & JOHNSON, C. M. 2011c. Stable Iron Isotope Fractionation Between Aqueous Fe(II) and Hydrous Ferric Oxide. *Environmental Science & Technology,* 45**,** 1847-1852.

XIANG-ZHAO, K., TUTOLO, B. M. & SAAR, M. O. 2013. DBCreate: a SUPCRT92-based program for producing EQ3/6, TOUGHREACT, and GWB thermodynamic databases at user-defined T and P. *Computers & Geosciences,* 51**,** 415-417.

YUCEL, M., GARTMAN, A., CHAN, C. S. & LUTHER, G. W. 2011. Hydrothermal vents as a kinetically stable source of iron-sulphide-bearing nanoparticles to the ocean. *Nature Geoscience,* 4**,** 367-371.

YUCEL, M. & LUTHER, G. W. 2013. Temporal trends in vent fluid iron and sulfide chemistry following the 2005/2006 eruption at East Pacific Rise, 9 degrees 50 ' N. *Geochemistry Geophysics Geosystems,* 14**,** 759-765.

ZENG, Z. G., OUYANG, H. G., YIN, X. B., CHEN, S., WANG, X. Y. & WU, L. 2012. Formation of Fe-Si-Mn oxyhydroxides at the PACMANUS hydrothermal field, Eastern Manus Basin: Mineralogical and geochemical evidence. *Journal of Asian Earth Sciences,* 60**,** 130-146.